UNIVERSITÉ CLAUDE BERNARD - LYON 1

N° d'ordre : 160 LYON 2000

THÈSE

présentée et soutenue publiquement

pour obtenir le titre de

DOCTEUR DE L'ÉCOLE NORMALE SUPÉRIEURE DE LYON

par

Monsieur Dimitrios SAKELLARIOU

le 15 Septembre 2000

Titre :

DÉVELOPPEMENT DE NOUVELLES MÉTHODES POUR LA HAUTE RÉSOLUTION EN RÉSONANCE MAGNÉTIQUE NUCLÉAIRE DES SOLIDES

Sous la direction du Pr. Lyndon EMSLEY

JURY:	Pr. B. MEIER	Rapporteur
	Dr. S. CALDARELLI	Rapporteur
	Pr. L. EMSLEY	Directeur
	Pr. G. BODENHAUSEN	Examinateur
	Dr. D. MARION	Examinateur

UNIVERSITY CLAUDE BERNARD - LYON 1

DEVELOPMENT OF NEW METHODS FOR HIGH RESOLUTION IN NUCLEAR MAGNETIC RESONANCE OF SOLIDS

DOCTORAL THESIS
Presented to the École Normale Supérieure de Lyon

by
Dimitrios SAKELLARIOU

Examined by a jury composed of

Prof. B. MEIER	ETH, Zurich
Dr. S. CALDARELLI	Institut de Recherche sur la Catalyse, Lyon
Prof. L. EMSLEY	Directeur de Thèse
Prof. G. BODENHAUSEN	École Normale Supérieure, Paris
Dr. D. MARION	Institut de Biologie Structurale, Grenoble

Lyon 2000

Acknowledgment

A lot of persons contributed directly and indirectly, more or less, to the achievement of this work.

I would like to thank particularly **Pr. Beat Meier** for accepting to be rapporteur of my thesis.

I am greatful to **Pr. Geoffrey Bodenhausen** and **Dr. Dominique Marion** for accepting to participate the jury of my thesis.

I would like to thank particularly **Dr. Stefano Caldarelli** for being rapporteur for my thesis. I had the pleasure to meet him during my thesis, in different scientific (and not only) events and I thank him for his energy, for his deep thinking and the great ambiance he brings with him.

Then, I would like to thank **Dr. Stefan Steuernagel**, for many useful hints on the spectrometer, for the nice collaboration we had during two weeks in Germany.

Many thanks to **Dr. Michel Bardet** for giving me the opportunity to work in the laboratories of CEA-Grenoble, during my difficult period of experimental data collection. I want also to thank **Mme Foray** for all her help with the spectrometer.

I am greatful to all the members of the **STIM** laboratory and particularly to those of the **ENS NMR group**, past and present with whom I spent almost 5 years of my scientific life. It was a real pleasure to work in this team.

Many thanks to my office partners, **Patrick Charmont** and **Gaël DePaëpe** for the wonderful atmosphere they provided.

Next, I would like to thank three persons who completed my solid-state NMR education. First of all, a unmeasurable thanks to **Dr. Anne Lesage** for her constant help throughout this work. Without her, a great part of the work presented here, would never exist. I would like also thank **Dr. Paul Hodgkinson**, for showing me the world of numerical simulations. The numerous and long and (maybe) profound discussions we had, proved fruitful and are at the core of many of the ideas presented here. I also thank him for the nice collaboration we had in the University of Durham.

I would also like to thank **Dr. Sabine Hediger** for all the illuminating discussions we had on almost all NMR domains.

I would like to thank especially **Pr. Lyndon Emsley** for having me in his team for the last 5 years. It was a pleasure to learn from him a lot of things about NMR (and not only) and participate actively in many scientific events (congress, magnet installations (many), collaborations, restaurants, clubs, etc.). I would like to thank him for his enthusiasm, and the permanent encouragement during the course of this work and for the freedom I had to develop (what I though were) my own ideas during my PHD thesis. His patience in front of difficult situations taught me a lot.

Finally, I would like to thank all the people I met in France with whom I had great moments. I don't forget to thank my friends in Greece who contributed in their way, during my holidays.

Special thanks to **Bénédicte** for putting up with me and for making my life in France happy.

As a small token of my gratitude for what they have done for me, I dedicate this work to **Eleni** and **Takis**, my parents.

Contents

Résumé

L'utilisation de la Résonance Magnétique Nucléaire (RMN) pour l'étude de la structure et la dynamique des molécules à l'état solide devient de plus en plus courante grce au développement et à l'utilisation de nouvelles techniques [1–4]. L'utilisation combinée de la spectroscopie de corrélation multi-dimensionelle, de la rotation à l'angle magique [5], de la polarisation croisée [6, 7] et du découplage à haute puissance de champ radiofréquence, a donné les conditions nécessaires mais pas toujours suffisantes pour effectuer des expériences utiles d'un point de vue analytique. Les noyaux rares tels que le carbone-13 dans les composés cristallins, sous les conditions de RMN haute résolution, donnent des résonances fines aux fréquences de Larmor isotropes. Ceci facilite énormément l'extraction de l'information structurale. L'attribution de ces résonances fines reste néanmoins un des problmes actuels à la RMN du solide. Des techniques d'édition spectrale existent en RMN du liquide pour caractériser les spectres ^{13}C et elles utilisent les couplages scalaires comme mécanisme de transfert de polarisation. Ces expériences donnent des sous-spectres de carbones, en fonction du nombre d'hydrognes qui leur sont chimiquement liés. Ainsi, l'attribution est facilitée en utilisant des spectres simples unidimensionnels. Des séquences analogues existent pour l'état solide, mais le mécanisme du transfert est basé sur les couplages dipolaires, qui sont forts et qui constituent l'interaction dominante à l'état solide. Dans la premire partie de cette thse on examinera la possibilité d'utiliser les couplages scalaires J à l'état solide pour créer des séquences de filtrages à plusieurs quanta et de cette façon faire de l'édition spectrale. L'extension de ces idées va donner lieu au développement de la spectroscopie de corrélation hétéronucléaire via les interactions J en solide. Toujours dans ce premier chapitre, on appliquera ces nouvelles séquences à des composés organiques ordinaires, pour démontrer leur efficacité et leur utilité.

La clé pour effectuer de la spectroscopie haute résolution afin de pouvoir observer et utiliser les interactions scalaires en solide, est le découplage homonucléaire entre les noyaux d'hydrogne (protons). Quand le "bain" de protons est fortement couplé il empêche l'observation d'interactions faibles comme les couplages scalaires, même en présence de rotation à l'angle magique trs rapide. L'efficacité du découplage étant un des facteurs expérimentaux les plus importants, dans le deuxime chapitre de cette thse on développera une nouvelle approche basée sur l'optimisation numérique. Cette approche, appelée DUMBO, sera appliquée dans le cadre du découplage homonucléaire entre protons et les résultats obtenus seront détaillés. En même

temps, le cadre théorique de cette approche sera établi et quelques applications de la même approche numérique sur d'autres problmes en RMN seront également discutées.

Il est alors évident qu'une compréhension théorique de la dynamique du spin en solide donnerait un support solide pour la modélisation numérique et pour le développement de nouvelles séquences. Le phénomne de la diffusion de spin traite ce problme dans son intégralité. Nous nous sommes focalisés sur deux expériences à la fois complexes et trs utiles: celle de la diffusion de spin induite par les protons et celle de la polarisation croisée. La premire expérience est l'équivalent de la spectroscopie NOESY en solide et contient beaucoup d'information structurale (distances internucléaires, angles etc.) mais elle est aussi trs difficile à exploiter. Dans le troisime chapitre de cette thse on essaiera de modéliser numériquement ce phénomne en résolvant exactement l'équation de mouvement pour un nombre important de spins nucléaires. Le comportement dans une échelle de temps trs longue a un intérêt particulier et dans cette dernire partie on présentera quelques arguments théoriques pour soutenir l'idée que le systme garde toujours ses caractéristiques quantiques même à long terme. Cette même théorie prédit que cet état de quasi-équilibre doit être synchronisé avec la modulation lorsque le systme de spins est modulé dans le temps et des preuves expérimentales seront présentées. Finalement on utilisera l'idée de l'exploitation de la périodicité spatiale de l'Hamiltonien afin de pouvoir traiter un grand nombre de spins en simulation numérique exacte.

Filtres à Multiples Quanta

En utilisant la spectroscopie de RMN de haute résolution à l'état liquide on peut simplifier considérablement des spectres trs compliqués et extraire des informations sur des molécules assez grandes comme des membranes ou des protéines. Si on se limite aux spectres unidimensionnels, une manipulation appropriée de l'Hamiltonien de spin nous donne la possibilité de diviser un spectre qui contient plusieurs résonances en plusieurs sous-spectres dont chacun contient un groupe différent de résonances. On appelle cette méthode de simplification *édition spectrale* et elle est régulirement utilisée par les chimistes pour analyser efficacement des molécules compliquées.

Il y plusieurs techniques d'édition spectrale en liquide (DEPT [8], INEPT [9], APT [10–14]). A l'état solide quelques techniques existent [15–22]. La plupart d'entre elles sont des expériences de champ local séparé (Separated Local Field) et elles sont basées sur la différence de dynamique de spin entre les différents groupes de carbones. L'interaction sur laquelle reposent toutes ces expériences est le couplage dipolaire hétéronucléaire entre les noyaux de carbone et d'hydrogne.

L'utilisation des couplages J en solide a été jusqu'alors limitée aux cristaux plastiques ou à des matériaux ayant une forte mobilité. Des développements récents ont permis de résoudre des couplages J hétéronucléaires sur des composés organiques beaucoup plus rigides [23, 24], et bien sûr de les utiliser comme à l'état liquide. Le

test des protons attachés (Attached Proton Test) a été implémenté en introduisant des changements appropriés à l'état solide [24].

L'idée que l'on développe ici est l'utilisation des interactions scalaires J hétéronucléaires pour créer des cohérences à multiple quanta, comme à l'état liquide. Si on filtre ces cohérences à multiples quanta, par exemple, par un cyclage de phase approprié, on obtiendra de l'édition spectrale n'ayant pas les problmes d'ambiguïté intimement liés avec l'utilisation des interactions dipolaires.

Afin d'utiliser les interactions J qui sont petites devant les interactions dipolaires, il est nécessaire de générer un Hamiltonien effectif pour lequel les interactions dipolaires sont moyennées à zéro. Ceci est obtenu en combinant la rotation rapide à l'angle magique (Magic Angle Spinning) avec le découplage homonucléaire des protons. Dans le développement de nos séquences nous considérons que le découplage homonucléaire est parfait, et donc que le reste de l'Hamiltonien dipolaire qui contient les couplages hétéronucléaires, devient inhomogne [23, 25]. Dans ce cas la rotation rapide à l'angle magique moyenne toutes les interactions inhomognes anisotropes et l'Hamiltonien effectif du systme ressemble à celui des liquides. L'interaction bilinéaire dominante dans cet Hamiltonien est le couplage scalaire hétéronucléaire multiplié par un facteur d'échelle, lié à la séquence de découplage homonucléaire.

Une nouvelle séquence d'édition spectrale est proposée. Elle est basée sur des calculs faits à partir de cet Hamiltonien effectif, à l'aide du formalisme d'opérateur densité, largement utilisé en liquide. Avec un cyclage de phase approprié, on est capable de filtrer des cohérences à multiples quanta et d'obtenir une attribution de multiplicité non-ambigüe. Ainsi les groupes CH_3 sont les seuls à pouvoir générer des cohérences à trois quanta en proton, ce qui permet d'avoir un sous-spectre contenant seulement les CH_3 de la molécule. Des filtrages à un et deux quanta sont aussi possibles et sont démontrés expérimentalement sur des composés organiques ordinaires.

Spectroscopie de Corrélation Hétéronucléaire à travers des Liaisons

Contrairement aux noyaux rares comme le carbone-13 ou l'azote-15, qui donnent des spectres fins et bien résolus en RMN du solide (pour des composés cristallins sous des conditions de haute résolution), les spectres du proton (^{1}H) des molécules organiques en poudre, présentent des résonances larges à cause des interactions dipolaires homonucléaires. Les largeurs de raies en proton peuvent être partiellement réduites en combinant la rotation à l'angle magique et la spectroscopie de multi-impulsionelle (Combined Rotation And Multiple Pulse Spectroscopy: CRAMPS) [26–30]. Afin d'améliorer encore la résolution du spectre ^{1}H et éviter le recouvrement des résonances, il est possible d'utiliser ces techniques CRAMPS dans des expériences bi-dimensionnelles de corrélation hétéronucléaire (HETeronuclear CORrelation) [31–39]. La résolution du spectre proton est alors augmentée par

l'introduction de la deuxime dimension de déplacement chimique du carbone et des informations sur le déplacement isotrope des protons deviennent accessibles. Ainsi, le proton devient un noyau-sonde attractif dans le développement des études structurales par RMN du solide.

Toutes les expériences de corrélation proton-carbone dans la littérature, utilisent les couplages dipolaires comme mécanisme de transfert de polarisation [31–33]. Ici on propose l'utilisation des couplages scalaires hétéronucléaires (comme en liquide) afin de transférer l'aimantation et corréler les noyaux entre eux. La modification de la spectroscopie des filtres à multiples quanta en une expérience deux dimensions est directe. Si on laisse évoluer les cohérences à multiples quanta pendant une période de temps t_1, on peut observer leur fréquence d'évolution aprs une transformée de Fourier. Cette fréquence est égale au déplacement isotrope des protons.

La dynamique du spin de cette séquence est presque identique à celle développée pour les filtres à multiples quanta. Aprs une étape de polarisation croisée à partir des spins abondants ^{1}H (spins I), l'aimantation des spins rares (spins S), typiquement ^{13}C ou ^{15}N, évolue pendant un premier intervalle de temps τ sous un Hamiltonien qui contient seulement le couplage hétéronucléaire scalaire. Cet Hamiltonien effectif est obtenu en utilisant la séquence de découplage homonucléaire Frequency-Switched Lee-Goldburg [40–42] dans un régime de rotation à l'angle magique assez rapide. Pour une paire de noyaux liés par liaison chimique I–S, l'aimantation transverse S_x évolue dans le temps et devient une cohérence en anti-phase ($2I_zS_y$) par rapport au proton attaché. Cette anti-phase est transformée par une impulsion $\pi/2$ en cohérence hétéronucléaire à multiple quanta ($2I_yS_y$) qui évolue pendant t_1, seulement sous l'effet du déplacement chimique isotrope du proton. la fin de cette période d'évolution t_1, les cohérences à multiples quanta sont converties en anti-phases par une deuxime impulsion $\pi/2$ sur le proton. Pendant la deuxime intervalle τ les anti-phases évoluent et deviennent des cohérences S observables pendant t_2.

Des expériences sont présentées qui démontrent la validité et l'utilité de cette technique. Tout d'abord nous montrons, sur un échantillon de cristal plastique (camphre), pour lequel il est facile de découpler efficacement les protons, que l'expérience fonctionne et nous mettons en évidence la présence de corrélations à plusieurs liaisons. Les couplages scalaires à 2 ou 3 liaisons peuvent, en effet, donner des corréélations si l'intervalle τ de création des anti-phases est suffisamment long. Cet effet va nous servir dans la suite pour combiner l'expérience à courte portée (τ court) avec celle à longue portée (τ long) afin d'attribuer compltement les spectres proton, carbone et azote d'un tripeptide en abondance naturelle à l'état de poudre. Le déplacement chimique isotrope des protons pour des molécules de taille assez grande comme le cholesteryl acetate sont extraits à l'aide de cette l'expérience de corrélation. Finalement, une simple comparaison sur la sensibilité et la sélectivité entre les expériences de corrélation par les couplages dipolaires et par les couplages scalaires est faite.

Découplage Homonucléaire

Dans le deuxime chapitre, on montre comment on peut construire des séquences qui utilisent les interactions scalaires, comme en liquide, pour faire de l'attribution de spectres de molécules en abondance naturelle à l'état de poudre. La clé pour l'élaboration de telles séquences est le découplage homonucléaire entre les protons. Il est évident que plus le découplage homonucléaire est efficace, plus les séquences de type liquide vont être performantes. Ainsi, dans le troisime chapitre nous nous intéressons au développement de nouveaux outils pour améliorer le découplage en solide.

Le découplage homonucléaire a toujours été la pierre angulaire pour la RMN de haute résolution en solide. Lee et Goldburg [43] ainsi que Waugh, Huber et Haeberlen [44] ont proposé les premiers développements dans le domaine. Depuis, beaucoup de schémas de découplage ont été proposés, qui reposent soit sur une irradiation continue off-résonance [40, 42, 43, 45], soit sur des impulsions multiples on-résonance [44,46–53]. D'autres schémas qui n'ont pas eu le succs expérimental des précédents ont été développés dans la littérature [54–56]. La quasi totalité des ces schémas ont été développé en utilisant la théorie de l'Hamiltonien moyen (Average Hamiltonian Theory), qui a été introduite par Haeberlen et Waugh [57].

Ce troisime chapitre débute par une brve introduction à cette théorie. On démontre par la suite que le facteur d'échelle dû au découplage homonucléaire est obligatoirement plus petit que $1/\sqrt{3}$ dans le cas des échantillons statiques et que pour les échantillons en rotation, une telle restriction n'existe pas.

La combinaison de la rotation et de la spectroscopie d'impulsions multiples (CRAMPS) a été introduite assez tôt en RMN du solide [26–29]. Les échelles de temps pour faire la moyenne par la rotation de l'échantillon et par les impulsions de radio-fréquence sont trs différentes ce qui permet d'éviter des interférences destructives entre les deux techniques. Une situation intéressante se produit lorsque les deux échelles de temps sont comparables. Dans ce cas, l'approximation quasi-statique n'est plus valable et des arguments de synchronisation doivent être évoqués pour adapter les séquences existantes [51, 52, 58] ou élaborer de nouvelles séquences synchronisées avec la rotation [59, 60].

Expérimentalement, CRAMPS a toujours été considéré comme une technique assez compliquée [30]. Ceci est dû au fait qu'il est nécessaire d'avoir dans la séquence d'impulsions des intervalles d'évolution libre afin de pouvoir observer le signal. Dans les séquences développées au deuxime chapitre ce qui importe est seulement l'efficacité du découplage, puisque l'on observe directement le carbone ou l'azote. En revanche, on peut observer le proton *indirectement*, dans une expérience de corrélation bi-dimensionelle ayant une meilleure résolution par rapport au spectre CRAMPS uni-dimensionel. On présente alors des spectres 2D HMQC de l'alanine qui montrent que la résolution atteinte en proton est comparable à celle obtenue avec des schémas synchronisés [51, 52]. L'avantage de cette méthode d'observation indirecte est que dans la suite on va pouvoir développer des séquences qui n'ont

pas de fenêtres d'observation et qui peuvent envoyer le maximum de puissance radiofréquences pendant toute la période du découplage.

L'Approche DUMBO

Comme on vient de le dire, la grande majorité des séquences de découplage ont été développées sur la base de la théorie analytique de l'Hamiltonien moyen [57]. On peut noter que ces séquences multi-impulsionelles, comme leur nom le suggre, consistent en une série d'impulsions discrtes qui ont souvent des phases relatives de 90°, et des durées de 90° pour chaque impulsion. Ceci est dû au fait que leur performance a été calculée à partir de calculs analytiques qui peuvent être faits jusqu'à un ordre plus ou moins élevé dans le développement de Magnus. Ainsi la performance de la séquence est fixée par le calcul, et ne peut pas être facilement adaptée à des problmes spécifiques.

On propose ici une nouvelle famille de séquences de découplage basée sur une modulation continue de phase. Ainsi la phase est décrite par une fonction du temps continue qui peut être facilement paramtrisée. On décrit certaines possibilités de paramétrisation et les problmes théoriques qui peuvent apparatre. La paramétrisation qui parait être le mieux adaptée pour ce type de problme consiste à décrire la phase comme une série de Fourier tronquée à un certain ordre maximum. La fréquence de modulation de la série est égale à l'amplitude de l'irradiation radio-fréquence que l'on envoie. On décrit alors une séquence par ces coefficients de Fourier qui peuvent être variés afin d'améliorer sa performance. Ainsi on augmente le nombre de "degrés de liberté" de la séquence et on la rend plus flexible et potentiellement adaptable aux spécifications voulues.

Cette paramétrisation permet d'effectuer des optimisations numériques sur la performance du découplage. Pour faire ceci, on doit modéliser le comportement du systme de spins sur ordinateur. Dans les simulations on ne considre pas la rotation de l'échantillon, ce qui revient à se placer dans l'approximation quasi-statique. Pour estimer la performance du découplage on calcule exactement l'Hamiltonien effectif pendant une période de découplage. Ceci est fait numériquement par multiplication successive des propagateurs temporels pour chaque instant pendant la séquence. Ensuite on décompose l'Hamiltonien effectif sur une base d'opérateurs produits [61]. Cette décomposition nous informe sur l'importance relative des termes linéaires (déplacement chimique) et multi-linéaires (couplages) présents dans l'Hamiltonien effectif. Notre but est de minimiser les termes multi-linéaires et de maximiser les termes linéaires, rendant la résolution optimale.

Un nombre important de combinaisons de coefficients de Fourier est généré, comme dans une procédure de type Monte-Carlo et la performance des séquences issues est testée numériquement. Seuls les meilleurs résultats sont ensuite introduits dans une procédure d'optimisation numérique, par rapport à un facteur de qualité qui a été choisi pour représenter la résolution due au découplage. L'optimisation de

ce facteur sur une surface de couplages dipolaires et d'amplitudes radiofréquences variables, garantie la robustesse de la séquence par rapport à l'inhomogénéité de la sonde pour un échantillon solide à l'état de poudre.

Le premier résultat de cette approche appelé DUMBO-1 (Decoupling Under Mind Boggling Optimizations) est expérimentalement testé et les résultats montrent que cette séquence découple au moins aussi bien que les meilleures séquences actuelles. La robustesse de DUMBO-1 par rapport à l'inhomogénéité de la sonde est démontrée expérimentalement en utilisant une sonde de diamtre 7 mm (donc inhomogne), pour laquelle les techniques actuelles (FSLG) ne fonctionnent pas aussi bien. Il est aussi expérimentalement montré que DUMBO-1 est robuste par rapport à la fréquence d'irradiation des protons. Des exemples de spectroscopie de corrélation proton-carbone et proton-proton sont montrés en utilisant cette nouvelle séquence et les résultats montrent des largeurs de raies en proton plus petites que celles obtenues par FSLG.

la fin de ce chapitre quelques extensions de l'approche DUMBO à d'autres problmes de RMN sont présentées. L'application de la méthode pour trouver des séquences insensibles ou spécifiques en B_1 donnent des séquences performantes. L'application de l'approche DUMBO au problme du découplage hétéronucléaire parait aussi trs interessante.

Diffusion de Spin

La diffusion de spin nucléaire à l'état solide est un phénomne complexe qui présente un intérêt fondamental et pratique dans son utilisation à la spectroscopie de RMN. Le terme de diffusion de spin a été introduit par Bloembergen [62, 63] et décrit l'échange d'aimantation entre noyaux via une interaction de couplage. Les transitions flip-flop entre des paires de noyaux successifs constituent un mécanisme de transport d'aimantation dans l'échantillon.

Au troisime chapitre nous présentons de nouvelles méthodes pour limiter au maximum la diffusion entre les protons (decouplage homonucléaire). Dans ce quatrime chapitre, on essaiera de comprendre davantage le phénomne de diffusion de spin afin de pouvoir mieux le modéliser pour l'exploiter. On étudiera quelques exemples de diffusion de spin en essayant de comparer les résultats expérimentaux avec les prévisions théoriques à partir de calculs numériques.

La diffusion entre les noyaux de ^{13}C est trs intéressante puisque les résonances des carbones sont mieux résolues que celles des protons et que l'expérience est trs simple. Cette diffusion homonucléaire est induite par la présence des protons (proton-driven) et contient de l'information sur les connectivités du squelette de la molécule et sur les distances internucléaires. Si les expériences d'échange présentées ici ressemblent beaucoup à la spectroscopie qui exploite l'effet NOE en liquide, l'extraction des information structurales parait trs complexe.

Des expériences bi-dimensionnelles d'échange et des mesures de vitesse de diffu-

sion sont présentées sur un échantillon de poudre de L-alanine compltement marqué en carbone-13. Nous essayons ensuite de modéliser numériquement les résultats expérimentaux, sans pourtant arriver à un accord satisfaisant. Il semble que le nombre de protons explicitement inclus dans les simulations n'est pas assez grand pour décrire correctement le "bain" de protons. En fait, dans les simulations numériques exactes on est limité à un petit nombre de spins, ce qui nous oblige à développer de nouveaux moyens pour traiter ce problme à plusieurs corps. On est alors obligé d'introduire des méthodes approximatives et on présentera quelques résultats théoriques sur le comportement de l'aimantation à long terme, issus de l'application de la théorie des perturbations indépendantes du temps.

L'état de Quasi-équilibre en Solide

Dans les premires discussions sur l'échange d'aimantation nucléaire à l'état solide, sa dynamique est décrite en termes d'équilibration de "températures de spin" [64]. Pourtant, les systmes de spin nucléaire ne correspondent pas toujours (surtout sous des conditions de haute résolution) à des systmes o des arguments thermodynamiques simple sont valables. Ceci peut être démontré expérimentalement par la réversibilité de la diffusion de spin [65]. Dernirement, plusieurs discussions dans la littérature ont été focalisées sur l'idée de simulations de type *ab initio* de diffusion de spin [66, 67]. Pourtant, les simulations de dynamique de polarisation dans de petits systmes de spin ne peuvent pas être applicables à des expériences qui traitent des échantillons macroscopiques. Si on veut faire des études de mécanique quantique statistique en accord avec les résultats expérimentaux, on doit considérer l'effet du couplage entre le systme de spin et son environnent.

L'état de quasi-équilibre est défini par rapport à l'évolution sous l'Hamiltonien libre (sans relaxation) d'un systme de spin. Il correspond à l'état o le systme se trouve aprs un trs grand intervalle de temps. Pour les petits systmes de spin isolés cet état est purement théorique, parce que les oscillations transitoires entre les états propres de l'Hamiltonien sont toujours présentes, même à de trs longues échelles de temps. Ici on va tenir compte de l'effet de l'environnement dans le déphasage de ces oscillations transitoires, en utilisant la théorie de perturbations, introduite dans la section précédente.

Ce cadre théorique prévoit alors, que l'état du quasi-équilibre peut être atteint par un systme de spins couplé avec son environnent, dans des temps expérimentalement réalisables. D'autre part, la réversibilité dans le temps est préservée dans ce contexte ce qui est en accord avec les expériences. L'application de ces idées dans le cas des échantillons tournants à l'angle magique, prévoit des états de quasi-équilibre périodiques et synchronisés avec la rotation. Des expériences sont effectuées et les résultats sont en accord avec la théorie, dans le cas d'échantillons modles (ferrocne) ou ordinaires (L-alanine). Il semble alors que les caractéristiques quantiques ne sont pas perdues lorsque le systme atteint une taille mésoscopique.

Systmes Spatialement Périodiques

Une autre faon pour augmenter le nombre de spins qui peuvent être traités numériquement de faon exacte, est d'utiliser la symétrie de translation qui existe dans les cristaux. Ceci est une idée présente dans la physique de la matire condensée (théorie de bandes), mais qui n'a pas été appliquée à un grand systme de spins dans le cas de la RMN, o la température est considérée comme infinie. Si l'opérateur densité est spatialement périodique, sous l'influence d'un Hamiltonien spatialement périodique, on peut facilement démontrer qu'il suffit de considérer l'évolution d'une cellule du réseau pour décrire tout le systme. De plus, si on utilise l'opération de symétrie liée à la translation, on peut facilement diagonaliser par bloc l'Hamiltonien total du systme.

Numériquement, il est plus efficace de créer les éléments de matrice de l'Hamiltonien directement dans la base adaptée à la symétrie, ce qui nous a permis de traiter des systmes jusqu'à 15 spins. Les résultats concernant le comportement du spectre en fonction du nombre de spins montrent une convergence, vers une forme de raie lisse qui a pourtant une structure. Ceci peut bien sûr être interprété comme une particularité d'un systme uni-dimensionel monocristallin, mais démontre que les hypothses théoriques sur les formes de raies sans structure (Gaussiennes, Lorentziennes etc.) peuvent dans certains cas être controversées.

Chapter 1

Introduction

This is an effort to condense the work of the last three years, within the framework of my PHD thesis in the Laboratory of Stereochemistry and Molecular Interactions of the cole Normale Suprieure de Lyon.

Nuclear Magnetic Resonance Spectroscopy (NMR) is one of the most powerful tools for the characterization of molecules in liquid state. Solid-state NMR has performed a important evolution during last decades, and nowadays has the potential to compete standard solid-state techniques, such as X-ray diffraction, or neutron scattering. Recent developments in the area of solid-state NMR are using ideas from the liquid-state background. Technical advances in probe design allow very fast Magic Angle Spinning frequencies (50 kHz) and high radio-frequency powers (200 kHz). It becomes thus possible to obtain isotropic spectra for polycrystalline organic compounds in natural isotopic abundance. We were interested in the evolution of solid-state methods towards high resolution liquid-like methods.

The assignment of a natural abundance organic compound is one of the remaining problems in solid-state NMR. In Chapter 2 we use the scalar heteronuclear interactions in order to perform coherence transfer between the protons and their chemically bonded rare nuclei. This gives to possibility to create liquid-like sequences for multiple quantum filtering and heteronuclear correlation spectroscopy.

The success of these techniques depends crucially on the homonuclear proton decoupling techniques. If it is to use liquid-like methods, special care has to be paid to improve their sensitivity and selectivity. Both problems can be overcome if we have powerful decoupling schemes. In Chapter 3 we developed an approach based on numerical optimization, in order to find better homonuclear decoupling schemes. The key idea behind our approach is the use of continuous schemes that cannot be treated analytically but can be optimized and easily adapted to the problems in hand. This approach is general and can be applied to other problems in NMR.

Finally, in Chapter 4 we discuss on the problem of spin diffusion. The motivation for this subject comes from the idea to use it as the NOESY experiment in liquids. Spin diffusion rates are measured and an attempt is made to correlate them with structural information. Sophisticated simulation methods have to be used in order

to simulate *ab initio* spin diffusion dynamics. However some approximation methods can be used to predict semi-quantitatively short and long time behavior. We finish our discussion by making use of the spatial periodicity in order to describe better large spin systems.

Though the structure in this document might seem more or less linear, it might be interesting to examine its time-ordered evolution! The idea of multiple quantum filtering was first examined within the framework of my undergraduate stage in the team of Lyndon, but at that period the laboratory did not have a solid-state spectrometer and the polarization transfer was proposed using dipolar couplings. During the stage of my masters degree, waiting for the spectrometer to arrive, we have tried to study spin diffusion using numerical models. The first year of my thesis the main effort was focused on spin diffusion and the first experimental results came with the periodic quasi-equilibria. Simultaneously Anne had already developed the use of J couplings in solids so the multiple-quantum filters and the heteronuclear correlation experiments became reality. In the second year the DUMBO approach was developed essentially on homonuclear spin decoupling and since, a lot of work was made to incorporate DUMBO-1 in different two dimensional sequences. One of the main problems we had during the elaboration of this work (probably the biggest) was the stability of the magnetic field! After, 4 quenches the last magnet seems robust (until now ...). Thus, most of the experiments were done either away from the laboratory (Bruker Germany, Grenoble CEA) either, with a lot of stress, the last year of my thesis.

In what follows I suppose the reader familiar with general NMR and particularly solid-state NMR vocabulary. The main effort was made in order to present *new* ideas rather than repeating already established theories. Two exceptions are present in the beginning of the third Chapter where a short résumé of the average Hamiltonian theory is made, and in the beginning of the forth Chapter in spin diffusion where a long résumé on theoretical methods is made. The formalism might seem a bit dense but I think that it can be easily reproduced and further developed. References at the end of this thesis constitute almost a part of it, since only few repetitions of established ideas are included.

Chapter 2

High Resolution in Solid State NMR

2.1 Introduction

The use of solid state NMR spectroscopy to explore both structure and dynamics becomes widespread with the advent of high resolution techniques [1–4]. The combination of multidimensional correlation spectroscopy with magic angle spinning (MAS) [5, 68, 69], cross polarization (CP) [6, 7, 70] and high radio frequency power decoupling techniques, gives the necessary, though not always sufficient, conditions to perform interesting experiments for analytical purposes. Rare nuclei under high resolution conditions give narrow resonances at the isotropic frequencies that can provide precise chemical information. The assignment of such sharp peaks in natural abundance samples is one of the current problems in solid state NMR.

Editing techniques exist in liquids which use the scalar couplings as the polarization transfer mechanism. They provide sub-spectra of the rare nucleus based on proton multiplicities and thus facilitate the assignment using simple one-dimensional spectra. Analogous pulse sequences exist for solids [20, 71], but the polarization transfer mechanism is based on the dipolar interaction, which is strong in the solid state. In this Chapter, we examine the possibility of using scalar J couplings in the solid state in order to create multiple quantum filters and perform spectral editing. Extension of these ideas will give rise to heteronuclear correlation spectroscopy using the J interaction in solids.

Unlike rare nuclei such as carbon-13 or nitrogen-15, which give narrow and well resolved solid-state NMR spectra under high resolution conditions, the proton (^{1}H) spectra of powdered organic molecules yield broad resonances due to the strong homonuclear proton-proton dipolar couplings. The characterization of proton spectra in solid-state NMR is of considerable interest, since proton chemical shifts provide a powerful source of information for analytical applications as well as yielding additional structural information for more detailed studies. One additional motivation to study proton spectroscopy is its 100% natural abundance and thus its intrinsic

sensitivity. Proton linewidths can be partially reduced using combined rotation and multiple pulse spectroscopy (CRAMPS) [26–30, 72] techniques, which further average the homonuclear dipolar couplings. However, the improvement in resolution often remains insufficient to characterize the proton spectra, even in relatively simple molecular systems, because the residual linewidths remain significant in comparison to the dispersion of the chemical shift. One way to unravel the overlapping one-dimensional proton spectra is to combine homonuclear decoupling techniques with two-dimensional heteronuclear correlation (HETCOR) experiments, which correlate the protons with a rare nucleus such as carbon-13 [31–33] or nitrogen-15. These correlation techniques have been numerously applied to the structural study of organic molecules or biological systems in the solid state [34–38]. Using special homonuclear decoupling schemes (the Frequency-Switched Lee-Goldburg (FSLG) technique [40–42, 73] seems very appropriate), the HETCOR experiment is practicable at moderately fast MAS frequencies [39], making the experiment useful for relatively complex molecular systems. Additionally, proton spectral resolution may be improved at the higher static magnetic field strengths that are currently available. Thus, the proton is becoming an increasingly attractive probe nucleus in the development of structural studies by solid-state NMR.

All the carbon-proton correlation experiments which have been reported so far are based on a dipolar coupling driven magnetization transfer. Various schemes for polarization transfer have been proposed [31–33]. All these experiments act through space, so one of the main problems is to ensure a sufficient selectivity in the magnetisation transfer for the spectrum to be usefully interpreted, i.e. to transfer magnetization only to directly bonded carbon nuclei and not to carbon nuclei that are further away. While correlation peaks between non-bonded pairs can provide valuable information on the conformation of the molecule, they dramatically complicate the initial analysis of the 2D spectrum.

Lesage et al. showed that heteronuclear scalar couplings can be resolved in powder samples under MAS [24]. In this Chapter, a summary of the observation of J couplings in the solid state is made and then their use in one-dimensional spectral editing and two-dimensional HETCOR spectroscopy is studied in detail. A new multiple quantum filter sequence is presented, where multiple quantum coherences are created by means of the J couplings. The same ideas can be used in a new proton-carbon correlation experiment, which relies on a polarization transfer using heteronuclear couplings, and which we call MAS-J-HMQC. In analogy to the liquid-state HMQC experiment [74], the sequence uses heteronuclear multiple quantum coherences to provide isotropic chemical-shift correlation between pairs of directly bonded nuclei. We show that the experiment is sensitive and that scalar couplings provide a more selective means of correlation than dipolar couplings. This experiment, provided that the rare spin spectrum is assigned, lead to the unambiguous identification of proton chemical shifts in solids.

Part of the results presented in this Chapter have been published [75] or will be submitted for publication [76, 77].

2.2 Using J couplings in Solid-State NMR

High resolution techniques are responsible for the significant line narrowing in solid state NMR. Until the end of 90's only highly mobile solids, like plastic crystals, were yielding sharp spectra [23,25]. On such compounds J couplings were easily resolved and liquid-like sequences gave interesting results [23, 25]. On the other hand, on ordinary organic compounds, where motion is reduced, the strong dipolar couplings hide all smaller interactions like J couplings. Magic angle spinning together with heteronuclear phase modulated decoupling (TPPM) [78] contributed to reducing the linewidth. As a concrete example we mention that in simple CP/MAS spectra of natural abundance crystalline organic compounds, the linewidth for a quaternary carbon or a methyl group is approximately 20 Hz, while for a CH group the linewidth is $\sim$30 Hz. These data are obtained from a powder sample of alanine on a 500 MHz wide-bore spectrometer, under relatively ordinary experimental conditions (decoupling power 100 kHz, spinning frequency 12 kHz), and reflect the resolution one can routinely achieve.

In carbon-13 enriched samples, this resolution is enough to resolve the *homonuclear* carbon J couplings. Two examples of the use of such homonuclear J couplings on crystalline solids are the TOBSY [79] and the INADEQUATE [80] experiments. In Fig. 2.1 we show how the latter experiment allows the unambiguous assignment of the carbon spectrum, though our attention is focused for the rest of this Chapter on *heteronuclear* J couplings.

The key to assign *natural abundance* organic solids is the *heteronuclear* proton-carbon couplings. The obvious strong interaction in solids being the dipolar coupling, correlation techniques using these direct couplings were developed in the past. Here, we propose to use the heteronuclear J couplings, an interaction much weaker and often hidden in solids, in order to work out the assignment of organic molecules. Thus, we have to find a way to resolve these scalar couplings and be able to use them.

To do this, all spin interactions in organic solids have to be taken into account. The total Hamiltonian $\mathcal{H}$, under MAS and RF irradiation, is time dependent and can be written:

$$\mathcal{H}(t) = \mathcal{H}_I(t) + \mathcal{H}_S(t) + \mathcal{H}_{II}(t) + \mathcal{H}_{SS}(t) + \mathcal{H}_{IS}(t) + \mathcal{H}_{\mathrm{RF}}(t) \tag{2.1}$$

with:

$$\mathcal{H}_I(t) = \sum_n [\omega_I + \delta_n^I(t)] I_{nz} \tag{2.2}$$

$$\mathcal{H}_S(t) = \sum_m [\omega_S + \delta_m^S(t)] S_{mz} \tag{2.3}$$

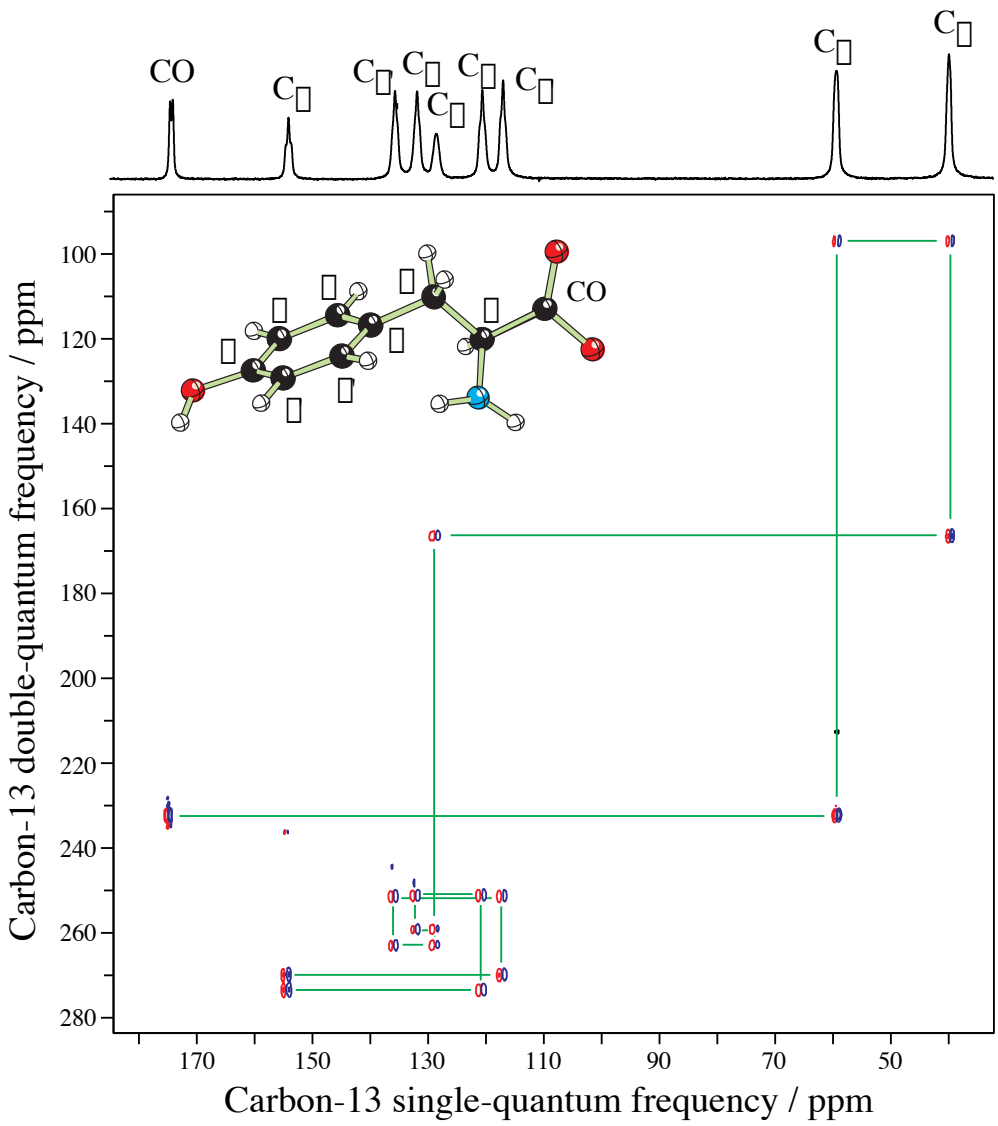

Figure 2.1: Two-dimensional INADEQUATE spectrum of a fully ^{13}C labeled sample of L-tyrosine hydrochloride. The spinning frequency was 20 kHz and the decoupling radio-frequency power was 120 kHz. Starting from the carbonyl carbon, we can follow through all the carbon skeleton of the molecule. This spectrum gives unambiguous assignment of the carbon backbone of the molecule. This spectrum was obtained by Dr. S. Steuernagel (Bruker Analytik Germany) and is reproduced from [81].

$$\mathcal{H}_{II}(t) = \sum_{n<m} d^I_{nm}(t)(3I_{nz}I_{mz} - \vec{I}_n \cdot \vec{I}_m) + 2\pi J^I_{nm}\vec{I}_n \cdot \vec{I}_m \quad (2.4)$$

$$\mathcal{H}_{SS}(t) = \sum_{n<m} d^S_{nm}(t)(3S_{nz}S_{mz} - \vec{S}_n \cdot \vec{S}_m) + 2\pi J^S_{nm}\vec{S}_n \cdot \vec{S}_m \quad (2.5)$$

$$\mathcal{H}_{IS}(t) = \sum_{n,m}[d^{IS}_{nm}(t) + \pi J^{IS}_{nm}]2I_{nz}S_{mz} \quad (2.6)$$

and

$$\mathcal{H}_{RF}(t) = \omega_{1I}(t)\{\cos[\phi_I(t)]I_x + \sin[\phi_I(t)]I_y\} \quad (2.7)$$

$$+ \omega_{1S}(t)\{\cos[\phi_S(t)]S_x + \sin[\phi_S(t)]S_y\} \quad (2.8)$$

where ω_X is the Larmor frequency and $\delta^X_n(t)$ the anisotropic chemical shift for the n spin of $X = \{I, S\}$ species. Anisotropic interactions are orientation dependent so under MAS they become explicitly time dependent. The time dependent anisotropic homonuclear $d^X_{nm}(t)$ and heteronuclear $d^{IS}_{nm}(t)$ dipolar couplings between n and m and the time independent homonuclear J^X_{nm} and heteronuclear J^{IS}_{nm} scalar couplings are the only two-spin interactions. A general time dependent radio frequency field ω_{1X} can be applied on one or both nuclei, having a time dependent amplitude $\omega_{1X}(t)$, and/or phase $\phi_X(t)$. The spin operator X_α is the *total* spin X component $\alpha = \{x, y, z\}$. The total Hamiltonian, in general, is quite complicated, but some simplifications can be made. In the following we are dealing with ordinary natural abundance organic solids (I refers to the ^{1}H nuclei and S refers to the rare nucleus ^{13}C or ^{15}N nuclei). Thus, the homonuclear Hamiltonian between rare spins (Eq. (2.5)) can be reasonably neglected.

We are interested in recording the rare nucleus S spectrum. Under homonuclear proton-proton decoupling a number of interesting things happen. Firstly, the proton-proton dipolar interaction is, at least to the first order, averaged to zero. The efficiency of the proton-proton decoupling depends on the decoupling sequence and a lot of experimental parameters. We will develop in detail the dipolar decoupling techniques in Chapter 3. Secondly, the linear proton terms are scaled by a scaling factor λ, so the proton chemical shift *and* the heteronuclear coupling interactions (dipolar and scalar) are scaled down by the same factor. Thirdly, under homonuclear decoupling, the heteronuclear dipolar interactions become *inhomogeneous* [82–84], to the first order, and can be refocused by magic angle spinning[1].

[1]In what follows we use the Maricq and Waugh definitions. Thus *inhomogeneous* are the Hamiltonians that commute with themselves at all times, have the same eigenvectors at all times and their effect can be completely refocused over a rotor period.

This leads to a considerable simplification of the effective Hamiltonian under homonuclear decoupling and MAS conditions:

$$\mathcal{H}_{\text{eff}} = \lambda \sum_n \delta_n^I I_{nz} + \sum_m \delta_m^S S_{nz} + 2\pi \sum_{n \neq m} J_{nm}^I \vec{I}_n \cdot \vec{I}_m + \lambda\pi \sum_{n,m} J_{nm}^{IS} 2 I_{nz} S_{mz} \qquad (2.9)$$

This effective Hamiltonian is written in the doubly rotating frame and the homonuclear scalar coupling terms between I spins, which are relatively small, will be neglected in what follows.

In Fig. 2.2(a) we show the carbon-13 spectrum of a powder sample of L-alanine recorded under proton-homonuclear decoupling and magic-angle spinning. Fig. 2.2(b) shows the methyl resonance of a powder sample of 2-^{13}C-sodium acetate recorded under the same conditions. Fig. 2.2(c) shows the nitrogen-15 spectrum of a powder sample of glycine recorded under the same conditions. The Frequency Switched Lee-Goldburg (FSLG) [40,41] decoupling scheme was used with a rf decoupling amplitude of 100 kHz, and the MAS spinning frequency was set to 12 kHz. A short explicative diagram for the FSLG decoupling technique is shown in Fig. 2.3. Splittings are observable in these spectra corresponding to the multiplet fine structure due to the heteronuclear J couplings. The α carbon in L-alanine gives a doublet, while the methyl carbon in alanine and in sodium acetate give a "quartet" which is poorly resolved and appears on the spectrum as a doublet. Even though the proton-nitrogen J interactions are smaller (~ 90 Hz) than the proton-carbon ones (~ 130 Hz), they can be resolved, as we can see from the "quartet" present in the spectrum of glycine. It corresponds to the 1:3:3:1 fine structure of the NH_3^+ group.

2.3 Multiple Quantum Filters and Spectral Editing

Using high resolution liquid state NMR techniques we can simplify considerably very complicated spectra and get information about large molecules such as membranes and proteins [85]. Appropriate manipulation of the spin Hamiltonian gives us the possibility to break the spectrum of many resonances into many subspectra of different groups of resonances. This is called *spectral edition*, a technique commonly used by chemists in order to analyze efficiently complicated molecules. For example, in ^{13}C spectroscopy one can extract from one 1D carbon-13 spectrum, four sub-spectra containing the CH_3, CH_2, CH and quaternary C resonances. The simplification in the assignment is enormous, especially when such techniques are combined with multidimensional correlation spectroscopy.

There are a lot of techniques in liquid state NMR in order to perform spectral editing, such as DEPT [8], INEPT [9] and APT [10–14]. In the solid state one of the most routinely used techniques is the delayed-decoupling sequence [15]. This technique being unable to distinguish between CH and CH_2 signals, several other

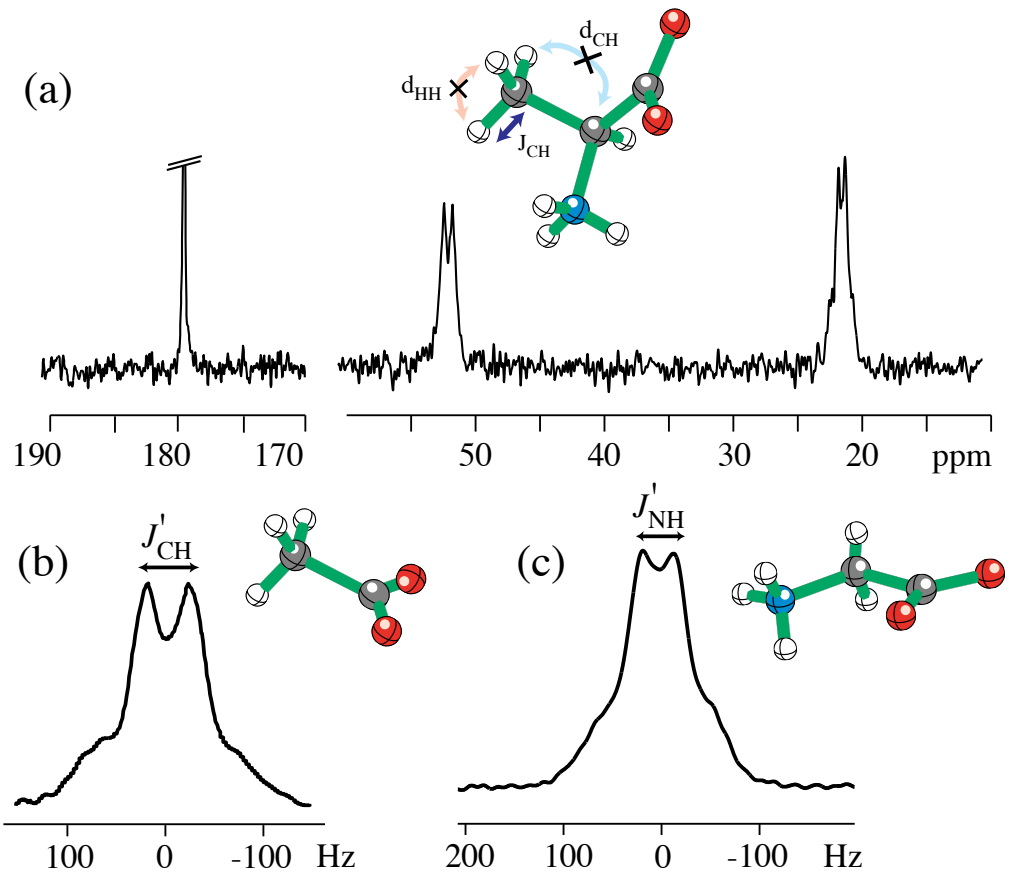

Figure 2.2: Carbon-13 (a,b) and nitrogen-15 (c) NMR spectra of powdered organic compounds under MAS and homonuclear proton dipolar decoupling. The homonuclear dipolar couplings are averaged by the rf sequence and the heteronuclear dipolar couplings by MAS, leaving the heteronuclear scalar couplings. (a) In the carbon spectrum of L-alanine we can distinguish the doublet of the α carbon and the quartet of the methyl carbon. (b) Carbon spectrum of an enriched sample of sodium acetate at the methyl position. Only the methyl resonance is shown. A quartet is expected for the CH_3 group, which appears as a doublet in the spectrum because of the poor resolution of the outer transitions. (c) The same "doublet" appears in the nitrogen-15 spectrum of glycine and hides the fine structure of the 1:3:3:1 quartet. Note that the heteronuclear proton-nitrogen couplings are smaller that the proton-carbon ones. In all spectra the scalar couplings are scaled by the scaling factor of the decoupling sequence. In these experiments the FSLG decoupling sequence was used (see Fig. 2.3).

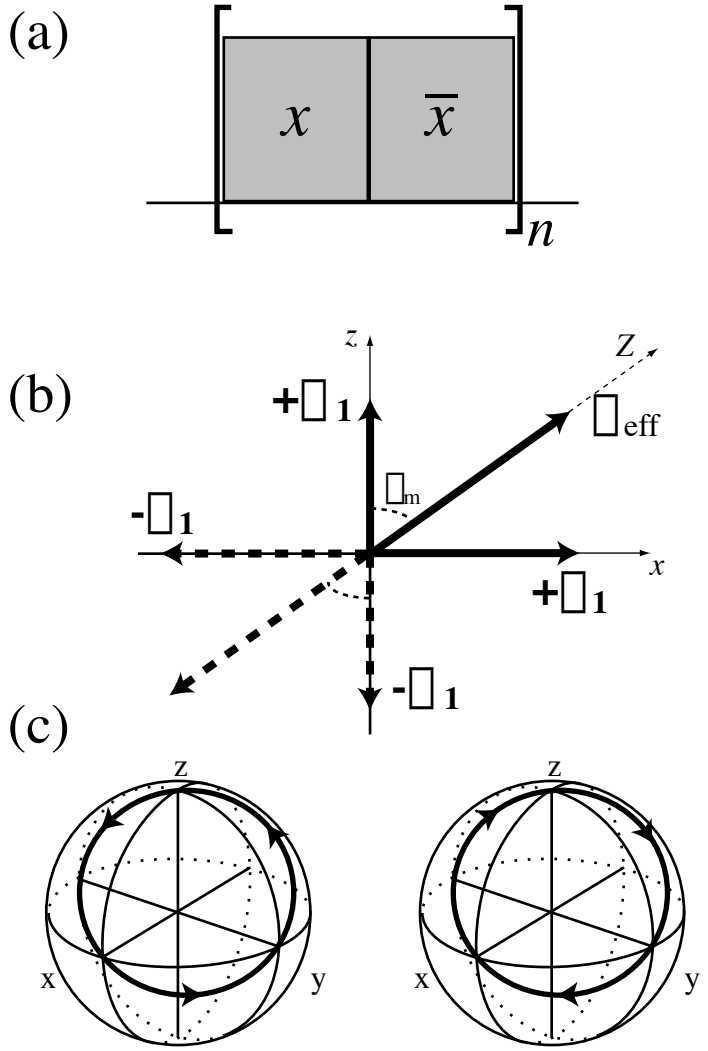

Figure 2.3: (a) The Frequency Switched Lee-Goldburg sequence for homonuclear dipolar decoupling in solids. Two back-to-back pulses are repeated n times. In both pulses the rf irradiation is applied off-resonance, $\pm\Omega_1$, and there is a frequency coherent π phase shift between them. The length of each pulse corresponds to a full 2π rotation around the effective field. (b) Representation of the two components and the total effective field ω_{eff}. The off-resonance frequency Ω_1 is set so as the angle between the effective field and the z axis is equal to the magic angle $\theta_m = \arctan\sqrt{2}$. (c) Trajectories of the z axis in the interaction frame. From this schematic illustration we can see the similarity with magic angle spinning and other decoupling sequences based on cubic symmetry averaging. Note however that the FSLG scheme averages only in the spin space, so chemical shift anisotropies are only scaled by the scaling factor of $\lambda = 1/\sqrt{3}$.

schemes have been proposed [16–20]. Most of them are separated local field experiments (SLF) [16–18] and are based on the fact that a CH_2 group has two dipolar couplings, a CH group only one and a CH_3 group is treated as a non-protonated carbon, because its heteronuclear dipolar couplings are reduced by rapid methyl rotation. Windowless isotropic mixing spectral editing (WIMSE) [19] requires multiple-pulse techniques, where high spinning frequencies are excluded because of the interference in the spin dynamics. Polarization inversion dynamics [20] have been used in order to separate the different groups using the fact that the Hamiltonian of a CH group is nearly inhomogeneous [83], while the Hamiltonian of a CH_2 is homogeneous at high MAS frequency. For low MAS frequencies, the differences of cross relaxation rates and heat capacities are sufficient to induce different spin dynamics. Combining de-polarization with cross polarization and polarization inversion, Wu *et al.* presented a technique [21] that allows reasonable separation under appropriate evolution times. However, the spin diffusion dynamics can be very complicated and *depend crucially on the mobility and the geometry of the spin system.* This often leads to ambiguities for the assignment of the spectrum. Recent developments have led to modified spectral editing methods [22].

The use of J couplings in solids has always been limited to plastic crystals or highly mobile materials. Recent developments allowed to resolve J heteronuclear couplings in ordinary organic solids [23,24] and of course to use them as in the liquid state. The attached proton test (APT) sequence has been implemented including appropriate changes for the solid state [24]. The idea we are going to develop through this Chapter is the use of scalar J heteronuclear interactions in order to create multiple quantum (MQ) coherences as in the liquid state. Filtering these MQ coherences would lead to unambiguous spectral edition. At the same time, we start to develop the basis for more complicated liquid-like sequences, going towards multi-dimensional J spectroscopy in the solid-state

Here we describe the formal development of multiple quantum coherences, using heteronuclear J couplings in solid state NMR. In order to evolve under a liquid state type Hamiltonian, moderate MAS is combined with homonuclear proton decoupling, as described in the previous section. In what follows we *assume* that the homonuclear decoupling sequence is perfect, i.e. it averages out completely the dipolar ^{1}H–^{1}H Hamiltonian. On the other hand, fast MAS helps in averaging out all inhomogeneous anisotropic interactions. We are thus left with the liquid type Hamiltonian of Eq. (2.9), containing the isotropic chemical shifts and the scalar J couplings.

This description is of course a simplification. In practice we never have a perfect averaging technique, because of its limited efficiency and experimental imperfections. However, the previous description is valid within the *first* order approximation in the Average Hamiltonian Theory (see section 3.2), and this means that it should perform well, even if minor spin effects are underestimated for the moment. The effect of non-averaged higher orders can be included phenomenologically as a T_2 homogeneous damping of the coherences. This time constant can be initially assumed as

common for all the transitions, though the experimental lineshapes suggest that the outer transitions are more broadened than the inner ones. This phenomenological description is valid within the assumptions that the line broadening function has no fine structure (i.e. Gaussian, Lorentzian). If non-zero higher orders give some fine structure to this broadening, this would be a complicated function of all parameters (proton and carbon chemical shift anisotropies, dipolar couplings, etc.). In this case it is reasonable to consider that the effective scaling factor contains some contributions from "non-averaged" dipolar couplings. Because of the r^{-3} dependence of the dipolar couplings, most of higher order effect is due to closest neighbors (chemically linked protons). Thus, even if higher order terms are non-zero, dynamics are governed mostly by scalar J couplings. In what follows, we shall use the Hamiltonian of Eq. (2.9) and work out the evolution of the density operator, as if in the liquid state.

Special care has to be taken in order to respect some solid-state features such as the short T_2 relaxation time (even under dipolar decoupling) in the solid state. We must spend the most of the time for coherence evolution in the carbon "channel", because the proton coherences relax too rapidly. Having this in mind we propose the sequence shown in Fig. 2.4.

After a first step of magnetization enhancement by ramped cross-polarization [86, 87] for the rare spin S we can generate multiple spin antiphase coherences with respect to the abundant spin I, using a homonuclear spin decoupling scheme. Under MAS and homonuclear proton decoupling conditions the Hamiltonian of a spin system $I_N S$ can be written (neglecting the small homonuclear proton J coupling):

$$\mathcal{H} = \delta_S S_z + \lambda \sum_n^N \delta_n^I I_{nz} + \lambda \pi J_{IS} \sum_n^N 2 I_{nz} S_z \tag{2.10}$$

where the z axis in Eq. (2.10) of the spin I is the proton dipolar decoupling effective field axis and λ is a scaling factor which depends on the decoupling sequence. In what follows we shall use the scaled coupling $J' \equiv \lambda J$. Since all terms in the Hamiltonian commute with each other, we can use standard product operator algebra [61], and propagate the initial state of the density operator $\sigma_0 = S_x$, at arbitrary time τ[2]:

$$\sigma_0 \xrightarrow{\mathcal{H}\tau} \sigma(\tau) \tag{2.11}$$

For the three common organic spin systems, IS, I_2S and I_3S, we have:

$$\sigma_{IS}(\tau^-) = \cos(\pi J' \tau) S_x + \sin(\pi J' \tau) 2 I_z S_y \tag{2.12}$$

[2]It is useful to notice that the spin S chemical shift is refocused by the π pulse in the middle of the sequence and does not have to be taken into account in the calculations.

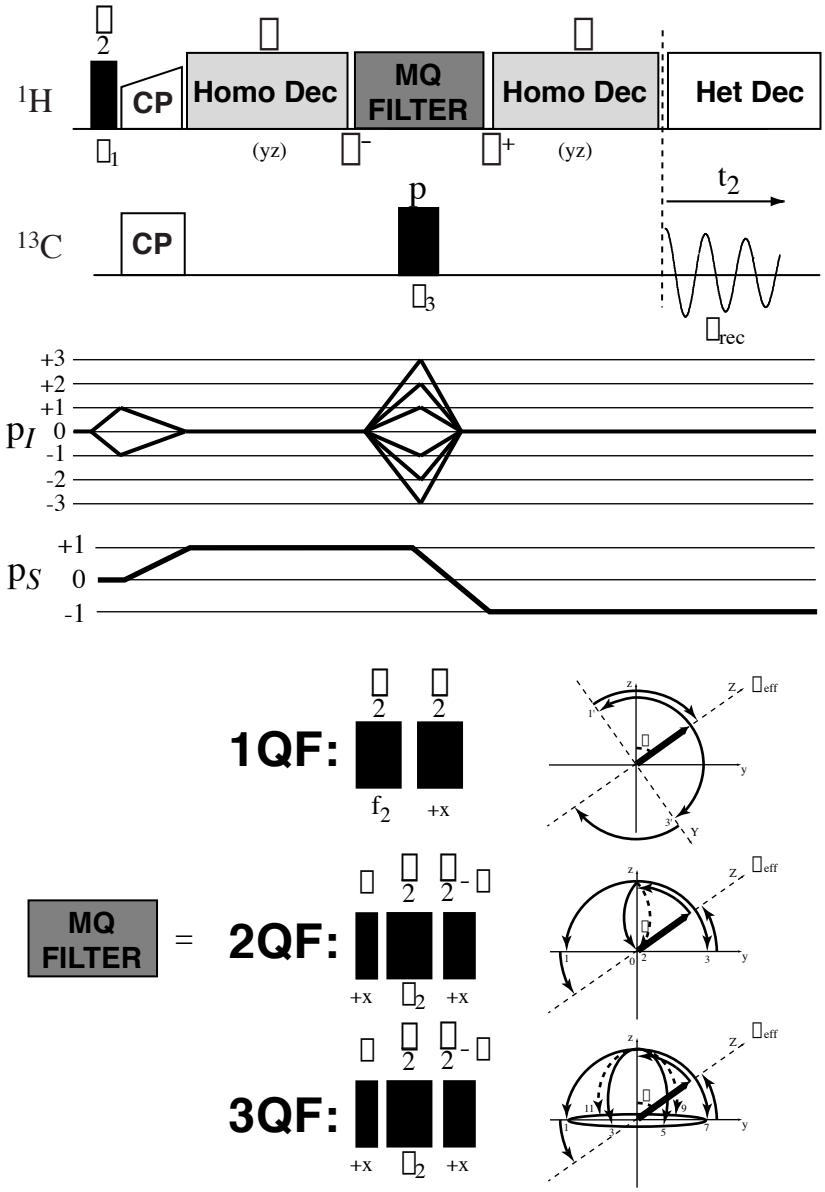

Figure 2.4: (a) Pulse sequence and coherence transfer pathways for the J-MQ-Filter experiment. Using the Frequency Switched Lee-Goldburg sequence as the homonuclear proton decoupling scheme, $\theta = \theta_m$ i.e. is a 54.7° pulse. Other sequences can also be used instead of FSLG, by fixing appropriately θ. The phase ϕ_1 was cycled together with the receiver ($\{+x, -x\}$) in order to select carbon magnetization coming only from polarization transfer from protons (spin temperature inversion). The phase ϕ_2 was cycled to select changes of Δp_I according to the Table 2.2. Additional phase cycling on the carbon 180° pulse was added to suppress artifacts.

$$\begin{aligned}\sigma_{I_2S}(\tau^-) &= \cos^2(\pi J'\tau)S_x \\ &+ \cos(\pi J'\tau)\sin(\pi J'\tau)2(I_{1z}+I_{2z})S_y \\ &- \sin^2(\pi J'\tau)4I_{1z}I_{2z}S_x\end{aligned} \tag{2.13}$$

$$\begin{aligned}\sigma_{I_3S}(\tau^-) &= \cos^3(\pi J'\tau)S_x \\ &+ \cos^2(\pi J'\tau)\sin(\pi J'\tau)2(I_{1z}+I_{2z}+I_{3z})S_y \\ &- \cos(\pi J'\tau)\sin^2(\pi J'\tau)4(I_{1z}I_{2z}+I_{1z}I_{3z}+I_{2z}I_{3z})S_x \\ &- \sin^3(\pi J'\tau)8I_{1z}I_{2z}I_{3z}S_y\end{aligned} \tag{2.14}$$

If we chose $\tau = 1/2J'$, we obtain pure antiphase excitation:

$$\sigma_{IS}(1/2J') = 2I_zS_y \tag{2.15}$$

$$\sigma_{I_2S}(1/2J') = -4I_{1z}I_{2z}S_x \tag{2.16}$$

$$\sigma_{I_3S}(1/2J') = -8I_{1z}I_{2z}I_{3z}S_x \tag{2.17}$$

Multiple quantum coherences are created by the $\pi/2$ pulse on the I spin, whereas the π pulse on the S spin is used to refocus the S chemical shift after the second τ period. Doing the propagation step by step we have:

$$\sigma(\tau^-) \overset{(\pi/2)I_x}{\longrightarrow} \overset{\pi S_x}{\longrightarrow} \sigma^{\mathrm{MQ}} \tag{2.18}$$

For the three spin systems, we get:

$$\sigma_{IS}^{\mathrm{MQ}} = \cos(\pi J'\tau)S_x + \sin(\pi J'\tau)2I_yS_y \tag{2.19}$$

$$\begin{aligned}\sigma_{I_2S}^{\mathrm{MQ}} &= \cos^2(\pi J'\tau)S_x \\ &+ \cos(\pi J'\tau)\sin(\pi J'\tau)2(I_{1y}+I_{2y})S_y \\ &- \sin^2(\pi J'\tau)4I_{1y}I_{2y}S_x\end{aligned} \tag{2.20}$$

$$\begin{aligned}\sigma_{I_3S}^{\mathrm{MQ}} &= \cos^3(\pi J'\tau)S_x \\ &+ \cos^2(\pi J'\tau)\sin(\pi J'\tau)2(I_{1y}+I_{2y}+I_{3y})S_y \\ &- \cos(\pi J'\tau)\sin^2(\pi J'\tau)4(I_{1y}I_{2y}+I_{1y}I_{3y}+I_{2y}I_{3y})S_x \\ &- \sin^3(\pi J'\tau)8I_{1y}I_{2y}I_{3y}S_y\end{aligned} \tag{2.21}$$

Table 2.1: Phase for coherences having a variation of their coherence level of Δp_I. ϕ_2 is the phase of the first $\pi/2$ proton pulse in the MQ-Filter block (see Fig. 2.4). In bold are the transients that contribute to the observable wanted signal. We can clearly see that 1Q filtering does not filter 3Q coherences. The full phase cycling is described on Table 2.2.

	ϕ_2	Δp_I					
		$+1$	-1	$+2$	-2	$+3$	-3
1QF	0°	**0°**	**0°**	0°	0°	**0°**	**0°**
	180°	**180°**	**180°**	0°	0°	**180°**	**180°**
2QF	0°	0°	0°	**0°**	**0°**	0°	0°
	90°	90°	270°	**180°**	**180°**	270°	90°
	180°	180°	180°	**0°**	**0°**	180°	180°
	270°	270°	90°	**180°**	**180°**	90°	270°
3QF	0°	0°	0°	0°	0°	**0°**	**0°**
	60°	60°	300°	120°	240°	**180°**	**180°**
	120°	120°	240°	240°	120°	**0°**	**0°**
	180°	180°	180°	0°	0°	**180°**	**180°**
	240°	240°	120°	120°	240°	**0°**	**0°**
	300°	300°	60°	240°	120°	**180°**	**180°**

The key idea is to filter out only signal from particular multiple quantum coherences. This is performed experimentally using the phase cycling described in Tables 2.1 and 2.2. Note that we deal with a heteronuclear spin system so using a $\Delta p_I = \pm 1$ phase cycling on the proton channel does not guarantee a $\Delta p_{\text{tot}} = \pm 2$. In this example, we cannot select only all total double quantum coherences without keeping all total zero quantum ones. Therefore, in the following *we note the MQ coherences with respect to the coherence order of the spin I*. Then, the different multiple quantum components for the three spin systems are:

$$\sigma_{IS}^{1\text{QF}} = \frac{1}{2}\sin(\pi J'\tau)(I_+ - I_-)(S_- - S_+) \tag{2.22}$$

$$\sigma_{I_2S}^{1\text{QF}} = \frac{1}{2}\cos(\pi J'\tau)\sin(\pi J'\tau)(I_{1+} + I_{2+} - I_{1-} - I_{2-})(S_- - S_+) \tag{2.23}$$

$$\sigma_{I_2S}^{2\text{QF}} = \frac{1}{2}\sin^2(\pi J'\tau)(I_{1-}I_{2-} + I_{1+}I_{2+})(S_+ + S_-) \tag{2.24}$$

Table 2.2: Phase cycling schemes for the J-MQ-Filter experiments. ϕ_1 is the phase of the first $\pi/2$ proton pulse before the CP step, ϕ_2 is the phase of the first $\pi/2$ proton pulse in the MQ-Filter block and ϕ_3 is the phase of the π carbon pulse (see Fig. 2.4). ϕ_{rec} is the phase of the receiver for the appropriate MQ filtering.

	ϕ_1	ϕ_2	ϕ_3	ϕ_{rec}
1QF	0°	0°	{0°, 90°, 180°, 270°}	{0°, 180°, 0°, 180°}
	0°	180°	{0°, 90°, 180°, 270°}	{180°, 0°, 180°, 0°}
	180°	0°	{0°, 90°, 180°, 270°}	{180°, 0°, 180°, 0°}
	180°	180°	{0°, 90°, 180°, 270°}	{0°, 180°, 0°, 180°}
2QF	0°	0°	{0°, 90°, 180°, 270°}	{0°, 180°, 0°, 180°}
	0°	90°	{0°, 90°, 180°, 270°}	{180°, 0°, 180°, 0°}
	0°	180°	{0°, 90°, 180°, 270°}	{0°, 180°, 0°, 180°}
	0°	270°	{0°, 90°, 180°, 270°}	{180°, 0°, 180°, 0°}
	180°	0°	{0°, 90°, 180°, 270°}	{180°, 0°, 180°, 0°}
	180°	90°	{0°, 90°, 180°, 270°}	{0°, 180°, 0°, 180°}
	180°	180°	{0°, 90°, 180°, 270°}	{180°, 0°, 180°, 0°}
	180°	270°	{0°, 90°, 180°, 270°}	{0°, 180°, 0°, 180°}
3QF	0°	0°	{0°, 90°, 180°, 270°}	{0°, 180°, 0°, 180°}
	0°	60°	{0°, 90°, 180°, 270°}	{180°, 0°, 180°, 0°}
	0°	120°	{0°, 90°, 180°, 270°}	{0°, 180°, 0°, 180°}
	0°	180°	{0°, 90°, 180°, 270°}	{180°, 0°, 180°, 0°}
	0°	240°	{0°, 90°, 180°, 270°}	{0°, 180°, 0°, 180°}
	0°	300°	{0°, 90°, 180°, 270°}	{180°, 0°, 180°, 0°}
	180°	0°	{0°, 90°, 180°, 270°}	{180°, 0°, 180°, 0°}
	180°	60°	{0°, 90°, 180°, 270°}	{0°, 180°, 0°, 180°}
	180°	120°	{0°, 90°, 180°, 270°}	{180°, 0°, 180°, 0°}
	180°	180°	{0°, 90°, 180°, 270°}	{0°, 180°, 0°, 180°}
	180°	240°	{0°, 90°, 180°, 270°}	{180°, 0°, 180°, 0°}
	180°	300°	{0°, 90°, 180°, 270°}	{0°, 180°, 0°, 180°}

$$\begin{aligned}\sigma_{I_3S}^{1\mathrm{QF}} &= \frac{1}{2}\cos^2(\pi J'\tau)\sin(\pi J'\tau)(I_{1+}+I_{2+}+I_{3+}-I_{1-}-I_{2-}-I_{3-})\times \\ &\times\ (S_- - S_+) \\ &+ \frac{1}{2}\sin^3(\pi J'\tau)(S_- - S_+)\times \\ &\times\ [(I_{1+}I_{2-}I_{3-}+I_{1-}I_{2+}I_{3-}+I_{1-}I_{2-}I_{3+}-I_{1-}I_{2+}I_{3+}-I_{1+}I_{2-}I_{3+} \\ &-\ I_{1+}I_{2+}I_{3-})+(I_{1+}I_{2+}I_{3+}-I_{1-}I_{2-}I_{3-})] \end{aligned} \tag{2.25}$$

$$\begin{aligned}\sigma_{I_3S}^{2\mathrm{QF}} &= \frac{1}{2}\cos(\pi J'\tau)\sin^2(\pi J'\tau)(S_+ + S_-)\times \\ &\times\ (I_{1-}I_{2-}+I_{1+}I_{2+}+I_{2-}I_{3-}+I_{2+}I_{3+}+I_{1-}I_{3-}+I_{1+}I_{3+}) \end{aligned} \tag{2.26}$$

$$\sigma_{I_3S}^{3\mathrm{QF}} = \frac{1}{2}\sin^3(\pi J'\tau)(I_{1+}I_{2+}I_{3+}-I_{1-}I_{2-}I_{3-})(S_- - S_+) \tag{2.27}$$

The second $\pi/2$ pulse on the I spin converts the multiple quantum coherences into I spin antiphases (τ^+ indicates the instant just after the MQ Filter, see also Fig. 2.4):

$$\sigma^{\mathrm{MQF}} \xrightarrow{(\pi/2)I_{\bar{x}}} \sigma^{\mathrm{MQF}}(\tau^+) \tag{2.28}$$

with:

$$\sigma_{IS}^{1\mathrm{QF}}(\tau^+) = -\sin(\pi J'\tau)2I_zS_y \tag{2.29}$$

$$\sigma_{I_2S}^{1\mathrm{QF}}(\tau^+) = -\cos(\pi J'\tau)\sin(\pi J'\tau)2(I_{1z}+I_{2z})S_y \tag{2.30}$$

$$\sigma_{I_2S}^{2\mathrm{QF}}(\tau^+) = \frac{1}{2}\sin^2(\pi J'\tau)4(I_{1x}I_{2x}-I_{1z}I_{2z})S_x \tag{2.31}$$

$$\begin{aligned}\sigma_{I_3S}^{1\mathrm{QF}}(\tau^+) &= -\cos^2(\pi J'\tau)\sin(\pi J'\tau)2(I_{1z}+I_{2z}+I_{3z})S_y \\ &+ \sin^3(\pi J'\tau)8I_{1z}I_{2z}I_{3z}S_y \end{aligned} \tag{2.32}$$

$$\begin{aligned}\sigma_{I_3S}^{2\mathrm{QF}}(\tau^+) &= \frac{1}{2}\cos(\pi J'\tau)\sin^2(\pi J'\tau)4S_x\times \\ &\times\ [(I_{1x}I_{2x}-I_{1z}I_{2x})+(I_{1x}I_{3x}-I_{1z}I_{3z})+(I_{2x}I_{3x}-I_{2z}I_{3z})] \end{aligned} \tag{2.33}$$

$$\sigma_{I_3S}^{3\mathrm{QF}}(\tau^+) = \sin^3(\pi J'\tau)8I_{1z}I_{2z}I_{3z}S_y \tag{2.34}$$

(2.35)

The last τ period refocuses the S spin chemical shift and converts the I spin antiphases into S_x observable magnetization detected in t_2:

$$\sigma^{\mathrm{MQF}}(\tau^+) \xrightarrow{\mathcal{H}\tau} \sigma^{\mathrm{MQF}}(2\tau) \tag{2.36}$$

with:

$$\sigma_{IS}^{1\mathrm{QF}}(2\tau) = \sin^2(\pi J'\tau)S_x + \ldots \tag{2.37}$$

$$\begin{aligned}
\sigma_{I_2S}^{1\mathrm{QF}}(2\tau) &= \frac{1}{2}\sin^2(2\pi J'\tau)S_x + \ldots && (2.38)\\
\sigma_{I_2S}^{2\mathrm{QF}}(2\tau) &= \frac{1}{4}\sin^4(\pi J'\tau)S_x + \ldots && (2.39)
\end{aligned}$$

$$\begin{aligned}
\sigma_{I_3S}^{1\mathrm{QF}}(2\tau) &= \frac{1}{2}[3 + 2\cos(2\pi J'\tau) + \cos(4\pi J'\tau)]\sin^2(\pi J'\tau)S_x + \ldots && (2.40)\\
\sigma_{I_3S}^{2\mathrm{QF}}(2\tau) &= \frac{3}{4}\sin^4(\pi J'\tau)\cos^2(\pi J'\tau)S_x + \ldots && (2.41)\\
\sigma_{I_3S}^{3\mathrm{QF}}(2\tau) &= \frac{1}{4}\sin^6(\pi J'\tau)S_x + \ldots && (2.42)
\end{aligned}$$

where the dots ... account for non observable terms of the density operator. We can include phenomenologically the effect of transverse relaxation during the the two τ periods, by multiplying the signal by a single damping exponential. Thus, we obtain the expressions for the multiple quantum filtered signals as functions of the initial (after cross-polarization) intensities I^0, relaxation times T_2 and evolution period τ.

For the single quantum filtered signals:

$$\begin{aligned}
I_{IS}^{1\mathrm{QF}}(\tau) &= \sin^2(\pi J'\tau)\exp(-2\tau/T_2^{IS})I_{IS}^0 && (2.43)\\
I_{I_2S}^{1\mathrm{QF}}(\tau) &= \frac{1}{2}\sin^2(2\pi J'\tau)\exp(-2\tau/T_2^{I_2S})I_{I_2S}^0 && (2.44)\\
I_{I_3S}^{1\mathrm{QF}}(\tau) &= \frac{1}{2}[3 + 2\cos(2\pi J'\tau) + \cos(4\pi J'\tau)]\sin^2(\pi J'\tau)] \times \\
&\times \exp(-2\tau/T_2^{I_3S})I_{I_3S}^0 && (2.45)
\end{aligned}$$

For the double quantum filter:

$$\begin{aligned}
I_{I_2S}^{2\mathrm{QF}}(\tau) &= \frac{1}{4}\sin^4(\pi J'\tau)\exp(-2\tau/T_2^{I_2S})I_{I_2S}^0 && (2.46)\\
I_{I_3S}^{2\mathrm{QF}}(\tau) &= \frac{3}{4}\sin^4(\pi J'\tau)\cos^2(\pi J'\tau)\exp(-2\tau/T_2^{I_3S})I_{I_3S}^0 && (2.47)
\end{aligned}$$

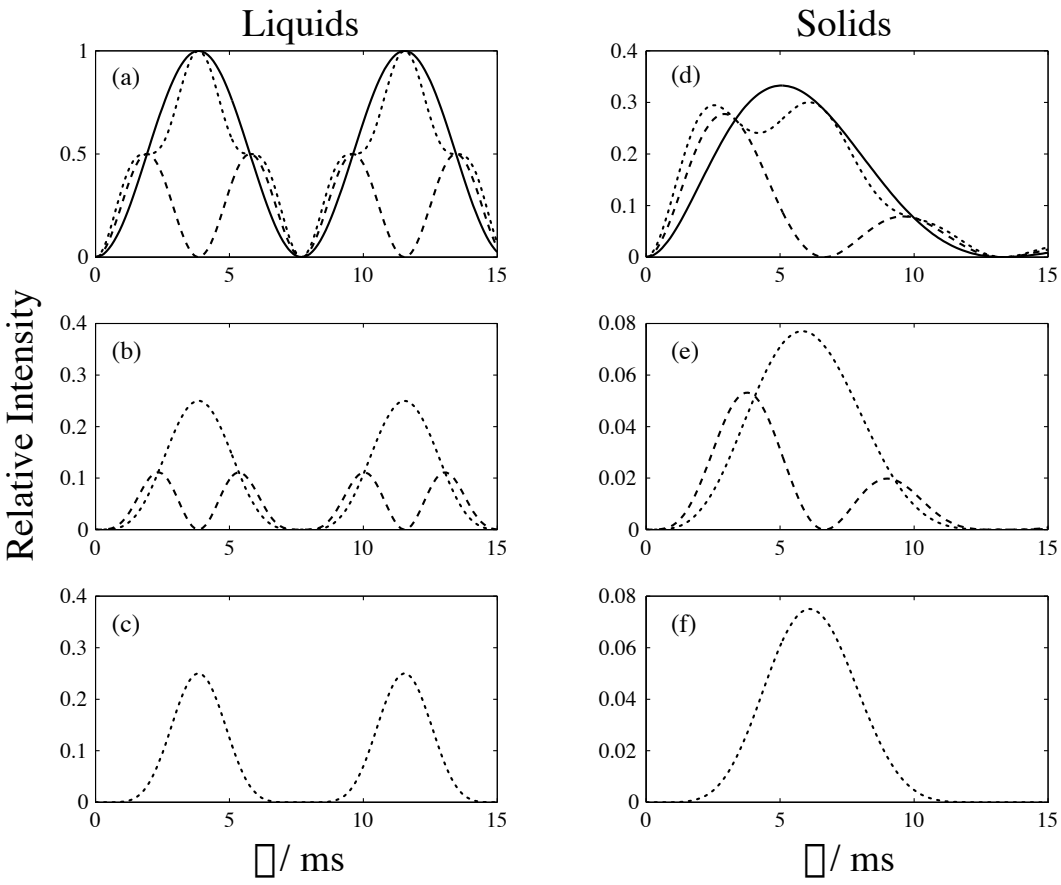

Figure 2.5: Functional dependences for multiple quantum filtered signals for the CH (solid line), CH_2 (dashed line) and CH_3 (dotted line) groups. Plots (a,b,c) correspond to the ideal liquid-state evolution where no linewidth is present and the scalar coupling is set to 130 Hz, i.e. a typical value for a one-bond coupling for an aliphatic carbon. Plots (d,e,f) correspond to the solid-state case, where the scalar couplings are scaled by the scaling factor $\lambda = 1/\sqrt{3}$ due to the FSLG decoupling and a the finite linewidth exists. In this latter case the linewidth was phenomenologically introduced by multiplying by a damping function: $\exp(-2\tau/T_2)$. T_2 is the transverse relaxation (dephasing) time during the 2τ period ($T_2 = 1/\pi\Delta$) and Δ is the full linewidth at half height of one component in a J-coupled multiplet. In this example Δ was set to 30 Hz. Note that the differences between liquids and solids with respect to the relative intensities of the signals. The efficiency of the MQ-Filters in solids is low because of the fast T_2 damping of the signal.

and for the triple quantum filter:

$$I_{I_3S}^{3\mathrm{QF}}(2\tau) \;=\; \frac{1}{4}\sin^6(\pi J'\tau)\exp(-2\tau/T_2^{I_3S})I_{I_3S}^0 \tag{2.48}$$

In Fig. 2.5 the dependence of these signals as functions of τ are presented for the ideal case of liquids, and the case of solid-state compounds. Figures 2.5 show the theoretical evolution curves of the intensity of the observable magnetization as a function of the delay τ. These curves were calculated for all types of carbon multiplicity and all orders of MQ filtering in the "solid-state" case (Fig. 2.5(d–f)) and compared for reference to the "ideal liquid-state" case (Fig. 2.5(a–c)). In solid samples, the effective scalar coupling is reduced by the scaling factor of the FSLG decoupling sequence $\lambda = 1/\sqrt{3}$ (a coupling of 130 Hz, which is a typical value for a sp^3 carbon in hydrocarbons [88], will give an effective scaled coupling of 75 Hz) and a line-broadening of several tens of Hertz has to be considered, which strongly attenuates the signal intensity by transverse T_2 relaxation. However, if the homonuclear decoupling sequence applied during the 2τ period is efficient enough to yield linewidths comparable to the size of the scaled heteronuclear scalar coupling, then a significant signal should be observed, rendering the experiment practicable. The optimal delay to excite double-quantum *heteronuclear* coherences, independent of the number of attached protons, is about 2 ms (see Fig. 2.5(d). From the relative intensities of the signals we can see that the 1Q-Filter is intrinsically more sensitive than the 2Q- and 3Q-Filters. Finite linewidth due to the imperfect decoupling diminishes further the MQ filtered signals. So the efficiency of this technique depends crucially on the efficiency of the homonuclear proton decoupling.

2.3.1 Experiments

In this section we present experimental results using the multiple quantum filters. Powder samples of camphor, L-alanine and the tripeptide Boc-Ala-Ala-Pro-O-Bzl were used, in a volume restricted 4 mm diameter rotor. The sample of camphor and L-alanine were purchased from Sigma and used without further purification. The tripeptide Boc-Ala-Ala-Pro-O-Bzl (where Boc stands for ter-butoxycarbonyl and Bzl for Benzyl) was synthesized in our laboratory and crystallized from diisopropyloxide [89].

All pulse programs are included in appendix A.3. Results for the camphor plastic crystal are shown in Fig. 2.6, and confirm the theoretical predictions. Note that camphor is a plastic crystal so all intramolecular dipolar couplings are averaged to zero on the NMR time scale (i.e. it would be impossible to perform spectral editing using dipolar methods). Using two pulse phase modulation (TPPM) [78] heteronuclear decoupling very narrow resonances can be obtained (linewidth less than 2 Hz), so to avoid wiggles due to the truncation of the FID an exponential apodization of 3 Hz was applied. Clear distinction with respect to the multiplicities of the signal can be made, especially between the CH and CH_2 carbon resonances.

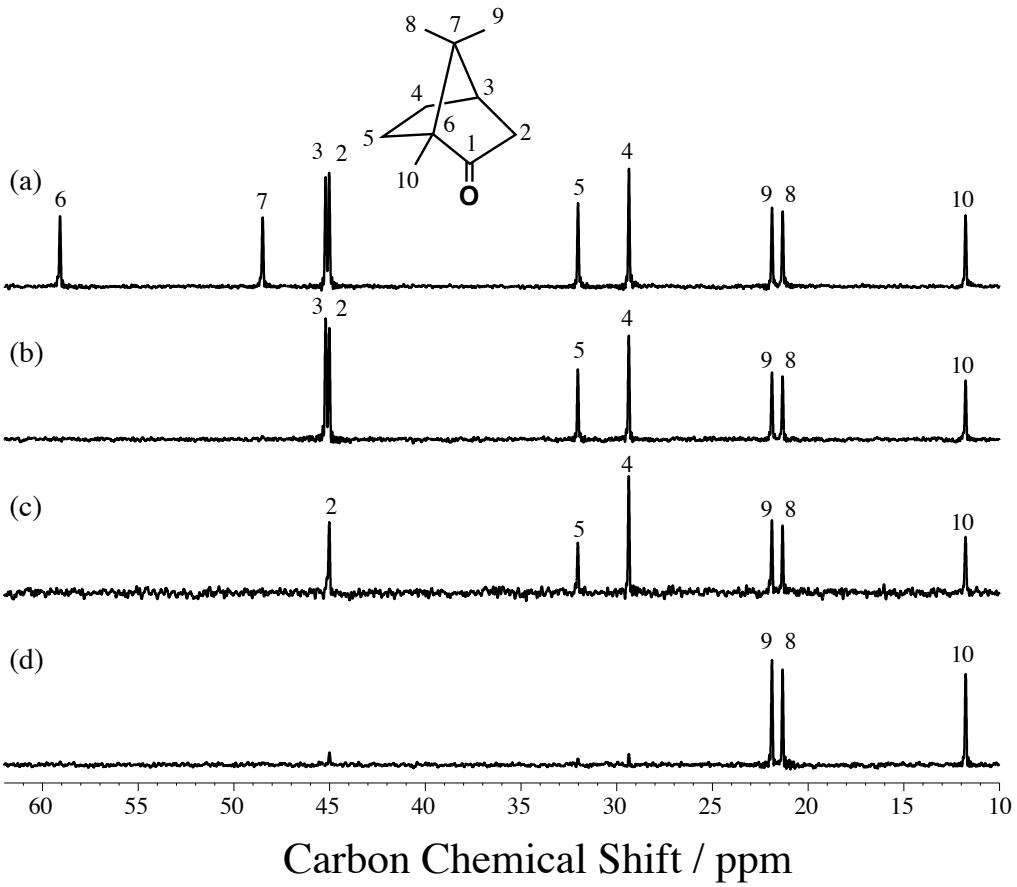

Figure 2.6: *J*-MQ filtered solid-state NMR spectroscopy on camphor. (a) Standard CP/ MAS spectrum of a powder sample of camphor. The spinning frequency was set to 6 kHz and a 5 ms cross-polarization contact time was used. (b) 1QF spectrum of camphor. As predicted signals from the CH, CH_2 and CH_3 groups are present. (c) 2QF spectrum of camphor. Only signal from the CH_2 and CH_3 groups are present. The evolution time was set to $\tau = 3.2$ ms for (b) and (c). (e) 3QF spectrum of camphor. Only signal from the CH_3 groups are present. The evolution time was set to $\tau = 7.0$ ms in order to enhance the 3Q proton coherences.

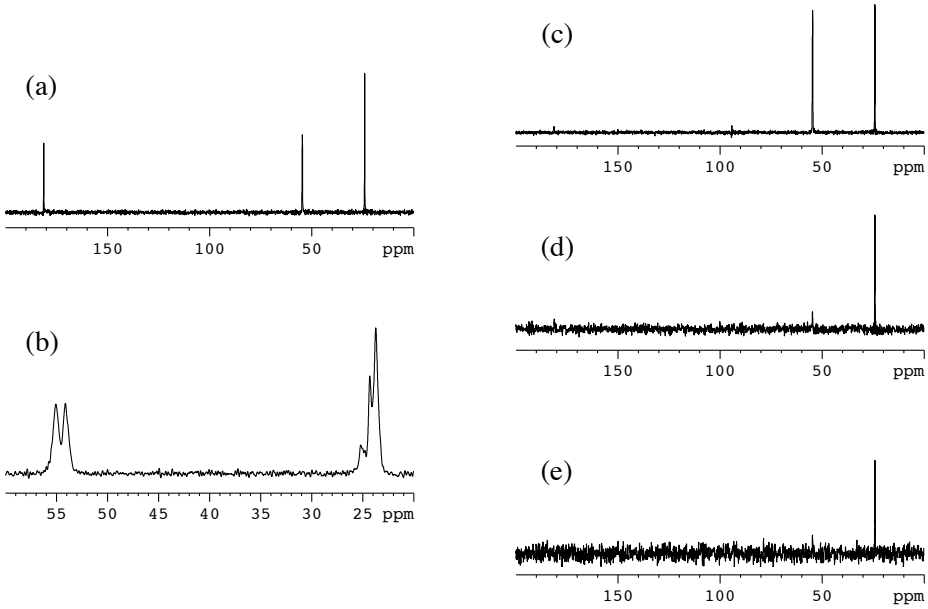

Figure 2.7: J-MQ filtered solid-state NMR spectroscopy on L-alanine. (a) Standard CP/ MAS spectrum of a powder sample of L-alanine. The spinning frequency was set to 12 kHz and a 1 ms cross-polarization contact time was used. Using TPPM decoupling (100 kHz decoupling amplitude) during acquisition narrow peaks are obtained. The linewidth for the carbonyl and the methyl carbons were 20 Hz while for the α carbon it was 27 Hz. (b) Carbon spectrum recorded under homonuclear FSLG decoupling. Only the region where splittings due to the heteronuclear J couplings are present is shown. We can clearly distinguish the doublet of the α carbon and the quartet of the methyl carbon. (c) 1QF spectrum of L-alanine. As predicted the signal from the CH and CH_3 groups is present. The evolution time was set to $\tau = 2$ ms. 320 scans were recorded. (d) 2QF spectrum of L-alanine. Only signal from the CH_3 group is present. The evolution time was set to $\tau = 2$ ms. 640 scans were recorded. (e) 3QF spectrum of L-alanine. Only signal from the CH_3 group is present. 1260 scans were recorded. The evolution time was set to $\tau = 5$ ms. No apodization of the FID's was performed.

Results for a powder sample of L-alanine are shown in Fig. 2.7, and also confirm the theoretical predictions. Experimental conditions are explained in Fig. 2.7, while we can see the low signal to noise, arising form the low sensitivity of the of the technique. However, clear distinctions can be made even in rigid organic solids such as L-alanine. Results form the tripetide Boc-Ala-Ala-Pro-O-Bzl are given in Fig. 2.8, together with experimental details. Again, inambiguous attribution of carbon multiplicities were obtained. The results we had using the MQ filters will also be confirmed in the following sections where more sophisticated, two-dimensional sequences will be used.

Clear distinction between all carbon multiplicities, and especially between CH and CH_2 groups can be made using J-MQ-Filters. The results are insensitive to mobility and to MAS[3], because the polarization transfer is performed using scalar coupling. J-MQ Filters are thus, easy and fast techniques that could be used in solid state NMR routine experiments, for the attribution of carbon multiplicities.

2.4 HETCOR by Through Bond Multiple Quantum Spectroscopy

2.4.1 2D Multiple Quantum Filtered HETCOR

The extension of the multiple quantum filtered spectroscopy to two dimensions is straightforward. If we let the multiple quantum coherences evolve during a time period t_1, we can observe their evolution frequency during t_1 after a Fourier transform, in full analogy with the liquid state correlation spectroscopy. In the solid state variant of the HMQC experiment, named MAS-J-HMQC, small differences are present, revealing that we deal with solid powder samples.

2.4.2 Pulse scheme

The pulse sequence for the MAS-J-HMQC experiment is shown in Fig. 2.9. The spin dynamics of this sequence being almost identical to that of J-MQ-Filter, here we simply describe the pulse scheme. After cross-polarization from ^{1}H (I spins), the magnetization of the rare spin (S spin), typically ^{13}C or ^{15}N, evolves during the delay τ under only an isotropic scaled heteronuclear coupling Hamiltonian (see Eq. (2.9)). During this period the proton-proton dipolar couplings are removed by using FSLG whereas the remaining inhomogeneous interactions, i.e. the chemical shift and the heteronuclear dipolar couplings, are averaged by rapid MAS to their isotropic components, leaving only the isotropic chemical shift and the heteronuclear scalar coupling. For a pair of covalently bonded I–S spins, the S magnetization evolves from in-phase (S_x) into antiphase ($2I_zS_y$) coherence with respect to

[3]This is always true as long as no destructive interference between the two averaging time scales takes place.

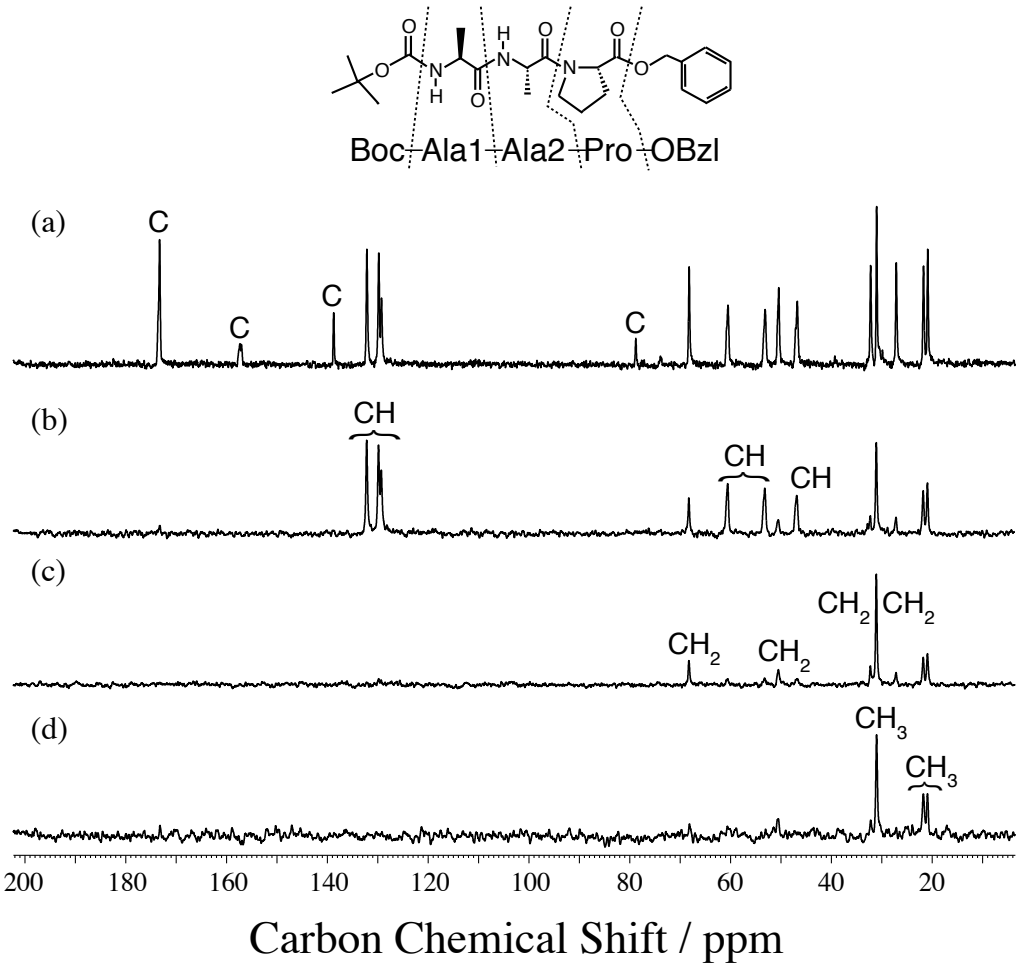

Figure 2.8: *J*-MQ filtered solid-state NMR spectroscopy on the tripeptide Boc-Ala-Ala-Pro-O-Bzl. (a) Standard CP/ MAS spectrum of a powder sample of the tripeptide. The spinning frequency was set to 12.5 kHz and a 1 ms cross-polarization contact time was used. Using TPPM decoupling (100 kHz decoupling power) during acquisition narrow and well resolved peaks are obtained. (b) 1Q filtered spectrum. As predicted signals from the CH, CH_2 and CH_3 groups are present. (c) 2Q filtered spectrum. Only signals from the CH_2 and CH_3 groups are present. (e) 3Q filtered spectrum. Only signals from the CH_3 groups are present. The evolution time was set to $\tau = 3.2$ ms synchronized with the MAS. Spectra (c) and (d) were acquired within 2 and 4 hours respectively.

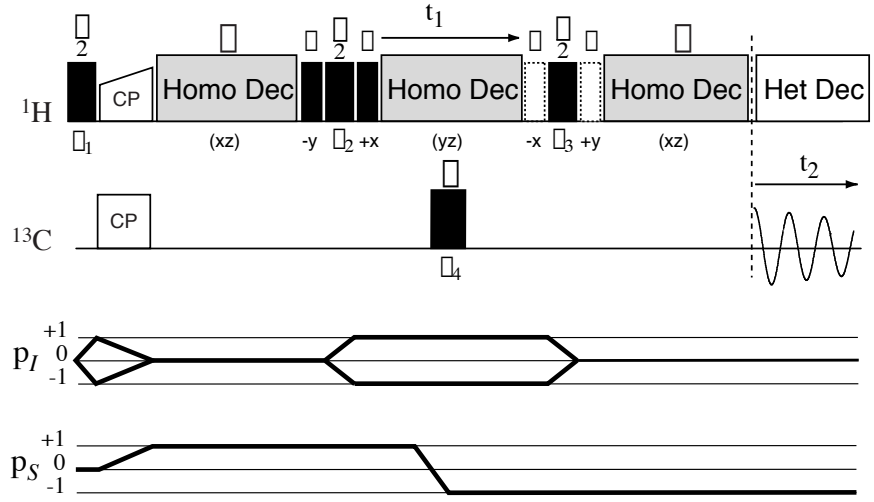

Figure 2.9: Pulse sequence and coherence transfer pathways for the MAS-J-HMQC experiment. We used the FSLG homonuclear decoupling so θ is a 54.7° pulse. The phases ϕ_1, ϕ_2 and ϕ_3 can independently cycled to select changes of $\Delta p = \pm 1$ (2 step phase cycles for each of the three pulses). Additional phase cycling on the 180° carbon pulse can be added to suppress artifacts. The shortest phase cycling for single quantum coherence selection during t_1 is given in Table 2.3. A significant simplification occurs if we group the last sandwich of the three pulses $\theta - \pi/2 - \theta$ into a single $\pi/2$ pulse, as shown (single quantum proton selection). This simplification gives practically artifact free 2D spectra, does not alter the theoretical description and performance.

the attached proton (see Eq. (2.12)). A $\pi/2$ pulse applied on protons transforms the antiphase S coherence into a double-quantum heteronuclear coherence ($2I_yS_y$) which evolves during t_1 only under the effect of the proton chemical shift. Carbon chemical shift evolution during t_1 (and during the periods τ) is refocused by the π pulse applied in the middle of the pulse sequence. Heteronuclear multiple-quantum coherences are insensitive to heteronuclear couplings between the two spins involved in the coherence, proton-proton dipolar couplings are removed during t_1 by the FSLG decoupling and the residual heteronuclear dipolar couplings to other spins by MAS and the π pulse. At the end of the t_1 evolution period, the MQ coherence is converted back into an antiphase S coherence by the second $\pi/2$ proton pulse. During the second τ period this coherence evolves to become an in-phase observable S coherence.

Some details about the homonuclear decoupling scheme have to be mentioned. Under FSLG decoupling, the effective field Z axis is aligned with the magic angle (see

Fig. 2.3). The first 54.7° "magic angle pulse" applied on protons at the end of the first τ period compensates for the tilted precession around the effective field axis by rotating the proton longitudinal magnetization into the z axis of the rotating frame. In the same way, the second and third magic angle pulses applied on both sides of the t_1 evolution period bring the proton transverse magnetization perpendicular to the effective field, and back to the xy plane respectively. The fourth magic angle pulse rotates the proton longitudinal magnetization from the z axis to the Z axis so that it is aligned with the effective field during the second τ delay. The magic angle pulses associated with the τ periods serve to increase the sensitivity of the experiment, while those associated with t_1 serve also to minimize axial peaks and quadrature images.

During the acquisition period, TPPM heteronuclear decoupling [78] is applied. A two-dimensional Fourier Transform yields pure in-phase chemical shift correlations between pairs of bonded protons (in ω_1) and carbons, or nitrogens (in ω_2) [90]. The heteronuclear couplings as well as the proton chemical shift in ω_1 are scaled by the scaling factor of the homonuclear decoupling sequence. Note that for a CH_2 or a CH_3 group, higher orders of coherences are created at the end of the t evolution period, i.e. triple or quadruple heteronuclear MQ coherences as discussed previously. The phase cycle on ϕ_1 and ϕ_3, in Fig. 2.9, selects only the double quantum *heteronuclear* coherences, but more complicated phase cycles are possible in order to select higher order coherences like in the MQ-Filter experiments. This work is currently in progress. For this description we see that the MAS-J-HMQC experiment has many aspects in common with the well-known HMQC liquid-state NMR experiment [74].

Table 2.3: Phase cycling for coherences having a variation of their coherence level of $\Delta p_I = \pm 1$ for the MAS-J-HMQC sequence shown in Fig. 2.9.

ϕ_1	ϕ_2	ϕ_3	ϕ_{rec}
0°	0°	0°	0°
180°	0°	0°	180°
0°	180°	0°	180°
180°	180°	0°	0°

2.4.3 Experiments

The natural abundance samples of camphor, L-alanine, L-tyrosine hydrochloride and cholesteryl acetate were purchased from Sigma and used without further purification. The tripeptide Boc-Ala-Ala-Pro-O-Bzl (where Boc stands for ter-butoxycarbonyl and Bzl for Benzyl) was synthesized in our laboratory and crystallized from diisopropyloxide [89]. Approximately 20 mg of each sample was used. The experiments were performed on a Bruker DSX 500 spectrometer (^{1}H frequency 500 MHz) using

a 4 mm triple resonance MAS probe. The sample volume was restricted to about 25 μl in the center of the rotor to increase the radio-frequency field homogeneity. With our probe, we found that the sample restriction was necessary to resolve, under FSLG decoupling, the multiplet fine structure due to scalar couplings in real samples like L-alanine. The proton rf field strength was set to 100 kHz during both the τ delays (FSLG decoupling) and during acquisition (TPPM decoupling). The FSLG sequence consists of two off-resonance pulses with opposite phases (i.e. $\{+x, -x\}$ or $\{+y, -y\}$, see Fig. 2.3), and opposite offsets so that the effective field is always aligned along the magic angle axis. As pointed out previously [40], we found that the best performance of the FSLG sequence was achieved when we used a mean frequency offset of about 5 kHz from the center of the ^{1}H resonance line, i.e. best results were obtained using "asymmetric" offsets. These offsets for FSLG decoupling were carefully adjusted experimentally on a natural abundance sample of L-alanine, for which the multiplet fine structure due to scalar couplings can be resolved. The overall duration of each of the two off-resonance pulses was 8.2 μs ($\omega_1 = 100$ kHz yields a 360° pulse around the 122 kHz total effective field of 8.2 μs). For technical reasons specific to our spectrometer, each pulse was divided into two successive pulses: a 1.25 μs pulse during which the frequency was changed, and a pulse of 6.95 μs with the correct phase. This programming was necessary so that the phase and frequency changes occur simultaneously in reality. The pulse sequence is given in appendix A.4. For the cross-polarization step, the rf field was set to 80 kHz for carbon (60 kHz for nitrogen), while a ramped rf field [87,91] was applied on protons, and matched to obtain optimal signal. A 16 step phase cycle was used to select the coherence transfer pathway shown in Fig. 2.9. The phase cycling of the sequence is presented in Table 2.3. The τ delay was synchronised to be an integral number of rotor periods. Quadrature detection in ω_1 was achieved using the States-TPPI method [92].

2.4.4 Comments

First Results on Camphor: Testing on a Plastic Crystal

Fig. 2.10 shows the MAS-J-HMQC spectrum recorded on camphor, a plastic crystal having exceptionally narrow linewidths. The assignment of the one-dimensional carbon spectrum has been previously reported (see also Fig. 2.6). As expected, the quaternary carbons (peaks 6, 7 and 1) give no correlation peaks in the 2D map, as they are not directly bonded to any protons, whereas all the protonated carbons are correlated with their attached protons. Note that for each CH_2 group (peaks 2, 4 and 5), there are two distinct correlation peaks corresponding to the two different chemical shifts of the two (diastereotopic) protons. The proton chemical shifts for camphor can be measured quite straightforwardly and without ambiguity using this MAS-J-HMQC spectrum, and they are listed in Table 2.4.

Note that *the correlation spectra obtained on plastic crystals cannot be obtained*

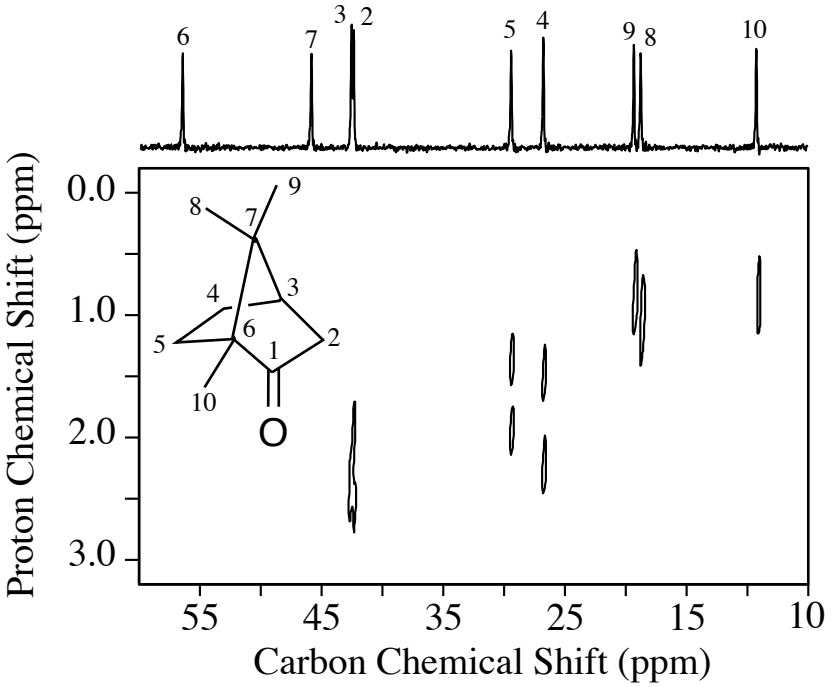

Figure 2.10: Two-dimensional MAS-J-HMQC spectrum of a powder sample of natural abundance camphor. A total of 256 t_1 increments with 8 scans each were collected. The spinning frequency was 6 kHz and τ was set to 2 ms. The 1D CP-MAS ^{13}C spectrum is shown above the 2D spectrum. The carbonyl C1 resonance lies far away (150 ppm) and is not shown. See Table 2.4 for details on the proton reference frequency and chemical shifts measured from this spectrum. From Ref. [75].

Table 2.4: Proton chemical shifts for camphor measured from the 2D MAS-J-HMQC spectrum of Fig. 2.10.

Nucleus	δ^a/ppm
H2	2.57, 1.95
H3	2.34
H4	2.21, 1.47
H5	1.95, 1.35
H8	1.07
H9	0.84
H10	0.88

[a]Frequencies in the proton dimension are given with respect to proton H10 which was set to 0.88 ppm with respect to TMS by analogy with a liquid state spectrum recorded in $CDCl_3$ at 20°C. Errors on the reported chemical shifts are estimated to be around ±0.05 ppm.

using a dipolar coupling driven polarization transfer. Plastic crystals are crystalline compounds, so they do not have any translation degrees of freedom below a critical phase transition temperature. They do have however, rotational mobility at ordinary temperatures and therefore all intramolecular dipolar couplings are averaged to zero. Intermolecular dipolar couplings are still present. All correlations in dipolar correlation spectroscopy come from *intermolecular* dipolar couplings and they do not inform us about the molecular structure of the compound. Using such dipolar techniques long strips in the proton dimension are obtained [93] making the assignment of the proton dimension impossible.

Long-Range Couplings on Camphor

The two-dimensional spectrum of Fig. 2.10 was recorded with a short value of τ (2 ms), so that the contribution of two and three-bond J_{CH} couplings remains negligible. However long-range scalar couplings, which are also active during the evolution periods, can lead to the excitation of heteronuclear double-quantum coherences for longer values of τ. This is illustrated in Fig. 2.11, showing the experimental and simulated evolution of signal intensity as a function of the τ delay for three different carbons: carbon 10 (methyl carbon), carbon 7 (quaternary carbon) and carbon 5 (methylene carbon). For the quaternary carbon, Fig. 2.11(b), we observe a significant signal whose evolution can be fitted with a small value of the coupling, $J = 5.4$ Hz, which is in agreement with the order of magnitude expected for two-bond couplings. The methyl group (Fig. 2.11(a)) is "isolated" from other protons as can be seen from the molecular structure of camphor, and indeed its signal evolution as a function of τ can be fitted without taking into account any long-range couplings (see Fig. 2.5(a)). Once again the fitted value (144.5 Hz) corresponds well to what can be expected for a one-bond coupling in an organic compound [88]. In order

to fit correctly the experimental data of the methylene carbon 5 (Fig. 2.11(c)), we accounted for both two equivalent one-bond $^1J_{CH}$ couplings and two different two-bond couplings, which would correspond to the couplings with protons 4 (fitted values $^1J = 146$ Hz, $^2J_1 = 8.2$ Hz, $^2J_2 = 5.5$ Hz). The values for the one-bond $^1J_{CH}$ couplings found by these fitting procedures are in agreement with the experimental couplings that can be measured in the one-dimensional carbon spectrum acquired under FSLG decoupling (129 and 139 Hz for carbons 10 and 7 respectively, data shown in Fig. 2.11). The fitted values of the T_2 relaxation times are not obvious to relate with structural information. This is because they depend on a complicated way on the dipolar decoupling sequence, on the proton relaxation times, and on the molecular structure (dipolar couplings etc.). They have to be treated carefully, as simple phenomenological parameters, reflecting the damping of the signal.

This study on the model sample of camphor confirms that the experiment does yield scalar coupling driven magnetization transfer, and shows that two-bond couplings, despite the fact that they are quite small, can also lead to the creation of multiple-quantum heteronuclear coherences. In summary, short values of τ should be used to ensure only one-bond chemical shift correlations, while the use of longer τ values would give useful information about the neighboring spins.

Application to a tripeptide

Fig. 2.12 shows the ^{1}H-^{13}C MAS-J-HMQC spectrum recorded for a tripeptide Boc-Ala-Ala-Pro-O-Bzl. If the carbon spectrum is assigned, a MAS-J-HMQC experiment leads to the unambiguous assignment of the proton spectrum, thereby allowing the measurement of the proton chemical shifts in solids. For this tripeptide we do not know the assignment of the carbon spectrum. Indeed, whereas several methods have been proposed to characterize MAS spectra of rare nuclei in isotropically enriched compounds, nevertheless the assignment of the carbon spectrum at natural abundance remains a difficult task. However, we know for the MQ Filters spectra of Fig. 2.8 the carbon multiplicities. Here, we will see that in natural abundance samples correlation with the proton dimension can provide an additional source of information which is useful to characterize the carbon spectrum.

For example, for this tripeptide we can state without ambiguity that the three carbon resonances at low field as well as the one around 76 ppm, which are not correlated to any proton chemical shift, correspond to quaternary carbons. From carbon chemical shift considerations [88], the carbon resonance at 76 ppm can be tentatively assigned to the quaternary carbon of the ter-butyl group, and that at 136 ppm to the quaternary carbon of the benzyl group; the remaining two quaternary resonances must therefore correspond to the three amino acid carbonyl groups (170 ppm) and to the carbonyl carbon of the Boc group (155 ppm). The carbon peaks between 126 and 130 ppm yield correlations with the proton dimension at about 7 ppm, and are therefore likely to correspond to the protonated carbons of the benzyl group. In the high-field part of the spectrum ten correlation peaks can be clearly

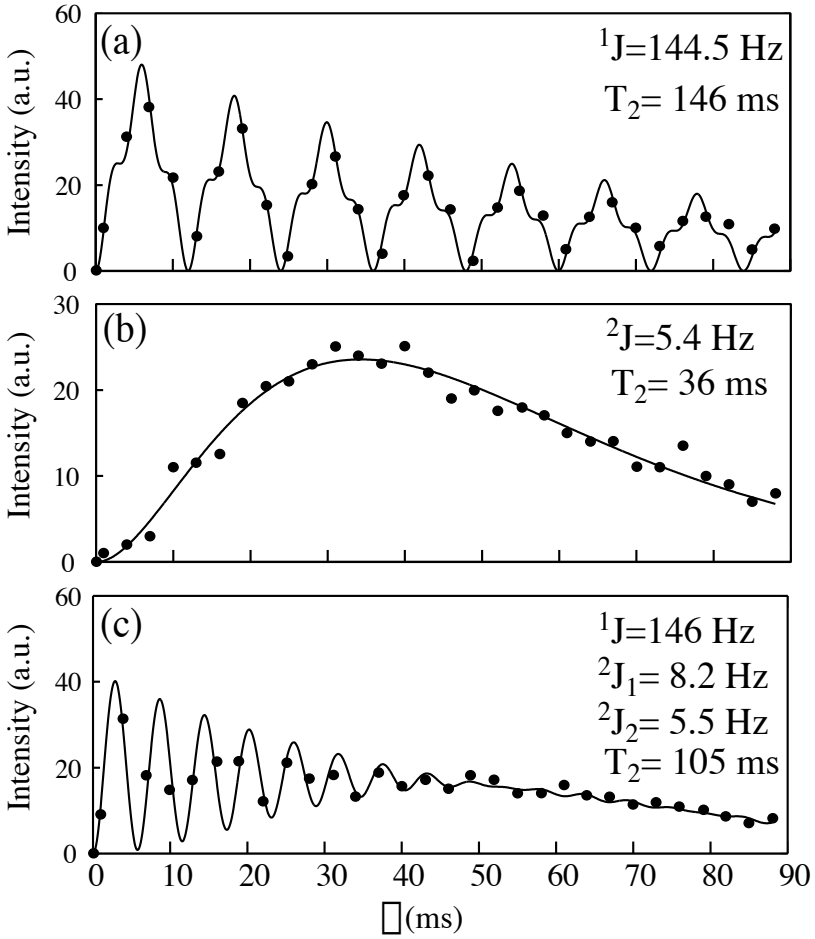

Figure 2.11: Evolution of the signal intensity in one-dimensional MAS-J-HMQC experiments ($t_1 = 0$) as a function of the τ delay for peaks number 10 (a), 7 (b) and 5 (c) of camphor corresponding respectively to a methyl carbon, a quaternary carbon and a methylene carbon. The spinning frequency was set to 6 kHz. The points are the measured values whereas the solid curves correspond to fittings from equations 2.43, 2.44, 2.45. The adjustable parameters were the overall intensity, the couplings and the transverse relaxation time. The simulations were done by considering three equivalent couplings for peak 10 (a), one coupling for peak 7 (b), and two equivalent (one-bond) and two different (two-bond) couplings for peak 5 (c). From Ref. [75].

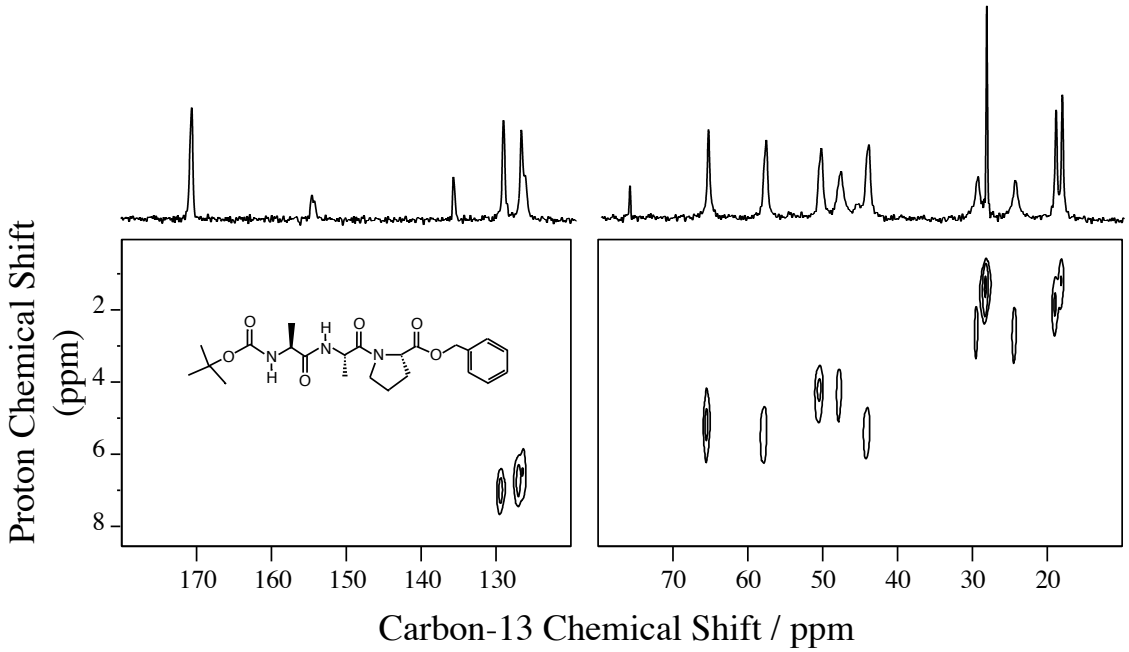

Figure 2.12: Two-dimensional MAS-J-HMQC spectrum of a natural abundance sample of the tripeptide Boc-Ala-Ala-Pro-O-Bzl. The spinning frequency was 15 kHz and τ was 1.3 ms. A total of 256 t_1 increments with 448 scans each were collected. In the proton dimension, the methyl resonance of the Boc group (see text for details on the assignment of the 2D spectrum) is referred to 1.4 ppm with respect to TMS by analogy with a liquid state spectrum recorded in $CDCl_3$ at 20°C. From Ref. [75].

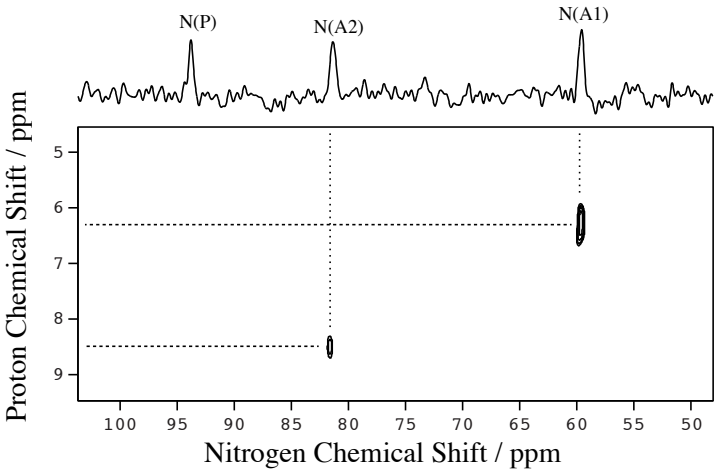

Figure 2.13: Two dimensional MAS-J-HMQC ^{1}H-^{15}N spectrum of a natural abundance sample of the tripeptide Boc-Ala-Ala-Pro-O-Bzl. The spinning frequency was 12.5 kHz and τ was 4.32 ms. A total of 110 t_1 increments with 256 scans each were collected. In the proton dimension we referenced the methyl resonance of the Boc group (see text for details on the assignment of the 2D spectrum) to 1.4 ppm with respect to TMS by analogy with a liquid state spectrum recorded in $CDCl_3$ at 20C. From Ref. [76].

distinguished, which is exactly the number of expected correlations. The three carbon resonances which correlate with protons around 1.5 ppm (carbon chemical shifts of 18.3, 19 and 28.3 ppm) can be assigned to methyl groups. Tentatively, from carbon chemical shifts, we assume that the peak at 28.3 ppm corresponds to the ter-butyl methyl groups, and the other two to the alanine methyl groups. Of the remaining peaks the two carbons at 24.5 and 29 ppm correlate with protons at around 2.6 ppm and can be therefore tentatively assigned to the proline γ and β-carbons respectively. The O–CH_2 can be assigned to the peak at 65.8 ppm which has a proton correlation at 5.2 ppm. The remaining four peaks between 40 and 60 ppm therefore correspond to the proline α and δ-carbon resonances and to the alanine α-carbons. Note that this assignment is in accordance with the results on carbon multiplicities of Fig. 2.8.

Additionally, interesting information can also be obtained from the ^{1}H-^{15}N MAS-J-HMQC spectrum shown in Fig. 2.13. From the lack of the correlation peak we can immediately conclude that the ^{15}N at 94 ppm belongs to the proline amino-acid. Then the difference in proton chemical shift between the two correlation peaks can give us useful information about the formation of intra of intermolecular hydrogen bonds in the solid state. In this case it is likely to have intermolecular hydrogen bonds between the alanine amino-acids.

The assignment of the carbon and nitrogen spectrum can be performed by combining the information from: the 1D MQ filtered spectra, the 2D MAS-J-HMQC spectra of figures 2.12, 2.13 and the 2D MAS-J-HMQC spectrum of Fig. 2.14 obtained using a mixing time τ of 16 ms. In this last experiment, multiple quantum coherences are excited using long-range scalar couplings and information about the neighboring atoms in the molecule is obtained. Thus, the Boc methyl groups do not give long-range correlations, as expected, but the quaternary carbon does with the protons of the three CH_3 groups. The carbonyl carbon of the Boc group gives a long-range correlation with the proton having a chemical shift of 6.5 ppm which is attached with a nitrogen atom. From the proton-nitrogen 2D spectrum we can thus assign the nitrogen at 60 ppm. Using similar arguments we can assign the last nitrogen atom at 82 ppm to belong to the second L-alanine of the tripeptide. The assignment of the benzene cycle is also possible: the quaternary carbon gives long-range correlation with the O–CH_2 and with the C2 and C6 of the cycle. Both C2 and C6 correlate with C3 and C5 but not with C4. The relative intensity between C3,5 and C4 in the 1D spectrum supports also this assignment. We can distinguish between the α carbon of the first L-alanine (Ala1) and the α carbon of the second L-alanine (Ala2). The α carbon of Ala1 gives a long-range correlation with the proton of the NH_3 whose proton has a chemical shift of 6.5 ppm, while the α carbon of Ala2 would give a correlation with the proton of the NH_3 whose proton has a chemical shift of 8.5 ppm. This correlation is not observable at this contour level. However, since the CH_3 groups of the two alanines give long-range correlations with their respective α carbons, we can assign their resonances at around 19 ppm. Further details of the complete assignment procedure making use of the long-range couplings are given by Lesage et al. in [76].

From this simple example, we see how in an unknown spectrum we can go a long way towards assignment (in this case a complete assignment of the ^{13}C, ^{15}N and ^{1}H spectra) without any additional information, simply by analysing the one- and/or two-bond ^{1}H-^{13}C and/or ^{1}H-^{15}N correlations which combine carbon, nitrogen and proton chemical shift information. Further simplification can be obtained by combining these ideas with multiple quantum filtering.

Cholesteryl Acetate

In cases where the carbon-13 assignment can be obtained, the amount of detailed information about the proton chemical shifts that can be obtained using these experiments is impressive. We have applied the MAS-J-HMQC experiment to cholesteryl acetate (Fig. 2.15), for which a tentative assignment of the one-dimensional carbon spectrum can be proposed on the basis of ^{13}C spectral editing experiments and comparisons with the fully assigned liquid state carbon spectrum [24]. As for the tripeptide, proton-carbon chemical shift correlations were used to resolve some of the ambiguities in the assignment. Our assignment is given in Table 2.5.

This relatively large compound (25 protonated carbons) crystallizes with two

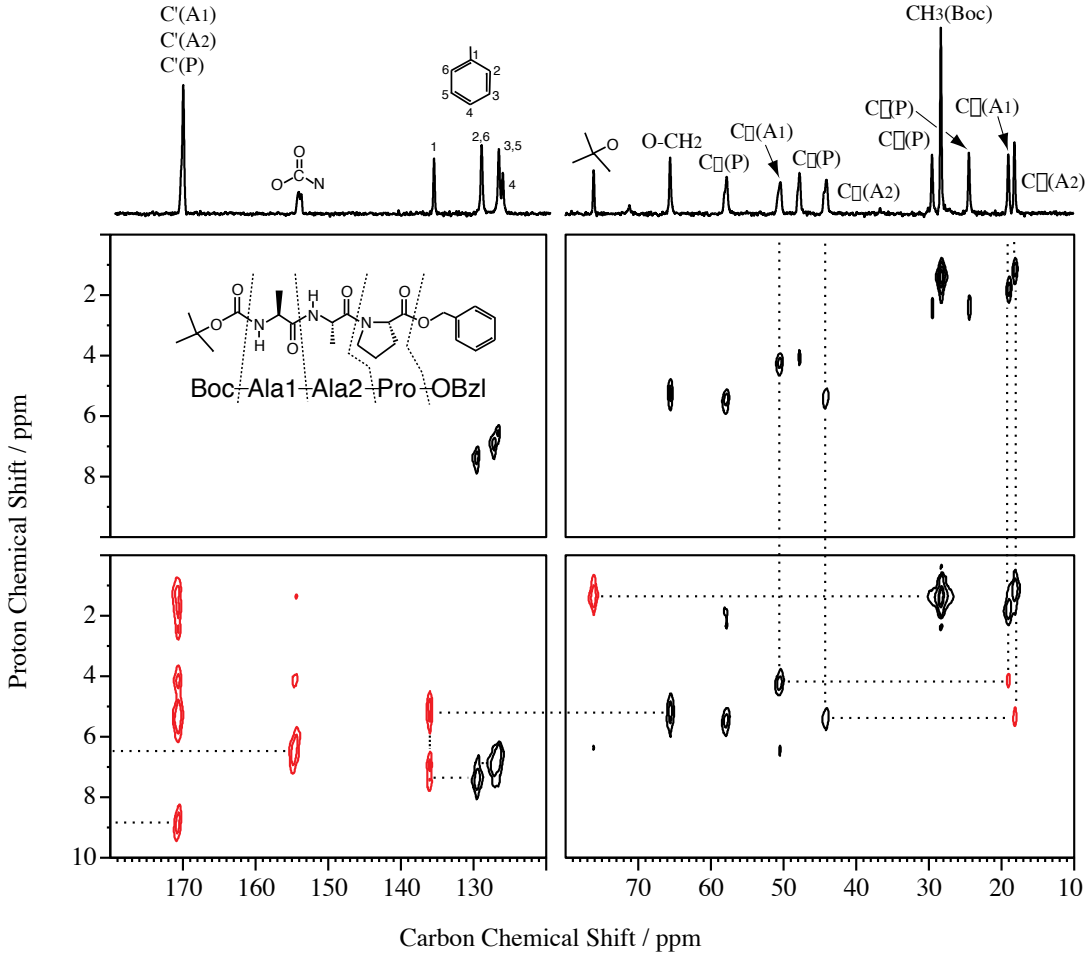

Figure 2.14: Two dimensional MAS-J-HMQC spectra of a natural abundance sample of the tripeptide Boc-Ala-Ala-Pro-O-Bzl. The top spectrum corresponds to a short mixing time $\tau = 1.6$ ms, while the bottom spectrum corresponds to a long mixing time of $\tau = 16$ ms. Both spectra are shown for comparison and extra resonances on the second spectrum are shown in red. Using the long-range correlations and previous information the total assignment of the tripeptide is possible [76] (see text for details). Kindly offered by Dr. A. Lesage [76].

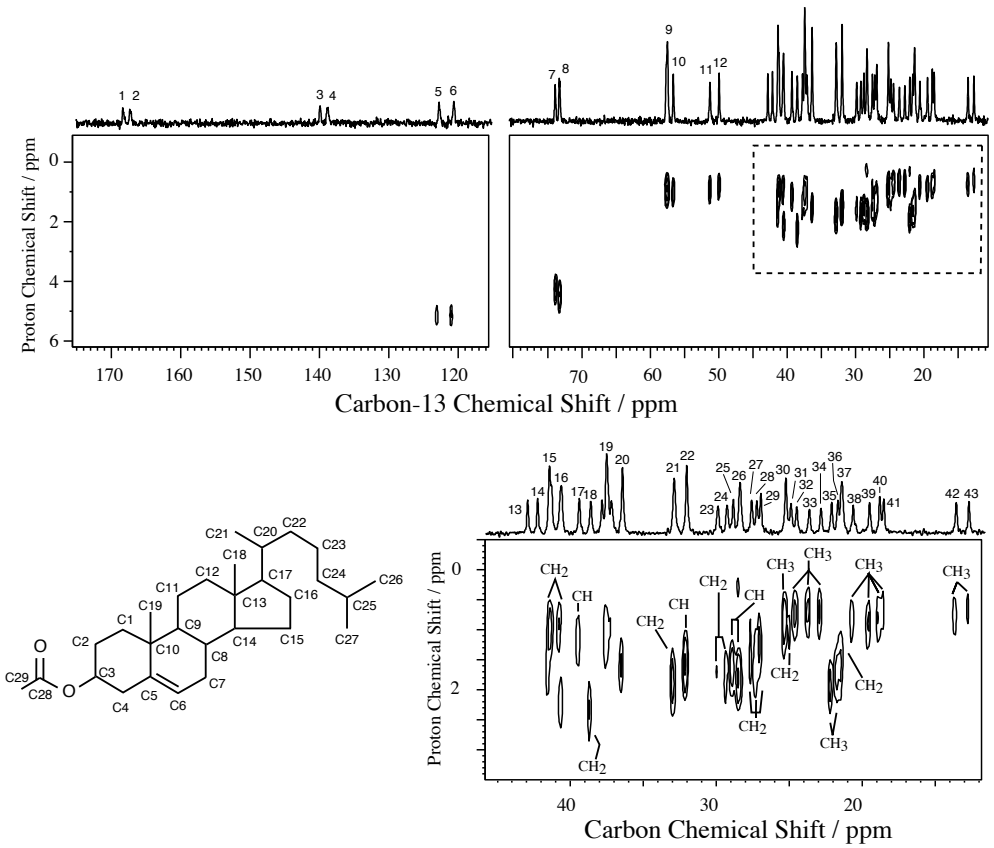

Figure 2.15: Two dimensional MAS-J-HMQC spectrum of cholesteryl acetate. The spinning frequency was 15 kHz and τ was 1.3 ms. A total of 140 t_1 increments with 320 scans each were collected. On the expansion of the high field region of the 2D spectrum, we indicate the identification of the carbon multiplicities as determined by scalar coupling based spectral editing experiments [24]. See Table 2.5 for details on the proton reference frequency and chemical shifts measured using this spectrum. From Ref. [75].

molecules per unit cell. Despite the very small proton chemical shift range in the high field region of the spectrum, the resolution of the 2D map is outstanding. With the spectrum of Fig. 2.15, we were able to measure for each peak of the one-dimensional carbon spectrum the corresponding proton chemical shift (if present) and the measured values are given in table 2.5. The 2D spectrum yields all the proton chemical shifts in the molecule. This is by far the most complex system for which proton chemical shifts in the solid state have ever been reported.

2.5 Discussion

Selectivity *vs* Sensitivity

The selectivity in terms of one-bond *vs* many bond transfer of the MAS-J-HMQC experiment can be compared in a semi-quantitative manner to that of a dipolar-based HETCOR experiment. This is illustrated in Fig. 2.16 showing the efficiencies of one-bond and geminal transfers in the MAS-J-HMQC experiment (a), and in the dipolar HETCOR experiment (b). In the MAS-J-HMQC experiment, the transfer is oscillatory because the scalar couplings are orientation-independent and all the crystallites behave identically. On the other hand, in a cross-polarization experiment, it is well known that, for an isolated two spin system, the transfer has a damped oscillatory behaviour due to integration over the whole powder[4]. The transfered S magnetization is : $\langle S_x \rangle(t) = [1 - g(t)]/2$, where:

$$g(t) = 1/2 \int_{\theta} \cos[b(\theta)t] \sin(\theta) \mathrm{d}\theta \tag{2.49}$$

with $b(\theta)$ the orientation dependent dipolar coupling [95]. As a result, the selectivity of the heteronuclear coherence transfer process is much weaker for the dipolar case as illustrated in figures 2.16(c) and (d) which compare the ratio of the direct and geminal transfers for the two types of experiments. We see clearly that in the MAS-J-HMQC experiment, the contribution to the signal intensity of two-bond couplings is proportionally much less than the contribution of geminal dipolar couplings in a dipolar HETCOR experiment. In addition to the difference in dynamics, the difference in selectivity is also related, to a lesser extent, to the fact that the ratio of direct and geminal couplings is more favorable for scalar interactions. For the calculations of the selectivity of the dipolar HETCOR experiment, we considered a Hamiltonian which contains only heteronuclear dipolar coupling terms and which corresponds to selective transfer schemes like WIM-24 or other schemes like cross polarization under FSLG, which decouple the proton bath during heteronuclear polarization transfer. In other words, the homonuclear dipolar couplings between

[4]Here we consider an isolated spin system assuming that during the cross-polarization transfer homonuclear proton decoupling is present. This simplifies the calculation and *corresponds to the most favorable case for the dipolar HETCOR experiment.*

Table 2.5: Proton chemical shifts for solid-state cholesteryl acetate measured from the 2D MAS-*J*-HMQC spectrum of Fig. 2.15.

Peak Number[b]	δ (ppm)[a]	Carbon nuclei (tentative assignment)[c]	Peak Number	δ (ppm)	Carbon nuclei (tentative assignment)
1	-	C28	23	1.63	*C2 (C15, C12)*
2	-	C28	24	1.72	*C2 (C15, C12)*
3	-	C5	25	1.56	C25
4	-	C5	26	1.75	C25
5	5.15	C6	27	1.49	*C15, C12 (C2)*
6	5.12	C6	28	1.59	*C15, C12 (C2)*
7	4.17	C3	29	1.19	*C15, C12 (C2)*
8	4.42	C3	30	0.77	*C27 (C26)*
9	0.89	*C14, C17*	31	0.97	C23
10	0.99	*C14, C17*	32	0.67	*C27 (C26)*
11	0.90	C9	33	0.65	*C26 (C27)*
12	0.80	C9	34	0.66	*C26 (C27)*
13	-	C13	35	1.85	C29
14	-	C13	36	1.65	C29
15	0.90,1.65	*C16, C24*	37	1.49	C11
16	2.14,0.84	*C16, C24*	38	0.78	*C19 (C21)*
17	1.11	C20	39	0.86	*C19 (C21)*
18	2.29	C4	40	0.78	*C21 (C19)*
19	1.01	C10 and C22 *(C1)*	41	0.64	*C21 (C19)*
20	1.54	C10 and C1 *(C22)*	42	0.73	C18
21	1.78	C7	43	0.65	C18
22	1.53	C8			

[a]In the proton dimension, we referenced the proton signal which correlates to carbon peak 43 at 0.65 ppm with respect to TMS by analogy to a liquid state spectrum recorded in $CDCl_3$ at 20°C. This peak corresponds to the methyl group 18 of one of the two cholesteryl acetate molecules in the unit cell. Errors on the reported chemical shifts are estimated to be around ±0.05 ppm.

[b]Peak number in the one-dimensional carbon spectrum of cholesteryl acetate, as indicated in Fig. 2.15.

[c]The proposed assignment of the carbon one-dimensional spectrum was done by combining previous spectral editing experiments [24], with the knowledge of the proton and carbon [94] spectra in the liquid state. We report the unambiguous assignments in plain text and those that are uncertainties in italic (most probable assignment first, with potential alternatives in parenthesis).

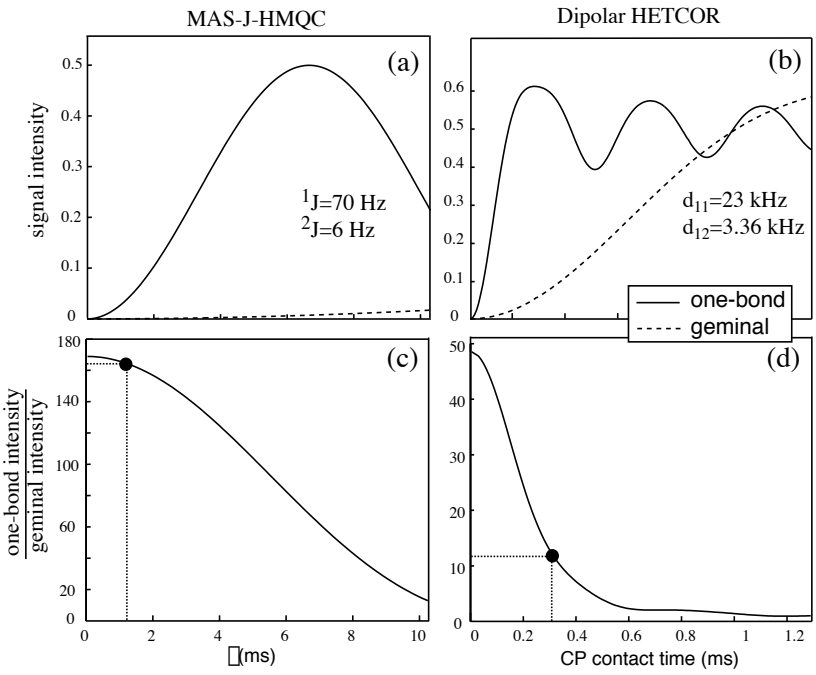

Figure 2.16: Simulated coherence transfer efficiency as a function of τ in the MAS-J-HMQC experiment (a) and τ_{CP} in the dipolar HETCOR experiment (b). In (a) the curves were calculated according to the Eq. (2.37) for a CH group. The solid line corresponds to transfer through a one-bond coupling (70 Hz), while the dashed line corresponds to the transfer through a two-bond coupling (6 Hz). For the dipolar HETCOR experiment (b), a cross-polarization scheme was considered for the polarization transfer. The calculations were performed using Eq. (2.49) for the case of a directly bonded carbon-proton pair, using an inter-nuclear distance of 1.1 Å corresponding to a dipolar coupling of 23 kHz (solid line), and in the case of two geminal nuclei, using a distance of 2.1 Å for a dipolar coupling of 3.3 kHz (dashed line). Relaxation was not taken into account. In (c) and (d), the ratio of the transfer efficiencies between directly-bonded and geminal nuclei is represented for the two types of heteronuclear correlation experiments. The MAS-J-HMQC experiment has a better selectivity than the dipolar HETCOR with respect to transfer from closest neighbours. For mixing times of 1.3 ms and 300 μs for the MAS-J-HMQC experiment and the dipolar HETCOR experiment respectively, the selectivity of transfer is predicted to be 16 times greater in the MAS-J-HMQC than in the dipolar HETCOR. From Ref. [75].

neighboring protons have not been considered. If the dipolar experiment uses simple Hartmann-Hahn cross-polarization, these couplings will lead to a worsening of the selectivity of the dipolar experiment.

None of the spectra that we have so far recorded using the MAS-J-HMQC experiment with τ values less than 2 ms contain cross-peaks with quaternary carbons or with non-bonded protons, which is a good experimental indication that the experiment is as selective as we predict. Note however, that for longer τ values we expect that the excitation of quaternary carbons by long-range couplings will be comparatively more efficient than that of protonated carbons, due to differences in linewidths.

The difference in selectivity between the two experiments can be appreciated in Fig. 2.17 which shows two heteronuclear correlation spectra of a natural abundance sample of L-tyrosine hydrochloride, recorded with the MAS-J-HMQC experiment, and with a dipolar HETCOR experiment (transfer through Hartmann-Hahn cross-polarization). The assignment of the 1D CP-MAS spectrum indicated on the top of the figure, was obtained from a fully-labeled sample of L-tyrosine using the INADEQUATE experiment [80]. The INADEQUATE spectrum in shown in Fig. 2.1. Note that a dipolar HETCOR experiment on a fully carbon-13 enriched L-tyrosine sample has already been reported [39]. In the MAS-J-HMQC spectrum the CH groups (peaks 2, 5, 6, 7, 8) yield only one correlation with their attached proton, as expected, whereas there is no correlation for the quaternary carbons (even at lower contour levels). Carbon 3 (α CH_2 group) correlates with two different proton chemical shifts arising from the two diastereotopic protons. In the dipolar HETCOR spectrum shown in Fig. 2.17(b) many additional peaks are present due to long-range transfer. In particular the three non-protonated carbons (peaks 1, 9 and 4) yield correlations with adjacent protons. At lower contour levels, correlations with all types of proton moieties (like the COOH, NH_3^+ or OH) are visible, some of which even correspond to intermolecular correlations. These peaks, which reflect spatial proximities between heteronuclei, can obviously be very useful for structural studies, but they nevertheless greatly complicate the correlation spectrum and render the identification and assignment of the carbon-bonded protons much more difficult. This is particularly visible when the dispersion of the proton spectrum is small, and many correlations with similar intensities are present. In contrast, assignment is straightforward and unambiguous using the MAS-J-HMQC spectrum for which the effective proton resolution is greatly improved. Of course, the selectivity of the dipolar HETCOR experiment could be improved by using a shorter contact time. However, this would be at the expense of a significant loss in signal intensity, which poses a real problem for natural abundance samples. Under our experimental conditions (cross-polarization contact time of 300 μs for the dipolar HETCOR, and a τ delay of 1.3 ms for the MAS-J-HMQC experiment), we found that the sensitivity of the MAS-J-HMQC experiment was approximately half that of the dipolar HETCOR experiment. (Note that, at longer mixing times ($\tau > 2$ ms), weak signals from the quaternary carbons (peaks 1 and 9) appear in the MAS-J-HMQC spectrum.

The evolution of the signal intensity of these peaks as a function of τ was found to be compatible with a two-bond coupling transfer.)

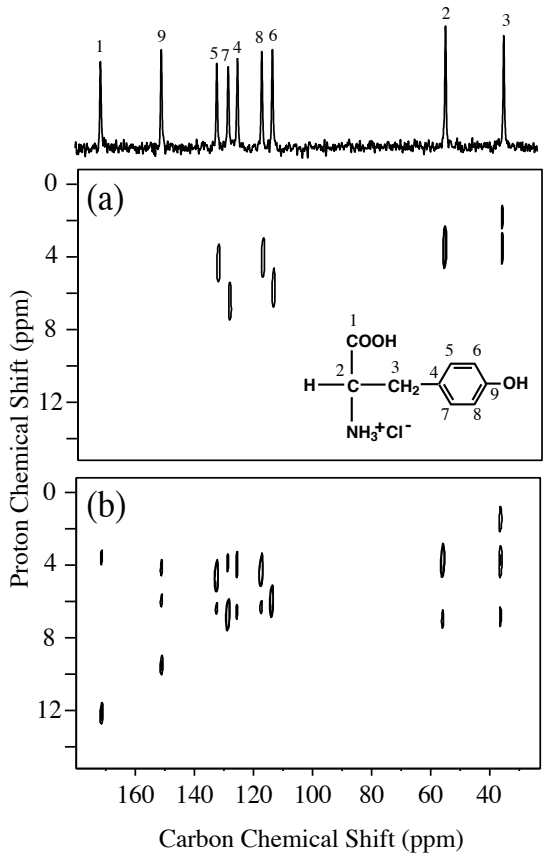

Figure 2.17: Two-dimensional MAS-J-HMQC spectrum (a) and dipolar HETCOR [39] spectrum (b) of a natural abundance sample of L-tyrosine hydrochloride. The spinning frequency was 15 kHz. τ was set to 1.3 ms for the MAS-J-HMQC experiment, and the contact time τ_{CP} in the dipolar HETCOR was 300 μs. A total of 256 t_1 increments with 96 scans each were collected for both experiments.

The long range selectivity is also another important difference between the two techniques. Dipolar transfer becomes very complicated and thus non selective when mixing is allowed for a long period. In this case correlations from all proton spins will be obtained. On the other hand, scalar couplings are much more selective especially for long mixing periods. Only correlations from proton nuclei being 2 or 3 bond away are possible, giving valuable structural information.

The two experiments also differ in terms of homogeneity of the transfer. The intensity of correlation peaks in the dipolar HETCOR experiment is dependent on

the size of the effective heteronuclear couplings. These effective couplings may vary considerably within a molecule. Particularly, some groups may be more mobile than others, and as a result have smaller effective dipolar couplings. In this case, using a short CP contact time to ensure selectivity will prevent efficient polarization transfer to these groups, and some one-bond correlation peaks will be absent from the 2D spectrum. In contrast, the J couplings are much more homogeneous over the molecule. The sensitivity of the MAS-J-HMQC experiment is largely independent of molecular motion or conformation. It is only dependent on the homogeneous linewidths of the carbon and proton coherences under FSLG. Finally, since the spin dynamics of the sequence do not depend on rotation, there is no intrinsic limitation in terms of spinning frequency to the MAS-J-HMQC experiment. The experiment can be applied at any spinning frequency for which the homonuclear decoupling scheme is efficient.

From the above considerations we can conclude that the heteronuclear correlation spectroscopy using dipolar couplings is more sensitive but less selective than using scalar couplings. On the other hand the sensitivity of the later technique lies on the efficiency of the homonuclear decoupling. We can legitimately say that both techniques are, for the actual NMR experimental conditions, complementary. Through-bond and through-space correlations, are the basis for structural determination in liquid-state NMR. However, further progress (more efficient decoupling, faster MAS, better probe sensitivity) would undoubtably favor the liquid-like techniques.

Further development is undertaken but not presented here. The experimental realization of 2D multiple quantum filtered spectra, is the next obvious step. 2D-HSQC, 3D-proton-carbon-nitrogen, or proton-proton-carbon spectra are experiments that would provide unvaluable information in characterization and structural determination of organic molecules in the solid state.

Chapter 3

Homonuclear Dipolar Decoupling

3.1 Introduction

Proton-proton homonuclear dipolar decoupling is an essential component of many high-resolution solid-state NMR experiments [1–3, 96]. As we have seen in the previous chapter, the efficiency of liquid-like techniques we developed (spectral editing, MAS-J-HMQC) are crucially dependent on the efficiency of the decoupling scheme. Additionally, homonuclear dipolar decoupling is the cornerstone for high-resolution solid state NMR spectroscopy of abundant nuclei such as ^{1}H and ^{19}F. In fact, the attainable resolution of proton spectra in solids is actually limited in crystalline organic compounds purely by the performance of the currently available dipolar decoupling sequences. Lee and Goldburg [43] and Waugh, Huber and Haeberlen [44] are responsible for the first important developments in this area. Since then, many decoupling schemes have been introduced to make homonuclear decoupling sequences less sensitive to diverse experimental imperfections, and to increase decoupling performance and thus spectral resolution and sensitivity. Some originate from the Lee and Goldburg school and are based on *off-resonance continuous irradiation* [40, 42, 43, 45, 73]. The second and most developed family of decoupling schemes arises from the Waugh ideas and is based on *on-resonance multiple pulse irradiation* [44, 46–53]. Other schemes based on static magnetic field modulation [54], numerical optimization [55] and rf amplitude modulation [56] have been developed in the literature.

Almost all of these schemes have been developed using Average Hamiltonian Theory (AHT), first introduced by Haeberlen and Waugh [57]. In the next section we are briefly resume the fundamentals of average Hamiltonian theory and we use it to prove an interesting theorem concerning the scaling factor of homonuclear decoupling sequences. Then we introduce a new approach to improve homonuclear decoupling in solids.

Part of the results presented in this chapter have been published [97] or will be submitted for publication [98].

3.2 Average Hamiltonian Theory

Average Hamiltonian theory has been developed in order to treat problems where the Hamiltonian of the physical system is periodically time dependent and where the observation is stroboscopic [90]. Perhaps, the most important feature of NMR spectroscopy is the possibility to manipulate the Hamiltonian of the system, by introducing strong perturbations (rf fields, sample spinning etc). These perturbations render the Hamiltonian of the system time dependent and, in the time scale of the observation, they can "average" some internal interactions. Following the notation of Haeberlen [3], any Hamiltonian for a nuclear spin system can be written:

$$\mathcal{H} = \sum_{\lambda} \sum_{l,m} R^{\lambda}_{l,m} T^{\lambda}_{l,m} \tag{3.1}$$

where λ accounts for each interaction, R^{λ} are 3D-spatial tensors and T^{λ} are irreducible spin tensor operators. In Eq. (3.1), l and m are the rank and the order of each tensor. We can write *any* interaction Hamiltonian as a linear combination of tensor products since, the Hamiltonian is invariant under rotations. Contractions (most commonly called tensor products) of tensors of the same rank, are also invariants [99] and constitute a basis in the rotationally invariant operator space. In solid-state NMR the 3D-spatial tensor components can become time-dependent by spinning or melting the sample, and in liquid state NMR they are time dependent because of molecular tumbling. Continuous or pulsed rf irradiation can render the spin part of the Hamiltonian time-dependent. Spectra are affected to lower order by the time-independent parts or, in other words, the time averages of the interaction Hamiltonians, thus the above-mentioned perturbations can induce a truncation of the internal Hamiltonian. A nice alternative description of AHT based on the group properties of unitary transformations is used in the frame of quantum computing [100, 101].

Going into the details of average Hamiltonian theory, we consider a system whose Hamiltonian can be separated into a time independent part $\mathcal{H}_{\rm int}$ describing the internal interactions, and a time dependent one $\mathcal{H}_1(t)$, describing the external perturbations:

$$\mathcal{H}(t) = \mathcal{H}_{\rm int} + \mathcal{H}_1(t) \tag{3.2}$$

In the interaction representation of the perturbation :

$$\tilde{\mathcal{H}}_{\rm int}(t) = U_1^{-1}(t)\, \mathcal{H}_{\rm int}\, U_1(t) \tag{3.3}$$

$$\sigma(t) = U_1(t)\, \tilde{\sigma}(t)\, U_1^{-1}(t) \tag{3.4}$$

$$U_1(t) = \mathrm{T} \exp\left[-i \int_0^t \mathcal{H}_1(t')\, \mathrm{d}t\right] \tag{3.5}$$

the system evolves under only the internal Hamiltonian, which in this interaction

representation becomes time-dependent:

$$\frac{\mathrm{d}}{\mathrm{d}t}\tilde{\sigma}(t) = -i[\tilde{\mathcal{H}}_{\mathrm{int}}(t), \tilde{\sigma}(t)] \tag{3.6}$$

and the solution of the previous equation can be formally written:

$$\tilde{\sigma}(t) = U_{\mathrm{int}}(t)\,\tilde{\sigma}(0)\,U_{\mathrm{int}}^{-1}(t) \tag{3.7}$$

where:

$$U_{\mathrm{int}}(t) = \mathrm{T}\exp\left[-i\int_0^t \tilde{\mathcal{H}}_{\mathrm{int}}(t')\,\mathrm{d}t\right] \tag{3.8}$$

T is the Dyson time-ordering operator [102, 103] and its action on a product of time dependent operators is to order them in a time decreasing order:

$$\mathrm{T}[\mathcal{H}(t_1)\mathcal{H}(t_2)] = \begin{cases} \mathcal{H}(t_1)\mathcal{H}(t_2), & \text{if} \quad t_1 > t_2 \\ \mathcal{H}(t_2)\mathcal{H}(t_1), & \text{if} \quad t_1 \leq t_2 \end{cases} \tag{3.9}$$

In the original representation we can prove [57] that the evolution of the density operator can be written:

$$\sigma(t) = U(t)\,\sigma(0)\,U^{-1}(t) \tag{3.10}$$

where the propagator $U(t)$ can be split into two parts: $U(t) = U_1(t)U_{\mathrm{int}}(t)$, even though the commutator between the internal Hamiltonian and the perturbation is non zero: $[\mathcal{H}_{\mathrm{int}}, \mathcal{H}_1(t)] \neq 0$ [57]. If we choose $\mathcal{H}_1(t)$ to be *cyclic*, that means:

1. $\mathcal{H}_1(t)$ is periodic: $\mathcal{H}_1(t + t_h) = \mathcal{H}_1(t)$
2. $U_1(t)$ is periodic: $U_1(t + t_c) = U_1(t)$

the period t_c of $U_1(t)$ will be an integer multiple of the period t_h of $\mathcal{H}_1(t)$. Several consequences must be mentioned:

1. $U_1(Nt_c) = U_1(0) = \mathbf{1}$, $\forall\, N$ (unitarity)
2. $\mathcal{H}_{\mathrm{int}}(t)$ is periodic with period t_c: $\mathcal{H}_{\mathrm{int}}(t + nt_c) = \mathcal{H}_{\mathrm{int}}(t)$
3. $U_{\mathrm{int}}(nt_c) = [U_{\mathrm{int}}(t_c)]^n$

Thus, the evolution of the density operator over any integral multiple of cycle time t_c, can be fully described by the propagator $U_{\mathrm{int}}(t_c)$:

$$\begin{aligned} \sigma(nt_c) &= U(nt_c)\,\sigma(0)\,U^{-1}(nt_c) \\ &= U_1(nt_c)\,U_{\mathrm{int}}(nt_c)\,\sigma(0)\,U_{\mathrm{int}}^{-1}(nt_c)\,U_1^{-1}(nt_c) \\ &= U_{\mathrm{int}}(nt_c)\,\sigma(0)\,U_{\mathrm{int}}^{-1}(nt_c) \\ &= [U_{\mathrm{int}}(t_c)]^n\,\sigma(0)\,[U_{\mathrm{int}}^{-1}(t_c)]^n \end{aligned} \tag{3.11}$$

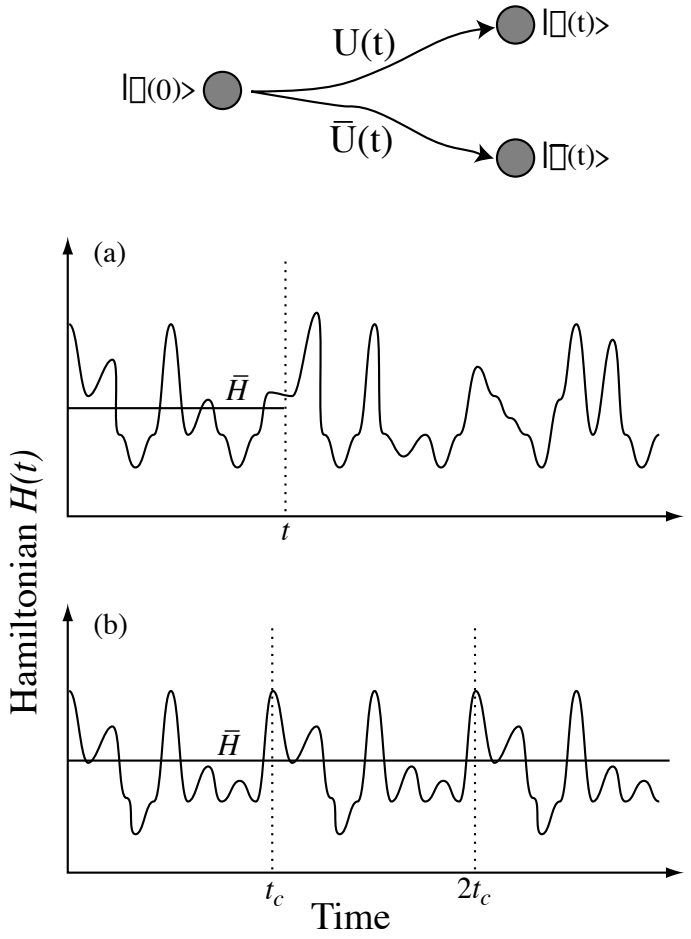

Figure 3.1: Whereas the system might naturally evolve under the propagator $U(t)$, we apply a perturbation so that the system evolves under a different propagator $\overline{U}(t)$, due to the Hamiltonian $\overline{\mathcal{H}}$, arriving perhaps at a different state at time t. The perturbation may be a pulse sequence and/or mechanical rotation. For a time-dependent Hamiltonian, the evolution can be characterized by an average time-independent Hamiltonian $\overline{\mathcal{H}}$. In general, if $\mathcal{H}(t)$ is not periodic (a), then $\overline{\mathcal{H}}$ depends on t. If $\mathcal{H}(t)$ is periodic (b), then the same $\overline{\mathcal{H}}$ is relevant for all multiples of the period, and the spin system evolves under an average time independent Hamiltonian that has the same effect as the time dependent one. Adapted from Ref. [4].

We can clearly see that for *synchronous observation*, a single propagator over one cycle is sufficient to describe the evolution. In other words, we can imagine that the spin system evolves under an average time-independent Hamiltonian that has exactly the same effect at the end of the cycle as the true time-dependent one. If we observe in multiples of the cycle time we will not see any difference between the effective and the true evolution. This is schematically explained in Fig. 3.1. Formally this can be written:

$$U_{\text{int}}(t_c) \equiv \mathrm{T}\exp\left[-i\int_0^{t_c}\tilde{\mathcal{H}}_{\text{int}}(t)\,\mathrm{d}t\right] \tag{3.12}$$

$$= \exp(-i\overline{\mathcal{H}}t_c) \tag{3.13}$$

Until this point, we did only some constraining assumptions about the periodicity of the problem but no approximations. However, to find analytical solutions we have to explicit $\overline{\mathcal{H}}$ as a series and approximate it with the first orders in the development. Using the Magnus expansion [104, 105] we can develop the average Hamiltonian as a series:

$$\overline{\mathcal{H}} = \overline{\mathcal{H}}^{(0)} + \overline{\mathcal{H}}^{(1)} + \overline{\mathcal{H}}^{(2)} + \ldots \tag{3.14}$$

where:

$$\overline{\mathcal{H}}^{(0)} = \frac{1}{t_c}\int_0^{t_c}\mathrm{d}t\,\tilde{\mathcal{H}}_{\text{int}}(t) \tag{3.15}$$

$$\overline{\mathcal{H}}^{(1)} = \frac{-i}{2t_c}\int_0^{t_c}\mathrm{d}t_2\int_0^{t_2}\mathrm{d}t_1\,[\tilde{\mathcal{H}}_{\text{int}}(t_2),\tilde{\mathcal{H}}_{\text{int}}(t_1)] \tag{3.16}$$

$\ldots$

Most of the existing decoupling sequences were designed using this average Hamiltonian decomposition. The first orders can in principle be easily calculated, as long as we assume perfect infinitely narrow pulses. However, the difficulty becomes tremendous as we try to calculate higher orders, or we try to include experimental imperfections [46, 48]. Nevertheless, some effort can be economized using symmetry properties, like the time reversal symmetry:

- if $\tilde{\mathcal{H}}_{\text{int}}(t) = \tilde{\mathcal{H}}_{\text{int}}(t_c - t)$ then: $\overline{\mathcal{H}}^{(k)} = 0, k = 2n+1, \forall\, n$
- if $\tilde{\mathcal{H}}_{\text{int}}(t) = -\tilde{\mathcal{H}}_{\text{int}}(t_c - t)$ then: $\overline{\mathcal{H}}^{(k)} = 0, \forall\, k$

Even numerical optimization studies using AHT have been limited to the first orders [55]. The most elaborate treatments to date use interesting theorems, based on commutator relations between irreducible tensor operators, that allow analytical calculations up to 6^{th} order [45].

The currently best performing homonuclear decoupling sequences have been designed in such a way that the different orders in the average Hamiltonian expansion

do not contain multi-linear terms in spin operators. These multi-spin terms account for the coupling between spins, so their presence is unwanted. Robustness has been gained by combining several cycles, generating super-cycles, that compensate for several experimental imperfections. However this renders the super-cycle quite long and, as we shall see in the next section, this complicates the situation in the presence of fast MAS.

3.2.1 The scaling factor theorem

We know that the biggest scaling factor λ found so far for homonuclear decoupling is $1/\sqrt{3}$, and that the spectral resolution is proportional to this scaling factor. We might be tempted to look for sequences having a scaling factor bigger than $1/\sqrt{3}$. It is demonstrated here that for the case of static solids (or in the limit of slow MAS), if the pulse sequence is responsible for averaging the dipolar Hamiltonian to the zeroth order, the maximum scaling factor is $1/\sqrt{3}$.

Proof: Suppose $\mathcal{H}_{\text{int}} = \Omega_1 I_{1z} + \Omega_2 I_{2z} + d(3I_{1z}I_{2z} - \vec{I}_1 \cdot \vec{I}_2)$ to be the internal Hamiltonian of the system. The restriction to a two spin system does not alter the final result but it makes the demonstration much shorter. The rf irradiation Hamiltonian of *any* sequence can be written as:

$$\mathcal{H}_{\text{rf}}(t) = \omega_1(t)\{\cos[\phi(t)]I_x + \sin[\phi(t)]I_y\} \tag{3.17}$$

The total propagator of this Hamiltonian can be written as:

$$U_{\text{rf}} = U_{\text{rf}}(0,t) = \exp[-i\alpha(t)F_z]\exp[-i\beta(t)F_y]\exp[-i\gamma(t)F_z] \tag{3.18}$$

where $\alpha(t)$, $\beta(t)$ and $\gamma(t)$ are time dependent Euler angles [106–108]. So the effective internal Hamiltonian can be written as:

$$\tilde{\mathcal{H}}_{\text{int}} = U_{\text{rf}}^{-1}\mathcal{H}_{\text{int}}U_{\text{rf}} \tag{3.19}$$

After some simple algebra we can extract the coefficient of the terms I_{1z} and $I_{1z}I_{2z}$ in the decomposition of $\tilde{\mathcal{H}}_{\text{int}}$ onto the Cartesian product operators basis:

$$\text{Tr}(\tilde{\mathcal{H}}_{\text{int}}\, 2I_{1z}I_{2z}) = \frac{d}{2}\{1 + 3\cos[2\beta(t)]\} \tag{3.20}$$

$$\text{Tr}(\tilde{\mathcal{H}}_{\text{int}}\, I_{1z}) = \Omega_1 \cos[\beta(t)] \tag{3.21}$$

Note that these results are independent of α and γ because of the invariance around the main magnetic field z axis and because of the non relevance of the main phase of the effective field. In other words, the decoupling efficiency and the scaling factor of a decoupling scheme are the same for any phase of the effective field [53]. In order to average the dipolar interaction to zero to the first order for a periodic rf sequence with period t_c, we need *at least*:

$$\int_0^{t_c} \{1 + 3\cos[2\beta(t)]\}\,\mathrm{d}t = 0 \tag{3.22}$$

or

$$\int_0^{t_c} \cos[2\beta(t)]\,\mathrm{d}t = -\frac{1}{3} \tag{3.23}$$

If we develop $\cos[2\beta(t)]$ as a Fourier series we can write:

$$\cos[2\beta(t)] = -\frac{1}{3} + \sum_{n=1}^{\infty} a_n \cos(n\omega_c t) \tag{3.24}$$

where $\omega_c = 2\pi/t_c$. The scaling factor is the coefficient of linear I terms, say the operator I_z. Then we have:

$$\lambda = \frac{1}{t_c}\int_0^{t_c} \cos[\beta(t)]\,\mathrm{d}t = \frac{1}{t_c}\int_0^{t_c} \sqrt{\frac{1+\cos[2\beta(t)]}{2}}\,\mathrm{d}t \tag{3.25}$$

Now including the constraint that the bilinear terms must, on average, be zero, we find:

$$\lambda = \frac{1}{t_c}\int_0^{t_c} \sqrt{\frac{1}{3} + \sum_{n=1}^{\infty} \frac{a_n}{2}\cos(n\omega_c t)}\,\mathrm{d}t \tag{3.26}$$

The Schwarz inequality says [109]: $(f,g)^2 \leq (f,f)(g,g)$, with $(f,g) \equiv \frac{1}{t_c}\int_0^{t_c} fg\,\mathrm{d}t$. If we take $g = 1$, we have:

$$\left(\frac{1}{t_c}\int_0^{t_c} f\,\mathrm{d}t\right)^2 \leq \frac{1}{t_c}\int_0^{t_c} f^2\,\mathrm{d}t$$

If $f = \sqrt{\frac{1}{3} + \sum_{n=1}^{\infty}\frac{a_n}{2}\cos(n\omega_c t)}$, then :

$$\left(\frac{1}{t_c}\int_0^{t_c} \sqrt{\frac{1}{3} + \sum_{n=1}^{\infty} \frac{a_n}{2}\cos(n\omega_c t)}\,\mathrm{d}t\right)^2 \leq \frac{1}{t_c}\int_0^{t_c} \left(\frac{1}{3} + \sum_{n=1}^{\infty}\frac{a_n}{2}\cos(n\omega_c t)\right)\mathrm{d}t \tag{3.27}$$

or

$$\frac{1}{t_c}\int_0^{t_c} \sqrt{\frac{1}{3} + \sum_{n=1}^{\infty} \frac{a_n}{2}\cos(n\omega_c t)}\,\mathrm{d}t \leq \sqrt{\frac{1}{t_c}\int_0^{t_c}\frac{1}{3}\,\mathrm{d}t} = \frac{1}{\sqrt{3}} \tag{3.28}$$

From Eq. (3.26) we have:

$$\lambda \leq \frac{1}{\sqrt{3}} \tag{3.29}$$

Thus, *if the pulse sequence averages the first order of the average Hamiltonian to zero, the scaling factor cannot be greater than* $1/\sqrt{3}$.

Extension of this theorem to higher orders in the AHT description, though possible in principle, is out of the scope here. The possibility to find larger scaling factors, and so to improve the resolution of homonuclear decoupling is an open question in the case of synchronized rotation and multiple pulse decoupling, where the rotation alone is sufficient for the zeroth order averaging.

3.3 CRAMPS

Combined Rotation and Multiple Pulse Sequences (CRAMPS) were introduced early in solid state NMR [26–29]. Averaging caused by MAS and averaging caused by multiple pulses, operate on different spaces and can have very different time scales. The separation of these time scales avoids any destructive interference between the two techniques. Notably, if the rotation is "slow" compared with the frequency of the multipulse scheme, the dipolar couplings do not change significantly during a period of the averaging sequence. We call this *the quasi-static regime*. Thus, the averaging due to the sequence and predicted by AHT (assuming constant dipolar couplings) is almost perfect. The chemical shift, which is an anisotropic interaction, is just scaled by the multiple pulse sequence. Thus, we need magic angle spinning together with multiple pulse decoupling in order to get "isotropic" well resolved spectra.

An interesting situation occurs when the two time scales are similar. In this case the quasi-static approximation is no longer valid and the two averaging methods may interfere. Synchronization arguments have been presented in the literature [51, 52, 58]:

$$n\,\omega_{\mathrm{mod}} = m\,\omega_{\mathrm{MAS}} \tag{3.30}$$

where n, m are integers and ω_{mod} stands for the modulation frequency of the multipulse sequence. Standard sequences such as WHH [44] have then been adapted with minor changes to perform well in the high MAS frequency regime. The results are interesting and demonstrate the validity of the synchronization conditions, though so far the best performance is always achieved using standard quasi-static approach and very short multipulse cycles.

An other new approach, that has not yet been used in the area of homonuclear dipolar decoupling, has recently been presented in the literature [59, 60]. Special symmetry-adapted rotor synchronized sequences are presented for heteronuclear decoupling, but the basic theorems are valid and can be used in order to generate homonuclear decoupling sequences, as well as other types of sequences.

Experimentally, CRAMPS has always been considered as an experimentally very demanding technique. Many experimental details about the setup of the CRAMPS techniques exist in the literature [30, 110, 111]. This is mainly due to the fact that most of the time we want to observe the proton signal under homonuclear decoupling. Thus we need to have observation periods, called *windows*, during which the free evolution Hamiltonian operates. In the next section, we will follow a different "indirect" way to probe the proton homonuclear decoupling efficiency.

3.3.1 Indirect detection

By using 2D NMR one can avoid the windows constraint, since observation can be performed directly on the carbon or nitrogen channel. Then, what matters is

simply the efficiency of the decoupling. In other words, we can observe the proton *indirectly*, in a two-dimensional experiment, where the proton frequency is in the f_1 dimension correlated with its bonded carbon or nitrogen, having a significantly better resolution, than observing a 1D proton spectrum. This can be appreciated from the 2D HMQC spectra of L-alanine shown in Fig. 3.2. The observed proton linewidths in the case of a 4 mm volume restricted sample are of the order of 170 Hz, while those of a full 7 mm sample of the order of 210 Hz. The performance of the decoupling sequence can be easily evaluated using this correlation experiment, and from the results of Fig. 3.2(a), we observe that the performance of the FSLG sequence (a sequence designed to work in the quasi-static regime) is comparable to or even better than that obtained by rotor synchronized schemes [51, 52]. Indirect observation of proton decoupling performance gives us the possibility to develop new homonuclear decoupling schemes that can be fully windowless.

An alternative to heteronuclear correlation spectroscopy, in order to probe decoupling performance, is homonuclear proton correlation [112–114]. In the literature delayed acquisition [113] or isotopic dilution [112] are responsible for the high proton resolution, whereas here, proton-proton decoupling is applied during t_1 (CRAMPS dimension) and detection is accomplished during t_2. During t_1 proton magnetization precesses in a plane perpendicular to the decoupling effective field, with the isotropic frequency. Under fast MAS the small proton anisotropies are averaged out. Appropriate prepulses have to be inserted in order to minimize axial peaks and perform suitable phase cycling. The pulse sequence for this experiment is shown in Fig. 3.3 and its phase cycling is shown in Table 3.1. An example of homonuclear correlation spectrum is shown in Fig. 3.4. This spectrum was obtained using the FSLG decoupling scheme during t_1. The MAS frequency was 12.5 kHz and the rf amplitude was set to 100 kHz. From this spectrum we can extract proton linewidths for the CH_3, CH and NH_3^+ protons. These linewidths, corrected with respect to the FSLG scaling factor $1/\sqrt{3}$ are listed latter in this chapter, on the Table 3.4.

Table 3.1: Phase cycling for the homonuclear correlation sequence shown in Fig. 3.3.

ϕ_1	ϕ_2	ϕ_{rec}
90°	0°	0°
270°	0°	180°
90°	90°	90°
270°	90°	270°
90°	180°	180°
270°	180°	0°
90°	270°	270°
270°	270°	90°

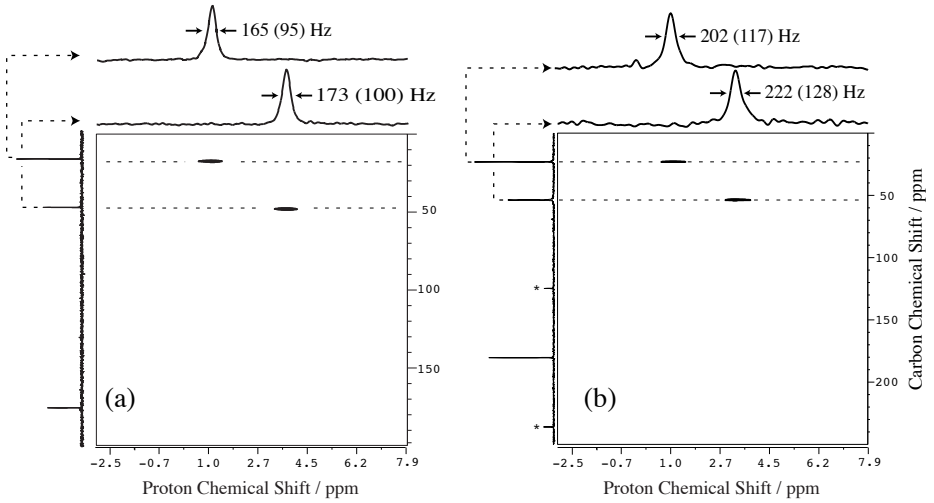

Figure 3.2: HMQC proton-carbon spectra of L-alanine obtained using the MAS-J-HMQC sequence of Fig. 2.9. The spectrum in (a) was recorded in a 4 mm spatially restricted rotor, using a MAS frequency of 12 kHz. 256 t_1 increments with 32 scans were collected and the total experimental time was 4 hours. The spectrum in (b) was recorded in a 7 mm probe using a full rotor and the MAS spinning frequency was set to 7 kHz (spinning sidebands are labeled). A total of 256 t_1 increments with 4 scans were collected. Using a repetition delay of 3 s the total experimental time was less than an hour. FSLG was used in both cases and decoupling powers were $\omega_1/2\pi = 100$ kHz for (a) and $\omega_1/2\pi = 80$ kHz for (b). Proton traces are shown. The outstanding proton resolution can be easily appreciated from the linewidths. In (b) the rf inhomogeneity of the probe is responsible for the larger proton linewidth. The linewidths were corrected with respect to the *theoretical* scaling factor of FSLG (uncorrected values are given in parenthesis) and the calibration of the proton dimension was made by setting arbitrarily the methyl proton frequency at 1 ppm.

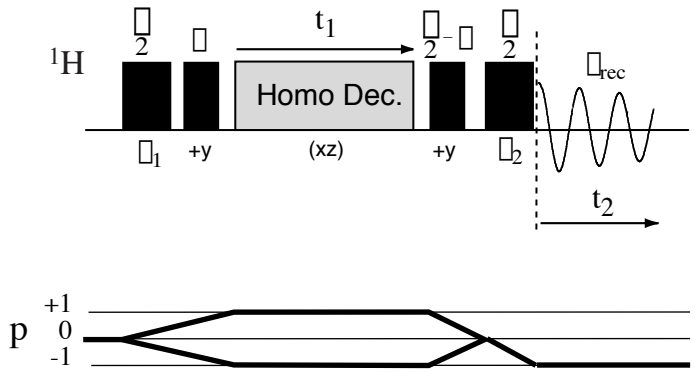

Figure 3.3: Homonuclear proton-proton correlation pulse scheme under MAS [114]. During t_1 homonuclear decoupling is on and proton coherences evolve under their isotropic chemical shift. The effective field of the homonuclear decoupling scheme lies on the xz plane in the laboratory frame. During t_2 the standard proton spectrum is acquired. Phase cycling was performed on the first and last $\pi/2$ pulses and combines the States method [115] for quadrature detection during t_1 with CYCLOPS. The phase cycling we used is shown in Table 3.1. The length and the phases of the two prepulses must be suitably adjusted depending on the decoupling sequence. For example, if the FSLG scheme is used, $\theta = \theta_m$. The pulse programs of this sequence using FSLG and DUMBO-1 are included in the appendix A.1 and A.2. They are slightly different than those in [114].

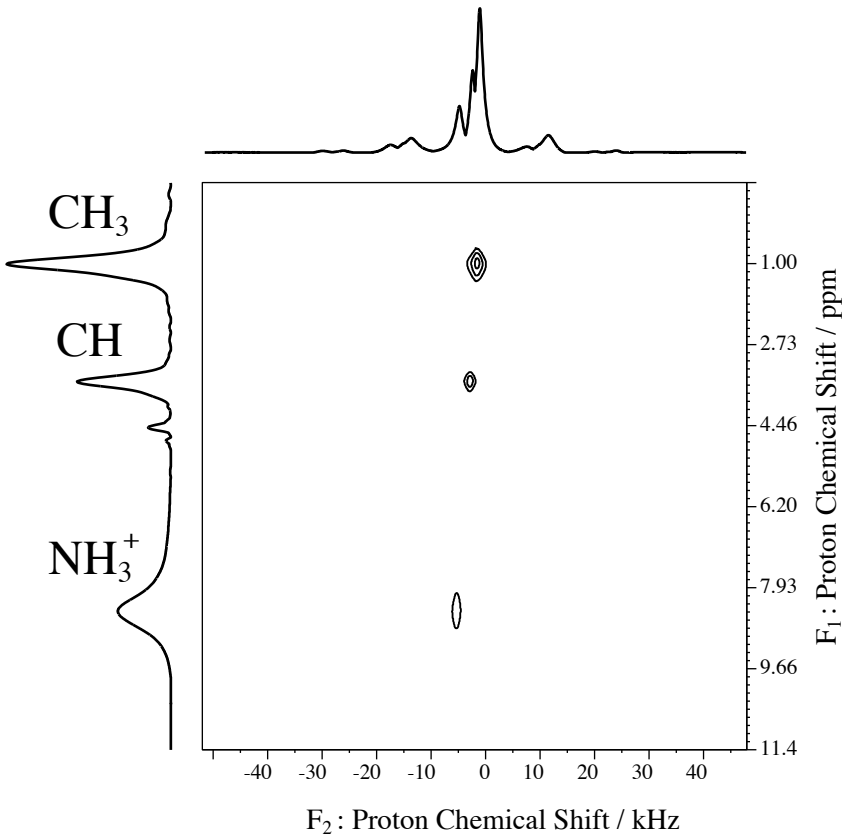

Figure 3.4: Homonuclear proton-proton correlation spectrum of L-alanine using FSLG. Projections on both dimensions are shown on the top and the right. Along F_1 the high resolution proton spectrum is obtained while along F_2 broad lines due to residual (under MAS) proton dipolar couplings are obtained. The MAS frequency was set to 12.5 kHz and the decoupling rf amplitude to $\omega_1/2\pi = 100$ kHz. A powder sample of L-alanine was used in a volume restricted 4 mm diameter rotor. The chemical shift scale in F_1 was calibrated by setting the methyl proton chemical shift to 1 ppm and correcting (dividing) for the scaling factor of FSLG.

3.4 The DUMBO approach

3.4.1 Introduction

To improve homonuclear decoupling in the following we propose a new family of homonuclear decoupling sequences based on continuous phase modulation. This parameterization allows numerical optimization of decoupling performance. We find new decoupling sequences which improve upon the performance of some of the most commonly used sequences, and we show experimental demonstrations of these properties on ordinary organic solids.

3.4.2 Continuous phase modulation

We note that existing multiple-pulse decoupling sequences, as their name suggests, consist of a series of discrete pulses, often having relative phase shifts of 90°, and often having on-resonance flip angles of 90° for each pulse. The currently most often used sequences are windowless or semi-windowless, and we shall concentrate on windowless sequences in the following. We remark that a windowless sequence, such as BLEW-12 [49], can be represented by a diagram of phase as a function of time, with the overall radio-frequency field amplitude being constant, as illustrated in Fig. 3.5(a). For the numerical approach we wish to adopt, a series of discrete pulse does not appear to be a very convenient starting point. However, we can replace the sequence by a continuous function of time, using the Hamiltonian of Eq. (3.17) where the phase $\phi(t)$ is a continuous periodic function of time. Several possibilities are present for the construction of conveniently parameterized $\phi(t)$ functions.

Simple Fourier decomposition

In a straightforward manner $\phi(t)$ can be developed as a Fourier series:

$$\phi(t) = \sum_{n=0}^{+\infty} a_n \cos(n\omega_c t) + b_n \sin(n\omega_c t) \tag{3.31}$$

where $\omega_c = 2\pi/t_c$ is the modulation frequency and t_c the time period of the irradiation. The complex Fourier coefficients $c_n = a_n + ib_n$ provide us with a set of parameters which can vary continuously and which allow us to explore a (potentially infinite) space of functions for decoupling. Note that the choice of a Fourier series as the basis set of functions is not restrictive, and we could envisage other more or less physically adapted basis sets. However, Fourier series forms a basis, i.e. can potentially generate all the space of real periodic functions [109], and do seem reasonably well adapted to the problem at hand.

Fig. 3.5(a) shows a Fourier series phase function which was obtained for the BLEW-12 sequence using 12 complex Fourier coefficients by expanding the phase function of the BLEW-12 sequence into a Fourier series, and keeping only the first 12

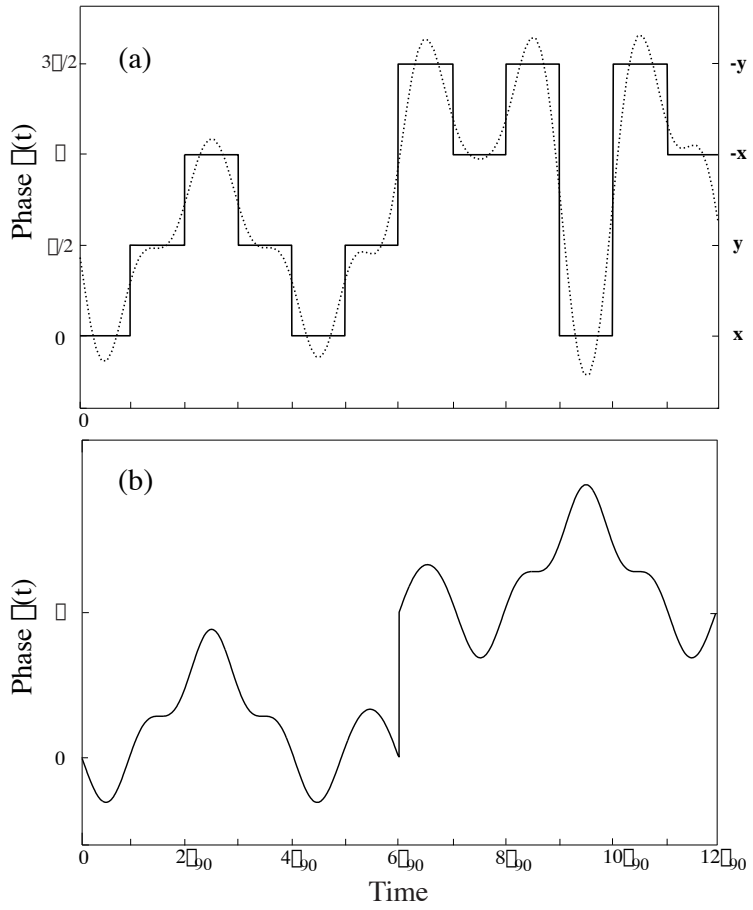

Figure 3.5: (a) Plot of phase as a function of time for the BLEW-12 multiple-pulse sequence (solid line) and its continuous version (dotted line). For BLEW-12 we consider 12 square pulses each of duration τ_{90}. In order to construct the smooth version, the original phase was expanded into a Fourier series and the first 12 complex coefficients were retained in order to roughly reproduce the twelve phase shifts. (b) Phase diagram for the final shaped version of BLEW-12. The first half of the diagram is obtained using only the first six Fourier coefficients. A π phase shift is then applied followed by the time reversed first half according to Eq. (3.34). From Ref. [97].

first coefficients. Note that if we retained an infinite number of coefficients, we could obtain a perfect representation, but that this is not really the objective. However, in keeping only several coefficients, an interesting problem arises. The time propagator for the rf field is no longer unity over one cycle, which is one of the most important characteristics of a good homonuclear decoupling sequence. The unitarity condition is:

$$U_{\mathrm{rf}}(t_c) = U_{\mathrm{rf}}(0) = \mathbf{1} \tag{3.32}$$

If the rf propagator is not unity over a cycle, the performance of the sequence depends strongly on the rf amplitude, since cyclicity is not respected. In that case an appropriate cycle time must be found for each value of the rf field. To remedy this problem we would have to impose some constraints on the Fourier coefficients c_n in Eq. (3.31). This is a non linear problem and there is no closed form solution, but one must find $\phi(t)$ functions that satisfy the following conditions:

$$\int_0^{t_c} \cos[\phi(t)]\,\mathrm{d}t = \int_0^{t_c} \sin[\phi(t)]\,\mathrm{d}t = 0 \tag{3.33}$$

These conditions are not satisfied in general for phases $\phi(t)$ yielded by the direct Fourier decomposition, so this type of sequences is not appropriate for further optimization.

π-shifted pulses (or the DUMBO family)

However, an obvious solution would be any function $\phi(t)$ with a π shift in the middle of its period, like:

$$\phi(t) = \begin{cases} f(t), & \text{if} \quad 0 \le t < t_c/2 \\ \pm\pi + f(t_c - t), & \text{if} \quad t_c/2 \le t < t_c \end{cases} \tag{3.34}$$

We can easily prove that any real periodic function $\phi(t)$ written in the form of Eq. (3.34), satisfies $\langle \cos\phi(t) \rangle_{t_c} = \langle \sin\phi(t) \rangle_{t_c} = 0$.

Proof:

$$\begin{aligned}
\langle \cos\phi(t)\rangle_{t_c} &= \int_0^{t_c} \cos\phi(t)\,\mathrm{d}t \\
&= \int_0^{t_c/2} \cos\phi(t)\,\mathrm{d}t + \int_{t_c/2}^{t_c} \cos\phi(t)\,\mathrm{d}t \\
&= \int_0^{t_c/2} \cos f(t)\,\mathrm{d}t + \int_{t_c/2}^{t_c} \cos[\pm\pi + f(t_c - t)]\,\mathrm{d}t \\
&= \int_0^{t_c/2} \cos f(t)\,\mathrm{d}t - \int_{t_c/2}^{t_c} \cos f(t_c - t)\,\mathrm{d}t \\
&= \int_0^{t_c/2} \cos f(t)\,\mathrm{d}t - \int_{t_c/2}^{0} \cos f(t')\,(-\mathrm{d}t') \\
&= \int_0^{t_c/2} \cos f(t)\,\mathrm{d}t - \int_0^{t_c/2} \cos f(t)\,\mathrm{d}t = 0
\end{aligned} \tag{3.35}$$

$$\begin{aligned}
\langle \sin\phi(t)\rangle_{t_c} &= \int_0^{t_c} \sin\phi(t)\,\mathrm{d}t \\
&= \int_0^{t_c/2} \sin f(t)\,\mathrm{d}t + \int_{t_c/2}^{t_c} \sin[\pm\pi + f(t_c - t)]\,\mathrm{d}t \\
&= \int_0^{t_c/2} \sin f(t)\,\mathrm{d}t - \int_{t_c/2}^{t_c} \sin f(t_c - t)\,\mathrm{d}t \\
&= \int_0^{t_c/2} \sin f(t)\,\mathrm{d}t - \int_0^{t_c/2} \sin f(t')\,(-\mathrm{d}t') \\
&= \int_0^{t_c/2} \sin f(t)\,\mathrm{d}t - \int_0^{t_c/2} \sin f(t)\,\mathrm{d}t = 0
\end{aligned} \tag{3.36}$$

for any function $f(t)$.

This form of functional dependence can be applied to the example of the BLEW-12 sequence giving rise to the sequence shown in Fig. 3.5(b), which we refer to as Smooth-BLEW-12. Note that in this case decomposition of the BLEW-12 phase onto a Fourier series was performed and the phase of the Smooth-BLEW-12 was generated using Eq. (3.34), where $f(t)$ was described by a Fourier series:

$$f(t) = \sum_{n=0}^{6} a_n \cos(n\omega_c t) + b_n \sin(n\omega_c t) \tag{3.37}$$

Only the first 6 coefficients of the decomposition of the original BLEW-12 phase were retained in Eq. (3.37). Under these conditions the rf propagator is unity over a

cycle i.e. $U_{\rm rf}(0,t_c) = \mathrm{T}\exp[\int \mathrm{d}t\,\mathcal{H}_{\rm rf}(t)] = 1$. Additionally, the sequence now also has time reversal symmetry, so that all odd order terms in the Magnus expansion vanish identically [3]. Although, we do not make use of AHT as a method of assessing the performance of the sequence, this property ensures that half of the terms in the Magnus expansion are zero. Thus, in the following we shall use functions of this type (see Eq. (3.34)), where the function $\phi(t)$ is expressed as a Fourier series (see Eq. (3.37)) and the Fourier coefficients are the variables for optimization.

Many other parameterizations are possible. For example the function $f(t)$ can be developed onto other basis sets of orthogonal functions, such as Legendre polynomials:

$$f(t) = \sum_{l=0}^{+\infty} c_n\, P_n(x) \tag{3.38}$$

where $x = 4t/t_c - 1$ and $-1 < x < +1$. Other decompositions onto orthogonal functions like the associated Legendre functions (spherical harmonics), Bessel functions, etc. are possible, but not performed here. The effect observed by choosing a different decomposition would affect only the rate of the convergence (assuming an sufficiently large decomposition order) and not the optimum in the optimization[1].

Specially constructed phases

We must note that $\phi(t)$ functions can be found that are continuous and satisfy the conditions of Eq. (3.33), but they are not conveniently parameterized. An example would be:

$$\phi(t) = \begin{cases} \arccos(1 - 8t/t_c) & \text{if} \quad 0 \le t \le t_c/4 \\ \arccos[-1 + 8/t_c(x - t_c/4)], & \text{if} \quad t_c/4 \le t \le t_c/2 \\ -\arccos[-1 + 8/t_c(x - t_c/4)], & \text{if} \quad t_c/2 \le t \le 3t_c/4 \\ -\arccos(1 - 8t/t_c) & \text{if} \quad 3t_c/4 \le t \le t_c \end{cases} \tag{3.39}$$

This phase function is shown in Fig. 3.6 and has apparent similarities with adiabatic schemes. Even though the parameterization of such phases is not obvious, their existence has not to be underestimated in the development of future versions of optimized sequences.

3.4.3 Optimization

To optimize the performance of a decoupling sequence we need to be able to distinguish between "good" and "bad" decoupling using computer models. This depends

[1] As a simple example consider the linear phase ramp in the Lee-Goldburg homonuclear decoupling scheme. Using Legendre polynomials, one decomposition coefficient is sufficient to reproduce perfectly the time dependence. However, if we use The Fourier functions basis set, we can reproduce the ramp using a large number of coefficients. This is the reason why using a single basis set and a limited (finite) number of decomposition coefficients limits the scanned space of phase functions

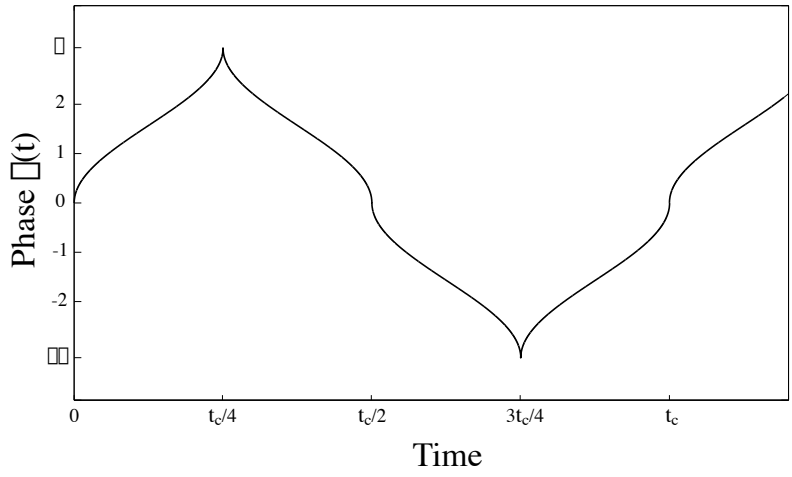

Figure 3.6: Plot of phase (in radian units) as a function of time. This is a example of fully continuous phase modulated sequence which satisfies the unitarity condition of Eq. (3.32).

crucially on the choice of the model spin system (which must respond in the same way as a real sample to variations in experimental parameters) and on the choice of the target function used to assess the result. For the problem of homonuclear proton decoupling we will use a simple two-spin system model, including the homonuclear dipolar coupling and chemical shifts. The model system Hamiltonian is:

$$\mathcal{H}_{\rm sys} = \Omega_1 I_{1z} + \Omega_2 I_{2z} + d_{12}(3I_{1z}I_{2z} - \vec{I_1}\cdot\vec{I_2}) \tag{3.40}$$

The system is static (we discuss the validity of this quasi-static approximation below) and perturbed by the presence of the rf decoupling field in Eq. (3.17). Thus the total Hamiltonian is :

$$\mathcal{H}_{\rm tot}(t) = \mathcal{H}_{\rm sys} + \mathcal{H}_{\rm rf}(t) \tag{3.41}$$

Good decoupling is performed when the effective Hamiltonian has the following form :

$$\mathcal{H}_{\rm eff}^{\rm ideal} = \lambda(\Omega_1 I_{1Z} + \Omega_2 I_{2Z}) \tag{3.42}$$

i.e. the dipolar contribution is entirely removed and the chemical shift terms (in a tilted frame of reference XYZ) are modified by a scaling factor λ which should be as large as possible, in order to enhance the spectral resolution. The effective Hamiltonian $\mathcal{H}_{\rm eff}$ has to be independent of any experimental variations as discussed bellow. Our objective is to find sequences that :

1. work for any proton spin system and

2. are insensitive to common experimental imperfections (rf field inhomogeneity, offset with respect to the carrier frequency etc.)

The first condition translates most simply into the optimization of the performance of the sequence over a broad range of dipolar couplings (assuming that the chemical shift spread in protons is small), and the second condition implies optimization with respect to a broad range of rf field amplitudes and offsets. Thus, for example, a sequence that is robust with respect to rf inhomogeneity should be optimized over a two-dimensional parameter surface of rf fields and dipolar couplings.

To assess decoupling performance we calculate the exact effective Hamiltonian[2] by stepwise multiplication the propagators for each instant in time during the sequence:

$$U(0,t_c) = \mathrm{T} \prod_{n=0}^{(t_c/\delta t)-1} U[n\,\delta t,(n+1)\,\delta t] = \exp(-i\mathcal{H}_{\mathrm{eff}}\,t_c) \tag{3.43}$$

where :

$$U[n\,\delta t,(n+1)\,\delta t] = \exp(-i\mathcal{H}_{\mathrm{eff}}\,\delta t) \tag{3.44}$$

The effective Hamiltonian is then decomposed into the components of an orthogonal basis set of Cartesian product operators $\{B_n\}$ [61]:

$$\mathcal{H}_{\mathrm{eff}} = \sum_{n=0}^{4^N} k_n B_n \tag{3.45}$$

This decomposition informs us about the relative importance of linear (chemical shift) and multi-linear (coupling) terms in the effective Hamiltonian. An example of the previous decomposition of Eq. (3.45) is presented in Fig. 3.7. We can thus optimize the performance of the sequence by maximizing the resolution function defined as:

$$q \equiv \frac{\sqrt{\sum_{\mathrm{lin}} k_n^2}}{\sqrt{\sum_{\mathrm{multilin}} k_n^2}} \tag{3.46}$$

where the sum in the nominator is taken over all single-spin operators and the sum in the denominator over all multiple-spin operators. This procedure will therefore maximize the scaling factor λ, which depends on the linear terms, and minimize the dipolar couplings, which are reflected by the multi-linear terms. For numerical purposes this is equivalent to minimizing $1/q$. In the case where a chemical shift, is one of the multidimensional parameters, i.e. robustness with respect to offset and dipolar couplings, it is more convenient to define the quality resolution function as:

$$q \equiv \frac{\sqrt{\sum_{\mathrm{lin}} k_n^2}}{\sqrt{\Omega_1^2+\Omega_2^2}\sqrt{\sum_{\mathrm{multilin}} k_n^2}} \tag{3.47}$$

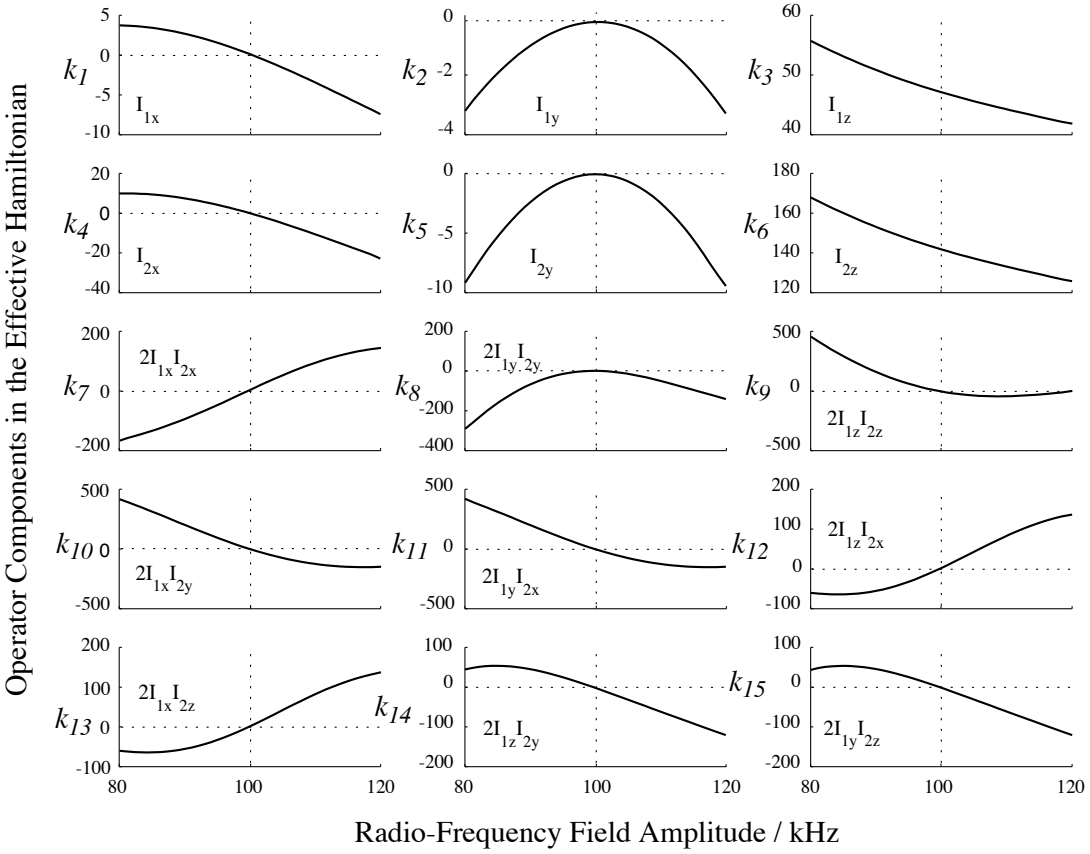

Figure 3.7: Decomposition into the Cartesian product operator basis set $\{B_n\}$ (see Eq. (3.46)). We present the values k_n of the different operator components of the effective Hamiltonian as functions of the radio frequency field amplitude for the BLEW-12 multipulse sequence. The time period for the sequence is set by the nominal value of the rf amplitude, taken for this example equal to 100 kHz. Deviations from the nominal value show the performance of the sequence with respect to the inhomogeneity of the rf field. We can observe that around the nominal values of the rf amplitude bilinear terms are almost zero, so decoupling is almost perfect. The axis of the spin operators are those in the effective field of the sequence, resulting around 100 kHz an effective field along the Z axis (linear X and Y components are close to zero).

This definition prevents artificial resolution enhancement due to large offset terms.

In the optimization procedure the length of the sequence was *arbitrarily* set to be equal to the length of a standard BLEW-12 multiple pulse sequence (i.e. 12 $\pi/2$ pulses for $\omega_1/2\pi = 100$ kHz, yielding $t_c = 30\mu$s). All sequences were simulated on a two ^{1}H spin system with both spins having a chemical shift difference of +1 kHz with respect to the carrier frequency. The function of the phase was described by equations 3.34, 3.37. In the first step of the optimization, random combinations of coefficients a_n and b_n ("seeds") were generated using the random number generator of numerical recipes [116]. The first time we performed an optimization, we constrained the interval of the random number generator to be $[0, 1]$. 2×10^6 random combinations were generated and stored. The second step of the optimization was to test each combination with respect to is numerically calculated performance. For each combination of six coefficients we calculated $1/q$ for a single value of the rf field (100 kHz) and the dipolar coupling (5 kHz). Then the sets of coefficients were ordered with respect their performance and we selected the 10^3 sequences with the lowest value of $1/q$. We hope this way to scan in a homogeneous way the parameter space, and begin the minimization procedure from points close to minima. In the third phase of the optimization, for each of these best "seeds", we further minimized the sum of $1/q$ over a range of 0–30 kHz homonuclear dipolar coupling (22 steps), and a $\pm$20 kHz variation from the nominal value of ω_1 (21 steps). This ensures that the resulting sequences should be robust with respect to variations in the rf field, and that they should not depend on spin system parameters.

The optimization was performed using a least squares steepest descent gradient method with respect to $1/q$ summed over the 462 points on the grid of rf fields and dipolar couplings (the ideal quality factor being zero). In these optimizations we cannot easily use a grid search to find systematically the global minimum because the dimension of the parameter space is too high. In any case the "global minimum" is somewhat arbitrary as it depends on how the system is parameterized. Therefore, we look for robust local minima, corresponding to good decoupling performance.

Some comments have to be made concerning the numerical simulations. Because of the periodicity in time of the problem, the effective Hamiltonian of the system is defined modulo $2\pi\mathbf{1}$, because:

$$\exp(-i\mathcal{H}_{\text{eff}}t_c) = \exp[-i(\mathcal{H}_{\text{eff}} + 2\pi K\mathbf{1})t_c] \tag{3.48}$$

Numerically we calculate the effective Hamiltonian by diagonalizing the propagator over a period of the modulation and calculating the argument of its eigenvalues u_r [117]:

$$\omega_r = -\frac{1}{i\,t_c}\log u_r = \omega_{\text{mod}}(-\text{Arg}(u_r)/2\pi + K) \tag{3.49}$$

[2]Note here that we could have calculated also the first orders in the AHT Magnus expansion, as in [55] but this is not necessary for the following optimizations.

with $1 \leq r \leq N$ and $K = 0, \pm 1, \pm 2, \ldots$. This procedure, has some intrinsic technical problems:

- The ordering of the eigenvalues, and most importantly of the eigenvectors, is not always respected. This comes from the numerical diagonalization routines and cannot be solved easily inside the diagonalization routine.
- The eigenvalues of the effective Hamiltonian are defined modulo $2\pi\omega_{\mathrm{mod}}$, so the diagonalization routine can add or subtract an integral number of modulation frequencies.

Both problems can be "corrected" by comparing for each point[3] the eigenvectors of the propagator with all the eigenvectors found in the previous points [41]. The comparison is made by taking the scalar product between the vectors. We find this way the parent vector of each of the new eigenvectors, provided that the difference from one point to another is small. Thus, we can identify the history of the new eigenvector, and in consequence the history of its eigenvalue. Thus, reordering of eigenvalues and eigenstates becomes possible. Within the previous assumption of small changes between neighbor points, all eigenvalues have to be continuous, so any time we observe a discontinuity of more than ω_{mod}, we add or subtract the appropriate integral multiple of ω_{mod}. The initial set of eigenvalues and eigenvectors are taken in the case of zero rf amplitude and zero dipolar couplings. In this case we can obtain analytical results and which we use to "calibrate" the numerical diagonalization.

Another problem can arise, though less frequently, and is due to an inconvenience of the description of the problem using the effective Hamiltonian tool [118]. In the presence of very weak rf fields and strong dipolar couplings, some resonance effects are present, giving rise to artificially increased chemical shift terms. Looking at the eigenvalues we have observed that these effects are due to non-avoided level crossings, so they correspond to true resonances [119], and have to be treated as such. The spectra show splittings that within the effective Hamiltonian description are interpreted as linear spin terms. Such effects being rarely observed and no special treatment was made to account for them.

3.4.4 Results

Using the previously described optimization procedure we have optimized 1000 sets of coefficients, giving rise to 1000 phase functions. We have observed that for all of them the scaling factor is lower than $1/\sqrt{3}$, as predicted by our theorem (see section 3.2.1). We have then sorted these sequences with respect to their scaling factor and here we present only the best sequence.

The resulting phase function is shown in Fig. 3.8 and the Fourier coefficients are given in Table 3.2. This sequence is the best result we have found so far, and we refer

[3]Point here means set of parameters like the rf amplitude and/or dipolar coupling and/or offset.

Table 3.2: Complex Fourier coefficients $c_n = a_n + ib_n$ for $f(t)$ in the DUMBO-1 sequence. The number of steps for half of the sequence is $M = 32$ so for the m^{th} step number, the phase in 2π units is: $f(m) = \sum_{n=0}^{6} a_n \cos(2\pi\frac{nm}{M}) + b_n \sin(2\pi\frac{nm}{M})$. The zeroth order coefficient c_0 defines only the mean phase of the pulse and is set *after* optimization to yield an effective field in the $+xz$ plane.

n	a_n	b_n
0	+0.1056	0.0000
1	+0.0325	+0.1310
2	+0.0189	+0.1947
3	+0.0238	+0.0194
4	+0.0107	+0.1124
5	+0.0038	−0.0456
6	−0.0013	+0.0869

to it as DUMBO-1 (Decoupling Using Mind-Boggling Optimization). The simulated performance of the sequence is shown in Fig. 3.9 where we plot the value of $1/q$ as a function of rf field amplitude and dipolar coupling, and we compare it with the performance of the normal BLEW-12 sequence. The DUMBO-1 sequence appears more robust than BLEW-12 as can be judged by the flatness of the surface around the nominal value. The scaling factor for linear interactions is calculated to be $\lambda = 0.524$ and the effective field lies at the following polar angles $(\theta, \phi) = (58°, 0°)$, where θ is the tilt from the z-axis and ϕ is the rotation from the $+x$ axis towards the $+y$ axis.

3.4.5 Experiments

The model that we have considered in the previous sections does not include explicitly MAS, and so the sequences are expected to work well in the quasi-static regime, similarly to sequences such as FSLG and BLEW-12. We find for most organic solids, good performance can be obtained from "quasi static" sequences up to spinning speeds of around 15 kHz. Thus, we have used powder samples, spinning at around 9 kHz to asses the performance of these sequences.

Preliminary experiments were performed on a sample of sodium 2-^{13}C-acetate. The sample was obtained from Cambridge Isotopes and used after drying overnight under vacuum space without further purification. All the experiments were performed on a 500 MHz DSX Bruker NMR spectrometer, using a double resonance 2.5 mm Bruker probe and a full rotor. The decoupling field was set to 100 kHz. In order to probe the performance of the proton-proton homonuclear decoupling we observe the carbon-13 CP/MAS signal with the decoupling sequence applied to protons during acquisition as discussed in section 2.3. Under perfect homonuclear ^{1}H decoupling the heteronuclear dipolar coupling becomes inhomogeneous and is

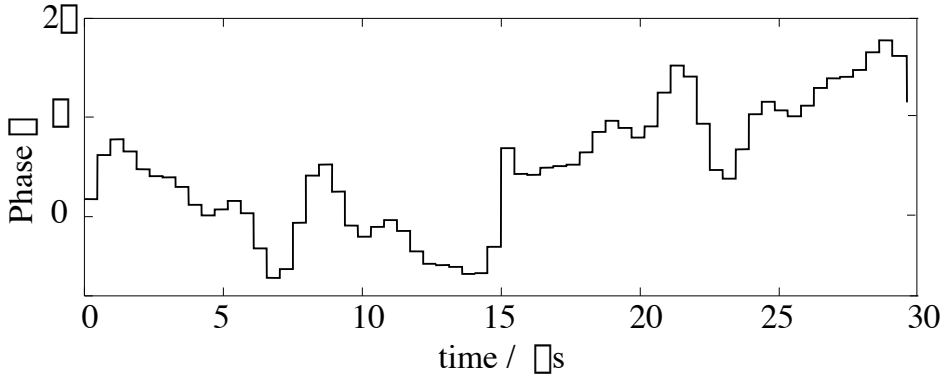

Figure 3.8: Phase diagram for the DUMBO-1 sequence. Eq. (3.31) was digitized using 64 steps per cycle, both in experiments and numerical simulations. This time resolution was chosen since it corresponds to a commonly attainable experimental setup. Note however, that at this time resolution, decoupling performance will deteriorate if the number of steps per cycle is varied in either sense. This is because the sequence has been optimized for this given number of steps and this is not large enough for the performance of the sequence to be independent of the number of steps. From Ref. [97].

Table 3.3: Theoretical and experimental values of the scaling factor for three sequences obtained from the J_{CH} splittings in the carbon-13 spectrum of 2-^{13}C-sodium acetate. The unscaled value for J_{CH} measured in the liquid state NMR spectrum was 127 Hz.

Sequence	λ_{theor}	λ_{exp}
BLEW-12	0.475	0.39
FSLG	0.577	0.52
DUMBO-1	0.524	0.41

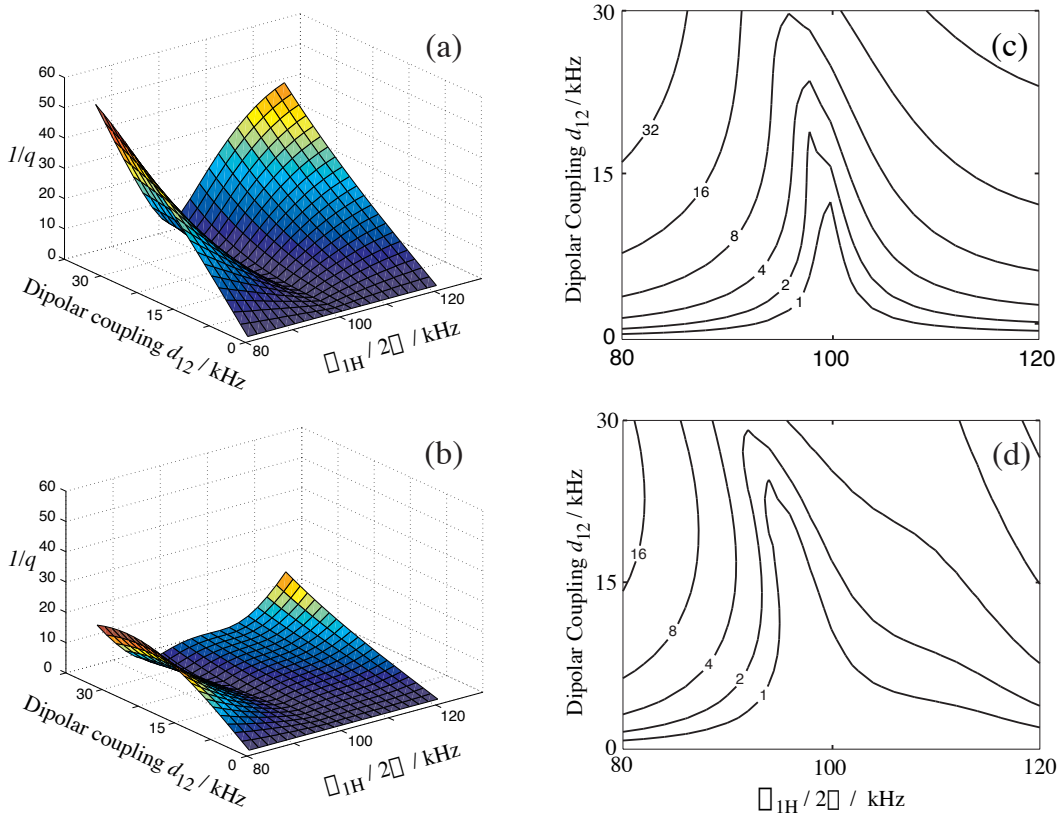

Figure 3.9: Numerical comparison between two windowless sequences with respect to their robustness for a range of homonuclear dipolar couplings and their performance towards probe rf inhomogeneity. d_{12} is varying from 0 to 30 kHz, and a mismatch of ± 20 kHz from the nominal value of 100 kHz for $\omega_1/2\pi$ is examined in these surface plots. The variable $1/q$ is plotted with respect to these two parameters and the robustness of each sequence can be judged from the flatness of the area around the minimum of the surface. BLEW-12 is shown in (a) and DUMBO-1 in (b). In (c) and (d) we present respectively the same contour levels for both sequences. From Ref. [97].

then averaged to zero by MAS. Thus, only the heteronuclear J coupling remains, yielding a fine structure of the peaks which for a CH_3 should be a 1:3:3:1 quartet with residual J splittings that are reduced by the scaling factor of the sequence. In practice, homonuclear decoupling is not perfect, and the lines in the quartet are broadened accordingly. Thus, observation of the J fine structure allows to probe the experimental scaling factor (since we know the unaveraged value) as well as the decoupling performance which is directly reflected by the resolution of the fine structure. We find that the resolution of these spectra are very sensitive to decoupling performance, and provide a very convenient probe for windowless sequences.

We have applied the new sequence to various model samples (camphor, adamantane) and on ordinary organic solids (L-alanine, sodium acetate). We first show representative data for the performance of three decoupling sequences on 2-^{13}C-sodium acetate. In Fig. 3.10 we compare the experimental performance of DUMBO-1, BLEW-12 and FSLG with respect to changes in the rf field amplitude. This reflects the dependence upon the experimental rf probe inhomogeneity. All sequences are set in order to perform optimum decoupling around $\omega_1/2\pi \simeq 100$ kHz. The theoretical and experimental scaling factors are given in Table 3.3. In Fig. 3.10 we compare the experimental performance of DUMBO-1, BLEW-12 and FSLG with respect to changes in the rf field amplitude. This reflects the dependence upon the experimental rf probe inhomogeneity. From Fig. 3.11, which shows the depth of the doublet splitting as a parameter for resolution, it is clear that the DUMBO-1 sequence is much more broadband with respect to differences in the value of the decoupling field, since we see that the J splitting is resolved over a much broader range of frequencies. (Note that we only observe the inner doublet of the methyl quartet for all the sequences as explained in section 2.3). FSLG, which is one of the best ordinarily used decoupling sequences, is actually quite sensitive to misset [41, 42].

The performance of the DUMBO-1 sequence is compared with BLEW-12 with respect to *both* off-resonance performance and rf-inhomogeneity robustness. Experiments where both parameters were changed in a grid were performed always on a powder sample of 2-^{13}C-sodium acetate, and the experimental results (depth of the doublet) are shown in Fig. 3.12. We also present on the same figure the equivalent simulated contours of $1/q$ for the simple 2 spin model. The agreement with experiments is qualitatively good. DUMBO-1 seems robust with respect to both parameters.

An obvious application of the DUMBO-1 sequence would be in experimental cases where the probe inhomogeneity is large. This is the usually the case in probes where the ratio of the diameter over the length of the coil is large. Such probes should allow the acquisition of spectra of large molecules under high resolution conditions having a good signal to noise ratio. However, their main drawbacks are the low maximum spinning MAS frequency together with the larger rf field inhomogeneity. In Fig. 3.13 we show the performance of the FSLG and DUMBO-1 decoupling sequences on a powder sample of L-alanine, using a rotor of 7 mm diameter. We can clearly see that the performance of DUMBO-1 is much better than

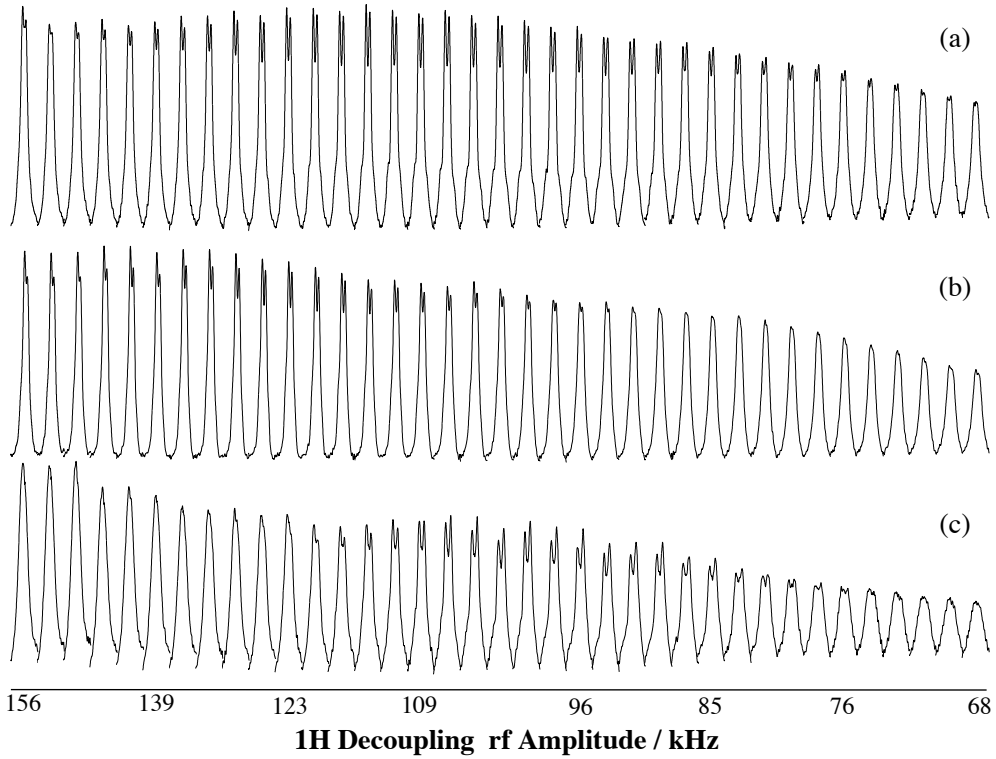

Figure 3.10: Experimental comparison of decoupling performance as a function of rf field amplitude for (a) DUMBO-1, (b) BLEW-12 and (c) FSLG. The experiments were performed on a sample of polycrystalline sodium 2-^{13}C-acetate and the diagram shows the region containing the CH_3 resonance which is the only appreciable signal in the spectrum. The BLEW-12 and the DUMBO-1 sequences were programmed as shape files containing 266 and 256 cycles respectively, in order to avoid software imperfections. Each cycle contained 60 and 64 steps respectively each of 500 ns duration. Optimum performance for all sequences is achieved around $\omega_1/2\pi = 110$ kHz. These experiments were performed by keeping the period of the sequence constant and varying the decoupling power level. For (a) and (b) the spinning frequency was set to $\omega_r/2\pi = 9$ kHz. The performance of FSLG being worse at 9 kHz (non resolved multiplet), data for (c) were obtained at $\omega_r/2\pi = 12$ kHz. From Ref. [97].

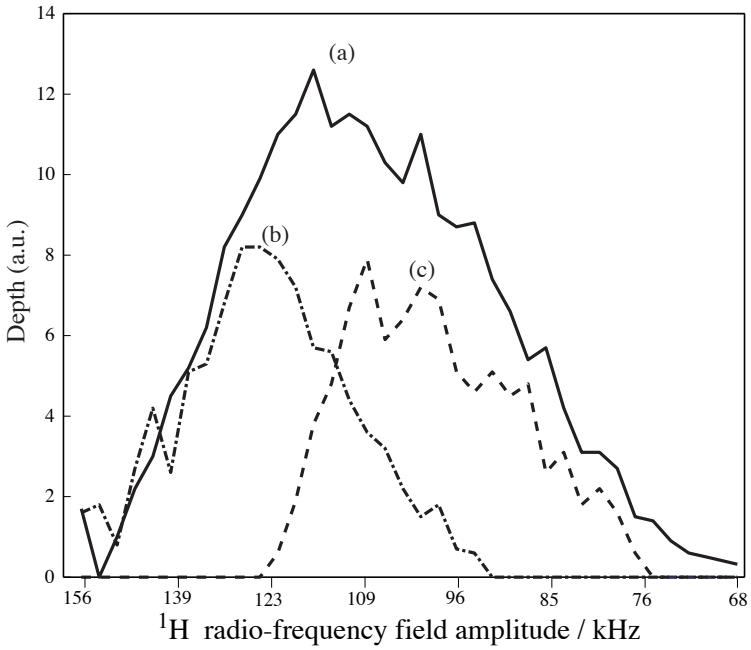

Figure 3.11: Plot of the experimental (see Fig. 3.10) depth of the methyl doublet as a function of rf field amplitude for (a) DUMBO-1, (b) BLEW-12 and (c) FSLG. The depth of the doublet can conveniently used to assess the performance of the decoupling of the sequence, since it depends crucially on the scaling factor *and* the linewidth. Maxima on these plot, correspond to the largest splitting which is equivalent to optimum decoupling. The DUMBO-1 sequence shows a more broadband behaviour with respect to rf inhomogeneity.

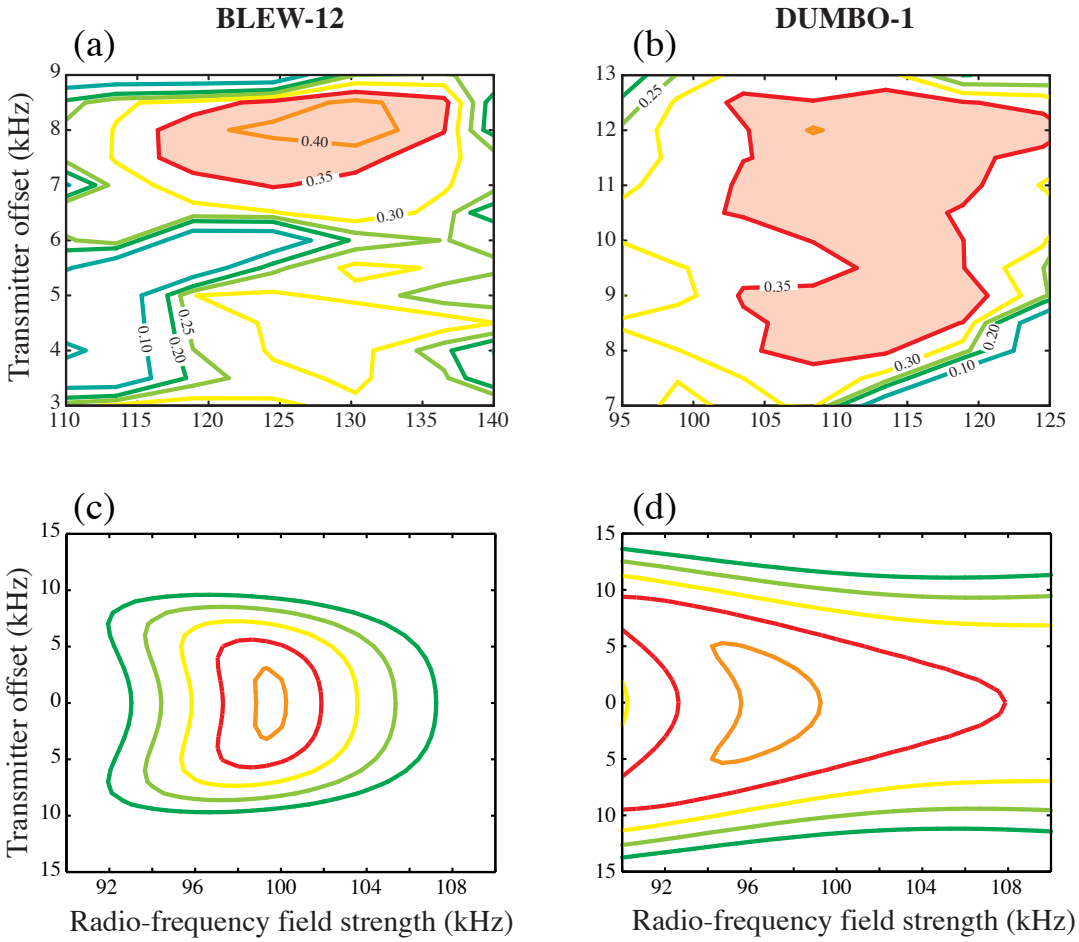

Figure 3.12: Plot of the depth of the methyl doublet as a function of rf field amplitude and offset for (a) BLEW-12 and (b) DUMBO-1. In both cases the spinning frequency was set to 9 kHz. Note that the optimum for the BLEW-12 sequence is centered at $\omega_1 = 130$ kHz, while for DUMBO-1 is centered at $\omega_1 = 110$ kHz. This difference explains the difference in optimum performance (contour levels), and accentuates the difference in robustness between the two sequences. Plots (c) and (d) correspond to the numerical simulation $1/q$ quality factor defined in Eq. (3.47) for BLEW-12 and DUMBO-1 respectively. The spin model we used, is far to simple and different from the experimental reality. Only two proton spins were included and magic angle spinning was not taken into account. This is why only a qualitative agreement between the experiments and simulations can be seen.

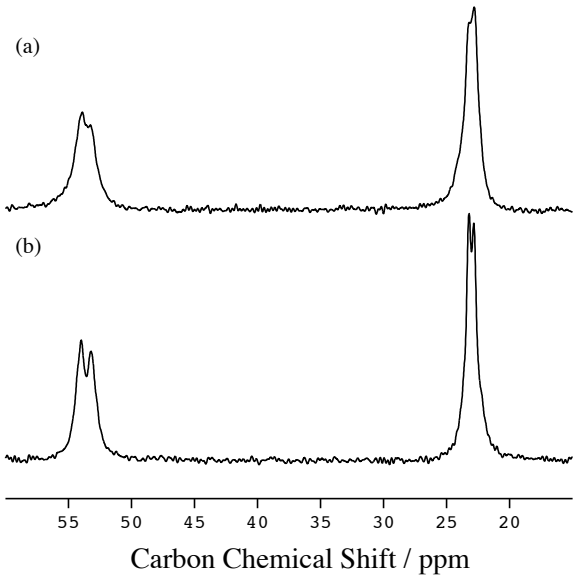

Figure 3.13: Comparison between the performance of the FSLG (a) and the DUMBO-1 (b) homonuclear decoupling sequences. A powder sample of L-alanine in full rotor of 7mm diameter was used. Signals from carbons of the methine and the methyl groups are shown. Each of the sequences was carefully optimized and the MAS frequency was 7 kHz.

the performance of FSLG. This demonstrates that DUMBO-1 is robust with respect to rf inhomogeneities and can replace standard homonuclear decoupling schemes in solid state NMR experiments.

We have performed the HMQC experiment on the previous sample of L-alanine using the 7 mm rotor and the DUMBO-1 decoupling sequence. The pulse program of this sequence is included the appendix A.5. The 2D spectrum together with F_1 proton traces are shown in Fig. 3.14. This experiment has to be compared with the one of Fig. 3.2(b), where for the decoupling FSLG was used also on a 7 mm sample. The resolution enhancement using DUMBO-1 can be clearly seen from the linewidths. Some signal loss is observed using DUMBO-1, towards axial peaks at zero F_1 frequency (observable on the traces). This is due to imperfect adjustment of the prepulses in the MAS-J-HMQC sequence and will be suppressed in the near future.

In Fig. 3.15 we can see 2D maps for proton homonuclear correlation using DUMBO-1 for two different MAS frequencies. Projections along F_1 are shown and experimental linewidths are given in Table 3.4. Proton resolution using DUMBO-1 is comparable and globally better than that obtained using FSLG.

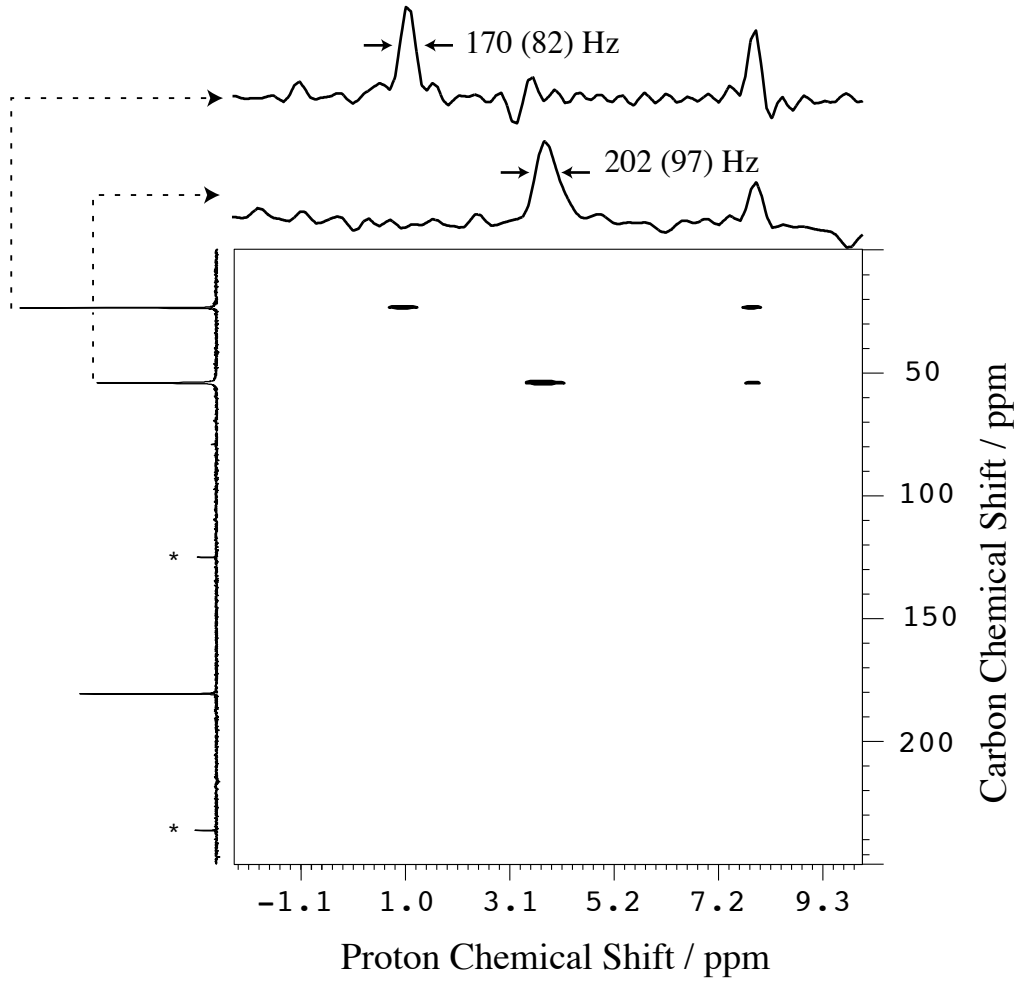

Figure 3.14: HMQC proton-carbon spectrum of L-alanine obtained using the MAS-J-HMQC sequence of Fig. 2.9 and DUMBO-1 for homonuclear decoupling. The spectrum was recorder in a 7 mm probe using a full rotor and the MAS spinning frequency was set to 7 kHz (spinning sidebands are labeled). A total of 128 t_1 increments with 8 scans were collected and using a repetition delay of 3 s the total experimental time was less than an hour. Comparison with the equivalent experiment using FSLG decoupling (see Fig. 3.2) shows an enhancement of proton resolution. This can be justified by the robustness of DUMBO-1 with respect to the rf inhomogeneity of the probe. The linewidths were corrected with respect to the *experimental* scaling factor of DUMBO-1 $\lambda = 0.48$ (uncorrected values are given in parenthesis) and the calibration of the proton dimension was made by setting arbitrarily the methyl proton frequency at 1 ppm.

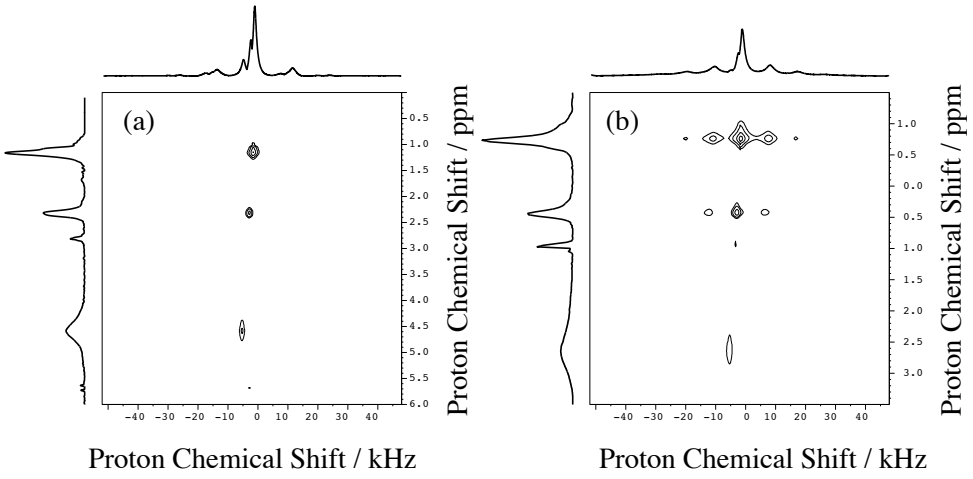

Figure 3.15: Homonuclear correlation proton spectra of a powder sample of L-alanine using the DUMBO-1 decoupling sequence. (a) The spinning frequency was set to 12.5 kHz and 256 t_1 increments were acquired each having 8 scans. (b) The spinning frequency was set to 6 kHz.

Table 3.4: Experimental linewidths in Hz (widths at half height) for the proton resonances of L-alanine obtained from the correlation spectra of figures 3.4 and 3.15. The values are corrected by the scaling factor of the sequences: for FSLG, $\lambda = 0.577$ (theoretical taken as the reference) and for DUMBO-1, $\lambda = 0.48$ (*experimental* with respect to the FSLG reference). The DUMBO-1 scaling factor was obtained by measuring the scaled chemical shift difference between the CH and CH_3 proton resonances. In parenthesis are the un-corrected values of the linewidths obtained from the 2D spectra. The performance of the DUMBO sequence was explored at two different spinning frequencies, lines (a) and (b). All other experimental conditions were identical for all three experiments.

Sequence	CH_3	CH	NH_3^+	$\omega_r/2\pi(kHz)$
FSLG	204 (118)	165 (95)	444 (256)	12.5
DUMBO-1 (a)	156 (75)	139 (67)	427 (205)	12.5
DUMBO-1 (b)	133 (64)	139 (67)	722 (347)	6.0

3.5 Discussion

We have introduced a new class of homonuclear dipolar decoupling sequences for use in static and moderate magic angle spinning solid-state NMR experiments based on numerical optimization. Numerical optimization is a well known method of improving the performance of pulse sequences in liquid state NMR and Magnetic Resonance Imaging (MRI). The success of numerical optimization depends crucially on the model used to simulate the physical system as well as the parameterization space and the target function. Here we are trying to use numerical optimization methods on a multi-spin system problem. This is significantly different from what has been done in the liquid state where one- or two-spin systems were considered as the simulation models. Including many spins and taking into account the sample rotation would improve the model spin system. However, trying to describe *ab initio* this multi-spin problem needs a detailed study of the spin diffusion problem. This will be done in the next chapter.

3.6 Other Applications of the DUMBO Approach

3.6.1 B_1-insensitive and B_1-selective pulses

We have already demonstrated the importance of the rf homogeneity of the probe in multiple pulse decoupling experiments. The idea to construct pulse sequences that are robust with respect to rf inhomogeneities is as old as homonuclear decoupling [46]. However, the analogue of this idea for simple pulses such as $\pi/2$ or a π pulse first appeared with the advent of composite pulses [120]. The domain of composite pulses is quite crowded, but we thought there might be enough space to check the performance of the DUMBO approach on such problems. Our goal is to find phase modulated pulses that are:

1. robust with respect to rf inhomogeneities and/or carrier frequency offset or

2. selective with respect to the amplitude ω_1 of the rf field.

The first set could potentially replace parts of longer multiple pulse schemes and render them B_1 insensitive, while the second set, could be used as filters for select highly homogeneous parts of the sample. Note that our effort is mainly focused on the application of the DUMBO approach rather that the theoretical development of new composite pulses. Thus for more detailed discussions on composite pulses we suggest some excellent reviews [121, 122]. The second goal lies in the domain of localized NMR and constitutes one of the subjects treated in detail in the thesis of P. Charmont. Here we are going to underline only the usage of the DUMBO approach to this problem and some preliminary results.

Standard Composite Pulses

There are many different techniques used in the development of composite pulses [121,122]. As a short summary we mention the use of geometric (intuitive) representations [120,123–125], analytical theory for rotations [126], coherent averaging theory [127–132], numerical optimizations [133–138], iterative expansion [125,130,139–144] and Floquet theory [145]. We have calculated the performance of many of these sequences with respect to rf inhomogeneity and offset, and contour plots are shown in appendix B. We can easily distinguish between the sequences developed in order to be robust with respect only to one of the two experimental parameters. However, we can see that only a few sequences are robust with respect to both parameters. On the other hand, for these dual compensation sequences the pulse becomes quite "long" compared with the nominal time length of a standard π pulse. This means that we have to take into account possible evolution due to the scalar J coupling during the pulse. Most of the interest in composite pulses lies in their short length that places them far from adiabatic schemes that perform differently [146–148]. Our goal is to apply the DUMBO approach in order to find short and robust phase modulated sequences.

Numerical optimizations have been used in the past [135–138, 149]. The minimization algorithms used in these numerical approaches were based on the simplex, the quasi Newton, simulated annealing and stochastic methods. The final pulse sequences being a discrete set of N *flip angles* and N *phases*. The efficiency of the sequences was optimized by minimizing the calculated and the wanted performance for different sets of $2N$ parameters. The main advantage of these methods is the tolerance with respect to both rf inhomogeneity and offset mismatch, together with the short length of the pulse. The constrains on the phase can also give a low phase dispersion for the response of the pulse rendering it suitable for spin refocusing [136]. However, because the optimization affects also the flip angle, this makes them subject of experimental imperfections. One slightly different approach [149] was to look for a $2N$ set of flip angles and *frequencies* rather than phases. Of course phase and frequency are related, but the results of this optimization with respect to offset dependence are interesting.

In 1994 Wimperis [132] introduced, using semi-analytical arguments, another class of composite pulses that are broadband, narrow-band or passband with respect to the ω_1 rf field and can be easily adjusted to perform on any overall flip angle. This class of composite pulses does not introduce any phase shifts but is relatively sensitive with respect to offset mismatch, so its performance is satisfactory mostly for ^{1}H NMR spectroscopy.

Application of the DUMBO approach for B_1 insensitive pulses

Broadband population inversion by adiabatically phase modulated pulses, has already be reported by Tycko et al [150]. In this reference an analytical solution is given and discretized into steps for the flip angles and the phases. Here we ex-

tend this idea using numerical optimization on a continuous phase modulated pulse as described in the previous sections. The initial state of the system in thermal equilibrium is:

$$\sigma(0) = I_z \tag{3.50}$$

and the final state after the pulse is ideally fully inverted:

$$\sigma(T)_{\text{ideal}} = -I_z \tag{3.51}$$

The Hamiltonian of the one-spin system under phase modulated rf is:

$$\mathcal{H}(t) = \Omega_1 I_z + \omega_1[\cos\phi(t) I_x + \sin\phi(t) I_y] \tag{3.52}$$

As before, the phase of the pulse is written as a Fourier series, truncated at a maximum order $n_{\max}$, like in Eq. (3.37). and discretized into a finite number of steps. During each step the Hamiltonian is supposed time independent and the step propagator can be numerically calculated [151] by:

$$U_n = \exp[-i\mathcal{H}(n\delta t)\delta t] \tag{3.53}$$

The overall propagator in obtained by time ordered multiplication of the individual step propagators, and the resulting action on the initial density operator is obtained by:

$$\langle I_z \rangle = \text{Tr}[I_z\, U(T)\, \sigma(0)\, U^\dagger(T)] \tag{3.54}$$

This calculation is performed for range of rf amplitudes ω_1 and a range of offsets Ω_1. If we define a target function as :

$$\langle I_z \rangle_{\text{ideal}}(\omega_1, \Omega_1) = \begin{cases} -1, & \text{if} \quad \omega_1^{\text{nom}} - \omega_1^{\text{cutoff}} \leq \omega_1 \leq \omega_1^{\text{nom}} - \omega_1^{\text{cutoff}} \\ & \text{and} \quad -\Omega_1^{\text{cutoff}} \leq \Omega_1 \leq \Omega_1^{\text{cutoff}} \\ \text{any}, & \text{elsewhere} \end{cases} \tag{3.55}$$

the function to minimize can be simply written:

$$q = \sum_{\omega_1, \Omega_1} [\langle I_z \rangle(\omega_1, \Omega_1) - \langle I_z \rangle_{\text{ideal}}(\omega_1, \Omega_1)]^2 \tag{3.56}$$

This quality factor q is a function of the Fourier coefficients, so the minimization procedure shall give coefficient sets that generate pulses robust with respect to rf amplitude mismatch and offset, in a region defined by ω_1^{cutoff} and Ω_1^{cutoff}. The total duration of the pulse is a parameter that has to be set in the beginning of the minimization and defines the number of the intervals for the integration, which is also the number of discretized steps of the phase in the experiment.

By suitably changing the parameters ω_1^{cutoff} and Ω_1^{cutoff}, special performance pulses are generated. Four results called BIMBO (B_1 Insensitive pulses under Mind Boggling Optimizations) will be presented. Their Fourier coefficients are given in the Table 3.5 and contours showing the performance of these new selective pulses are shown in Fig. 3.16.

Table 3.5: Fourier coefficients a_n, b_n for $\phi(t)$ in the BIMBO-N pulses (see Eq. (3.52)). BIMBO-1 is a 2π pulse and was optimized for dual compensation. All other pulses have a flip angle of 4π. BIMBO-2 was optimized to be robust with respect to rf inhomogeneity, BIMBO-3 was optimized to be robust with respect to offset, and BIMBO-4 for dual compensation.

	BIMBO-1		BIMBO-2		BIMBO-3		BIMBO-4	
n	a_n	b_n	a_n	b_n	a_n	b_n	a_n	b_n
0	0	0	0	0	0	0	0	0
1	+0.9862	+0.0584	-1.2751	-0.1271	-1.7791	-0.0899	+1.2358	+0.0673
2	+0.2969	+0.0185	-0.5325	-0.0801	-0.5630	-0.0588	+0.3399	+0.0443
3	-0.0027	+0.0109	-0.3368	-0.0656	-0.1445	-0.0213	+0.8674	+0.0994
4	+0.0025	-0.0330	-0.3309	-0.0917	-0.3797	-0.0922	-0.3327	-0.0316
5	-0.0015	+0.0167	-0.0852	-0.0551	-0.2800	-0.0568	+0.1666	+0.0238

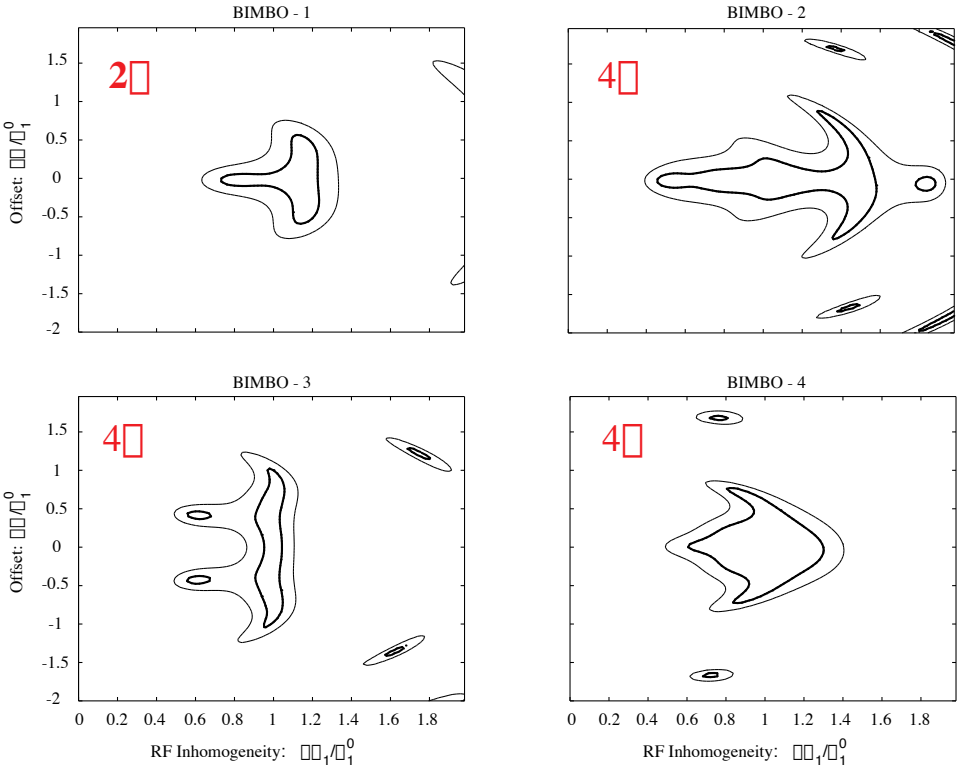

Figure 3.16: Contour levels for the BIMBO-N pulses of Table 3.5. The two contour levels presented here correspond to $I_z = -0.9$ and $I_z = -0.984$. On the top left corner of each figure the total flip angle of the pulse is shown.

Application of the DUMBO approach for B_1 selective pulses

Localized Nuclear Magnetic Resonance is particularly used in MRI. Several pulses have been developed in order to select a specific spatial region, using magnetic field gradients and/or selective pulses [133, 138, 140, 152–154]. We have applied the DUMBO approach in order to find B_1 selective pulses. In this way we would be able to select only all parts of the sample that experience the same B_1 field and thus behaves ideally with respect to the decoupling scheme. Not too many details will be presented here, the full discussion being exposed in the future thesis of P. Charmont, which will deal in details with localized solid-state NMR problems.

In this application, only the target function is different. In this problem it is defined as a Gaussian function centered around the nominal values of the rf amplitude, having a finite width. This width is a parameter that defines the selectivity of the optimized pulse.

The approach is then exactly the same as for B_1 insensitive pulses though much harder to find good solutions. Here we are interested in selecting a sharp region of B_1 amplitudes, around a nominal value, while leaving unperturbed all the sample that experiences other fields. However, because the probe does not generate all fields, for efficient minimization we restrict the calculation of q to around $\omega_1^{\text{nom}} \pm 20\%$. A preliminary result that confirms the validity of the DUMBO approach is presented in Fig. 3.17. The longitudinal magnetization, together with the target functions are plotted for an on-resonance pulse, as functions of the applied rf amplitude. Around the nominal value of $\omega_1^{\text{nom}} = 100$ kHz that we want to select the magnetization is not inverted for a range of $\omega_1 = 100 \pm 20$ kHz. Outside this region we are not interested, because the rf probe does not generate these rf fields. Note that the magnetization is almost fully inverted for the range of $\omega_1 = 100 \pm 4$ kHz, selecting a very homogeneous part of the sample.

The phase of the BISON (B_1 Is Selected by Optimising Numerically) pulse together with a preliminary experimental demonstration are shown in Fig. 3.18. The nominal total flip angle for the BISON pulse is 25π and its phase was discretized in numerical simulations and in the experimental procedure in 640 steps each of 300 ns duration at $\omega_1^{\text{nom}} = 100$ kHz.

Of course the nominal values for rf fields throughout this section were set to 100 kHz for numerical simulations. All pulses scale and can be used at any rf field provided that the total flip angle is the same.

3.7 Conclusions

We have introduced a new class of homonuclear dipolar decoupling sequences for use in static and moderate magic angle spinning solid-state NMR experiments. A new decoupling sequence is shown to be more robust than some of the currently most popular homonuclear decoupling sequences, especially with regard to its sensitivity to rf inhomogeneity. We expect this new sequence, dubbed DUMBO-1, to be useful

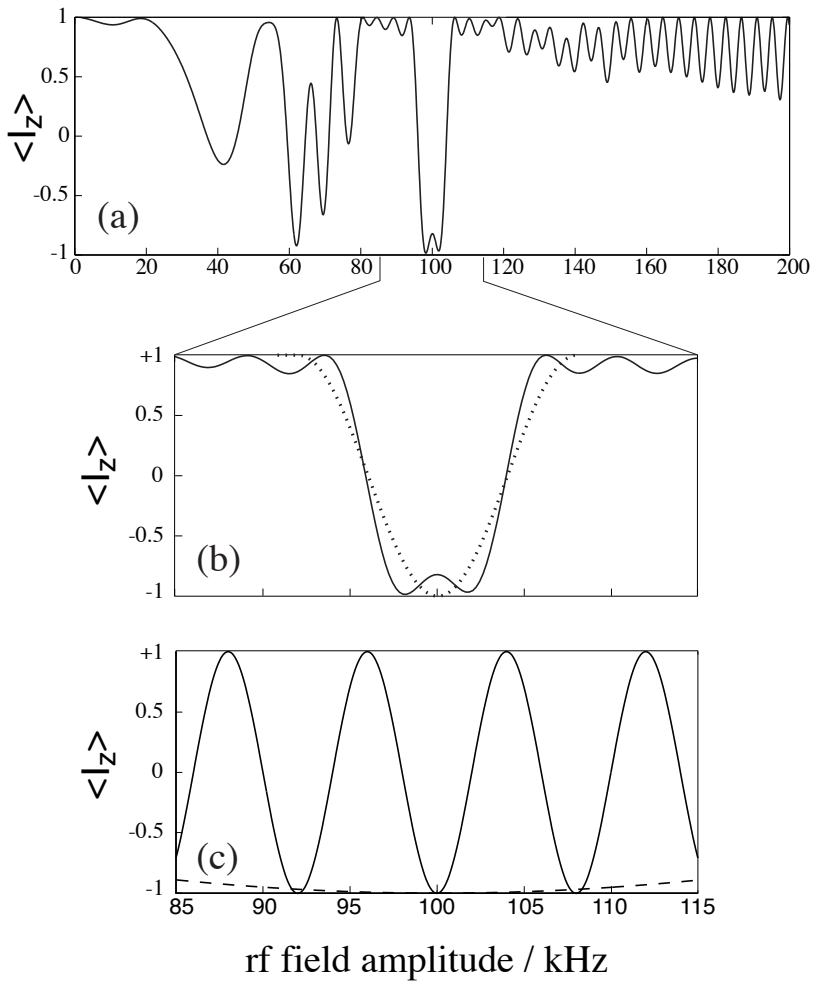

Figure 3.17: (a) Diagram representing the z magnetization component as a function of the amplitude of the applied rf field using the BISON pulse. The overall flip angle of the BISON pulse is 25π. (b) Zoom into the region around the nominal value of the rf field. The target function (Gaussian) is shown in dotted line. (c) Similar diagram for square pulse having a total flip angle of 25π (solid line) and for a simple π pulse (dotted line). We can easily observe the non-selectivity of these pulses around the nominal value of the field.

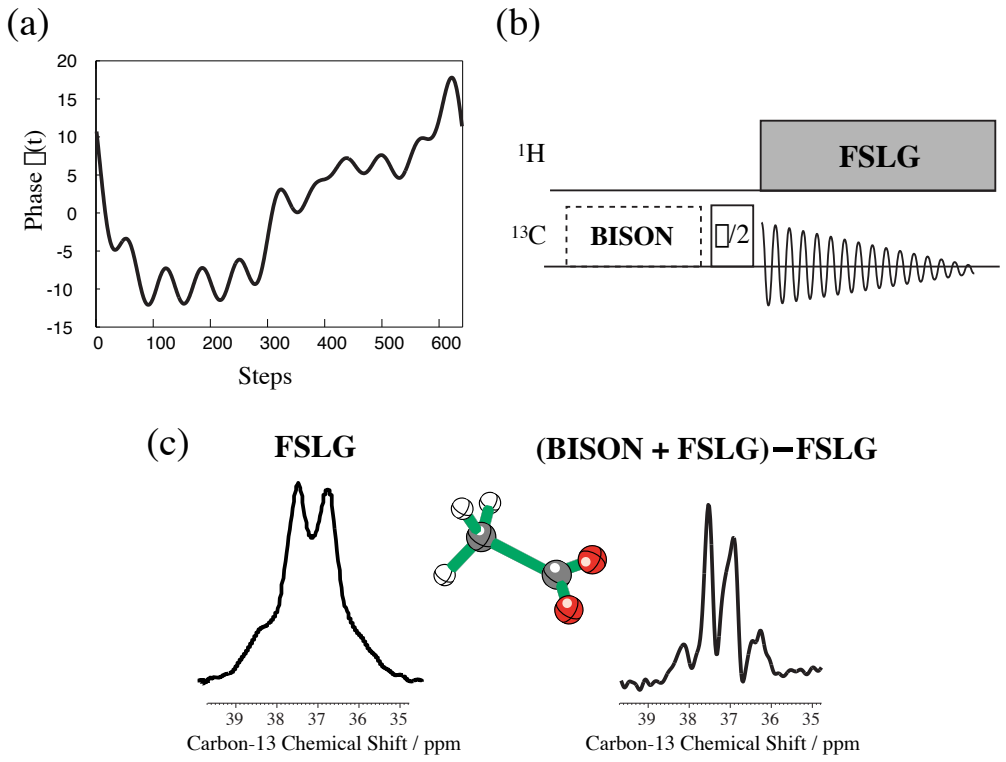

Figure 3.18: (a) Phase diagram for the BISON pulse. The phase is noted in π units. (b) The BISON pulse is used before a homonuclear FSLG decoupling sequence on sodium acetate. We have seen previously that FSLG is highly dependent on the rf inhomogeneity. By introducing the BISON pulse before the decoupling, we act only on the regions of the sample were the B_1 field is highly homogeneous, so only these regions are inverted. In (c) we performed two homonuclear decoupling experiments, with and without BISON and the results were subtracted (difference spectroscopy). The remaining signal was coming form highly homogeneous regions of the sample, where the decoupling works almost ideally. Thus the 1:3:3:1 fine structure of the CH_3 multiplet is fully resolved.

in many experiments where homonuclear decoupling is important.

We note that this is merely the first example of the application of this approach, and that in fact there are many other classes of better solutions potentially available by improving the model spin system, or by using different cycle periods, or different numbers of coefficients, or even using different basis functions (for example, spherical harmonics). For example, one could develop rotor synchronized sequences adapted to fast MAS frequencies.

The DUMBO approach can in principle be easily adapted to other averaging problems in NMR, and we have shown results for B_1 insensitive and B_1 selective pulses. Another obvious potential application is in heteronuclear dipolar decoupling.

Chapter 4

Spin Diffusion

4.1 The Spin Diffusion Problem

Nuclear spin diffusion in the solid state is a complex phenomenon that presents a fundamental and a practical interest related to its use in NMR spectroscopy. The term spin diffusion was first introduced by Bloembergen [62, 63] and describes the magnetization exchange processes via a coupling interaction. Flip-flops transitions involving successive pairs of nuclei provide a mechanism by which magnetization can be transported through the sample [155]. Spin diffusion is essential to nuclear spin-lattice relaxation of protons in many solids because it enables transfer of magnetization from sites where relaxation is slow (immobile crystalline regions) to sites where it is fast (amorphous regions). The transfer rate of spin diffusion depends on the size of the relaxing domains, thus measurements of spin diffusion are a means of estimating domain sizes [156].

In organic solids we are interested in different types of spin diffusion. Firstly, we are interested in spin diffusion among inequivalent ^{13}C nuclei because they provide better resolution than ^{1}H nuclei, especially when MAS is applied. This homonuclear carbon spin diffusion contains information about the connectivities in the carbon skeleton and internuclear carbon–carbon distances, and can be a local probe for the molecular 3D structure in solids [157–160]. Secondly, special attention has been paid to heteronuclear spin diffusion between a rare nucleus, such as ^{13}C or ^{15}N, and protons. Cross polarization [6, 7] is one the most useful techniques in solid state NMR and is based on such heteronuclear polarization transfer. Last but not least in this discussion, spin diffusion among the ^{1}H nuclei is probably one of the subjects where current and future development is most promising [159, 161]. Spin diffusion occurs rapidly in spin systems composed of abundant nuclei such as protons (or fluorines). However, because the proton signals often overlap, direct detection of the magnetization transfer between protons is hindered. On the other hand, in the previous Chapter we have shown the importance of homonuclear decoupling. Decoupling of proton-proton interactions, or in other words quenching of the spin diffusion in the proton bath, leads to high resolution conditions where liquid-like

techniques become possible in the solid state. Thus, we feel that if we have a better understanding of spin diffusion mechanisms, we may be in a better position to explain or control them.

One other way to look at spin diffusion is with respect to its transport characteristics. Thus we talk about *spatial* spin diffusion [62,63,162,163], when the transfer of magnetization occurs between spatially distant regions, and about *spectral* spin diffusion [164–169], when the transfer occurs between nuclei having different resonant frequencies.

In order to give a global picture of spin diffusion, we have to mention that magnetization transfer occurs by means of energy conserving microscopic spin flip processes. Energy conservation is of primary importance and the mechanisms that provide the energy for the spin flip can be very different [155]:

- **proton-driven spin diffusion**: in this case the energy for the flip-flops of two carbon spins comes from the proton bath with which they are strongly coupled.
- **motionally-driven spin diffusion**: in this case the energy comes from molecular movements or chemical reactions.
- **rf-driven spin diffusion**: here the energy is provided by an extraneous rf field.
- **rotor driven spin diffusion**: in which the sample rotation provides the energy for energy conserving magnetization transfer.

Our goal here is to obtain some physical insight into the mechanisms of spin diffusion, especially for the cases of proton driven spin diffusion and cross polarization. The objectives we have fixed in this Chapter is to try to simulate spin diffusion dynamics from *ab initio* numerical quantum calculations and try to invert the problem (need working).

4.2 Proton-Driven Spin Diffusion

Spin diffusion between nuclei with different chemical shifts (spectral spin diffusion) has been studied by the combination of two-dimensional NMR exchange techniques [165–167, 170] or by the application of selective pulse excitation methods [171–174]. Since spin diffusion is mainly induced by the homonuclear dipolar interaction, it is in principle possible to determine the strength of the this interaction, or the internuclear distance, from the observed spin-diffusion rates. Several applications of spectral spin diffusion measurements based on these ideas have been reported in the literature [156, 160, 165, 175–182]. Theoretical analyses of spectral spin diffusion in the case of static [166, 167, 183] and rotating [168] solids have been reported. The applicability of such theories to static single crystals was reported [158] while the effect of the spinning frequency on spin diffusion was studied sparsely [184, 185].

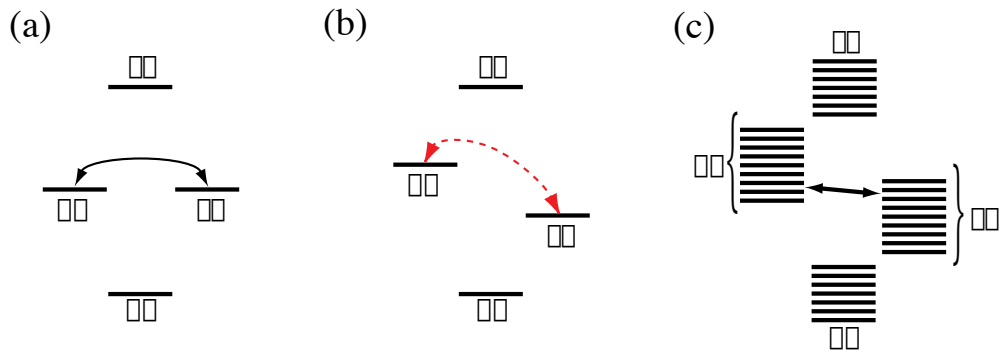

Figure 4.1: Schematic diagram of energy levels for a two spin system. (a) Case of equivalent nuclei: both nuclei have the same chemical shift so the $|\alpha\beta\rangle$ and $|\beta\alpha\rangle$ states are degenerate. The presence of a dipolar coupling between the two nuclei induces the energy conserving *flip-flop* transition between these two states, and thus magnetization transfer. (b) Case of non-equivalent nuclei: this time the transition is not-energy conserving and its probability is low. Thus, spin diffusion is quenched. (c) Case where the two spin system is coupled with an extraneous bath. Now all the energy levels of the two spin system are split because of these couplings and an overlap can occur between some of the levels $\alpha\beta$ and $\beta\alpha$. Transitions between these levels are now allowed and spin diffusion is reintroduced.

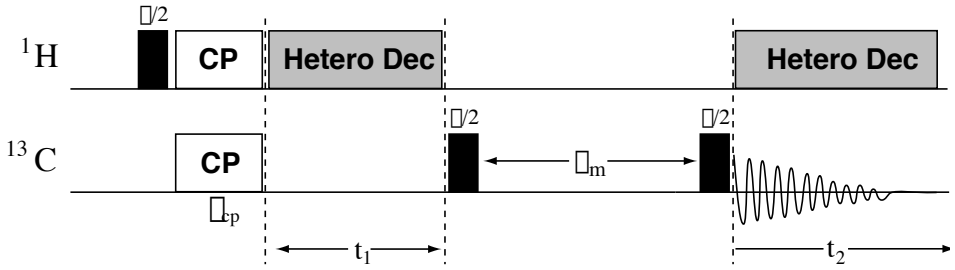

Figure 4.2: Sequence for spectral spin diffusion measurements. After a first step of cross polarization the enhanced carbon polarization evolves during t_1 only under the influence of its isotropic chemical shift because of heteronuclear decoupling and MAS. This serves as a labeling period. Then magnetization is stored along the z axis and exchange occurs during a mixing period τ_m. Finally magnetization is detected under heteronuclear decoupling conditions during t_2. Fourier transform of the signal with respect to both t_1 and t_2 gives the 2D correlation map.

Usually the carbon-13 resonances of crystalline organic compounds under high resolution conditions (MAS, high power decoupling) are well resolved because carbon nuclei have quite different chemical shifts. This means that exchange of magnetization between two non-equivalent nuclei, through flip-flop transitions, does not conserve energy, and therefore has little probability to occur. In other words, for spin diffusion to occur, a mechanism must be available by which the energy imbalance involved is compensated for. The mechanism that has been most often considered is the broadening of the carbon levels by the presence of the proton bath. This way a partial overlap between the energy distant levels is reestablished and spin diffusion can occur. A schematic diagram of this mechanism is shown in Fig. 4.1. Thus, the spin diffusion rate depends not only on the dipolar couplings between the exchanging nuclei but also on their couplings to the environment. We will see in what follows how this dramatically complicates the extraction of useful information.

4.2.1 Experiments

Monitoring spectral spin diffusion is an easy 2D experiment than does not need very demanding experimental conditions. The sequence we use here is a solid state analogue [165] of standard 2D exchange spectroscopy [170, 186]. The experiment is carried out under Magic Angle Spinning in order to average out all anisotropic interactions. First, the carbon polarization is enhanced by an initial cross polarization step. Then under heteronuclear decoupling the transverse carbon coherences evolve under the influence of their isotropic chemical shifts. After a $\pi/2$ pulse the transverse coherences are transformed to longitudinal magnetizations that are allowed to exchange during the τ_m mixing period.

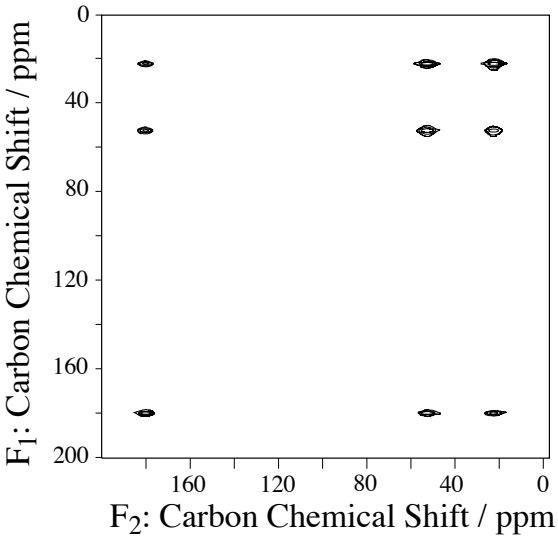

Figure 4.3: 2D Carbon-13 exchange spectrum of a powder sample of fully ^{13}C enriched L-alanine. A full 5 mm rotor was used. The mixing time was set to 100 ms and the MAS frequency to 7 kHz. Resonances from the methyl (1), methine (2) and carbonyl (3) carbons are resolved and off-diagonal peaks due to magnetization exchange are present.

The dynamics during τ_m are governed by the differential equation [187]:

$$\frac{\mathrm{d}}{\mathrm{d}t}M_z = L\{M_z - M_0\} \tag{4.1}$$

where M_0 is the vector of equilibrium magnetizations and L is the exchange matrix that describes both the spin-lattice relaxation and the spin diffusion:

$$L = R + K \tag{4.2}$$

The matrix R contains all relaxation contributions to the longitudinal magnetization vector M_z, including the diagonal spin-lattice relaxation, $-R_{1,j} = -1/T_{1,j}$ associated with magnetic site j, and the diagonal and non-diagonal contributions arising from cross-relaxation. The matrix K is the kinetic magnetic site exchange matrix. Its elements are defined as:

$$K_{ij} = -K'_j\delta_{ij} + k_{ij} \tag{4.3}$$

where K'_j obeys the equation:

$$K'_j = \sum_{i=1}^{N} k_{ij} = \sum_{i\neq j} k_{ij} + k_{jj} = K_j + k_{jj} \tag{4.4}$$

in which $K_j = 1/\tau_j$ represents the inverse of the preexchange lifetime of magnetic site j, and k_{jj} represents the rate of the unobservable transfer of magnetic site j into itself. The formal solution of Eq. (4.1) is:

$$M_z(t_1, \tau_m) = M_0 + \exp(L\tau_m)[M_z(t_1, \tau_m = 0) - M_0] \tag{4.5}$$

and after for quantitative information the volume intensities I_{kl} of the 2D map are related to the desired elements of the L matrix by :

$$I_{kl}(\tau_m) = [\exp(L\tau_m)]_{kl} M_{l0} \tag{4.6}$$

The equilibrium magnetization M_{l0} can be evaluated from the intensity of the corresponding auto-peak at zero mixing time:

$$M_{k0} = a_{kk}(\tau_m = 0) \tag{4.7}$$

Experiments were performed on two model powder samples. The sample of fully carbon-13 enriched L-alanine was first measured for different mixing times and the measured signal volumes as functions of τ_m are shown in Fig. 4.4. The same measurements were performed on a solid solution containing 12% of fully carbon-13 enriched L-alanine (fully protonated) and 88% of fully deuterated L-alanine (fully carbon-12). The sample was prepared by dissolving both solids in D_2O so all the mobile protons were replaced quantitatively by deuteriums. The solid solution was obtained by slow evaporation of the solvent. The utility of this sample in studying spin diffusion will be apparent in the discussion of the results. The signal volume intensities as functions of τ_m, for this sample, are shown in Fig. 4.5.

4.2.2 Results and discussion

Using Eq. (4.6) we can fit the experimental data to this simplified exchange model. A small complication arises since the intensities of the peaks in the 2D map are not symmetric with respect to the diagonal. The initial step of cross-polarization leads to the non equipartition of magnetization at the beginning of the experiment, and to non symmetric 2D intensities [188]. A modified description of Eq. (4.6), including this effect gives for the 2D signal intensities I_{kl}:

$$I_{kl}(\tau_m) = [\exp(L\tau_m)]_{kl} T_{ll}^{CP} M_{l0} \tag{4.8}$$

where T^{CP} is a diagonal matrix of cross polarization factors. Under this formalism we obtain symmetric peaks only if $T_{ll}^{CP} = T_{kk}^{CP}$, and this is not usually the case in solid-state NMR. In what follows we have used this modified description (Eq. (4.8)) as a model function in the fitting procedure. For the simple case of L-alanine we have to adjust 9 parameters rather than 6 in the case where the spectrum would

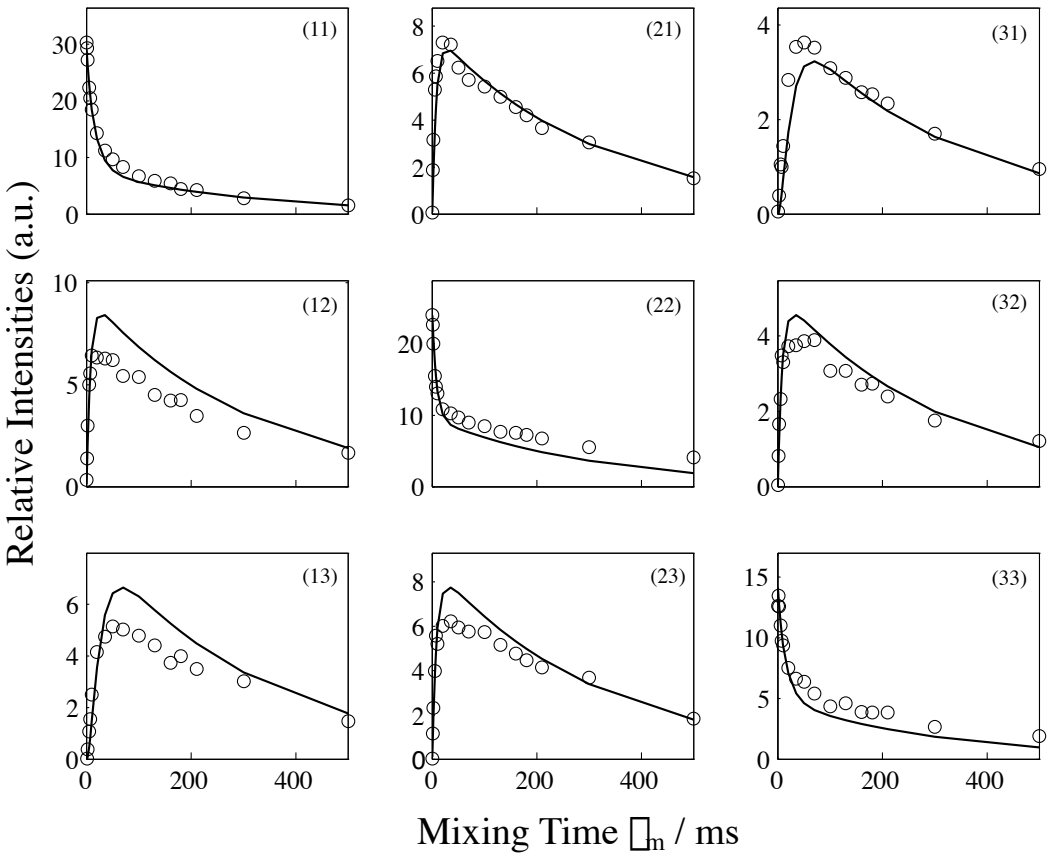

Figure 4.4: Peak intensities (volumes in the 2D exchange spectrum) for a powder sample of ^{13}C-L-alanine as functions of mixing time τ_m. Experimental points are indicated with circles whereas solid lines correspond to the best fitting using Eq. (4.8).

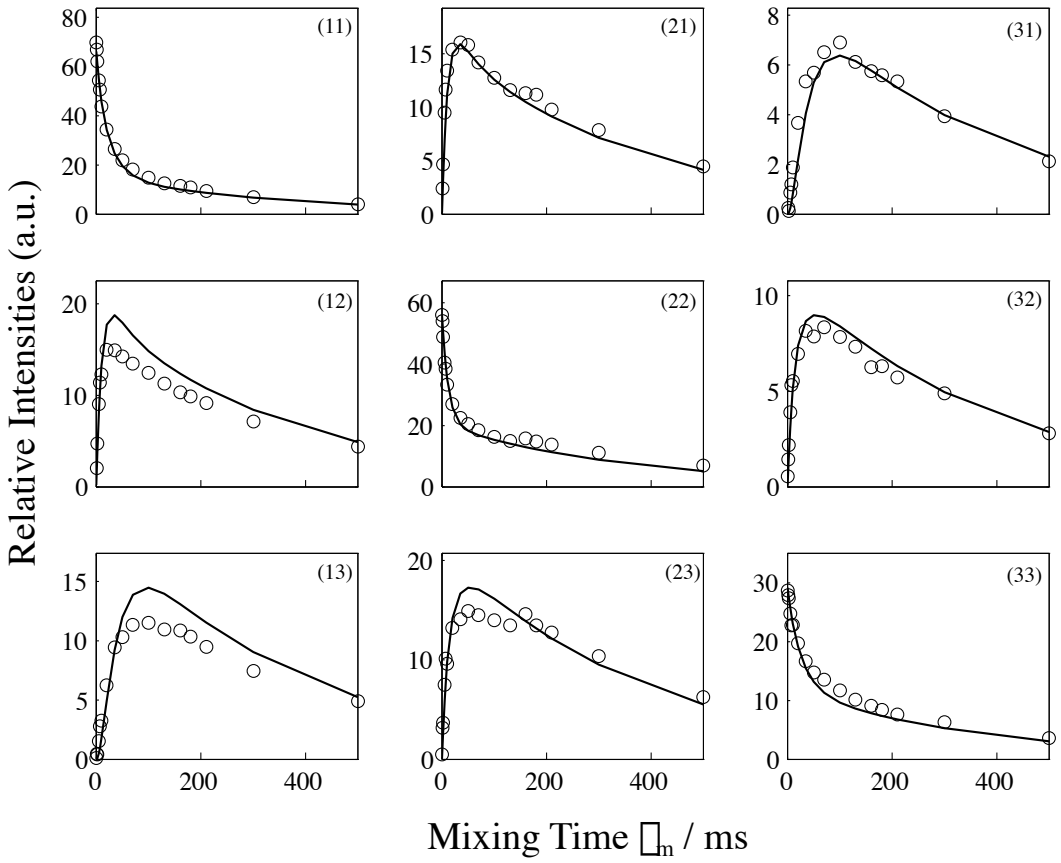

Figure 4.5: Peak intensities (volumes in the 2D exchange spectrum) for a powder sample of the solid solution (see text for details) as functions of mixing time τ_m. Experimental points are indicated with circles whereas solid lines correspond to the best fitting using Eq. (4.8).

have been symmetric. From Fig. 4.4 we appreciate that the fit is satisfactory[1]. The fitting routine was based on the standard least square steepest descent method and the results are given in Table 4.1.

The transfer among ^{13}C occurs at a measurable, though slow, rate in natural abundance samples [157]: the inverse of the rate constant is typically 50–100 s, whereas in ^{13}C enriched samples, the characteristic time for transfer is less than 1 s. It can be observed that our experimental values for the diffusion rates fall within the typical range for enriched samples. However, the diffusion rate between the methyl carbon and the carbonyl carbon cannot be measured precisely. In the fitting it seems that this direct spin diffusion rate is very slow compared with the two other rates. It is experimentally not obvious to quantify the transfer for the site (1) to the site (3). In principle, such quantification would be even more difficult in the case of more complicated spin networks [189].

i	$M_0^{(i)}$ (a.u.)	$T_1^{(i)}$ (ms)	W_{i1} (s^{-1})	W_{i2} (s^{-1})	W_{i3} (s^{-1})
1	29.2	18.5	—	-0.042	-0.000
2	24.2	12.8	-0.042	—	-0.044
3	14.2	19.9	-0.000	-0.044	—

Table 4.1: Diffusion parameters for the sample of ^{13}C-L-alanine from the fitting of Fig. 4.4.

The interest to use the solid-solution sample comes from the fact that in this case the proton bath is replaced by a deuterium bath having a coupling six times weaker with the carbons and 36 times weaker amongst the ^{2}H. This means that the carbon levels are not broadened as much as in the previous experiment. If the hypothesis of the mechanism for proton-driven spin diffusion as the only possible is valid, then in the solid solution sample there will be a significant slowing of spin diffusion. The fitted data for the solid solution are shown in Table 4.2. Firstly, we observe that the rate for the 1–3 transfer cannot be determined with precision, as in the previous experiment. Additionally, the diffusion rates are smaller, but not as weak as expected. There is a factor 1.5–2 with respect to the previous experiment, and we would expect that spin diffusion would be almost completely quenched because of the differences in carbon chemical shifts. This can be interpreted as an indication of the presence of extra mechanisms in carbon spin diffusion in solid-state.

The detailed interpretation of this kind of data, which is obviously very interesting, is very difficult and it motivates the theoretical studies that follow in the rest of this Chapter. In what follows we are going to try to reproduce such experimental data from exact spin dynamics simulations in order to understand possible

[1]Note that this is a remarkably simple model. Other phenomenological models based on multi-exponential (multi-bath) equilibrations were also tested without giving significantly better fits. Results are not shown here.

i	$M_0^{(i)}$ (a.u.)	$T_1^{(i)}$ (ms)	W_{i1} (s^{-1})	W_{i2} (s^{-1})	W_{i3} (s^{-1})
1	66.4	23.8	—	-0.032	-0.000
2	56.2	18.0	-0.032	—	-0.026
3	29.3	37.7	-0.000	-0.026	—

Table 4.2: Diffusion parameters for the sample of the solid solution from the fitting of Fig. 4.5.

mechanisms for spin diffusion.

4.3 Theoretical Approaches

The theoretical study of proton driven spin diffusion is complicated because of the strong interactions between multiple bodies. The treatment we present follows the method of second order perturbation theory introduced by Suter and Ernst [166,167] and the method of memory functions [190] of Henrichs, Linder and Hewitt [183]). The case of MAS was treated within the framework of perturbation theory by Kubo and McDowell [168].

In order to simplify the problem we consider a spin system of *two* S spins in an environment of I spins (I bath). The Hamiltonian of this system can be simply written:

$$\mathcal{H} = \mathcal{H}_S + \mathcal{H}_{SS} + \mathcal{H}_{SI} + \mathcal{H}_{II} + \mathcal{H}_I \tag{4.9}$$

$$\mathcal{H}_S = \Omega_1 S_{1z} + \Omega_2 S_{2z} \tag{4.10}$$

$$\mathcal{H}_{SS} = d^{SS}[2S_{1z}S_{2z} - \frac{1}{2}(S_1^+ S_2^- + S_1^- S_2^+)] \tag{4.11}$$

$$\mathcal{H}_{SI} = \sum_i 2(d_{1i}^{SI} S_{1z} + d_{2i}^{SI} S_{2z}) I_{iz} \tag{4.12}$$

$$\mathcal{H}_{II} = \sum_{i<j} d_{ij}^{II}[2I_{iz}I_{jz} - \frac{1}{2}(I_i^+ I_j^- + I_i^- I_j^+)] \tag{4.13}$$

with

$$d_{ij}^{xy} = -\frac{\mu_0}{4\pi}\gamma_x\gamma_y\hbar r_{ij}^{-3} P_2(\cos\theta_{ij}), \quad x, y = S, I \tag{4.14}$$

In the limit of identical I chemical shifts, the Zeeman interaction on the I spins commutes with the remainder of the Hamiltonian and has no effect on S–S spin diffusion. We are interested in spin diffusion between the S spins so in spin operators S_{1z} and S_{2z}. It is useful to note that the sum of these operators is a constant of the motion, i.e.:

$$[H, S_{1z} + S_{2z}] = 0 \tag{4.15}$$

and thus does not evolve in time. We can extract from the total Hamiltonian all terms that contain this constant of the motion (chemical shift and heteronuclear dipolar coupling) and we obtain the relevant part of the Hamiltonian:

$$\mathcal{H}_{\text{rel}} = \mathcal{H}_\Delta + \mathcal{H}'_{SS} + \mathcal{H}_{SI\Delta} + \mathcal{H}_{II} + \mathcal{H}_I \tag{4.16}$$

$$\mathcal{H}_\Delta = \frac{1}{2}(\Omega_1 - \Omega_2)(S_{1z} - S_{2z}) \tag{4.17}$$

$$\mathcal{H}'_{SS} = -d^{SS}\frac{1}{2}(S_1^+ S_2^- + S_1^- S_2^+) \tag{4.18}$$

$$\mathcal{H}_{SI\Delta} = \sum_i 2(d_{1i}^{SI} - d_{2i}^{SI})\frac{1}{2}(S_{1z} - S_{2z})I_{iz} \tag{4.19}$$

$$\mathcal{H}_{II} = \sum_{i<j} d_{ij}^{II}[2I_{iz}I_{jz} - \frac{1}{2}(I_i^+ I_j^- + I_i^- I_j^+)] \tag{4.20}$$

It is sufficient to consider the evolution of the difference de polarization $\frac{1}{2}(S_{1z}-S_{2z}) \equiv S_z^{(23)}$. We can thus place ourselves in the (23) subspace of the spins S and write the previous Hamiltonian keeping only the terms in this subspace. If we define the appropriate single transition operators [191–193] for the (23) subspace:

$$S_x^{(23)} = \frac{1}{2}(S_1^+ S_2^- + S_1^- S_2^+) \tag{4.21}$$

$$S_y^{(23)} = -\frac{i}{2}(S_1^+ S_2^- + S_1^- S_2^+) \tag{4.22}$$

$$S_z^{(23)} = \frac{1}{2}(S_{1z} - S_{2z}) \tag{4.23}$$

$$\tag{4.24}$$

we can finally write the simplest part of the Hamiltonian that describes exactly the spin system:

$$\mathcal{H}^{(23)} = \delta S_z^{(23)} - d^{SS}S_x^{(23)} + 2\sum_i d_i S_z^{(23)} I_{iz} + \mathcal{H}_{II}^{(23)} \tag{4.25}$$

where: $\delta \equiv \Omega_1 - \Omega_2$, $d_i \equiv d_{1i}^{SI} - d_{2i}^{SI}$. Until this point this description, where only the relevant terms have been kept, is exact.

4.3.1 Second order time-dependent perturbation theory

The idea of Suter and Ernst [166, 167](Kubo and McDowell [168] applied it later in the case of MAS) was to link the isolated spin system with a bath of extraneous spins, in the way it is done for semi-classical relaxation theory [64,194]. In this latter case there is an ensemble average and the environment is described by a (second-order) stochastic process, whereas in spin diffusion in solids the coupling to the bath (first order) is coherent [65].

To apply these ideas the total Hamiltonian is described as having a non-perturbed $\mathcal{H}_0$ part which contains the two S spins and the environment, and the perturbative part $\mathcal{H}_1$,which contains their interactions:

$$\mathcal{H} = \mathcal{H}_0 + \mathcal{H}_1 \tag{4.26}$$

with:

$$\mathcal{H}_0 = \mathcal{H}_{\text{Sys}} + \mathcal{H}_{\text{Env}}, \quad \mathcal{H}_1 = \mathcal{H}_{\text{Inter}} \tag{4.27}$$

In the interaction representation of $\mathcal{H}_0$ the evolution of the density operator is:

$$\tilde{\sigma}(t) = \exp(i\mathcal{H}_0 t)\sigma(t)\exp(-i\mathcal{H}_0 t) \tag{4.28}$$

and we substitute in the master equation of time evolution to obtain:

$$\dot{\tilde{\sigma}}(t) = -i[\tilde{\mathcal{H}}_1(t), \tilde{\sigma}(0)] - \int_0^t \mathrm{d}\tau \left[\tilde{\mathcal{H}}_1(t), [\tilde{\mathcal{H}}_1(t-\tau), \tilde{\sigma}(0)]\right] + \cdots \tag{4.29}$$

The traceless part of the density operator, can be developed in an orthonormalized set of basis operators $\{A_i\}$:

$$\tilde{\sigma}(t) = \sum_i a_i(t) A_i \tag{4.30}$$

Inserting Eq. (4.30) into Eq. (4.29), after some algebra we obtain:

$$\begin{aligned} \mathrm{Tr}\{A_k^2\}\dot{a}_k(t) &= -i\sum_i a_i(0)\mathrm{Tr}\left[[\tilde{\mathcal{H}}_1(t), A_i], A_k\right] \\ &+ \sum_i a_i(0)\int_0^t \mathrm{Tr}\{[\tilde{\mathcal{H}}_1(t), A_k][\tilde{\mathcal{H}}_1(t-\tau), A_i]\}\,\mathrm{d}\tau \end{aligned} \tag{4.31}$$

Within the limits of time dependent perturbation theory (short time scales, slow variation of $a_i(t)$ [195]) we obtain the following system for the decomposition coefficients [167]:

$$\dot{a}_k(t) = \sum_i W_{ki} a_i(t) \tag{4.32}$$

where the rate constants are given by:

$$W_{ki} = [\mathrm{Tr}(A_k^2)]^{-1}\left\{-i\mathrm{Tr}\{[[\tilde{\mathcal{H}}_1(t), A_i], A_k]\} + \int_0^\infty \mathrm{Tr}\{[\tilde{\mathcal{H}}_1(t), A_k][\tilde{\mathcal{H}}_1(t-\tau), A_i]\}\mathrm{d}\tau\right\} \tag{4.33}$$

This expression for diffusion rate constants is used in the following extreme cases.

Case 1: Weak dipolar S–S coupling

In this case the dipolar S–S interaction is treated as a perturbation and the diffusion rates of Eq. (4.33) for the relevant sub-block (23) depend on the lineshape of the zero-quantum spectrum:

$$W^{(23)} = -d^2 g^{(23)}(\delta) \tag{4.34}$$

where $g^{(23)}(\delta)$ represents the intensity of the zero-quantum lineshape at an offset frequency equal to the chemical shift difference δ between the two S spins. We can thus understand the importance of the zero-quantum spectrum in spin diffusion process and the effort made in the literature [158, 168] and in this Chapter we try to measure, predict or calculate this spectrum. The formal expression of $g^{(23)}(\omega)$ is given in [167].

Case 2: Weak dipolar S–I coupling

In this case the operator $S_z^{(23)}$ does not commute with $\mathcal{H}_0$, and is no longer a constant of the motion. In the limit of weak d coupling the diffusion rate is:

$$W^{(23)} = -\frac{d^2}{[(1/T_2^{ZQT})^2 + d^2]T_2^{ZQT}} \tag{4.35}$$

with T_2^{ZQT} = the zero-quantum coherence dephasing time[2]:

$$(T_2^{ZQT})^{-1} = 4[\mathrm{Tr}(1)]^{-1} \sum_i \sum_k b_i b_k \int_0^t \mathrm{Tr}[I_{iz} \exp(i\mathcal{H}_{II}\tau) I_{kz} \exp(-i\mathcal{H}_{II}\tau)] \tag{4.36}$$

We see that in the case where $|\mathcal{H}_{SI}| \ll |\mathcal{H}_{II}|$ the zero-quantum lineshape is *Lorentzian*. This is because the interaction is averaged by the rapid flip-flops of the I spins, like in the case of exchange narrowing [194].

Case 3: Weak dipolar I–I coupling

In this case we can replace the exponential $\exp(-i\mathcal{H}'_D t)$ in the expressions by $\exp(-i\mathcal{H}_{SI} t)$. After a bit of algebra we find that the lineshape this time is *Gaussian*:

$$g(\omega) = \sqrt{\frac{\pi}{B}} \exp(-\omega^2/2B) \quad \text{with} \quad B = \sum_i b_i^2 \tag{4.37}$$

With $|\mathcal{H}_{SI}| \gg |\mathcal{H}_{II}|$ the I spin flip-flops are slow compared with the time-scale of the $\mathcal{H}_{SI}$ interaction. The zero-quantum coherence decays in the presence of the static inhomogeneous $\mathcal{H}_{SI}$ field. If any I are very close to the S spins, the zero-quantum lineshape is split as can be observed in the single-quantum spectrum of the CH and CH_2 groups [168].

[2]Note that this is a coherent effect so we avoid to use the term of zero-quantum relaxation time here.

4.3.2 Use of Memory Functions

The rates of spin diffusion can be calculated using the tool of memory functions [190,196–199]. We will not extend our discussion of the calculations in the literature, and for more details on memory functions we propose [200]. The lineshape of the zero-quantum spectrum $g(\omega)$ is expressed [183] as the overlap of the resonances of the two spins S_1 and S_2:

$$g(\omega) = \int_{-\infty}^{+\infty} f_1(\omega') f_2(\omega' - \omega) d\omega' \tag{4.38}$$

where $f_1(\omega)$ et $f_2(\omega)$ are the single-quantum lineshapes of S_1 et S_2 obtained without proton decoupling. This formula is applicable only to systems where the two spins are far away from each other (weak S–S coupling) [158]. In this case we find again the result from Suter & Ernst [167].

4.4 *Ab-initio* Numerical Approaches

We have seen in Section 4.2.2 what kind of data we can obtain from proton-driven spin diffusion among carbon-13 nuclei. The first need is to understand the influence of the experimental (spinning frequency, decoupling) and molecular (distances, angles, anisotropies) parameters on the spin diffusion rates. We also saw that lot of theoretical discussions exist in the literature trying to treat this complicated many-body problem. The second step would ideally be to invert the problem, that is try to extract out of spin diffusion rates, useful structural parameters, such as distances and/or angles, in an analogous way the NOESY experiment does in the liquid state NMR [170, 201, 202].

In the following we try to reproduce the experimental results by simulating the exact quantum evolution of the spin system. In order to simulate exactly the evolution of the system all the interactions have to be included in the description of the spin system.

4.4.1 Exact Simulations

The evolution of the system is described by the density operator $\sigma(t)$ that represents the state of the system in the Liouville space. The evolution of the density operator describing an ensemble of identical spin systems is described by the master equation [90]:

$$\frac{\mathrm{d}}{\mathrm{d}t}\sigma(t) = -i[\mathcal{H}, \sigma(t)] - \hat{\hat{\Gamma}}\{\sigma(t) - \sigma_{\mathrm{te}}\} \tag{4.39}$$

where $\mathcal{H}$ is the spin Hamiltonian of the system and et $\hat{\hat{\Gamma}}$ is the relaxation superoperator. σ_{te} is the thermal equilibrium density operator.

In the absence of explicit time-dependence the spin Hamiltonian of a *general* heteronuclear system can be written as:

$$\mathcal{H} = \mathcal{H}_S + \mathcal{H}_{SS} + \mathcal{H}_{SI} + \mathcal{H}_{II} + \mathcal{H}_I \tag{4.40}$$

With:

$$\mathcal{H}_S = \sum_{i=1}^{N} \Omega_i^S S_{iz}, \quad \mathcal{H}_I = \sum_{i=1}^{M} \Omega_i^I I_{iz} \tag{4.41}$$

$$\mathcal{H}_{SS} = \sum_i \sum_{j>i} d_{ij}^{SS} [2S_{iz}S_{jz} - \frac{1}{2}(S_i^+ S_j^- + S_i^- S_j^+)], \tag{4.42}$$

$$\mathcal{H}_{SI} = \sum_{i,j} d_{ij}^{SI} 2S_{iz}I_{jz}, \tag{4.43}$$

$$\mathcal{H}_{II} = \sum_{i,j,i<j} d_{ij}^{II} [2I_{iz}I_{jz} - \frac{1}{2}(I_i^+ I_j^- + I_i^- I_j^+)], \tag{4.44}$$

and

$$d_{ij}^{xy} = -\frac{\mu_0}{4\pi} \gamma_x \gamma_y \hbar r_{ij}^{-3} P_2(\cos\theta_{ij}), \quad \text{with} \quad x, y = S, I. \tag{4.45}$$

It is possible to have explicit time dependent terms due to mechanical rotation, chemical reactions, rf fields. Our main interest lies in the first case where time dependence comes form the MAS. In order to write correctly the spin Hamiltonian in the laboratory frame a number of unitary transformations has to be performed:

$$\begin{array}{lll} \text{PAS(1)} & \xrightarrow{\Omega_1} & \\ \text{PAS(2)} & \xrightarrow{\Omega_2} & \\ \quad\vdots & & \text{CRS} \xrightarrow{\Omega} \text{Rot} \xrightarrow{\Omega'(t)} \text{Lab} \\ \text{PAS(n)} & \xrightarrow{\Omega_n} & \end{array}$$

where PAS(i) are the principal axis systems of all tensorial interactions (dipolar couplings and anisotropic chemical shifts), CRS is the crystal reference frame, Rot is the rotor reference frame and Lab is the laboratory frame of reference. The Ω_i Euler angles are time independent and fully determined by the molecular geometry and the crystal structure. In the following, these Euler angles were calculated from crystal structures from the Cambridge database. The Ω Euler angles are also time independent and correspond to the different orientation between each crystallite and the rotor frame. In a powder sample because of the large number of crystallites,

it is legitimate to assume than Ω constitute a random and uniform distribution of orientations in space. In the case of MAS, $\Omega' = (0, \theta_m, \omega_r t)$ where ω_r is the rotor frequency and $\theta_m = \arctan\sqrt{2}$ is the magic angle.

The secular part of this Hamiltonian (part that commutes with the static magnetic field) for the coupling between two homonuclear spins can be written:

$$\mathcal{H}^{ij}_{D_{\text{sec}}} = -\frac{\mu_0}{4\pi}\gamma_i^2 r_{ij}^{-3} \sum_{m'=-2}^{+2} \mathcal{D}^2_{m',0}(\Omega') \sum_{m''=-2}^{+2} \mathcal{D}^2_{m'',m'}(\Omega)\mathcal{D}^2_{0,m''}(\Omega_{ij})(3I_{iz}I_{jz} - \vec{I}_i \cdot \vec{I}_j) \tag{4.46}$$

and for the anisotropic chemical shift:

$$\mathcal{H}^{i}_{CSA_{\text{sec}}} = \gamma_i B_0 \sigma_i \sum_{m'=-2}^{+2} \mathcal{D}^2_{m',0}(\Omega') \sum_{m''=-2}^{+2} \mathcal{D}^2_{m'',m'}(\Omega)\mathcal{D}^2_{0,m''}(\Omega_{ij})I_{iz} \tag{4.47}$$

where $\mathcal{D}^l_{m,n}$ are the Wigner rotation matrix elements [99, 195].

4.4.2 Symmetry Simplifications

Using these equations and structural data (distances, angles and chemical shifts) we can construct the numerical Hamiltonian for a system of spins. The Hamiltonian is initially constructed in the basis of the tensor products of individual Zeeman states for each spin. For a pure homonuclear spin system, only the total M_z is a good quantum number. This means that no exchange of magnetization takes place between blocks having different M_z values, and each M_z block can be treated numerically as a separate spin diffusion problem. Thus, the maximum size of the system than can be treated numerically depends on the size of the biggest M_z block. For homonuclear spin systems the biggest block corresponds to $M_z = 0$ (even number of spins) or $|M_z| = 1$ (odd number of spins).

We can thus use the total projection along the z axis of the angular momentum in order to reorder the Zeeman states into diagonal blocks. Note that in heteronuclear spin systems spin diffusion occurs among each individual nuclear species. Thus, the total projection of the angular momentum of protons is a good quantum number, as it that for carbons. The result of reordering of the Zeeman states can be appreciated in Fig. 4.6. The efficiency of the calculation can be improved almost by three orders of magnitude with respect to the brute force diagonalization of the full Hamiltonian.

Available computer memory is also a problem, because it becomes very difficult to construct the full Hamiltonian matrices for large spin systems. Two solutions can be adopted: the construction of matrices directly in a reordered basis set [203, 204], or the use of sparse matrices. The first method allows the creation of each individual block directly, without ever having to generate the total Hamiltonian. The second approach is based on the fact that the matrices of the problem are sparse, thus only their non-zero elements have to be stored. This leads to a significant economy in

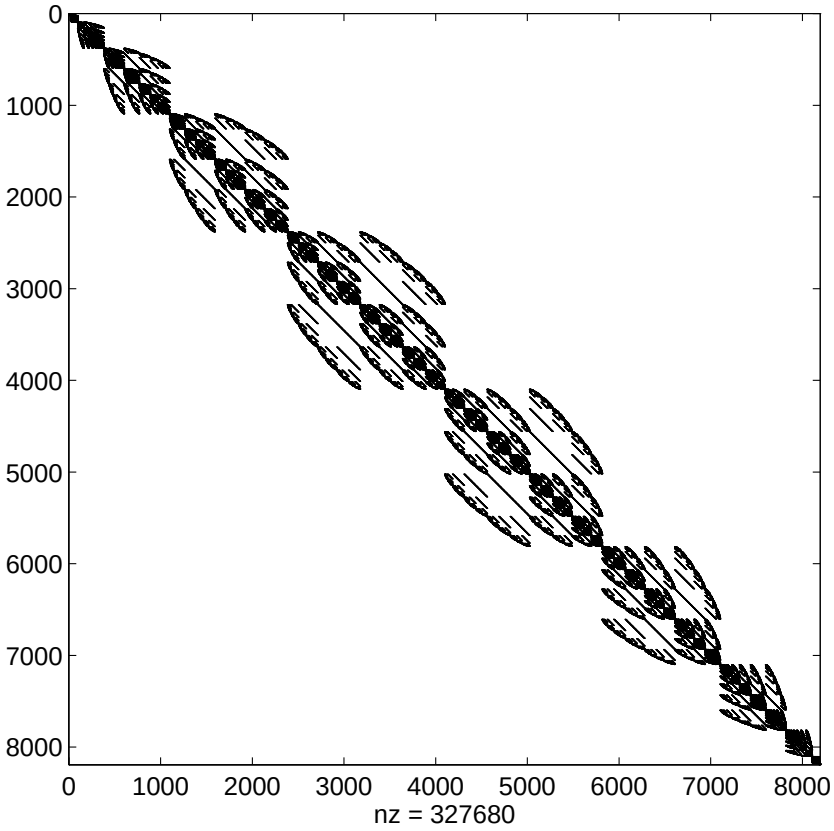

Figure 4.6: Matrix structure of the dipolar Hamiltonian for a homonuclear spin system of 13 spins. The block diagonal structure is obtained by a reordering of the Zeeman states with respect to their total M_z quantum number. This matrix is highly sparse and the number on non-zero elements nz is given. This matrix contains only 0.49% of non-zero elements (see Table 4.3).

Table 4.3: Theoretical (assuming than each M_z block is full) and real densities of the Hamiltonian for homonuclear and heteronuclear spin systems.

N	Real density %	Theoretical density %	Real $\overline{\text{Density}}$ %	Δ
	Homonuclear Systems		Heteronuclear Systems	
2	37.50	37.50	25.00	0.00
3	31.25	31.25	18.75	0.00
4	25.00	27.34	14.06	2.21
5	18.75	24.61	10.94	2.21
6	13.28	22.56	7.55	1.63
7	8.98	20.95	5.25	1.31
8	5.86	19.64	3.42	0.79
9	3.71	18.55	2.24	0.52
10	2.29	17.62	1.37	0.32
11	1.39	16.82	0.86	0.20
12	0.83	16.12	0.50	0.12
13	0.49	15.50	0.30	0.07
14	0.28	14.94	0.17	0.04

the memory needed to store such matrices, and makes it possible to generate them for a large number of spins [205]. Once generated, reordering can take place and a block separation routine can split the individual M_z blocks. The advantage of the second method is that in the case of a completely general problem the density of the matrix, i.e. the percentage of non-zero elements in each M_z block is very low. Data are shown in Table 4.3 for both homonuclear and heteronuclear spin systems. Δ represents the standard deviation from the mean value due the possible compositions of the heteronuclear spin system[3].

The most efficient way to simulate a large number of spins would be a combination of both methods, i.e. direct creation of matrices in the appropriate basis set using sparse algorithms. In both methods, the spin diffusion problem is treated individually for each block and the results are summed up at the end of the calculation. Finally, note also that spin diffusion is identical between blocks having the same absolute value of M_z, and this leads to further numerical simplification (only one half of the Hamiltonian has to be treated).

[3]For example lets consider two heteronuclear spin systems containing a total number 14 spins. Suppose the first contains 2 carbons and 12 protons and the second 7 carbons and 7 protons. The Hamiltonian of the former spin system is less sparse than the Hamiltonian of the latter.

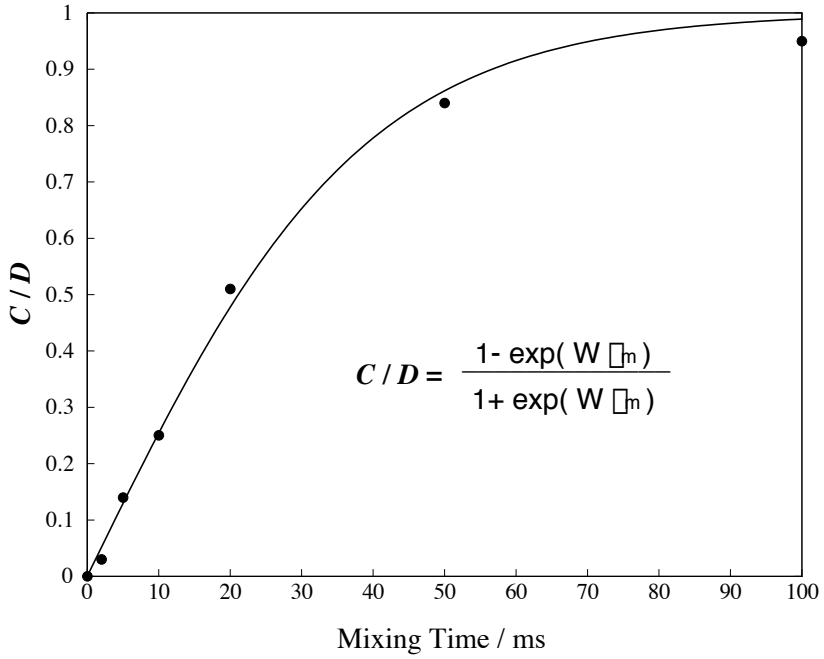

Figure 4.7: Experimental spin diffusion results for a single crystal of malonic acid. The ratio of the cross-peaks intensities **C** to the diagonal peaks intensities **D** is plotted as a function of the mixing time τ_m. The experimental behaviour fits well with an exponential equilibration of magnetization between the two spins, having a spin diffusion rate W, predicted by theory. From Ref. [167].

4.4.3 Results and Discussion

Malonic Acid

We start by considering the spin system of malonic acid, isotopically ^{13}C enriched at the two carboxyl positions, corresponding to the same system Suter and Ernst used in Ref. [167]. The results of Suter and Ernst can be summarized in Fig. 4.7, showing the ratio of magnetizations for the pair of carbons as a function of mixing time. Our objective here is to reproduce this figure numerically.

Distances and orientations with respect to the crystal frame were obtained from crystallographic data [206] and chemical shift differences from [167]. The dipolar coupling between the two carbons is weak (250 Hz) and the sample is static. Magnetization curves for many different crystal orientations were calculated and three of them are presented in Fig. 4.8. In Fig. 4.8 the magnetization of spin 1 is plotted as a function of mixing time τ_m for different spin systems including from 2 to 12 spins from the crystal structure. In the case where only two spins (the two carbons) are included the result, does not change with the orientation, because the three orientations were selected in order to give the same carbon-carbon homonuclear dipolar

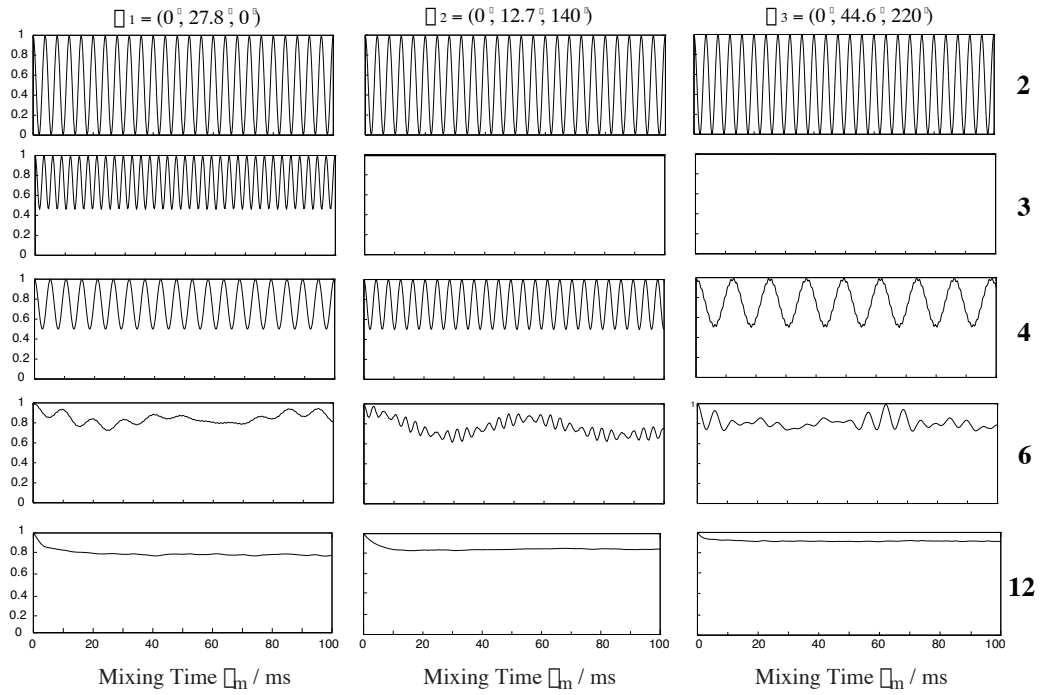

Figure 4.8: Spin diffusion profiles for the carbon magnetization of spin 1 as a function of the mixing time τ_m. The results for three different orientations are shown. Their relative orientations (Euler Angles) with respect to the crystal frame are given for each column. On the right in bold characters the number of spins included in the simulations is indicated.

coupling as observed by Suter and Ernst. When protons are included (1–10) the profile of the magnetization transfer changes significantly. We see than each orientation behaves differently when a small number of extraneous protons is included. However, for a large number of spins the results seem to converge to a diffusion like curve having an "exponential" decay and a stationary long-time behaviour. This long time behaviour does not correspond to the long-time behaviour experimentally observed where an equipartition (thermodynamic equilibration) of magnetization takes place. We will see in Section 4.6 the significance of this stationary state and how this quasi-equilibrium state is established. It is important to note that these results were obtained *without* including the chemical shift difference (1200 Hz) of Ref. [167]. When such chemical shift difference is included spin diffusion is completely quenched (see Fig. 4.9). *This means that the size of the spin system we simulate is not large enough to broaden the carbon levels sufficiently to overcome a chemical shift difference of 1200 Hz.*

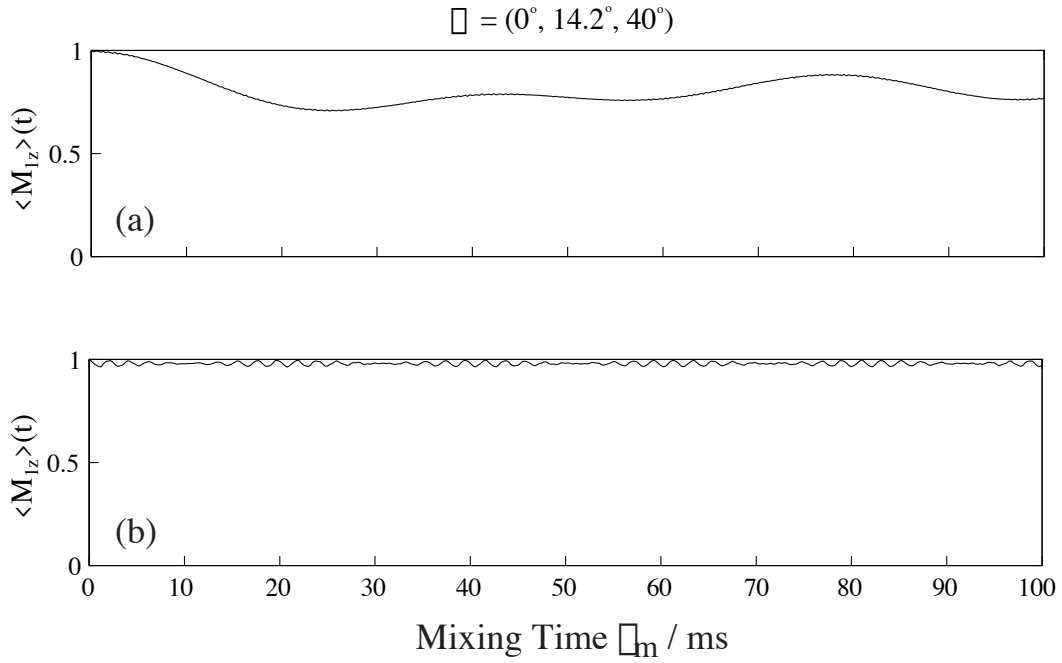

Figure 4.9: Magnetization transfer curves for the carbon magnetization of spin 1 as a function of the mixing time (a) with and (b) without including a chemical shift difference of 1200 Hz. The introduction of the chemical shift difference quenches spin diffusion.

L-Alanine

The experimental results we presented in Section 4.2.2, constitute a nice example of proton-driven spin diffusion in powder samples under Magic Angle Spinning. We have tried here first to simulate the spin system of L-alanine without including MAS. Crystallographic data about distances and orientations were obtained from Ref. [207].

We first show in Fig. 4.10 spin diffusion curves in the case of single crystals, for different model spin systems, having a random orientation. Initial magnetization ($\tau_m = 0$) lies on the carbonyl carbon. For the first diagram only the carbon skeleton was simulated whereas for the last the whole molecule (3 carbons and 7 protons) was included. As in the case of malonic acid the spin system moves towards a long time behaviour different from the simple thermodynamical prediction ($\langle M_z \rangle = 1/3$). No direct transfer from spin 1 to spin 3 is observed in the simulation including the maximum number of spins.

When we integrate the signal over 10^5 crystal orientations the result is not significantly different. The powder behaviour shown in Fig. 4.11 shows that whether any chemical shift difference between carbons are included or not, the long time behaviour is stationary and away from the thermodynamic limit. This means that the broadening due to the presence of the proton bath is enough to cover the energy difference of the chemical shift (spin diffusion is not completely quenched) but that the quasi-equilibrium value is far away from the true equilibrium one. We will study in more detail this state in Section 4.6.

The spinning case

One last (but not least) note has to be made about spinning samples. Fig. 4.12 presents spin diffusion curves for the malonic acid molecule of Section 4.4.3 under magic angle spinning for different spinning frequencies. We have simulated this spin system, rather than L-alanine, because of the smaller number of spins we need in order to include the whole molecule. Thus simulations were performed on a 6 spin system. We can clearly see that the spinning frequency has a significant influence on the dynamics of spin diffusion both in the short and the long time scale. The experimental results of the solid solution sample presented in Section 4.2.2 support this idea. In fact even if we substitute the proton bath with a deuterium one, there is no significant difference in the observed spin diffusion rate.

Thus, it seems that the proton bath is not the only mechanism, for the so called proton-driven spin diffusion in rotating solids. MAS can have a great influence in dynamics and can in fact induce spin diffusion. Note that by rotation we do not mean rotational resonance [208, 209](rotor-driven spin diffusion). Here the rotation modulates the proton levels increasing the overall area of overlap for the carbon states and thus spin diffusion. Though further development of these ideas requires the use of approximate models for the description of spin dynamics, these results clear evidence for the relevance of the rotation to spin diffusion in organic solids.

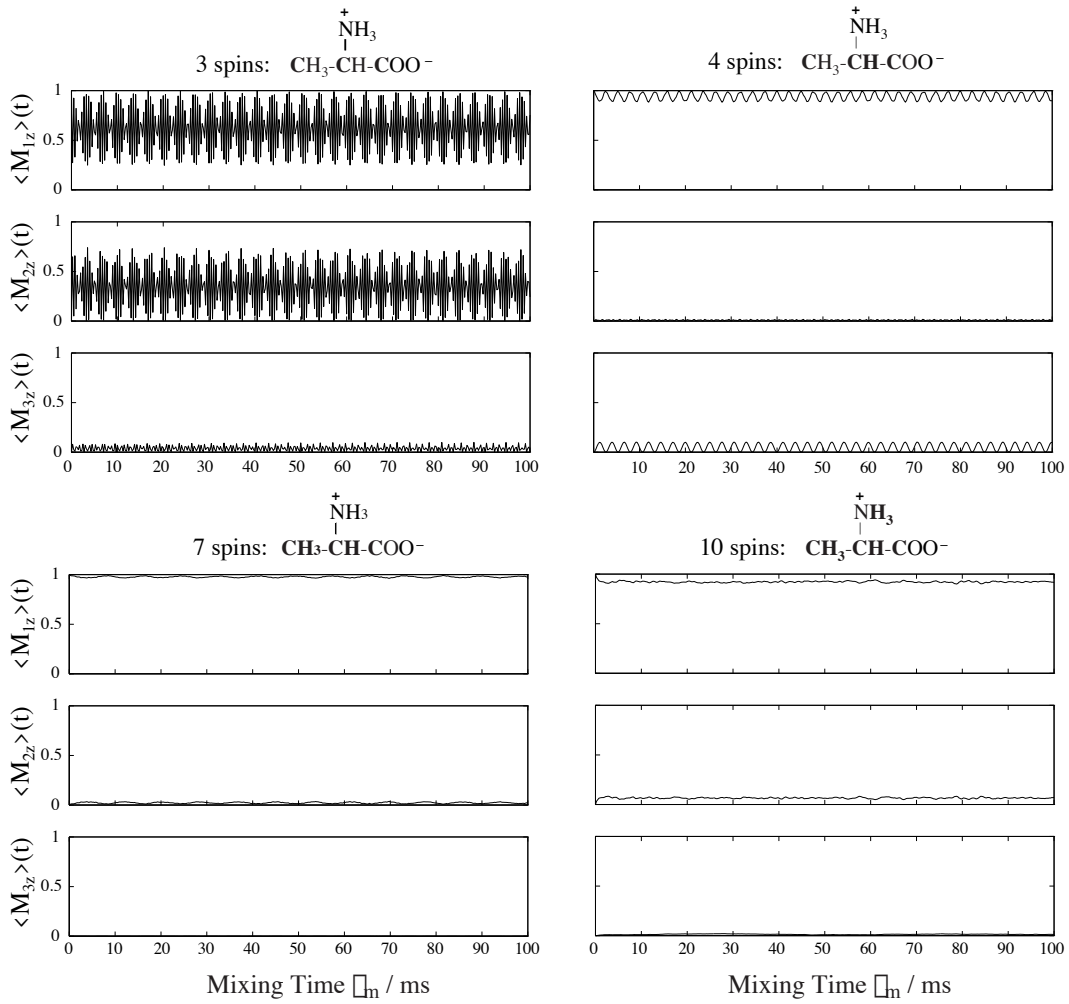

Figure 4.10: Magnetization transfer curves for the L-alanine carbon magnetizations as functions of the mixing time. Initial polarization lies on the carbonyl carbon. Only nuclei in bold were included in simulations spins. MAS is not included.

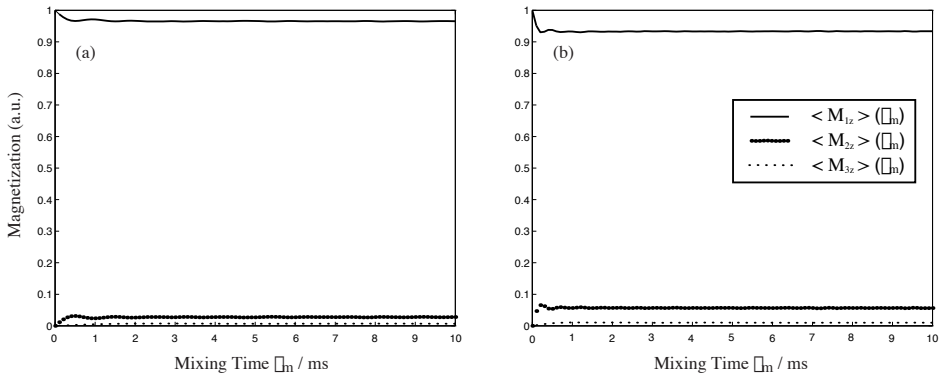

Figure 4.11: Spin diffusion profiles for the L-alanine carbon magnetizations as functions of the mixing time after a powder integration. Figures were obtained without including (a) and including (b) the isotropic chemical shift differences of the three carbons. The effect of chemical shift difference seems less important than in the case of single crystals.

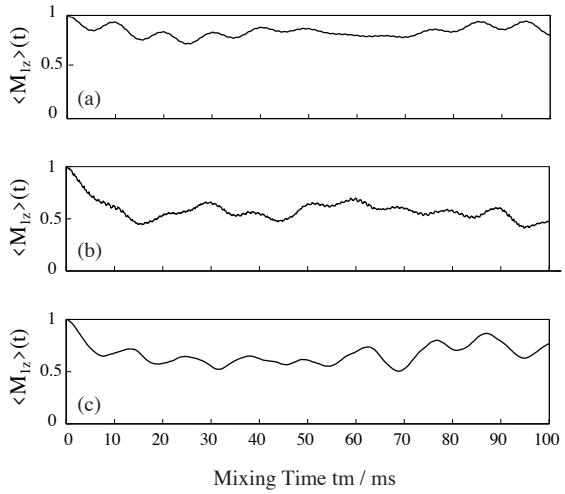

Figure 4.12: Spin diffusion profiles for a spinning single crystal of malonic acid simulated on 6 spin system. Carbon magnetizations as functions of the mixing time and spinning frequency are presented.

4.5 A Weak Perturbation Approach

From the previous sections it becomes obvious that approximation methods need to be developed in order to treat numerically a large number of spins. Here we are going to develop the theoretical frame together with some preliminary numerical ideas in order to overcome this problem.

4.5.1 Theory

The total Hamiltonian of an heteronuclear spin $I_M S_N$ system can be written:

$$\mathcal{H} = \mathcal{H}_S + \mathcal{H}_{SI} + \mathcal{H}_I \tag{4.48}$$

where $\mathcal{H}_S$ contains the Zeeman interaction and all homonuclear dipolar couplings for the S spins and $\mathcal{H}_I$ has the same significance for the I spins.

There are two relevant constants of the motion, corresponding to the total projections of the magnetizations along the z axis for the two nuclear species:

$$\left[\mathcal{H}, \sum_i S_{iz}\right] = \left[\mathcal{H}, \sum_i I_{iz}\right] = 0 \tag{4.49}$$

From now on we are looking for the appropriate basis set to express adequately the Hamiltonian for the perturbation approach. Using the M_z blocking for the S spin we can split the S spin Hamiltonian into blocks. We will work in the basis set of eigenvectors for the I spin Hamiltonian multiplied with the S Zeeman basis reordered according to their total M_z. To clarify this statement, in this basis set any basis function can be written as:

$$|\Psi_i\rangle = |\psi\rangle_I |\phi\rangle_S = |\lambda_i\rangle |M_{Sz}; \epsilon_1, \epsilon_2, \ldots, \epsilon_N\rangle \tag{4.50}$$

where the I, S indexes show that the states belong to the I, S nuclear species, and will be omitted in what follows. λ_i are the eigenvalues and $|\lambda_i\rangle$ the corresponding eigenstates of the I spin Hamiltonian. M_{Sz} is the total projection along z of the S spins angular momentum, and ϵ_i is the quantum number (α, β) for each spin S. The matrix elements of the I spin Hamiltonian in this basis can be written:

$$\langle \Psi_i | \mathcal{H}_I | \Psi'_j \rangle = \lambda_i \delta_{ij} \langle \phi | \phi' \rangle \tag{4.51}$$

Thus, in this basis, $\mathcal{H}_I$ is diagonal. For the S spin Hamiltonian expressed in this basis set, we have:

$$\langle \Psi_i | \mathcal{H}_S | \Psi'_j \rangle = \langle \phi | \mathcal{H}_S | \phi' \rangle \delta_{M_{Sz}, M'_{Sz}} \delta_{ij} \tag{4.52}$$

in other words, $\mathcal{H}_S$ is block diagonal.

In this basis set the coupling Hamiltonian can be written:

$$\mathcal{H}_{SI} = \sum_{k,l} d_{kl} I_{kz} S_{lz} \tag{4.53}$$

and its matrix elements are:

$$\begin{aligned}
\langle \Psi_i | \mathcal{H}_{SI} | \Psi'_j \rangle &= \langle \psi | \langle \phi | \mathcal{H}_{SI} | \phi' \rangle | \psi' \rangle & (4.54)\\
&= \sum_{k,l} d_{kl} \langle \psi | I_{kz} | \psi' \rangle \langle \phi | S_{lz} | \phi' \rangle & (4.55)\\
&= \sum_{k,l} d_{kl} \langle \lambda_i | I_{kz} | \lambda_j \rangle \epsilon_l \delta_{\epsilon_1,\epsilon'_1} \delta_{\epsilon_2,\epsilon'_2} \dots \delta_{\epsilon_N,\epsilon'_N} & (4.56)\\
&= \sum_{k,l} d_{kl} \langle \lambda_i | I_{kz} | \lambda_j \rangle \epsilon_l \langle \phi | \phi' \rangle & (4.57)
\end{aligned}$$

We see that since S_{jz} is diagonal in this basis set and I_{iz} is full, $\mathcal{H}_{SI}$ has a strip structure.

Finally the total Hamiltonian in this basis set has the same strip structure, apart from its diagonal where the SS blocks are full. Its general matrix element is:

$$\langle \Psi_i | \mathcal{H} | \Psi'_j \rangle = \lambda_i \delta_{ij} \langle \phi | \phi' \rangle + \langle \phi | \mathcal{H}_S | \phi' \rangle \delta_{M_{Sz},M'_{Sz}} \delta_{ij} + \sum_{k,l} d_{kl} \langle \lambda_i | I_{kz} | \lambda_j \rangle \epsilon_l \langle \phi | \phi' \rangle \tag{4.58}$$

The expectation value for an observable $\mathcal{O}$ can be written:

$$\begin{aligned}
\langle \mathcal{O} \rangle (t) &= \sum_{i \neq j} \sigma_{ij}(0) \mathcal{O}_{ji} \exp[-i(E_i - E_j)t] & (4.59)\\
&+ \sum_i \sigma_{ii}(0) \mathcal{O}_{ii}
\end{aligned}$$

where the matrix elements of the initial density matrix and of the observable are expressed in the eigenbasis of the total Hamiltonian. In our example both the initial density operator and the observables are I_{kz} magnetization operators. In the perturbation treatment that follows, the true eigenvalues E_i of the total Hamiltonian are approximated and their approximate expressions are inserted in Eq. (4.59).

Until this point, we have only written down the total Hamiltonian in a basis set adapted to apply directly static perturbation theory.

Perturbation treatment: Part 1

Suppose that the difference between any pairs of eigenvalues of the I spin Hamiltonian is larger than the coupling terms due to IS and SS, i.e. $|\lambda_i - \lambda_j| \gg ||\mathcal{H}_{SI} + \mathcal{H}_S||$. In this case we need to consider only each I spin Hamiltonian eigenvalue block separately. In other words the matrix elements between blocks having different I

eigenvalues are neglected. The general matrix element of the total Hamiltonian is then:

$$\langle\Psi_i|\mathcal{H}|\Psi'_j\rangle \simeq \lambda_i\delta_{ij}\langle\phi|\phi'\rangle + \langle\phi|\mathcal{H}_S|\phi'\rangle\delta_{M_{Sz},M'_{Sz}}\delta_{ij} + \sum_{k,l} d_{kl}\langle\lambda_i|I_{kz}|\lambda_i\rangle\epsilon_l\langle\phi|\phi'\rangle \quad (4.60)$$

Weak SS coupling If $||\mathcal{H}_{SI}|| \gg ||\mathcal{H}_S||$ there is no need to further diagonalize the Hamiltonian. Within the first order perturbation treatment, it is enough to consider only the diagonal elements of the total Hamiltonian. In this case, one diagonal matrix element of the total Hamiltonian can be written as:

$$\langle\Psi_i|\mathcal{H}|\Psi_i\rangle \simeq \lambda_i + \langle\phi|\mathcal{H}_S|\phi\rangle + \sum_{k,l} d_{kl}\langle\lambda_i|I_{kz}|\lambda_i\rangle\epsilon_l \quad (4.61)$$

Any energy difference between two states having different λ, can be written as:

$$\begin{aligned} E_i - E_j &= \lambda_i - \lambda_j + \sum_{k,l} d_{kl}\epsilon_l(\langle\lambda_i|I_{kz}|\lambda_i\rangle - \langle\lambda_j|I_{kz}|\lambda_j\rangle) && (4.62)\\ &= \lambda_i - \lambda_j + \Delta E_{ij}^{IS} && (4.63)\end{aligned}$$

where the perturbation ΔE_{ij}^{IS} depends on the configuration (ϵ_l) of the extraneous S spins. If we characterize the state of the extraneous spins by a collective index k the observable signal of Eq. (4.59) has to be summed over the states of the lattice:

$$\begin{aligned} \langle\mathcal{O}\rangle(t) &= \sum_{i\neq j}\sum_k \sigma_{ij}(0)\mathcal{O}_{ji}\exp[-i(E_i - E_j + \Delta E_{ij}^k)t] && (4.64)\\ &+ \sum_i \sigma_{ii}(0)\mathcal{O}_{ii} \end{aligned}$$

We can thus see that the quantities ΔE_{ij}^k are due to the presence of the heteronuclear coupling with the extraneous spins and lead to a *dephasing of the signal*. Note also that the diagonal elements of the signal are not affected. This will play an important role in the following Section 4.6.

Strong SS coupling If $||\mathcal{H}_S|| \geq ||\mathcal{H}_{SI'}||$, we need to further diagonalize the Hamiltonian within the M_z blocks for the S spins. In this case suppose K is the diagonal matrix having as elements the eigenvalues κ_j of $\mathcal{H}_S + \mathcal{H}_{SI}$. The diagonal elements of the total Hamiltonian can then be written as:

$$\langle\Psi|\mathcal{H}|\Psi\rangle \simeq \lambda_i + \kappa_j \quad (4.65)$$

and the observable signal as

$$\begin{aligned} \langle\mathcal{O}\rangle(t) &= \sum_{i\neq j} \sigma_{ij}(0)\mathcal{O}_{ji}\exp[-i(E_i - E_j + \Delta E_{ij})t] && (4.66)\\ &+ \sum_i \sigma_{ii}(0)\mathcal{O}_{ii} \end{aligned}$$

We can see that similarly the terms ΔE_{ij} lead to a dephasing of the signal. The difference now is that these terms are no longer so simply related to the heteronuclear couplings.

Perturbation treatment: Part 2

Suppose that the difference between two eigenvalues of the I spin Hamiltonian is small. This can occur or because of accidental (or systematic) degeneracies either because of the high density of states commonly encountered in solids. In this case we need to rediagonalize within the subspace of the almost degenerate I eigenvalues. In other words, the elements linking blocks having almost degenerate I eigenvalues cannot be neglected.

Weak SS coupling In the case where $||\mathcal{H}_{SI'}|| \geq ||\mathcal{H}_S||$, the off diagonal elements due to the SS coupling can be neglected and we need to diagonalize within the subspace of the degenerate I spin states. The perturbation will lift the degeneracy between these two states and the final values for the eigenvalues of the total Hamiltonian are going to be perturbed in a non trivial way.

Strong SS coupling In this case where $||\mathcal{H}_S|| \geq ||\mathcal{H}_{SI'}||$, the off diagonal elements due to the SI coupling can be neglected and we need to diagonalize within the M_{Sz} sublocks. In this case the two degenerate I spin blocks are not mixed by rediagonalization of the S blocks.

4.5.2 Practical considerations

The idea of applying static perturbation theory in order to increase the number of spins we can treat numerically is simple. We first split the total system in two parts: *the core*, which will be treated numerically exactly, and *the environment*, which will be included in an approximative manner. The Hamiltonian is:

$$\mathcal{H} = \mathcal{H}_{\text{Core}} + \mathcal{H}_{\text{Env}} \tag{4.67}$$

with

$$\mathcal{H}_{\text{Core}} = \mathcal{H}^{Z}_{\text{Core}} + \mathcal{H}^{HH}_{\text{Core}} + \mathcal{H}^{HC}_{\text{Core}} + \mathcal{H}^{CC}_{\text{Core}} \tag{4.68}$$

and

$$\mathcal{H}_{\text{Env}} = \mathcal{H}^{Z}_{\text{Env}} + \mathcal{H}^{HH}_{\text{Env}} + \mathcal{H}^{HC}_{\text{Env}} + \mathcal{H}^{CC}_{\text{Env}} \tag{4.69}$$

The big problem when the size of the spin system increases is the storage of large matrices. We propose here to generate only the vector space of states for the core. This means that the size we can treat will be that of the core. To simplify the

problem we consider that the environment contains only S Zeeman terms and SI coupling terms, i.e. the SS couplings for the moment are neglected:

$$\mathcal{H}_{\text{Env}} \simeq \mathcal{H}^{Z}_{\text{Env}} + \mathcal{H}^{HC}_{\text{Core–Env}} \tag{4.70}$$

Then we can generate the states of the environment directly because these states are diagonal in the original Zeeman states. Then we transform these states with respect to the diagonalization matrix of the core Hamiltonian and retain only the diagonal terms. This leads to an approximative inclusion of a vastly larger number of spins. Examples of the application of this perturbative method are given in the following sections.

4.6 The Quasi Equilibrium State in Solid-State NMR

Early discussions of the exchange of nuclear spin magnetisation in the solid-state generally described the dynamics in terms of an equilibration of "spin temperatures" [64, 200, 210]. However, nuclear spin systems do not usually correspond to the systems required for simple thermodynamic arguments to be valid. This can be demonstrated experimentally, for example, by the time reversibility of spin diffusion [65]. Concepts such as spin temperature can be modified in order to take into account quantum effects due to the limited size of the system, leading to very involved "thermodynamic" treatments. Recently attention has focused on the attractive idea of *ab initio* type simulations of spin diffusion by modeling explicitly the spin dynamics in a full quantum treatment [66, 67]. However, simulations of polarization dynamics of small spin systems are not obviously applicable to experiments involving macroscopic samples. If exact quantum-statistical studies are to be related to experimental results, we need to consider the effect of the coupling of the spin system to its environment. Only then we can hope to answer questions such as whether the quasi-equilibrium states predicted in simple simulations are related to the experimentally observed states.

The evolution of the density operator describing an ensemble of identical spin systems is described by the Eq. (4.39). In the high spin temperature approximation the traceless part of the thermal equilibrium density operator is given by:

$$\sigma_{\text{te}} = \frac{-H/kT}{\text{Tr}\{e^{-H/kT}\}} \tag{4.71}$$

We deal with only the traceless part of the density operators, since we can neglect the non-evolving identity component. In the absence of significant relaxation, the system evolves simply under the influence of the Hamiltonian towards a stationary state σ^{qe}, referred to as quasi equilibrium [66, 155, 211], for which :

$$[\sigma^{\text{qe}}, H] = 0 \tag{4.72}$$

and which can be expressed a sum of constants of the motion[4] $\{A_k\}$ [155]:

$$|\sigma_{\rm qe}\rangle = \sum_k \frac{|A_k\rangle\langle A_k|}{\langle A_k|A_k\rangle}|\sigma(0)\rangle. \tag{4.73}$$

This state is the result of equilibration amongst the internal degrees of freedom of the system, but is not in general the final equilibrium state of the system since the coupling to the external degrees of freedom (i.e. spin-lattice relaxation) has not been included. Very interesting discussions have appeared in the literature about the thermodynamic properties of this state. In particular this state is shown to be non-ergodic [66](sub-ergodic [67]). In what follows, though some comments will be made, our goal will not be to study such properties. The final state for the system defined as the thermal equilibrium is by definition ergodic (see Eq. (4.71).

In the context of solid-state NMR, however, it is important to distinguish so-called T_1 processes which involve exchange of magnetisation with the lattice (and which may be very slow), from T_2 processes which involve exchange of magnetisation between spins. If only T_2 processes are considered then the system does not return to true thermal equilibrium, but to a state proportional to it. The traceless part of the density operator at the internal thermal equilibrium is:

$$|\sigma_{\rm ie}\rangle = \frac{|H\rangle\langle H|}{\langle H|H\rangle}|\sigma(0)\rangle, \tag{4.74}$$

in other words, the only component of the initial density matrix that remains is the projection onto the Hamiltonian, which is now the only constant of the motion cf. Eq. (4.73).

However, it is not clear from the definitions above that the quasi-equilibrium concept has a firm physical basis. In particular, the time scale required for a small spin system to achieve the stationary state of Eq. (4.72) may be too long (infinite for an isolated spin system) for quasi equilibrium to be established on an experimentally useful time scale [67].

Here we will examine in detail the effect of the external lattice on the spin system dynamics to see whether such a state has any physical meaning, i.e. whether it is experimentally observable. In doing so, we are interested in the long-time behaviour of magnetisation exchange experiments such as cross-polarization and spin-diffusion.

4.6.1 Time-Independent Hamiltonian

For a time-independent Hamiltonian in the absence of relaxation, Eq. (4.39) has the simple solution :

$$\sigma(t) = U(t)\sigma(0)U^{-1}(t) \tag{4.75}$$

[4]Constants of the motion, or integrals of the motions, are operators that comute with the Hamiltonian.

where $U(t) = \exp(-iHt)$. If the density matrix is *expressed in the eigenbasis of the Hamiltonian*, the time dependence of its elements is given by :

$$\sigma_{ij}(t) = \sigma_{ij}(0) \exp[-i(E_i - E_j)t] \tag{4.76}$$

where E_i are the eigenvalues of the Hamiltonian. If we can assume that the oscillating terms of this equation interfere and cancel out at long time, the system will evolve towards the state defined by :

$$\sigma_{ij}^{\mathrm{qe}} = \sigma_{ij}(0)\delta_{E_i,E_j} \tag{4.77}$$

which satisfies Eq. (4.72), i.e. this is a time-independent quasi-equilibrium state. Only the populations (diagonal terms) and coherences (off-diagonal terms) corresponding to degenerate levels are retained. In general, so-called "accidental" eigenlevel degeneracies are rare, while the effect of "systematic" degeneracies resulting from a symmetry of the Hamiltonian can be removed by choosing a symmetrised representation of the Hamiltonian [212], in which case the off-diagonal terms connecting degenerate transitions are identically zero. We are going to treat this case in the example of a spatially periodic spin system, in subsection 4.7. It is important to note that the quasi equilibrium is poorly defined in the presence of accidental degeneracies and more importantly "almost degeneracies" [213][5]. For an isolated system, we can only really discuss the apparent equilibrium reached after a certain time, over which certain close degeneracies may have been resolved [67]. The difficulty is essentially a mathematical one rather than a physical one since real systems are never truly isolated and as we shall see below the time scale for equilibration is always finite.

(Non-) Ergodicity

Ergodicity plays a central role in statistical mechanics. The mathematical definition of non-ergodicity is as follows. Let $\mathcal{E}$ be a space and μ be a measurement in this space. We define a time translation operation $\hat{T}$. The system is called non-ergodic if we can separate $\mathcal{E}$ in two sub-spaces $\mathcal{E}_1$ and $\mathcal{E}_2$, that when translated in time do not communicate, that is: $\hat{T}\mathcal{E}_1 = \mathcal{E}_1$ and $\hat{T}\mathcal{E}_2 = \mathcal{E}_2$, for a non trivial measurement μ.

A system is called ergodic on a time-scale of t_s if every subsystem probes all configurations accessible under the macroscopic boundary conditions within the time t_s. The classical, more restrictive, use of the term ergodic leaves out the specification of a time scale and considers only the case $t_s \to \infty$. In an ergodic system, the time-average $\overline{\mathcal{O}}$ and ensemble-average $\langle Q \rangle$ of an observable Q are equal:

$$\overline{\mathcal{O}} \equiv \lim_{t\to\infty} \frac{1}{t} \int_0^t \mathcal{O}[q_i(t)]\mathrm{d}t = \langle \mathcal{O} \rangle \tag{4.78}$$

[5]It is difficult to define an "almost degeneracy" as an energy difference smaller than a cut-off energy, because this cutoff automatically defines the time scale for randomization of phases. Remember that energy and time are conjugate physical quantities.

The quasi-ergodic hypothesis (more precise) assumes that in the course of time (sufficiently long) every subsystem comes arbitrarily close to any accessible configuration. This hypothesis is based on the equiprobability in the space of phases. While the gases and liquids, usually considered in statistical mechanics, are quasi-ergodic, solids can remain non-ergodic on all practically relevant time-scales [1].

Discussions about ergodicity in solid state NMR started with Ref. [214] and followed with references [215] and [67]. In Ref. [214] the long time expectation values of observable magnetization in an isolated spin system did not correspond to equipartition among all nuclei. Fel'dman and Lacelle [215] have demonstrated the non-ergodic behaviour for the case of infinite size spin systems (with an XY Hamiltonian), by exploiting the exact analytic solution of this Ising Hamiltonian. J. S. Waugh [67] clarified the situation stating that the long time behaviour of an isolated spin system is not stationary and the thermodynamic behaviour of such system can be characterized as sub-ergodic. The expectation value for an observable is given in Eq. (4.59), and the time scale for even approximate phase randomization is inversely proportional to the minimum difference of non-degenerate eigenvalues (time and energy are conjugate quantities). For spin systems that are isolated from their environment, such as those described in Ref. [66], quasi equilibrium is *never* reached because the number of states is not sufficient to provide effective randomization of phases. In systems such as small organic molecules therefore, existing studies would seem to indicate that quasi equilibrium can never be reached. If the quasi-equilibrium concept is to have any physical significance, we need to examine in some detail the effect of coupling to the external lattice. Within the approximations of Redfield relaxation theory [216], this can be described in terms of two types of effect; additional terms in the system Hamiltonian (coherent effects), and relaxation (i.e., effects that are incoherent and irreversible).

Coherent level broadening

In this subsection we apply the perturbation treatment to a general heteronuclear spin system in order to "increase" its size and try to introduce physically "coherent level broadening". As an example of coherent level broadening we consider a general heteronuclear system of spins $I_n S_m$ and treat the heteronuclear coupling between the I and S spins as a perturbation to the evolution of the S spin system, neglecting the effect of homonuclear coupling between the I spins. We have already developed this perturbation treatment in Section 4.5, thus we consider the case where $\|E_i - E_j\| \gg \|H_{IS}\|$, where E_i are the eigenvalues of the unperturbed S spin system, within the same M_z manifold. The effect of the coupling to the I spin system is thus to split each S spin level into a set of states distinguished by the state k of the I spin system. This is illustrated schematically in Fig. 4.13.

The expectation value of an S spin observable $\mathcal{O}$ must be summed over the states

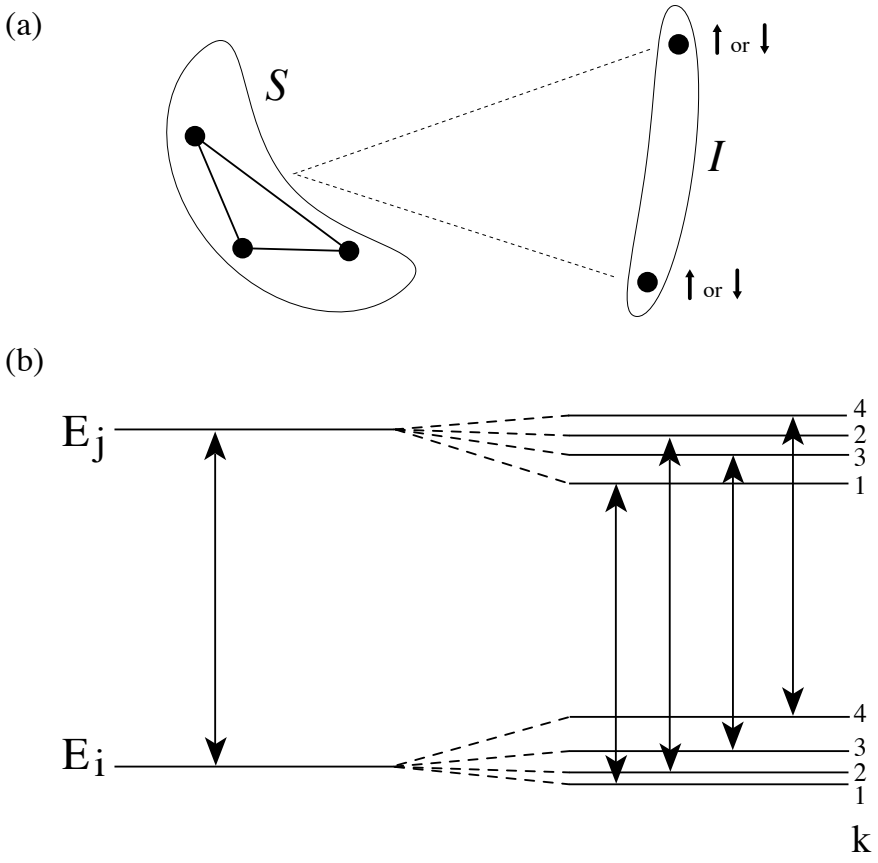

Figure 4.13: (a) Schematic representation for the coupling between the spin systems S and I. Each extraneous I spin having two possible orientations, splits the levels of the core S spin system. (b) Schematic diagram of energy levels before and after coupling. i and j are the manifolds corresponding to the unperturbed eigenvalues $E_i$and E_j for the S spins. The inclusion of the coupling to an external lattice, lifts the degeneracy of these levels. If the coupling is relatively weak and no coupling between the I spins is considered, the levels are not significantly mixed and only the transitions marked with arrows have non-zero transition probability.

of the lattice :

$$\begin{aligned}\langle\mathcal{O}\rangle(t) &= \sum_{i\neq j}\sigma_{ij}(0)\mathcal{O}_{ji}\sum_{k}\exp[-i(E_i-E_j+\varepsilon_i^k-\varepsilon_j^k)t] \\ &+ \sum_i \sigma_{ii}(0)\mathcal{O}_{ii}\end{aligned} \tag{4.79}$$

where ε_i^k is the perturbation of S spin level i corresponding to state k of the I lattice. These perturbations vary with i whenever the S spin Hamiltonian does not commute with H_{IS}, which is always the case for the systems of interest. In the limit of a continuous distribution of perturbations (of zero mean), the first term of Eq. (4.79) dephases, leaving only the term containing the diagonal elements. In other words, the quasi equilibrium is identical to that obtained from the isolated system (see Eq. (4.59), but the time scale of the approach to quasi equilibrium should now be physically realistic. Thus, we find that *the heteronuclear dipolar couplings to the lattice in organic solids provide a mechanism for the approach to quasi equilibrium.*

Note that this mechanism is coherent in the sense that it is fully time reversible. The first term in Eq. (4.79) corresponds to a *dephasing* rather than a *decay* of coherences. The quantum-statistical entropy of the system is therefore constant. Thus, if the sign of the effective Hamiltonian is inverted a polarization echo should arise. This is consistent with experimental demonstrations of the time reversibility of spin diffusion [65]. Unfortunately, Eq. (4.79) cannot be exactly simulated for large core spin systems because of the large number of states involved. However, we can replace the individual state perturbations by a line-shape function to give:

$$\begin{aligned}\langle\mathcal{O}\rangle(t) &= \sum_{i\neq j}\sigma_{ij}(0)\mathcal{O}_{ji}\int\exp\{-i[E_i-E_j+\omega]t\}\,\varepsilon_{ij}(\omega)\,\mathrm{d}\omega \\ &+ \sum_i \sigma_{ii}(0)\mathcal{O}_{ii}\end{aligned} \tag{4.80}$$

$\varepsilon_{ij}(\omega)$ is, in effect, the lineshape for the transition between levels i and j. This expression can be evaluated exactly (within the limits already imposed by perturbation theory on Eq. (4.79) for a large number of I spins, at the expense of losing the labeling of the I spin states. Such *simulations* are thus not time reversible, however, unlike the evolution of the full spin system.

The lineshape function can be determined for real solids by successive convolution of a starting delta function with the spectrum due to the effective dipolar coupling, d_{ij}^l, to each heteronuclear spin, l, for transition ij. This can be done very efficiently in the time-domain by multiplying their Fourier transforms, i.e. cosine functions:

$$\varepsilon_{ij}(\omega)=\prod_l^{\otimes}[\delta(\omega-d_{ij}^l/2)+\delta(\omega+d_{ij}^l/2)]=\mathrm{FT}\left[\prod_l\cos(d_{ij}^l t)\right] \tag{4.81}$$

We find from crystal structures that the resulting lineshape functions ε_{ij} are indeed continuous distributions, as shown in Fig. 4.14. These lineshapes were calculated

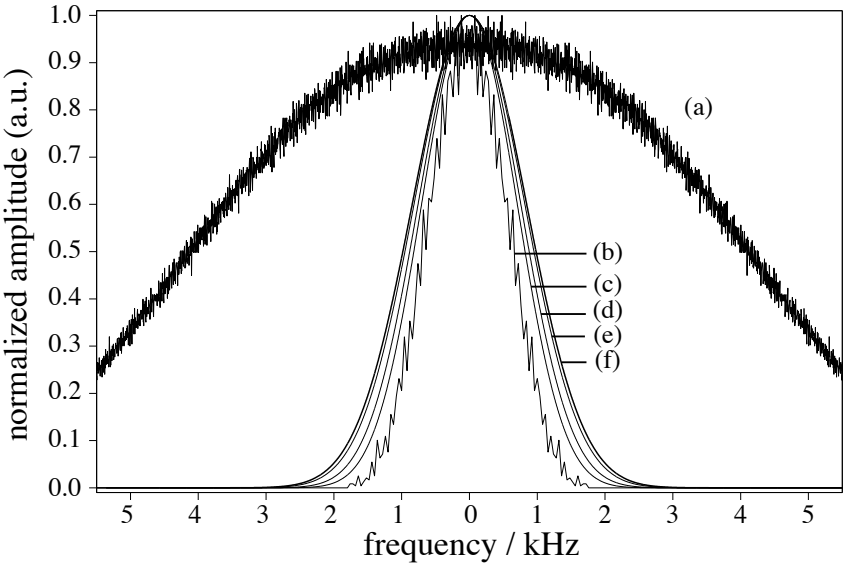

Figure 4.14: Lineshapes due to heteronuclear dipolar couplings for the carbonyl carbon in L-alanine calculated from crystallographic data using Eq. (4.81). (a) Broadening due to all the hydrogens within a radius of 4 Å. Broadening due to all the hydrogens within the shell between (b) 4 and 5 Å, (c) 4 and 6 Å, (d) 4 and 7 Å, (e) 4 and 10 Å, (f) 4 and 20 Å. The lineshape of (f) has essentially converged. From Ref. [217].

from the crystal structure of L-alanine [207] and include up to 2186 spins, corresponding to all the hydrogen spins within a radius of 20 Å. The lineshapes were calculated for the carbonyl carbon, but we find that the linewidths due to couplings with hydrogens outside a 4 Å radius are always continuous once a sufficient number of hydrogens is included. The lineshape is roughly Gaussian, as expected, although the exact form is not important for the quasi equilibrium.

Incoherent broadening

In order to complete the picture we need to include the effects of relaxation. The connection between quasi equilibrium and relaxation has recently been explored for a rather particular relaxation mechanism in the liquid state [218,219]. The situation is somewhat different in solids since molecular motion is efficiently suppressed and, as a result, the T_1 relaxation rate, which is proportional to the spectral density at the Larmor frequency, is very slow. Transverse T_2 relaxation is related to the spectral density at zero frequency, e.g. from random fluctuations of the local dipolar field, and is relatively efficient on the millisecond time scales of interest. In magnetisation exchange (spin diffusion) experiments, the appropriate time constant is T_2^{ZQ} which describes phenomenologically the decay of zero-quantum coherences [167]. The effect of adding such transverse relaxation is to put the system in contact with an infinitely large reservoir [220], and so the spin system is driven towards the state of internal thermal equilibrium of Eq. (4.74).

The mechanism of "coherent broadening" described in the previous Section leads to the *dephasing* of elements that are off-diagonal in the eigenbasis of the total system Hamiltonian. In contrast, relaxation involves the *destruction* of elements that are off-diagonal in the eigenbasis of the Zeeman Hamiltonian. This second process is irreversible and results in an increase in entropy.

Hence we expect the observability of the quasi equilibrium (as opposed to the internal thermal equilibrium) to be governed by the relative magnitude of these coherent and incoherent effects. *If the linewidth due to the coherent dipolar broadening is larger than that due to relaxation, then the quasi equilibrium should be experimentally observable.* In cross-polarization experiments, the relevant time constant is $T_{1\rho}$ rather than T_2. Since $T_{1\rho}$ is significantly longer than typical T_2 values, it is thus not surprising that quasi equilibria have been experimentally observed during such experiments [65, 197, 211, 221]. On the other hand, if the relaxation linewidth is larger than the linewidth due to the dipolar broadening, the internal thermal equilibrium state will be reached before quasi equilibrium can be established; this is expected to be the case in ^{13}C proton-driven spin diffusion experiments in ordinary organic solids. This would probably mean that the final state of the system in such experiments is governed by relaxation rather than coherent effects from its Hamiltonian.

Numerical Simulations

Single Crystals These ideas are illustrated by the numerical simulations of Fig. 4.15, in which we consider exchange of magnetisation along a linear chain of four equally spaced ^{13}C nuclei. The density operator at time zero corresponds to one unit of magnetisation on the first spin C1:

$$\sigma(0) = I_{1z} \tag{4.82}$$

and the Hamiltonian of this spin system is:

$$H = \sum_{n<m} d_{nm}(3I_{nz}I_{mz} - \vec{I}_n \cdot \vec{I}_m) \tag{4.83}$$

where the dipolar couplings d_{nm} were calculate from its geometry. No chemical shift differences were included, rendering the system (and the quasi equilibrium values for the expectation values) symmetric with respect to the center of the chain. Hence, the internal thermal equilibrium value of the C1 magnetisation is 1/4, whereas the quasi-equilibrium value calculated from Eq. (4.80) is 0.303. We see from Fig. 4.15(a) that the isolated system does not reach any steady state over a 20 ms time scale. If, however, we apply a Gaussian broadening of 25 Hz to the eigenlevels, the quasi-equilibrium is clearly reached, Fig. 4.15(b). Relaxation can be included (very simplistically), by damping the zero-quantum coherences with the time scale set by T_2^{ZQ}. In this case the system evolves towards internal thermal equilibrium, Fig. 4.15 (c).

Fig. 4.16 shows the frequency spectra of the time evolution for these three cases. Fig. 4.16(a) was obtained directly by summing the amplitudes of each transition, $\sigma_{ij}(0)\mathcal{O}_{ji}$, for each transition frequency $E_i - E_j$. It is identical to a Fourier transform of the time evolution, as can be seen from Eq. (4.80). The intensity of the zero frequency component is, by definition, identically equal to the expectation value at quasi equilibrium. In Fig. 4.16(b) we see that the broadening in the energy levels has the effect of broadening all the lines in the zero-quantum spectrum, apart from the zero frequency peak, i.e., the quasi equilibrium is unchanged. In the final spectrum, Fig. 4.16(c), where zero-quantum relaxation has been applied, all the transitions are broadened, and the intensity of the zero-frequency peak corresponds to the internal thermal equilibrium value of the observable.

Powders The orientational averaging required to calculate the magnetisation exchange for powder samples causes the time response to be smoothed. This is, of course, unrelated to the evolution of the individual spin systems; the resulting quasi equilibrium is now an orientational average, but is still distinct from the internal thermal equilibrium (which is independent of orientation). It is interesting to note that the calculation of the quasi equilibrium is very slightly "unstable" for powder samples due to the tiny fraction of orientations for which the Hamiltonian is accidentally degenerate. This instability occurs whenever the quasi equilibrium is distinct from the (well defined) internal thermal equilibrium, and applies equally well to the simulation of the time evolution in the absence of relaxation.

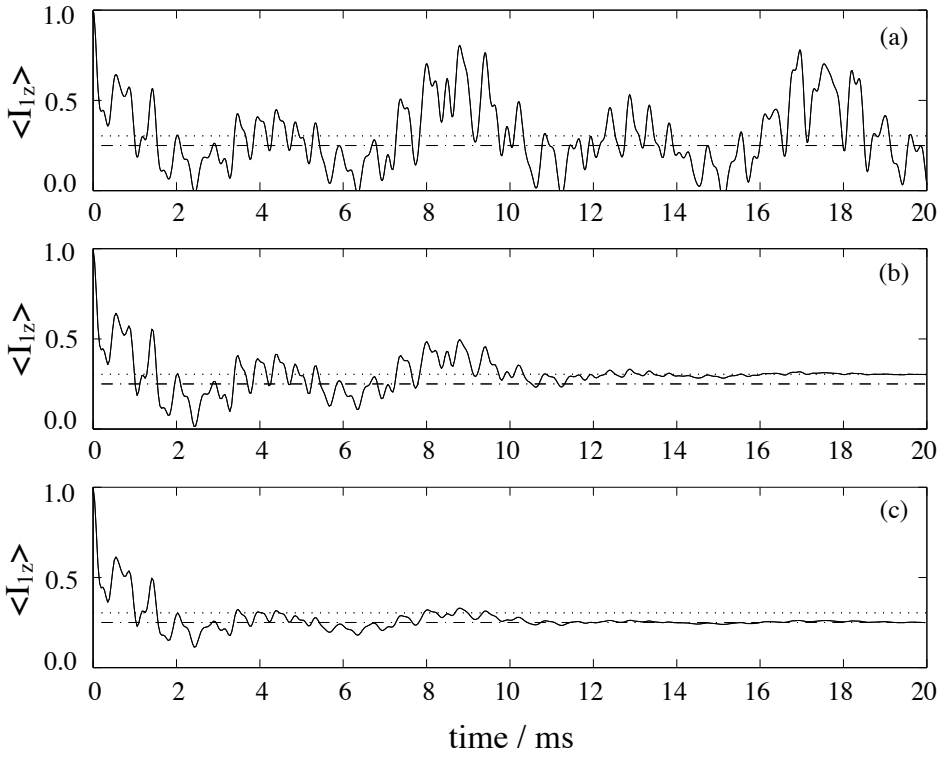

Figure 4.15: Numerical simulations of spin diffusion in a linear chain of four ^{13}C nuclei aligned with the z axis. The distance between two neighbours is 1.5 Å, and the initial magnetisation lies on the first spin. (a) Evolution only under the dipolar Hamiltonian; the quasi-equilibrium value (straight dotted line) is not reached. (b) Evolution in the presence of a Gaussian broadening of 25 Hz of the eigenlevels; the quasi-equilibrium state is reached. (c) Evolution in the presence of zero-quantum transverse relaxation, $T_2^{\mathrm{ZQ}} = 3\,\mathrm{ms}$; the final state of the system is the internal thermal equilibrium (dashed-dotted line). From Ref. [217]

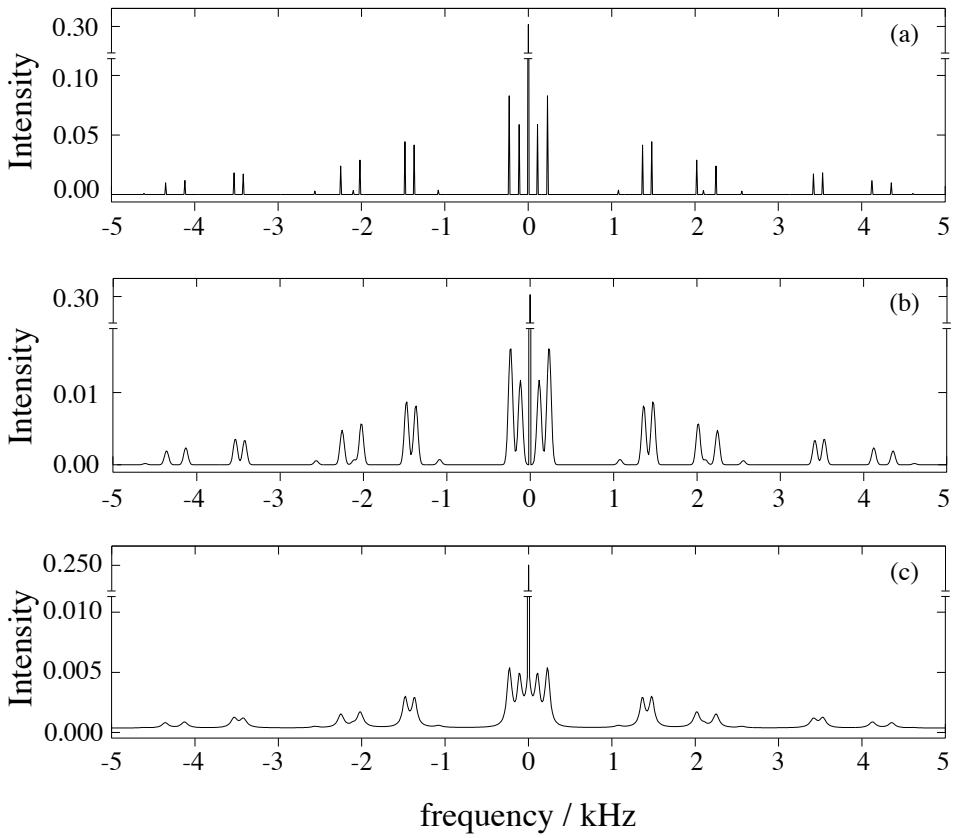

Figure 4.16: Histograms corresponding to inverse Fourier transforms of the time-domain signals of Fig. 4.15. See the text for discussion. From Ref. [217]

4.6.2 Time-Periodic Hamiltonians

Spinning of the sample about the "magic angle" and/or performing a periodic multiple pulse rf irradiation is of fundamental importance in solid-state NMR. Hence it is important to consider the situation of a periodically time-dependent Hamiltonian. The most effective approach for analysing this problem is in terms of Floquet theory. The application of Floquet theory to spectroscopy and magnetic resonance in particular has been comprehensively described elsewhere [222–226] and it will only be outlined here. In essence, the time-dependent terms such as the Hamiltonian, the density matrix, etc. are expanded as Fourier series with respect to the periodicity frequency ω_{mod}:

$$H(t) = \sum_{n=-\infty}^{\infty} H_n e^{in\omega_{\mathrm{mod}}t} \tag{4.84}$$

We then define a time-independent Floquet Hamiltonian, H_F, with matrix elements:

$$\langle pn|H_F|qm\rangle = n\delta_{nm}\delta_{pq} + \langle p|H_{n-m}|q\rangle. \tag{4.85}$$

The resulting matrix is infinite since each spin state p, is now "dressed" by a Fourier mode index $n = -\infty \ldots \infty$, to give a Floquet state $|pn\rangle$. The density matrix and observable operators can also be converted to Floquet representations [226]:

$$\langle pn|\mathcal{O}_F|qm\rangle = \langle p|\mathcal{O}|q\rangle\delta_{nm} \tag{4.86}$$

The evolution of this Floquet density matrix $\sigma_F(t)$, is now simply:

$$\sigma_F(t) = U_F(t)\sigma_F(0)U_F^{-1}(t) \tag{4.87}$$

where $U_F(t) = \exp(iH_F t)$. Note how the finite-dimensional time-dependent problem has been converted into an infinite-dimensional time-independent one. Fortunately, in numerical work it is possible to truncate the Floquet representation at a finite Fourier order $n_{\max}$. Roughly speaking the fewer the number of spinning sidebands in the MAS spectrum, the smaller the minimum dimensionality of the Floquet matrices.

Diagonalisation of the Floquet Hamiltonian yields the eigenvalues, λ_n^p, and eigenstates, $|\lambda_n^p\rangle$:

$$H_F|\lambda_n^p\rangle = \lambda_n^p|\lambda_n^p\rangle. \tag{4.88}$$

The eigenvalues always obey the relation $\lambda_n^p = \lambda_0^p + n\omega_{\mathrm{mod}}$, i.e. we need only consider the unique set of "fundamental" eigenvalues $\lambda^p \equiv \lambda_0^p$.

The expectation value of an observable operator $\mathcal{O}$ is then:

$$\begin{aligned}\langle\mathcal{O}\rangle(t) = \mathrm{Tr}[\sigma_F(t)\mathcal{O}_F] &= \sum_{p,q}\sum_{n=-\infty}^{+\infty}\langle\lambda_n^p|\mathcal{O}_F|\lambda_0^q\rangle\exp[i(\lambda^p-\lambda^q)t]\exp(in\omega_{\mathrm{mod}}t)\\ &\times \sum_{m=-\infty}^{+\infty}\langle\lambda_0^q|\sigma_F(0)|\lambda_m^p\rangle.\end{aligned} \tag{4.89}$$

Coherent broadening

We can now consider the effect of adding the lattice in terms of a line broadening of eigenlevels due to the heteronuclear dipolar couplings, in analogy to subsection 4.6.1, with the sole difference that the line broadening is being applied to eigenstates of the Floquet Hamiltonian. Again we assume that degeneracies can be neglected and that the coupling can be described in terms of first order perturbation theory. Note that the case of rotational resonance is not a problem for this treatment since it is simply a degeneracy between initial Floquet states $|pn\rangle$ and not in general a degeneracy between final Floquet states λ_n^p [223].

As before, a continuous broadening of the eigenlevels results in the cancellation of the terms $\exp[i(\lambda^p - \lambda^q)t]$ for $p \neq q$, and so the predicted quasi-equilibrium value of the observable $\mathcal{O}$ is given by:

$$\langle \mathcal{O} \rangle_{\mathrm{qe}}(t) = \sum_p \sum_{n=-\infty}^{+\infty} \langle \lambda_n^p | \mathcal{O}_F | \lambda_0^p \rangle \exp(in\omega_{\mathrm{mod}} t) \sum_{m=-\infty}^{+\infty} \langle \lambda_0^p | \sigma_F(0) | \lambda_m^p \rangle. \tag{4.90}$$

In terms of a Floquet density matrix for the S spins (i.e. summing over the I spin states), σ_F^{qe} is diagonal, and can be described as a "Floquet locked state" [224]. Such a state does not evolve under the Floquet Hamiltonian:

$$[H_F, \sigma_F^{\mathrm{qe}}] = 0. \tag{4.91}$$

It will, in general, be periodically time-dependent when transformed back into the ordinary Hilbert space, with the motion of the state synchronised with the Hamiltonian modulation (sample rotation in MAS).

Incoherent broadening

As in the static case, relaxation is expected to take the system towards internal thermal equilibrium. In terms of the Floquet density matrix, this corresponds to *damping* of the non-secular off-diagonal terms in the original basis, in contrast to the "coherent broadening" described above which causes the *dephasing* of terms that are non secular with respect to the I spin Hamiltonian eigenbasis.

This is demonstrated in the numerical simulations of Fig. 4.17. We consider a system of two homonuclear ^{13}C coupled spins having a non-negligible isotropic chemical shift difference under MAS. The Hamiltonian can be written:

$$H(t) = \Omega_1 I_{1z} + \Omega_2 I_{2z} + d(t)(3I_{1z}I_{2z} - \vec{I_1} \cdot \vec{I_2}). \tag{4.92}$$

The chemical shift difference ensures that the Hamiltonian is homogeneous, i.e., $[H(t), H(t')] \neq 0$ and so any observed periodicity cannot be simply ascribed to exact refocusing of the evolution. As for the static case, the magnetisation starts on C1 (see Eq. (4.82)) and we observe the evolution of the C1 magnetisation as a function of time. As Fig. 4.17 (a) shows, the undamped spin system does not

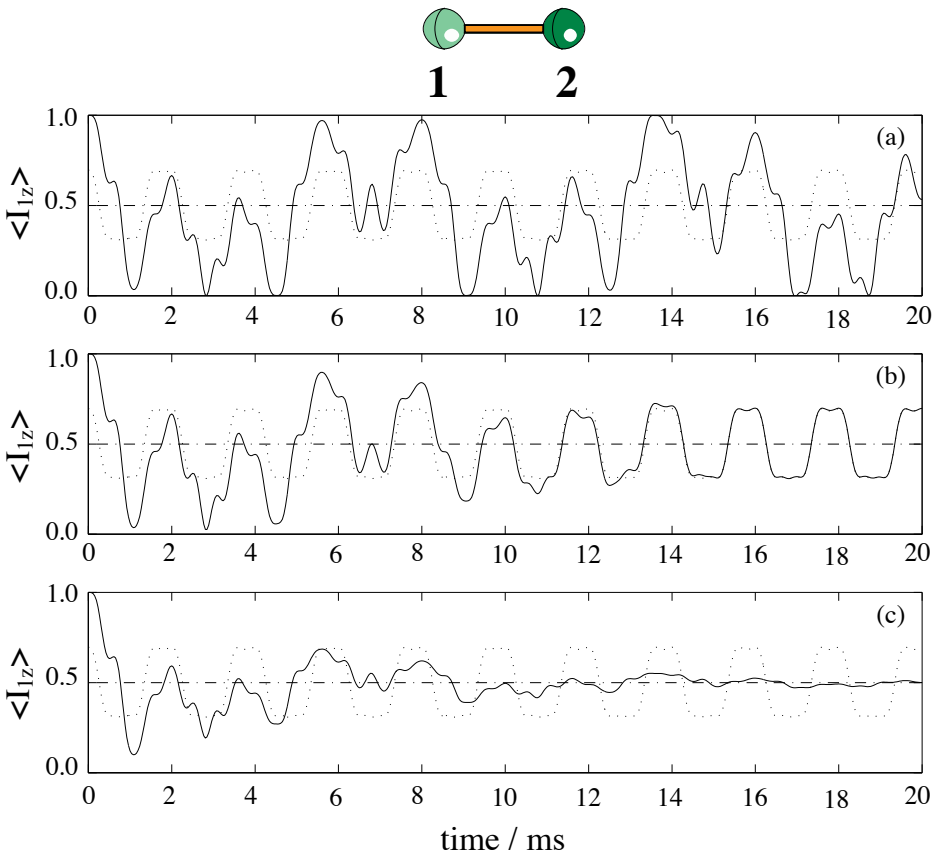

Figure 4.17: Simulation of the evolution of a two spin system under MAS. The two ^{13}C nuclei are separated by 1.73 Å and are oriented along the (1, 1, 1) vector in a crystal frame oriented at $(\alpha, \beta, \gamma) = (0,\ 35°,\ 0)$ with respect to the rotor frame. A time-independent chemical shift difference of 648 Hz is included and the spinning speed is $\omega_r/2\pi = 500\,\text{Hz}$. The initial magnetisation lies on the C1 carbon. The evolution is simulated in a Floquet space truncated at Fourier order $n_{\max} = 10$. (a) Evolution under the Hamiltonian. (b) Evolution in the presence of a Gaussian broadening of 25 Hz of the Floquet eigenstates; a periodic state is quickly established which corresponds to the predicted periodic quasi equilibrium (dotted curve). (c) Evolution in the presence of zero-quantum relaxation, $T_2^{\text{ZQ}} = 3\,\text{ms}$; the final state is the internal thermal equilibrium state (dot-dashed line). From Ref. [217].

reach a stationary state. If, however, a Gaussian broadening of 25 Hz is applied to the Floquet eigenlevels, the system rapidly attains the periodic quasi equilibrium predicted by Eq. (4.90) and demonstrated in Fig. 4.17 (b). In Fig. 4.17(c), T_2 relaxation is added by simple damping of the off-diagonal terms of the density matrix during the time evolution, and the system rapidly approaches the internal thermal equilibrium. A fuller treatment of the T_2 relaxation [227] would no doubt modify the time dependence slightly, but the overall approach towards thermal equilibrium would not be changed. Note that the same pattern of behaviour is observed in simulations of larger spin systems and so the results cannot be attributed to any special character of the two spin system.

4.6.3 Observation of Periodic Quasi Equilibria

The "Periodic Quasi Equilibria" [217] or so-called "Floquet Locked States" [224] that we predict in the previous Section, are expected to be physically observable in situations where relaxation is negligible compared to the coherent coupling of the spin system with the lattice. These conditions are satisfied during the cross-polarization (CP) step in CP/MAS NMR experiments. Indeed, very recently, numerical simulations of moderate size spin systems (6 spins) based on the Floquet formalism have appeared in the literature [228] showing phenomenologically periodic quasi-equilibria as predicted in [217].

In this Section experimental results are presented that confirm these predictions. Experiments are performed on powder samples of ferrocene and L-alanine. The short time behaviour ($\tau_{\mathrm{CP}} < 1$ ms) consists of oscillations with a frequency proportional to the heteronuclear dipolar coupling between ^{1}H and ^{13}C [95]. However, in all cases, the long time behaviour ($\tau_{\mathrm{CP}} > 5$ ms) consists of oscillations with multiples of the rotor frequency. We show that the effect can be very pronounced, even in ordinary organic solids.

Cross Polarization under MAS

Since the introduction of the cross-polarization methodology [6, 70] in solid-state NMR, many discussions have been presented in the literature in order to yield physical insight into the dynamics and thermodynamics of spin systems [64, 65, 155, 196, 197, 210, 211, 229–233]. In the most simple terms, the CP spin dynamics can be understood as the approach to a thermodynamic equilibrium between the "cold" bath of protons and the "hot" bath of the rare spins [64, 70, 210]. A modified thermodynamic description has been introduced to describe special cases of consecutive equilibrations [211], in the case where one can recognize several constants of the motion. Combination of CP with MAS provided the conditions necessary for the development of high resolution solid state NMR [234], but complicated the spin dynamics and thermodynamics [155, 220, 230, 235]. Recent experiments have clearly shown the time reversible character of the CP evolution which reveals continuing

coherent behaviour several ms after the beginning of the process [232]. This is related to general ideas about the time reversibility of polarization transfer spin dynamics [65, 233].

In what follows we will use numerical simulations based on the perturbative model we developed in Section 4.5 for cross-polarization spin dynamics. In order to apply this model to CP/MAS experiments we consider here the core system to contain only one ^{1}H and one ^{13}C nuclei for simplicity. The Hamiltonian of this two spin system, in the doubly rotating tilted frame [211], can be written (neglecting scalar couplings):

$$H(t) = \omega_{1I} I_z + \omega_{1S} S_z + d_{IS}(t) I_y S_y = \sum_{n=-\infty}^{+\infty} H_n e^{in\omega_r t} \tag{4.93}$$

where ω_{1I} is the rf field on the abundant nucleus (i.e. ^{1}H), ω_{1S} is the rf field on the rare nucleus (i.e. ^{13}C or ^{15}N etc), $d_{IS}(t)$ the time dependent dipolar coupling between the two nuclei, and ω_r is the rotation frequency. The time dependence is introduced by MAS. The Hamiltonian $H(t)$ can be expanded in a Fourier series with components H_n. Since the Hamiltonian is time periodic, we choose to treat the problem in the Floquet space. The static and MAS CP Hamiltonian can always be decomposed into uncoupled zero-quantum (23), and double-quantum (14) subspaces:

$$H(t) = \begin{array}{c} \\ \langle\alpha\alpha| \\ \langle\alpha\beta| \\ \langle\beta\alpha| \\ \langle\beta\beta| \end{array} \begin{array}{c} \begin{array}{cccc} |\alpha\alpha\rangle & |\alpha\beta\rangle & |\beta\alpha\rangle & |\beta\beta\rangle \end{array} \\ \begin{pmatrix} \Sigma & 0 & 0 & -d_{IS}(t)/4 \\ 0 & \Delta & d_{IS}(t)/4 & 0 \\ 0 & d_{IS}(t)/4 & -\Delta & 0 \\ -d_{IS}(t)/4 & 0 & 0 & -\Sigma \end{pmatrix} \end{array} \tag{4.94}$$

So does the Floquet Hamiltonian of Eq. (4.93) that describes CP under MAS. We assume $\omega_{1I}, \omega_{1S} \gg d_{IS}$ so that only zero-quantum transitions are relevant. The structure of the zero-quantum CP Floquet Hamiltonian is presented in the Table 4.4. The definitions of the different constants are:

$$\Delta = \frac{\omega_{1I} - \omega_{1S}}{2}, \quad \Sigma = \frac{\omega_{1I} + \omega_{1S}}{2} \tag{4.95}$$

$$d_{\pm 1} = -\frac{\mu_0 \gamma_I \gamma_S \hbar}{4\pi r_{IS}^3} \frac{1}{4\sqrt{2}} \sin(2\theta) \exp(\pm i\phi), \tag{4.96}$$

$$\text{and} \quad d_{\pm 2} = \frac{\mu_0 \gamma_I \gamma_S \hbar}{4\pi r_{IS}^3} \frac{1}{8} \sin^2(\theta) \exp(\pm 2i\phi). \tag{4.97}$$

where θ and ϕ are the polar angles defining the orientation of the internuclear vector with respect to the rotor axis system. Under MAS the modified Hartmann-Hahn (HH) conditions for zero-quantum cross polarization can be written as:

$$\omega_{1I} = \omega_{1S} + f\omega_r, \quad f = \pm 1, \pm 2. \tag{4.98}$$

Using secular approximations, it was shown that the evolution of S spin magnetization under CP gives rise in the frequency domain to two different Pake-like patterns depending on the matching condition used ($f = \pm 1, \pm 2$) [95]. In our study, the influence of non-secular terms (terms that do not commute with the rf field Hamiltonian [95]) is taken into account. In this case the Floquet Hamiltonian has to be diagonalized explicitly and the evolution of the S magnetization is calculated using Eq. (4.79).

Relaxation can be included either by damping phenomenologically all the off-diagonal matrix elements of the density matrix in the Zeeman basis set [217], or by using an average Liouvillian technique [236] or even by using a stochastic Liouvillian [219]. Transverse relaxation drives the spin system to internal thermal equilibrium, and longitudinal relaxation drives the system towards thermal equilibrium with the lattice. This is not altered by the presence of MAS since MAS can not significantly modify the populations. Periodic rf perturbations can however modify the position of the steady state [236]. This does not alter fundamentally the picture as relaxation always leads to a steady state which can be characterized as an internal thermal equilibrium state. This is the result of incoherent (i.e. time irreversible) process.

Coherent level broadening

We now consider the case of an extended I spin lattice coupled with the core spin system. This core system can in principle include an arbitrary number of I and S nuclei. Usually the number of nuclei in the core is limited by the size of the matrices to be diagonalized (numerically). The total Hamiltonian can be written:

$$H_{\text{tot}} = H_{IS}^{\text{core}} + H_{\text{lat}} \tag{4.99}$$

H_{IS} contains the core Hamiltonian of Eq. (4.93), and H_{lat} will contain the couplings of the system with the lattice and the couplings inside the lattice. In the case of weak dipolar couplings we can treat this by first order perturbation theory. In this limit H_{lat} will contain only the dipolar couplings d_n of the S spin of the core system with all the other I spins in the lattice. If V is the eigenbasis of the core Hamiltonian then $VH_{IS}^{\text{core}}V^\dagger = \Lambda$, where Λ is the diagonal eigenvalue matrix. In the expanded spin space the total Hamiltonian (in this case for a two-spin core system) can be expressed as :

$$VH_{\text{tot}}V^\dagger = \Lambda + VH_{\text{lat}}V^\dagger = \Lambda + \sum_n d_n \left(VI_{ny}S_yV^\dagger\right) \tag{4.100}$$

If we calculate the evolution of S spin polarization within this perturbative limit [217], we see that the presence of the perturbation acts as a dephasing of the off-diagonal coherences driving the system to a state of quasi equilibrium. For the periodic time dependent Hamiltonian considered here, the same discussion applies in the appropriate Floquet space. The presence of the coupling with the lattice broadens the Floquet eigenlevels, and the system is driven into a state that can be written as a linear combination of Floquet constants of motion $|A_k^F\rangle$:

$$|\sigma^F\rangle = \sum_k |A_k^F\rangle\langle A_k^F| \tag{4.101}$$

The Floquet constants of motion are defined as all the operators that commute with the Floquet Hamiltonian, in analogy to the constants of the motion of a time independent Hamiltonian [64, 155]. The state defined by Eq. (4.101) is termed a Floquet locked state [224] since it commutes with the Floquet Hamiltonian, and is therefore stationary in Floquet space. When transformed back in ordinary Hilbert space this state presents a periodic time dependence, synchronised with the rotor frequency, and leads to what we term a periodic quasi equilibrium.

The perturbative broadening of the Floquet eigenstates can in principle be calculated and there is no physical reason why all the eigenstates should be broadened in the same way. In this Section we will approximate this coherent effect by a single Gaussian broadening in the appropriate space [217]. The question which now arises is whether or not these states can be observed experimentally.

$\cdots$	$\lvert\alpha\beta,-2\rangle$	$\lvert\beta\alpha,-2\rangle$	$\lvert\alpha\beta,-1\rangle$	$\lvert\beta\alpha,-1\rangle$	$\lvert\alpha\beta,0\rangle$	$\lvert\beta\alpha,0\rangle$	$\lvert\alpha\beta,+1\rangle$	$\lvert\beta\alpha,+1\rangle$	$\lvert\alpha\beta,+1\rangle$	$\lvert\beta\alpha,+2\rangle$	$\cdots$
$\lvert\alpha\beta,-2\rangle$	$\Delta-2\omega_r$			d_1		d_2					
$\lvert\beta\alpha,-2\rangle$		$-\Delta-2\omega_r$	d_1		d_2						
$\lvert\alpha\alpha,-1\rangle$		d_1^*	$\Delta-\omega_r$			d_1		d_2			
$\lvert\beta\beta,-1\rangle$	d_1^*			$-\Delta-\omega_r$	d_1		d_2				
$\lvert\alpha\alpha,0\rangle$		d_2^*		d_1^*	Δ			d_1		d_2	
$\lvert\beta\beta,0\rangle$	d_2^*		d_1^*			$-\Delta$	d_1		d_2		
$\lvert\alpha\alpha,+1\rangle$				d_2^*		d_1^*	$\Delta+\omega_r$			d_1	
$\lvert\beta\beta,+1\rangle$			d_2^*		d_1^*			$-\Delta+\omega_r$	d_1		
$\lvert\alpha\alpha,+2\rangle$						d_2^*		d_1^*	$\Delta+2\omega_r$		
$\lvert\beta\beta,+2\rangle$					d_2^*		d_1^*			$-\Delta+2\omega_r$	
$\cdots$											$\cdots$

Table 4.4: Since the Floquet matrices have an infinite size, for numerical studies, we are obliged to truncate them to a maximum Fourier order $n_{\max}$. This table shows the Floquet zero-quantum CP Hamiltonian truncated at $n_{\max} = 2$.

4.6.4 Experimental

If $\omega_1 \gg h_{\text{local}}$ (well spin locked magnetization), where h_{local} represents the dipolar local field and ω_1 the spin locking rf field, then the I spin magnetization will not decay with the transverse dephasing time T_2^* but rather with a spin lattice relaxation time $T_{1\rho}$ which is relatively long [237]. Thus, we expect that the periodic quasi-equilibria should be observable in ordinary CP experiments before being damped by relaxation.

We have performed variable contact time CP experiments on powder samples of ferrocene and L-alanine. The ferrocene sample was purchased from Sigma Chemicals and cocrystallised with 1% cobaltocene in order to reduce its T_1 relaxation time to about 10 s. Cocrystallisation was performed in an acetone solution which was evaporated under inert gas environment to avoid oxidation of the cobaltocene. All experiments were performed on a DSX500 Bruker NMR spectrometer equipped with a Bruker 4mm triple resonance MAS probe. The sample volume was restricted in length to improve the radio-frequency field homogeneity.

Due to the fast molecular rotation on the NMR time scale of the C_5H_5 rings in ferrocene, the homonuclear and heteronuclear intra-ring interactions are scaled by a factor two[6], and the inter-ring interactions are also reduced. This spin system can therefore be well approximated by a core two-spin system in weak contact with its lattice, as in our theoretical model.

CP build-up curves at different HH matching conditions are presented for ferrocene in Fig. 4.18. One can clearly see that the system rapidly reaches a "steady-state" which is periodic from about 2 ms and continues without decaying. The Fourier transforms of $\langle S_z \rangle_{final} - \langle S_z \rangle$ for the different matching conditions are given in Fig. 4.19. $\langle S_z \rangle_{final}$ was set to the signal average over the last 20 points in the build-up curve. We observe that there are always strong narrow frequency components at multiples of the rotor frequency. These components confirm the existence of a periodic quasi-equilibrium state. Once this state established, the amplitude of the oscillations does not change over the acquisition time since the state is a constant of the motion. This stationary state is expected to have a lifetime related to $T_{1\rho}$, which is very long in the CP case. Since there is no significant decay of the periodic quasi equilibrium state, the phase of these peaks after FT is not well defined (even if the phase of the magnetization at $\tau_{\text{CP}} = 0$ is well defined). Thus the phase of the peaks depends sensitively on the number of points taken in the FT (which is intrinsically cyclic). Adjusting the number of points by ± 1 can have a large effect on the phase. Here we chose the number of points used in the FT in order to have spikes in phase with the central Pake-like patterns (corresponding to a total acquisition time which is an integral number of rotation periods). Apodizing the signal would give an identical result, at the expense of broadening the peaks. These signals are not

[6]The angle between the rotation axis $\mathcal{C}_5$ and the chemical bonds (dipolar PAS) is $\pi/2$. Because the rotation is fast on the NMR time scale we have the right to replace the time dependent dipolar couplings by their time averages: $\overline{d(t)} = \mathcal{P}_2[\cos(\pi/2)]\, d = d/2$

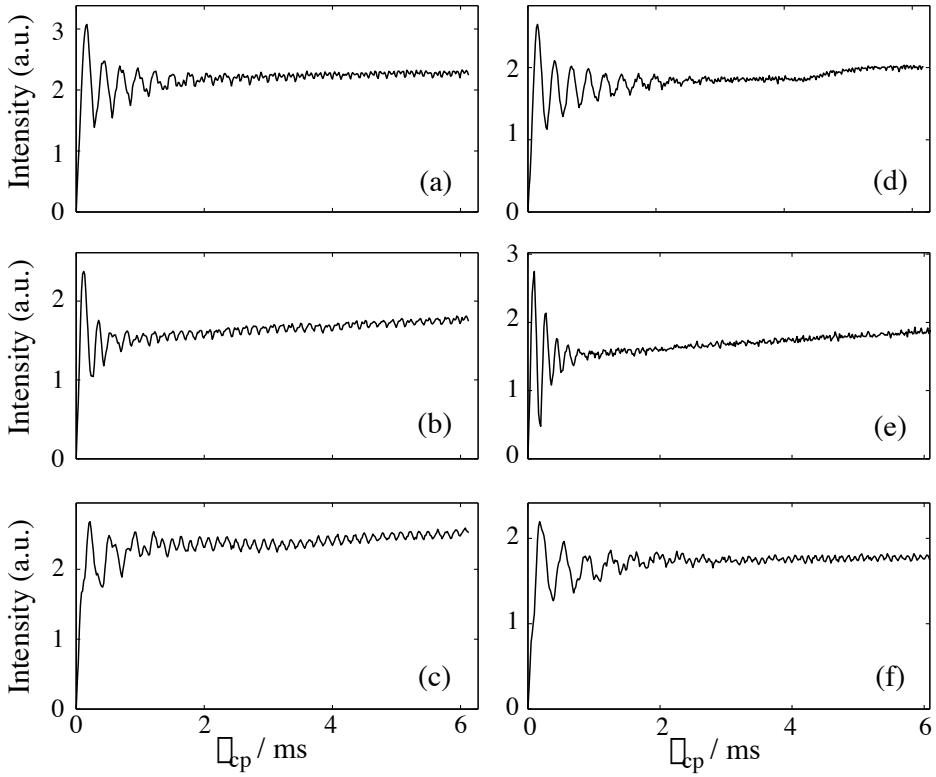

Figure 4.18: Evolution of the carbon signal intensity observed for ferrocene as a function of variable CP contact times. The initial transient oscillations are damped within several ms and the spin system is driven towards a periodic state which is synchronised with the rotation (clearly visible between 2 and 6 ms). For curves (a), (b) and (c) the rotor frequency $\omega_r/(2\pi)$ was set to 7 kHz for HH matching conditions of $f = 1$, 1.5 and 2 (see Eq. (4.98)) respectively. For curves (d), (e) and (f) $\omega_r/(2\pi)$ was 10 kHz and $f = 1$, 1.5 and 2 respectively. ω_{1S} was kept constant at $\omega_{1S}/(2\pi) = 55$ kHz while ω_{1I} was varied is order to satisfy the various matching conditions. The signal was recorded by incrementing τ_{CP} in steps of 16.6 μs for (a,b,c) and 16.1 μs for (d,e,f). The signal was observed with 32 scans per increment, using an 8 step phase cycle to select only coherences originating from ^{1}H. From Ref. [238].

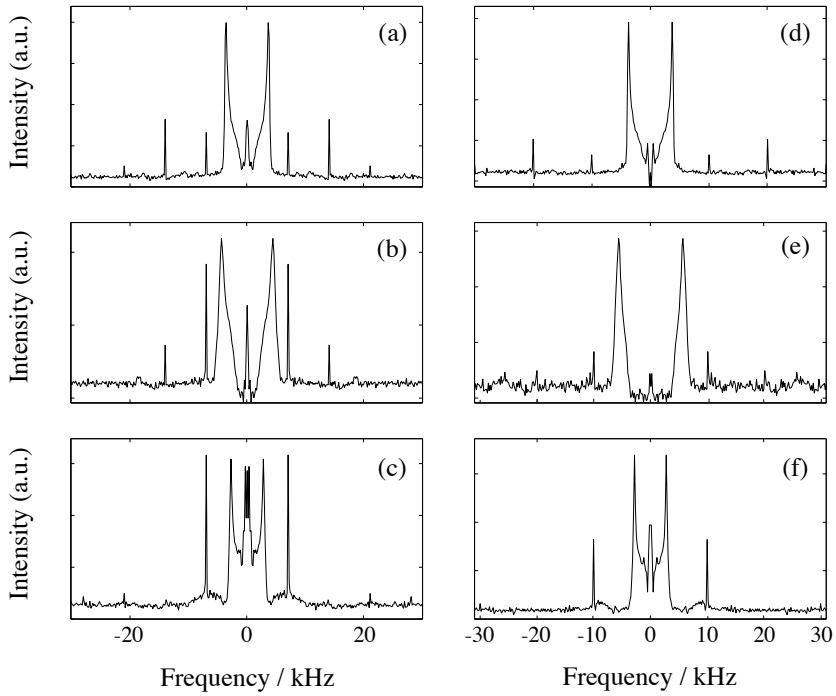

Figure 4.19: Fourier transforms of the curves shown in the Fig. 4.18 after removal of the offset. The Pake-like patterns are related to the initial transient oscillations. In addition, narrow spectral components are present at multiples of the rotor frequencies revealing the existence of periodic quasi-equilibrium states. The phase of these signals depends on the number of points we transform because the oscillations are not significantly damped within 6 ms. 369 points were used for (a,b,c) and 372 for (d,e,f). The signal to noise ratio is better for (a,c,d,f) because of the exact matching. In the cases (b) and (e) the influence of mismatch gives rise to larger Pake-like patterns. From Ref. [238].

zero-filled, so there are no "wiggles" present in the figures. Note that zero-filling induces wiggles but does not change the phase properties in the frequency domain.

For the $f = 1.5$ matching condition the mismatch of the fields with respect to the rotation frequency results in the introduction of extra offset-like terms, which increase the frequency of the transient oscillations and the width of the Pake-like pattern, but do not change the frequencies of the periodic quasi equilibrium signals which depend only on ω_r. This shows clearly that the peaks are associated with periodic quasi equilibria, and that they are not merely "non-secular" effects [95] as defined above (which can be seen in the broad sidebands observed clearly in Figures 4.19(c) and 4.19(f)). In order to confirm the ω_r dependence the experiments in Figures 4.18 and 4.19 were performed at two different spinning frequencies, 7 kHz and 10 kHz.

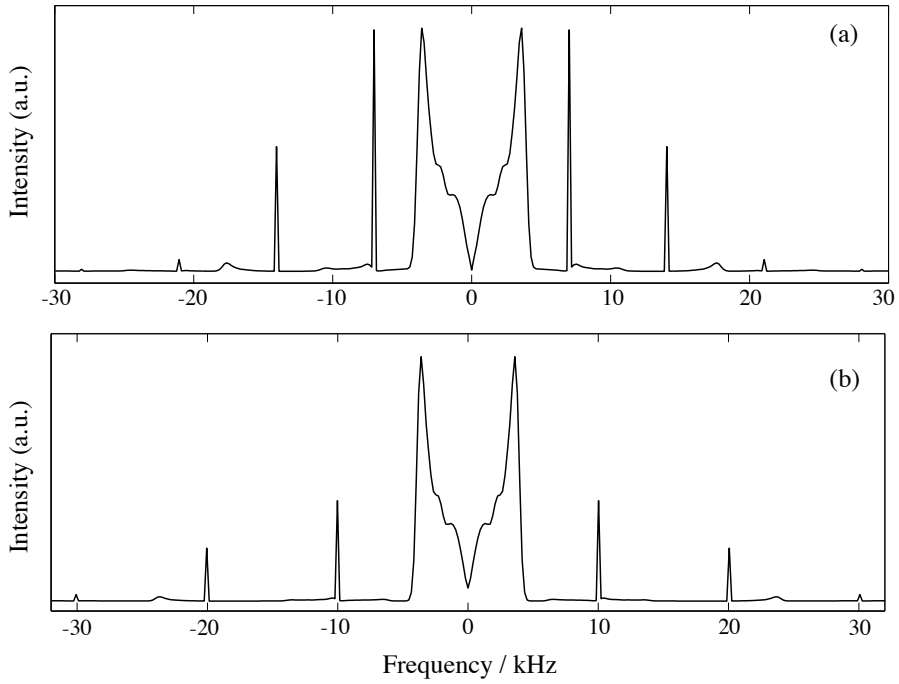

Figure 4.20: Fourier transforms of numerically simulated S spin evolution calculated as described in the text. $\omega_{1S}/(2\pi)$ was set to 50 kHz and the maximum Floquet order in the calculation was $n_{\max} = 8$. A uniform Gaussian broadening of 25 Hz was applied to all Floquet eigenstates. The integration over ω in Eq. (4.102) was carried out in 100 steps with $\omega_{\max}/(2\pi) = 50$ Hz. The spectra were calculated for the matching condition $f = 1$ and for (a) $\omega_r/(2\pi) = 7$ kHz and (b) $\omega_r/(2\pi) = 10$ kHz. 369 and 372 points were used in the FT respectively. From Ref. [238].

Fig. 4.20 shows numerical simulations, comparable to the experimental data of Figures 4.19(a) and 4.19(d). We simulated a core two spin system by diagonalizing numerically H^F and calculating Eq. (4.89). In order to have numerically converged eigenvalues, we set the maximum order in the Floquet expansion to 8, and only the fundamental eigenstates $|\lambda_0^q\rangle$ and eigenvalues λ_0^q for all four states q were kept. No secular approximations were made. The full set of eigenvalues and the Diagonalisation matrix V were constructed according to the method described by Schmidt and Vega [223]. Although direct propagation [117] is usually more efficient, we used the Floquet formalism in order to include the Gaussian broadening of the Floquet eigenstates. A powder average over 2000 equally spaced crystallite orientations was performed in order to compare the numerical results with experimental data on a powder sample. The distance between $I(^1\mathrm{H})$ and $S(^{13}\mathrm{C})$ nuclei was 1.41 Å, the spinning frequencies were $\omega_r/(2\pi) = 7$ kHz, 10 kHz respectively and the matching condition was $f = 1$. The presence of extraneous I spins was approximated by a coherent Gaussian broadening applied to all the Floquet transitions. This is carried out numerically by evaluating the following expression :

$$\begin{aligned}\langle S_z\rangle(t) &= \frac{1}{\Delta_{pq}\sqrt{2\pi}}\sum_{p,q}\int_{-\omega_{\max}}^{+\omega_{\max}} d\omega \sum_{n=-n_{\max}}^{+n_{\max}} \langle\lambda_n^p|S_z^F|\lambda_0^q\rangle \exp[-\omega^2/(2\Delta_{pq}^2)] \\ &\times \exp\{i(\lambda^p - \lambda^q + \omega)t\}\exp(in\omega_r t)\sum_{m=-n_{\max}}^{+n_{\max}} \langle\lambda_0^q|\sigma^F(0)|\lambda_m^p\rangle \qquad (4.102)\end{aligned}$$

in which we have effectively replaced each transition frequency by a large number of discrete transitions weighted by a Gaussian density of states with a fixed width $\Delta_{pq}/(2\pi) = 25$ Hz. In Eq. (4.102) there is the possibility for each transition to have a different width Δ_{pq}, although we used a constant width in the simulations. Fig. 4.20 shows the FT of the S spin evolution, after removal of the $\langle S_z\rangle_{final}$ offset. The results predict the rotor synchronised periodic quasi-equilibrium states observed experimentally.

We have seen from the discussion above that ferrocene is an "ideal" sample, since it fits fairly well into the approximations made in the theory section. However, we note that the breakdown of these approximations, made for theoretical convenience, should not have too much impact on the underlying physical process, so we expect periodic quasi equilibria to be observable in a wide range of systems. For example, the spin system in L-alanine is closer to an "ordinary" organic solid because the homonuclear ^{1}H–^{1}H dipolar interaction is strong. Fig. 4.21 shows the results from the same CP experiments for a powder sample of L-alanine, where we observe that the signal of the (rigid) CH carbon presents some initial transient oscillations and at longer times oscillates at multiples of ω_r. We note that the substantial periodic quasi equilibria signals observed in Fig. 4.21(b) are now slightly broadened by the decay due to a much shorter $T_{1\rho}$ than in ferrocene (the lifetime of the periodic quasi equilibria is given by $T_{1\rho}$). In spite of the various approximations made in the theory, the periodic quasi equilibria are striking, even in ordinary compounds. However, if

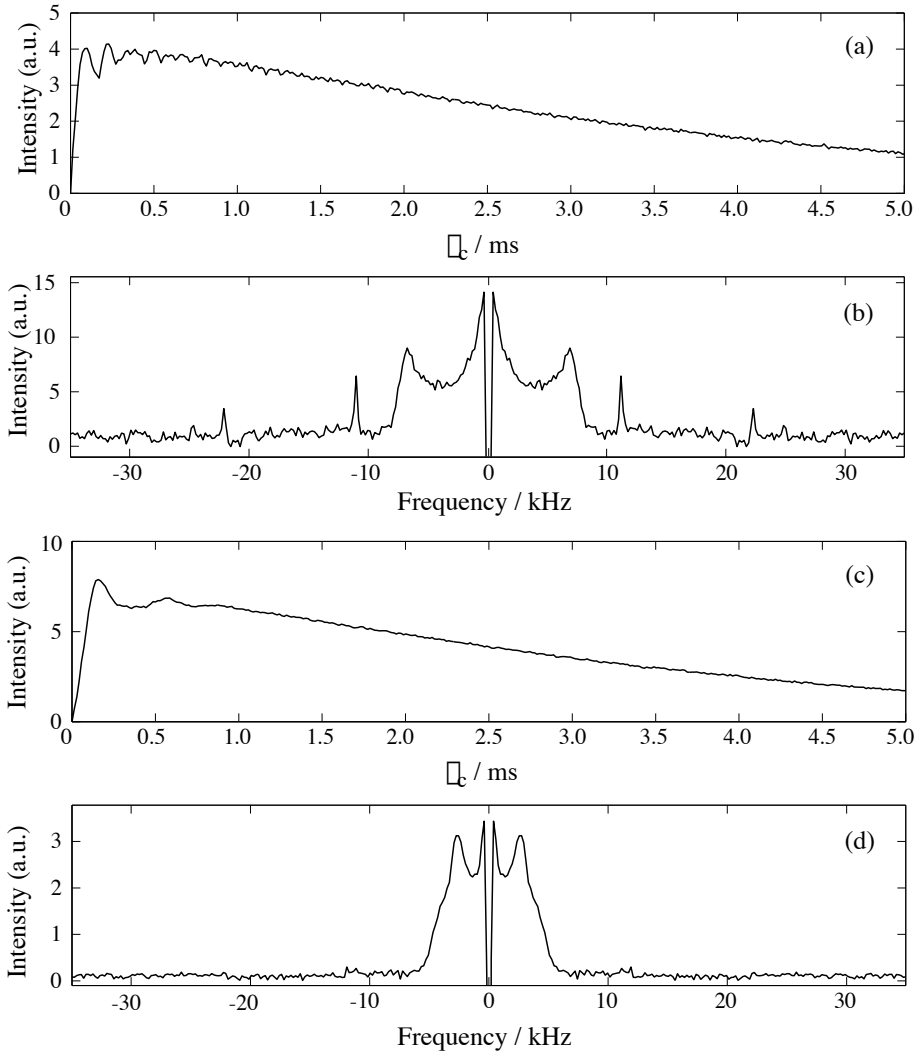

Figure 4.21: Variable contact time CP–MAS experiments for a powder sample of L-alanine. $\omega_r/(2\pi)$ was set to 11 kHz and the matching condition $f = 1$ was satisfied with $\omega_{1I} = 50$ kHz. (a) Time dependence of the CH carbon signal intensity as a function of the CP contact time. The first transient oscillations indicate the presence of a strong heteronuclear dipolar coupling with the bonded hydrogen nucleus. Very rapidly ($\tau_{\mathrm{CP}} < 0.5$ ms) the system gets locked into a state oscillating with the rotor which is then damped over several ms. These oscillations are clearly revealed in the FT spectrum shown in (b) as sharp resonances at multiples of the rotor frequency (the negative spike at zero frequency comes from the offset removal of the slowly decaying signal in (a)). The Pake-like pattern yields the CH dipolar coupling. The signal intensity of the methyl group carbon presented in (c), has similar initial behaviour, with lower frequency transient oscillations but no significant long time synchronised oscillation as seen in (d). The signal was recorded by incrementing τ_{CP} in steps of 14.3 μs, with 64 scans per increment, using an 8 step phase cycle to select only coherences originating from ^{1}H. 359 points were used in the FT. From Ref. [238].

$T_{1\rho}$ is short we expect a consequent damping of the synchronised oscillations since the system starts to behave as a thermodynamic bath. This is observed for the carbon signal of the CH_3 group of L-alanine, where the situation is aggravated by the relatively strong homonuclear ^{1}H–^{1}H dipolar coupling when compared to the heteronuclear ^{1}H–^{13}C one. In consequence, the amplitude of the periodic quasi equilibrium is negligibly small. We believe that a more detailed description of the core spin system for a CH_3 group would account for the absence of periodic quasi equilibria. Note finally that the periodic quasi equilibria are likely to be more pronounced in CP-MAS experiments under homonuclear ^{1}H decoupling.

4.6.5 Conclusions

Although the concept of quasi equilibrium has been frequently invoked in solid-state NMR to describe the behaviour of relatively small spin systems, the manner in which this quasi equilibrium is reached has received less attention. For completely isolated spin systems it is clear that simple coherent evolution under the system Hamiltonian does not lead to an equilibrium state [67]. Consequently, coupling to the external lattice must be included to explain the appearance (if at all) of quasi-equilibrium states. We have shown how a weak coupling to the external lattice allows a small spin system to approach quasi equilibrium within in a time scale set by the effective level broadening due to the coupling. However, relaxation is simultaneously driving the system towards internal thermal equilibrium. Hence the observability of quasi equilibrium depends on the relative linewidths introduced by the "coherent" and "incoherent" broadenings. In other words, its observability depends on the relative importance of first order effects of far away spins compared to second order effects of nearby spins.

This helps to explain why quasi-equilibrium states have been frequently proposed, and indeed observed, for cross-polarization experiments in which the ($T_{1\rho}$) relaxation processes are relatively slow. By contrast, in classic spectral spin diffusion experiments where the magnetisation is being exchanged between homonuclear spins in the absence of spin-locking, relaxation (T_2^{ZQ}) is more efficient and the systems evolve smoothly towards internal thermal equilibrium. We could hope to observe quasi equilibrium, however, by modifying the spin-diffusion experiment, for example by forcing the magnetisation exchange to occur under a spin-lock, i.e. the RF-driven spin-diffusion experiment [239].

These conclusions have been extended to the case of a rotating sample, in which case we predict a periodic quasi equilibrium, that is a time-dependent state whose Fourier series with respect to the rotor frequency is static. To prove these predictions variable contact time CP-MAS experiments on powder samples of ferrocene and L-alanine and they show a long time behaviour which is oscillatory at multiples of the rotor frequency. This is the first example of a direct connection between experimental spin thermodynamic properties and theoretical predictions made using *ab initio* spin dynamics calculations. These periodic quasi-equilibrium states have

undoubtedly been observed previously, but never, to our knowledge, recognised as such [95]. The amplitude of these states is often surprisingly large and the effect seems to be widespread. It is not limited to special samples, and we have observed these effects in ordinary organic solids. In the example we have considered the periodicity of the quasi equilibria is due to MAS. However, they should be present in any long time signal originating from a time periodic Hamiltonian (such as in multiple-pulse decoupling experiments [3, 240, 241]), and observable provided that relaxation is slow enough.

We note that it would obviously be interesting to correlate these quasi equilibria with structural characteristics. However, due to the influence of a great number of spins, this is probably not practical. On the other hand, these experimentally observable effects on the spin thermodynamics reflect subtle coherent effects due to the quantum nature of the spin system. In particular, they provide better understanding of the behaviour of spin systems under time-dependent interactions. They could provide an interesting window for the study of reversibility [65, 232, 233] and related phenomena in relatively complex quantum systems.

4.7 Periodic Spin Systems

4.7.1 Introduction

As we have seen above, the dynamics of systems of multiple spins raises many fundamental questions, not least how the behaviour of the system changes between the quantum behaviour of an isolated group of spins and the classical behaviour of a large network of coupled spins. Unfortunately, as we have previously seen exact simulation rapidly becomes intractable as the number of spins increases, and so exact simulations are currently limited to small numbers of spins [242] or to very simple spin systems where analytical solutions are possible [243, 244]. On the other hand numerical simulation restricts the spin system to include nuclei from the immediate environment and completely neglect the effects of far away spins. Usually such effect were "included" by adding a T_2 damping rendering the simulation dynamics time irreversible. Most importantly, effects due to the periodicity of the crystal lattice, would be completely lost in standard numerical simulation.

The idea we will to develop in this Section is based on the inclusion of spatial periodicity in numerical simulations. Spatial periodicity constitutes the corner stone of solid-state physics, since the band theory for electronic spins is a direct consequence of this property [245]. The advantages would be that the description of spin dynamics would be more accurate since the periodic boundary conditions would account for the crystal structure of solid-state crystalline compounds. Then, the efficiency of exact calculations would be greatly improved if symmetry of the system permitted the block-diagonalisation of the Hamiltonian and the density matrix. Here we propose the exploition of the translational symmetry of crystalline systems to achieve this "factorization". As well as allowing larger systems to be studied (or smaller

systems to be studied more efficiently), this symmetry constrains the problem in a physically meaningful way, making it easier to frame well-posed questions.

The principles of block-diagonalisation through symmetry are familiar in NMR from molecular systems where the point group of a molecule is used to factorise the nuclear spin Hamiltonian of isolated molecular systems [246–248]. Similarly, exact spin dynamics have been studied for systems such as one-dimensional chains or rings of spins [67, 214, 215, 244, 249] that have partial or complete translational symmetry. To our knowledge, however, this translational, i.e. *space* group, symmetry has been used only sparsely for treating a small number of nuclear spins [250, 251]. Translational symmetry is, of course, widely used in other applications in solid-state physics that deal with electron spins [195, 252, 253]. For example, the dynamics of *electron* spins has been extensively studied for the XXZ Hamiltonian, which has the same form as the dipolar coupling Hamiltonian for nuclear spins (apart from excluding all but nearest-neighbor couplings), [254] and references therein. In contrast to nuclear spin systems, however, electron spin states are generally strongly correlated at normal temperatures, and it is only in the extreme "high temperature" limit that the system reduces to a form comparable to the nuclear spin case. Low temperature nuclear spins behave the same way as electron spins and a wave theory is possible [255].

Another point of difference from existing work is that we consider the lattice points to be occupied by a general nuclear spin system (i.e. a molecule). The usual case of a linear chain (for one-dimensional systems) with a single spin at each lattice point is a somewhat special case which is very sensitive to breaking of the symmetry due to defects [256] or lattice distortion [67]. It is worth noting, however, that the framework developed here can also be applied to the primitive lattices.

4.7.2 Formal Theory

We define the Hamiltonian of the periodic system:

$$\mathcal{H}_{\text{sys}} = \sum_n \mathcal{H}_n + \frac{1}{2}\sum_{n,m} \mathcal{H}_{n,m} \tag{4.103}$$

where $\mathcal{H}_n$ accounts for the Hamiltonian of the n^{th} crystal unit cell and $\mathcal{H}_{nm}$ for the Hamiltonian of the interactions between the n^{th} and m^{th} crystal unit cells.

The translation operator T

We now consider a basis set for this system:

$$B = \left\{ |\Psi\rangle = \cdots |S, k_S\rangle \cdots = \prod_S |S, k_S\rangle \right\} \tag{4.104}$$

where S indicates the crystal unit cell and runs from 0 to $N-1$ and k_S indicates the state of the system S. This state can be or not an eigenstate of the system. We assume periodic boundary conditions for the crystal units i.e.:

$$|S+N, k_{S+N}\rangle = |S, k_S\rangle \tag{4.105}$$

As an example we give here the Zeeman basis set for 3 unit cells each containing 2 spins:

$$B = \{|\Psi\rangle = |0, \epsilon_1\epsilon_2\rangle|1, \epsilon_1'\epsilon_2'\rangle\ |2, \epsilon_1''\epsilon_2''\rangle\} \tag{4.106}$$

where any $\epsilon = \{\alpha, \beta\}$. We can compact the notation omitting the labels of the unit cells and writing the general state as: $|\epsilon_1\epsilon_2, \epsilon_1'\epsilon_2', \epsilon_1''\epsilon_2''\rangle$. The dimension of B, for this spin system, is 64.

We now define an operator (translation operator) T_+ that *relabels* the crystal units keeping the same states:

$$\begin{aligned} T_+|\Psi\rangle &= T_+ \cdots |S-1, k_{S-1}\rangle|S, k_S\rangle|S+1, k_{S+1}\rangle \cdots & (4.107)\\ &= e^{i\phi} \cdots |S-1, k_S\rangle|S, k_{S+1}\rangle|S+1, k_{S+2}\rangle \cdots & (4.108)\end{aligned}$$

where $e^{i\phi}$ is a phase factor without relevance in what we are interested [195] and in what follows is replaced by 1. By analogy we can define a backwards translation operator T_- that performs :

$$\begin{aligned} T_-|\Psi\rangle &= T_- \cdots |S-1, k_{S-1}\rangle|S, k_S\rangle|S+1, k_{S+1}\rangle \cdots & (4.109)\\ &= e^{-i\phi} \cdots |S-1, k_{S-2}\rangle|S, k_{S-1}\rangle|S+1, k_S\rangle \cdots & (4.110)\end{aligned}$$

T_- is the inverse operator of T_+ and from now on we will use only the T_+ operator, named for convenience T.

We can calculate the matrix elements of T in the basis set of Eq. (4.104):

$$\begin{aligned} \langle\Psi_i|T|\Psi_j\rangle &= \prod_{S,S'}\langle S, k_S^i|T|S', k_{S'}^j\rangle & (4.111)\\ &= \prod_{S,S'}\langle S, k_S^i|S', k_{S'+1}^j\rangle \\ &= \prod_{S}\langle S, k_S^i|S, k_{S+1}^j\rangle \\ &= \prod_{S}\delta(k_S^i, k_{S+1}^j) & (4.112)\end{aligned}$$

Some properties:

- The T operator is unitary but not hermitian.

- The effect of the unitary T transformation is "translation": $T^\dagger \mathcal{H}_n T = \mathcal{H}_{n+1}$

The proof of the first property is obvious, while the proof of the second follows. We consider k to be eigenstates of the first part of the total Hamiltonian of Eq. (4.103). We then have :

$$\begin{aligned}
\langle \Psi_i | T^\dagger \mathcal{H}_n T | \Psi_j \rangle &= \prod_{S,S'} \langle S, k^i_{S+1} | \mathcal{H}_n | S', k^j_{S'+1} \rangle && (4.113)\\
&= \prod_{S \neq n} \langle S, k^i_{S+1} | S', k^j_{S'+1} \rangle \langle n, k^i_{n+1} | \mathcal{H}_n | n, k^j_{n+1} \rangle && (4.114)\\
&= \prod_{S \neq n} \delta(k^i_{S+1}, k^j_{S+1}) \delta(k^i_{n+1}, k^j_{n+1}) E_{n+1} && (4.115)\\
&= E_{n+1} \prod_S \delta(k^i_S, k^j_S) && (4.116)\\
\langle \Psi_i | T^\dagger \mathcal{H}_n T | \Psi_j \rangle &= \prod_{S,S'} \langle S, k^i_S | \mathcal{H}_{n+1} | S', k^j_{S'} \rangle && (4.117)\\
&= \prod_{S \neq n+1} \langle S, k^i_S | S, k^j_S \rangle E_{n+1} \langle S, k^i_{n+1} | S, k^j_{n+1} \rangle && (4.118)\\
&= E_{n+1} \prod_S \delta(k^i_S, k^j_S) && (4.119)
\end{aligned}$$

so:

$$T^\dagger \mathcal{H}_n T = \mathcal{H}_{n+1} \tag{4.120}$$

We can define a factorizable translation superoperator [257] $\hat{\hat{\mathrm{T}}}$ which acts as: $\hat{\hat{\mathrm{T}}} | \mathcal{H}_n \rangle = | \mathcal{H}_{n+1} \rangle$. Of course since T is not hermitian, $\hat{\hat{\mathrm{T}}}$ is also non-hermitian. We shall also prove that $T^\dagger \mathcal{H}_{m,n} T = \mathcal{H}_{m+1,n+1}$. Consider k to be any state of the basis, then:

$$\begin{aligned}
\langle \Psi_i | T^\dagger \mathcal{H}_{m,n} T | \Psi_j \rangle &= \prod_{S,S'} \langle S, k^i_{S+1} | \mathcal{H}_{m,n} | S', k^j_{S'+1} \rangle && (4.121)\\
&= \prod_{S \neq m, S \neq n} \langle S, k^i_{S+1} | S, k^j_{S+1} \rangle \times \\
&\times \langle m, k^i_{m+1} | \langle n, k^i_{n+1} | \mathcal{H}_{m,n} | m, k^j_{m+1} \rangle | n, k^j_{n+1} \rangle && (4.122)\\
\langle \Psi_i | T^\dagger \mathcal{H}_{m,n} T | \Psi_j \rangle &= \prod_{S,S'} \langle S, k^i_S | \mathcal{H}_{m+1,n+1} | S', k^j_{S'} \rangle && (4.123)\\
&= \prod_{S \neq m+1, S \neq n+1} \langle S, k^i_S | S, k^j_S \rangle \times && (4.124)\\
&\times \langle m+1, k^i_{m+1} | \langle n+1, k^i_{n+1} | \mathcal{H}_{m+1,n+1} | m+1, k^j_{m+1} \rangle | n+1, k^j_{n+1} \rangle
\end{aligned}$$

but the interaction Hamiltonian is spatially periodic so are its matrix elements. Thus, we can conclude that $T^\dagger \mathcal{H}_{m,n} T = \mathcal{H}_{m+1,n+1}$.

Then we can write the total Hamiltonian as a sum of the translated one cell Hamiltonian plus of course its interactions:

$$\begin{aligned}
\mathcal{H}_{\text{sys}} &= \sum_{n=0}^{N-1} \mathcal{H}_n + \frac{1}{2} \sum_{n',m} \mathcal{H}_{n',m} && (4.125)\\
&= \sum_{n=0}^{N-1} T^{\dagger n} \mathcal{H}_0 T^n + \frac{1}{2} \sum_{p\neq 0}^{N-1} \sum_{n=0}^{N-1} T^{\dagger n} \mathcal{H}_{0,p} T^n && (4.126)\\
&= \sum_{n=0}^{N-1} T^{\dagger n} \left(\mathcal{H}_0 + \frac{1}{2} \sum_{p\neq 0}^{N-1} \mathcal{H}_{0,p} \right) T^n && (4.127)
\end{aligned}$$

From this decomposition it is obvious that the total Hamiltonian is invariant under translation $\hat{\hat{\mathrm{T}}} |\mathcal{H}_{\text{sys}}\rangle = |\mathcal{H}_{\text{sys}}\rangle$. Thus, for a perfectly crystalline system (neglecting edge effects), the system Hamiltonian in a homogeneous magnetic field, $\mathcal{H}_{\text{sys}}$, is invariant with respect to the unit cell translation operator T:

$$T \mathcal{H}_{\text{sys}} T^\dagger = \mathcal{H}_{\text{sys}} \Leftrightarrow [T, \mathcal{H}_{\text{sys}}] = 0 \qquad (4.128)$$

This symmetry will also apply to any additional radio-frequency terms, $\mathcal{H}_{\text{RF}}$, provided that any spatial inhomogeneities of the RF field are insignificant on the length scale of the periodicity. In the following, we consider only translation along a single axis e.g. T_x; extension to additional dimensions is straightforward. One other way of looking at the Eq. (4.128) is realize that *the system Hamiltonian commutes with the translation operator*. This means that common eigenvectors to both operators can be found, a property that is capital in what follows.

Although block-diagonalisation due to translational symmetry will allow the Hamiltonian to be diagonalized with muchgreater efficiency, the overall improvement in efficiency of the calculation of the system evolution is only significant if the density matrix can be block-diagonalized in an identical fashion. In other words, we require that the *density matrix* also be periodic. This must be true at thermal equilibrium. (However, it is clearly not the case for systems prepared in spatially non-uniform states, e.g., for the study of *spatial* spin diffusion [163].) It is then straightforward to show that an initially periodic density matrix, evolving under the influence of a spatially periodic Hamiltonian, remains invariant under translation. Note that this symmetry does not require periodicity of the individual *states* of the nuclear spins, which would imply the states were strongly *correlated*. It simply means that *coherences*—probabilities that different spin states are occupied—are unchanged as the system is translated. This is distinct from the collective behaviour resulting from strong spin correlation, and is not affected by the breakdown of the usual high temperature assumption of NMR [258]. As long as a density matrix treatment is valid, i.e. the total spin system can still be regarded as a statistical

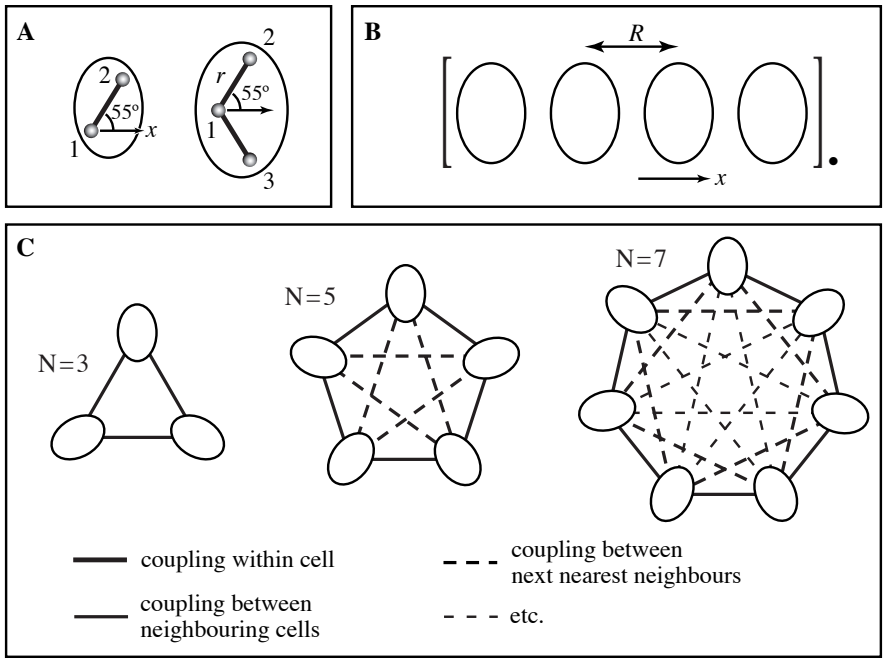

Figure 4.22: Schematic illustration of periodic one-dimensional spin-systems: (A) geometries of the two- ($M = 2$) and three-spin ($M = 3$) unit cell systems used, (B) geometry of the one-dimensional periodic system, (C) pattern of inter-cell couplings for $N = 3$, 5 and 7. To be truly periodic, the network of dipolar couplings, although calculated assuming a linear geometry (B), is considered to be cyclic. The static magnetic field, B_0, is oriented along the z-axis. From Ref. [204].

ensemble of (extended) systems, we would always expect the density matrix to be periodic in a periodic lattice. This picture will only break down for nuclear spins at extremely low temperatures.

Using numerical simulation, only a portion of the infinite crystal lattice can be simulated. To ensure translational symmetry, we must, therefore, impose periodic boundary conditions. As shown in Fig. 4.22, this means that the network of couplings between the spins must be identical under cyclic permutation of the lattice points. Both the density matrix and the Hamiltonian can then be block-diagonalized with respect to this "finite translation" symmetry. As we show below, this decreases the sizes of the matrices involved by a factor of about N, leading to a substantial improvement in efficiency which becomes more significant as N increases.

The particular problems considered below concern spin diffusion, that is, the exchange of z-magnetisation under the dipolar coupling Hamiltonian. Assuming a strong external magnetic field, and in the absence of RF irradiation, the Hamiltonian can immediately be factored into blocks of the same total magnetic quantum number,

M_z, as discussed in Section 4.4.2. Since we are dealing with the exchange of z-magnetisation, the initial density matrix and detection operators are diagonal and share this block structure. Hence it is only necessary to compute the evolution within the individual M_z blocks. For heteronuclear systems, M_z for each nuclear species will be a good quantum number, allowing further blocking. This block structure can be used with any free-precession Hamiltonian.

4.7.3 Simulations

In principle, we could calculate the matrix elements of the Hamiltonian and transform the resulting matrix (or matrices) into the translation symmetry adapted basis. This is, however, extremely demanding for large matrices, both in terms of time and memory. In order to extend the size of the spin systems we can consider, it is essential to compute diagonal blocks of the symmetrised Hamiltonian directly, i.e., to determine the matrix elements of $\mathcal{H}$ directly in the T eigenbasis. Fortunately, the simplicity of the T operator makes this relatively straightforward for a system of $I = 1/2$ spins.

Consider, for example, a system of four cells ($N = 4$) with one spin per cell ($M = 1$) and the initial state $|\alpha\alpha\alpha\beta\rangle$. The translation operator acting on this state would give $|\alpha\alpha\beta\alpha\rangle$ i.e. the spin states are permuted through M positions. Repeated application of this translation operator generates all the states linked by translation. In general, there will be N such states, but factors of N are also possible e.g. $|\alpha\alpha\alpha\alpha\rangle$ transforms into itself under translation. The states of the Hilbert space (or a subspace, such as the states of a given M_z) can thus be partitioned into sets of states linked by translation: $A = \{|\alpha\alpha\alpha\beta\rangle, |\alpha\alpha\beta\alpha\rangle, |\alpha\beta\alpha\alpha\rangle, |\beta\alpha\alpha\alpha\rangle\}$, $B = \{|\alpha\beta\alpha\beta\rangle|\beta\alpha\beta\alpha\rangle\}$ etc. If we consider the states of set A, then the translation operator for this subspace has the matrix representation:

$$T = \begin{array}{c} \\ \langle\alpha\alpha\alpha\beta| \\ \langle\alpha\alpha\beta\alpha| \\ \langle\alpha\beta\alpha\alpha| \\ \langle\beta\alpha\alpha\alpha| \end{array} \begin{array}{c} \begin{array}{cccc} |\alpha\alpha\alpha\beta\rangle & |\alpha\alpha\beta\alpha\rangle & |\alpha\beta\alpha\alpha\rangle & |\beta\alpha\alpha\alpha\rangle \end{array} \\ \begin{pmatrix} 0 & 1 & 0 & 0 \\ 0 & 0 & 1 & 0 \\ 0 & 0 & 0 & 1 \\ 1 & 0 & 0 & 0 \end{pmatrix} \end{array} \tag{4.129}$$

Since $T^4 = 1$, then the eigenvalues of T satisfy $\lambda^4 = 1$, i.e. $\lambda = 1$, i, -1, $-i$ or $\lambda = \exp(ik)$, where $k = 0$, $\pi/2$, π, $3\pi/2$ [195, 252]. In general, the eigenvectors and eigenvalues of the T operator for a set of n translation-linked states will be

$$\lambda_k = e^{2\pi ik/n} \tag{4.130}$$

$$V_{jk} = e^{2\pi i(j-k)/n}/\sqrt{n} \tag{4.131}$$

where $j, k = 0 \ldots n-1$.

To calculate the elements of the symmetrised Hamiltonian, we first need to calculate the Hamiltonian sub-matrix, $\mathcal{H}_{AB}$, for a given set of bra states linked by translation, A, and a given set of translation-linked ket states, B. For free-precession Hamiltonians, we need only consider sets A and B that have the same M_z value. For other Hamiltonians, it is necessary to consider other combinations. Note that we need to be able to calculate these sub-matrices elements directly, since it is impractical to calculate the Hamiltonian matrices for the complete Hilbert space using direct products of single-spin operators. This can be done using standard expressions for Hamiltonian matrix elements [259] and is particularly straightforward for systems composed entirely of spin-1/2 spins due to the natural correspondence between the number of spin states and binary arithmetic [203].

Given the Hamiltonian sub-matrix in the original (Zeeman) basis, $\mathcal{H}_{AB}$, the symmetrised Hamiltonian for the specific case considered above will be

$$\mathcal{H}_{aa} = V^{\dagger}\mathcal{H}_{AA}V = \begin{pmatrix} \mathcal{H}'_0 & 0 & 0 & 0 \\ 0 & \mathcal{H}'_1 & 0 & 0 \\ 0 & 0 & \mathcal{H}'_2 & 0 \\ 0 & 0 & 0 & \mathcal{H}'_3 \end{pmatrix} \tag{4.132}$$

where a denotes the symmetrised basis set corresponding to A, and the diagonal elements of the symmetrised Hamiltonian, $\mathcal{H}'_0$, $\mathcal{H}'_1$, $\mathcal{H}'_2$ and $\mathcal{H}'_3$, correspond to $k = 0$, $\pi/2$, π, $3\pi/2$ respectively. By definition, the elements linking states with different eigenvalues are zero [212]. Note how the symmetrised states are distributed evenly between the N different eigenvalues. This means that the individual eigenvalue blocks are close to a factor of N smaller than the original Hamiltonian block; the division is exact for prime N.

In general terms, the non-zero elements are given by:

$$\langle a_k|\mathcal{H}_{ab}|b_k\rangle = \sum_{p}^{n_A}\sum_{q}^{n_B} V^{\dagger}_{kp}\langle p|\mathcal{H}_{AB}|q\rangle V_{qk} \tag{4.133}$$

where the V matrices are given by Eq. (4.131) with $n = n_A$ (the number of states in set A) or n_B as appropriate.

This is repeated for all pairs of bra (a) and ket (b) sets in order to build up the complete Hamiltonian. The same procedure is then used to calculate the other matrices required i.e. the initial density matrix and the detection operator(s). Having calculated all these matrices in the symmetrised basis, the simulation can then proceed as normal.

It is important to note that it is only necessary to calculate the Hamiltonian for a single unit cell (say cell 0) and its couplings to the spins in the rest of the lattice, H^0. The corresponding Hamiltonian for cell 1 will be $TH^0T^{\dagger}$ and (taking care not to include couplings twice) the entire Hamiltonian will be:

$$H = \sum_{n}^{N} T^n H^0 T^{\dagger n} \tag{4.134}$$

where N is the number of unit cells. Since the translation-adapted states are eigenvectors of T, we find

$$\langle a_k|H|b_k\rangle = \sum_n^N \langle a_k|T^n H^0 T^{\dagger n}|b_k\rangle \quad (4.135)$$

$$= \sum_n \langle a_k|e^{ink} H^0 e^{-ink}|b_k\rangle \quad (4.136)$$

$$= N\langle a_k|H^0|b_k\rangle \quad (4.137)$$

Hence the non-zero matrix elements of the full Hamiltonian in the symmetrised eigenbasis, H, are identical (within a scaling factor of N) to those of the symmetrised "cell 0" Hamiltonian, H^0. From the linearity of Eq. (4.133), we can thus calculate the elements of the symmetrised Hamiltonian directly from H^0, rather than the full H whose elements become extremely slow to determine as the number of spins increases (due to the sheer number of dipolar couplings).

This is a significant computational detail, but it is also an important theoretical point which is relevant to the development of approximate models for many-spin systems. The addition of a unit cell to H cannot be treated in a simple perturbative fashion since the couplings to its neighbours are just as strong as the couplings between the existing cells. The addition of a remote cell to H^0 could, however, plausibly be treated as a perturbation, since it only involves the weak couplings connecting the new cell and unit cell 0. Clearly analytical work on periodic problems must be done using the symmetry-adapted basis.

As a more precise example let consider again the 6 spin system (see Fig. 4.23), with 3 unit cells each containing 2 spins. For this homonuclear spin system the Hamiltonian we consider contains all the dipolar couplings between all couples of spins. No chemical shift is included in order to simplify the analytic expressions, though inclusion of such terms would not alter the block-diagonalization procedure. We know that under the influence of the strong B_0 static magnetic field the obvious constant of the motion for this system is the z projection of the total magnetization. Thus, we can already block diagonalize the Hamiltonian according to the total M_z (eigenvalue of the F_z operator). For this spin system the 64×64 Hamiltonian can be split into 2 blocks 1×1 for the functions $|\alpha\alpha, \alpha\alpha, \alpha\alpha\rangle$ and $|\beta\beta, \beta\beta, \beta\beta\rangle$ having $|M_z| = 3$, 2 blocks 6×6 for the functions having $|M_z| = 2$, 2 blocks 15×15 for the functions having $|M_z| = 1$, and 1 block 20×20 for the functions having $M_z = 0$. Further block diagonalization can be performed using the periodicity of the Hamiltonian with respect to translation. We consider the first 6×6 block, for which $M_z = +2$. This block is generated by two subspaces containing 3 basis functions each that are not linked together by translation symmetry. In other words it is impossible to generate a function (or linear combination of functions) from the second subspace, by applying the translation operator on a function from the first subspace. These two subspaces are: $\mathcal{E}_1 = \{|\alpha\alpha, \alpha\alpha, \alpha\beta\rangle, |\alpha\alpha, \alpha\beta, \alpha\alpha\rangle, |\alpha\beta, \alpha\alpha, \alpha\alpha\rangle\}$ and $\mathcal{E}_2 = \{|\alpha\alpha, \alpha\alpha, \beta\alpha\rangle, |\alpha\alpha, \beta\alpha, \alpha\alpha\rangle, |\beta\alpha, \alpha\alpha, \alpha\alpha\rangle\}$. It is very important to note

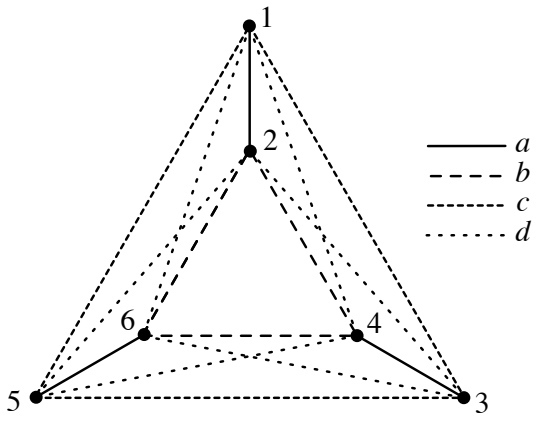

Figure 4.23: A six spin system having translation symmetry. Three unit cells are present each containing 2 homonuclear spins. All dipolar couplings are present, and the size of the different couplings is shown in the legend. These couplings were used for the analytical calculations that follow.

however, that coupling between these two subspaces exists trough the Hamiltonian, thus the 6×6 block is written:

$$H_6 = \frac{1}{2} \begin{array}{c} \begin{array}{cccccc} |\alpha\alpha,\alpha\alpha,\alpha\beta\rangle & |\alpha\alpha,\alpha\alpha,\beta\alpha\rangle & |\alpha\alpha,\alpha\beta,\alpha\alpha\rangle & |\alpha\alpha,\beta\alpha,\alpha\alpha\rangle & |\alpha\beta,\alpha\alpha,\alpha\alpha\rangle & |\beta\alpha,\alpha\alpha,\alpha\alpha\rangle \end{array} \\ \begin{pmatrix} a-b+3c+2d & -a & -b & -d & -b & -d \\ -a & a+3b-c+2d & -d & -c & -d & -c \\ -b & -d & a-b+3c+2d & -a & -b & -d \\ -d & -c & -a & a+3b-c+2d & -d & -c \\ -b & -d & -b & -d & a-b+3c+2d & -a \\ -d & -c & -d & -c & -a & a+3b-c+2d \end{pmatrix} \end{array} \tag{4.138}$$

The translation operator for the $M_z = +2$ block can be easily written:

$$T_6 = \begin{array}{c} \begin{array}{c} \langle\alpha\alpha,\alpha\alpha,\alpha\beta| \\ \langle\alpha\alpha,\alpha\alpha,\beta\alpha| \\ \langle\alpha\alpha,\alpha\beta,\alpha\alpha| \\ \langle\alpha\alpha,\beta\alpha,\alpha\alpha| \\ \langle\alpha\beta,\alpha\alpha,\alpha\alpha| \\ \langle\beta\alpha,\alpha\alpha,\alpha\alpha| \end{array} \\ \begin{pmatrix} 0 & 0 & 1 & 0 & 0 & 0 \\ 0 & 0 & 0 & 1 & 0 & 0 \\ 0 & 0 & 0 & 0 & 1 & 0 \\ 0 & 0 & 0 & 0 & 0 & 1 \\ 1 & 0 & 0 & 0 & 0 & 0 \\ 0 & 1 & 0 & 0 & 0 & 0 \end{pmatrix} \end{array} \tag{4.139}$$

Considering the spatial point group $\mathcal{C}_3$ that describes this ring we can write down the characters for the reducible representation of the two subspaces $\mathcal{E}_1$, $\mathcal{E}_2$

Table 4.5: Character table for the $\mathcal{C}_3$ point group. The characters for the reducible representations of the two subspaces $\mathcal{E}_1$, $\mathcal{E}_2$ is also shown.

$\mathcal{C}_3$	E	C_3	C_3^2
A	1	1	1
E_1	1	$\exp(2\pi i/3)$	$\exp(4\pi i/3)$
E_2	1	$\exp(4\pi i/3)$	$\exp(2\pi i/3)$
$\Gamma_{\mathcal{E}_1}$	3	0	0
$\Gamma_{\mathcal{E}_2}$	3	0	0

(see Table 4.5). We can decompose each reducible representation into a linear direct combination of the irreducible representations of the group:

$$\Gamma_{\mathcal{E}_1} = A \oplus E_1 \oplus E_2 \tag{4.140}$$
$$\Gamma_{\mathcal{E}_2} = A \oplus E_1 \oplus E_2 \tag{4.141}$$

We thus split the states into groups of the same symmetry using the projectors of the group. There are two totally symmetric states:

$$\psi_1 = \frac{1}{\sqrt{3}}\left(|\alpha\alpha,\alpha\alpha,\alpha\beta\rangle + |\alpha\alpha,\alpha\beta,\alpha\alpha\rangle + |\alpha\beta,\alpha\alpha,\alpha\alpha\rangle\right) \tag{4.142}$$
$$\psi_2 = \frac{1}{\sqrt{3}}\left(|\alpha\alpha,\alpha\alpha,\beta\alpha\rangle + |\alpha\alpha,\beta\alpha,\alpha\alpha\rangle + |\beta\alpha,\alpha\alpha,\alpha\alpha\rangle\right) \tag{4.143}$$
$$\tag{4.144}$$

for which we can assign a wave number $k = 0$. These states have the same symmetry (are basis for the same irreducible representation A) and interact through the dipolar Hamiltonian giving rise to a 2×2 sub-block.

For the rest of the functions we can form two states of $k = 2\pi i/3$:

$$\psi_3 = \frac{1}{\sqrt{3}}\left(\epsilon|\alpha\alpha,\alpha\alpha,\alpha\beta\rangle + \epsilon^*|\alpha\alpha,\alpha\beta,\alpha\alpha\rangle + |\alpha\beta,\alpha\alpha,\alpha\alpha\rangle\right) \tag{4.145}$$
$$\psi_4 = \frac{1}{\sqrt{3}}\left(\epsilon|\alpha\alpha,\alpha\alpha,\beta\alpha\rangle + \epsilon^*|\alpha\alpha,\beta\alpha,\alpha\alpha\rangle + |\beta\alpha,\alpha\alpha,\alpha\alpha\rangle\right) \tag{4.146}$$
$$\tag{4.147}$$

and two states of $k = 4\pi i/3$:

$$\psi_5 = \frac{1}{\sqrt{3}}\left(\epsilon^*|\alpha\alpha,\alpha\alpha,\alpha\beta\rangle + \epsilon|\alpha\alpha,\alpha\beta,\alpha\alpha\rangle + |\alpha\beta,\alpha\alpha,\alpha\alpha\rangle\right) \tag{4.148}$$
$$\psi_6 = \frac{1}{\sqrt{3}}\left(\epsilon^*|\alpha\alpha,\alpha\alpha,\beta\alpha\rangle + \epsilon|\alpha\alpha,\beta\alpha,\alpha\alpha\rangle + |\beta\alpha,\alpha\alpha,\alpha\alpha\rangle\right) \tag{4.149}$$
$$\tag{4.150}$$

where $\epsilon = \exp(2\pi i/3)$. Since functions with different spatial symmetry do not interact, we form another two 2×2 sub-blocks. Note that the previous decomposition corresponds to the diagonalization of the translation operator, and that the sub-blocks we finally created are due to symmetrised functions having the same eigenvalue of T.

The form of the Hamiltonian H_6 in this new basis is then:

$$H_6 = \frac{1}{2} \begin{array}{c} \begin{array}{cccccc} \psi_1 & \psi_2 & \psi_3 & \psi_4 & \psi_5 & \psi_6 \end{array} \\ \begin{pmatrix} a-3b+3c+d & -a-2d & 0 & 0 & 0 & 0 \\ -a-2d & a+3b-3c+2d & 0 & 0 & 0 & 0 \\ 0 & 0 & a+3c+2d & -a+d & 0 & 0 \\ 0 & 0 & -a+d & a+3b+2d & 0 & 0 \\ 0 & 0 & 0 & 0 & a+3c+2d & -a+d \\ 0 & 0 & 0 & 0 & -a+d & a+3b+2d \end{pmatrix} \end{array} \tag{4.151}$$

In other words the initial 6×6 matrix representation is split into three 2×2 sub-blocks representations by making use of the spatial periodicity of the problem.

If we consider the next block of the total dipolar Hamiltonian, $M_z = +1$, 15 functions are involved. In this case too, we can split them into subspaces, that do not communicate via the translation operator. There are 5 such subspaces and each of them contains three functions, as the subspaces of the previous block. Using the same decomposition we obtain the splitting of the initial 15×15 block into three 5×5 sub-blocks, each corresponding to a different irreducible representation of the translation point group. The same arguments apply for the rest of the M_z blocks of the Hamiltonian. A schematic view of the matrix representations for the translation operator and the Hamiltonian are shown in Fig. 4.24.

4.7.4 Results

The initial calculations using the scheme outlined in the previous section have considered the problem of spin diffusion in one-dimensional lattices of two- and three-spin unit cells, starting from an initial state where spin number 1 in each unit cell has unit magnetisation. For these spin-1/2 systems, the unfactorised Hamiltonian and density operator matrices have the dimension $2^{N_{\text{total}}}$. Since the time-consuming operations in the simulations are $O(n^3)$ processes (matrix diagonalisation, multiplication etc.), the time required for simulation increases by a factor of about eight (i.e., almost an order of magnitude) for each added spin. The maximum size of spin system that can be considered is largely determined by the largest matrix that can be effectively stored and diagonalized. For a typical workstation, this limit is about 1000×1000.

Fig. 4.25 shows how the overall efficiency and the limiting number of spins differs according to the level of factorization. If the Hamiltonian cannot be factorised at all (the completely general problem), the practical limit is reached at about 10 spins ($2^{10} = 1024$). For problems which can be blocked by total magnetic quantum

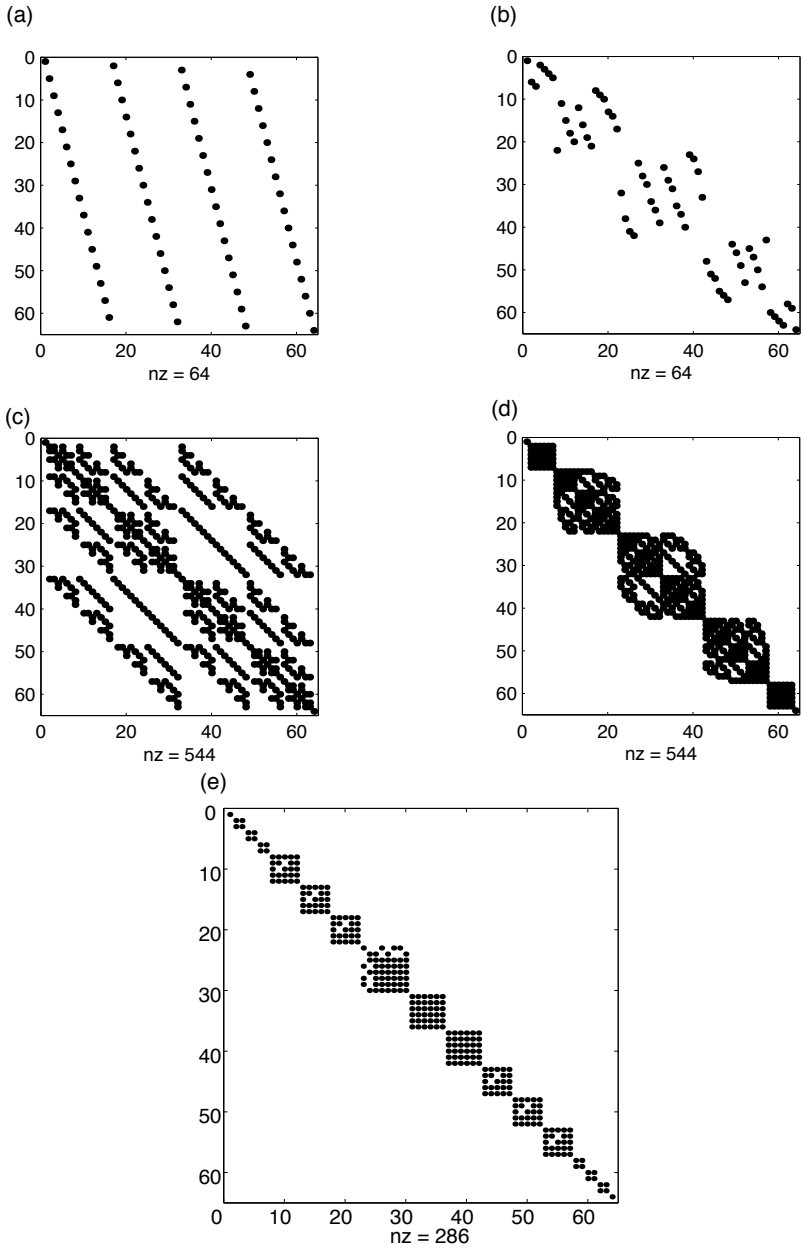

Figure 4.24: Matrix representations of the translation operator and the Hamiltonian in different basis sets. Only non zero matrix elements are shown. (a) The translation operator in the standard Zeeman basis. (b) The translation operator in the Zeeman basis ordered with respect to the total M_z. (c) The Hamiltonian in the standard Zeeman basis. (d) The Hamiltonian in the Zeeman basis ordered with respect to the total M_z. (e) The Hamiltonian in the eigenbasis of the translation operator, ordered with respect to the total M_z. Note that the number of non-zero elements nz does not change by simple rearrangement of the states, but it does change if the Hamiltonian operator is written in the appropriate symmetry adapted basis set.

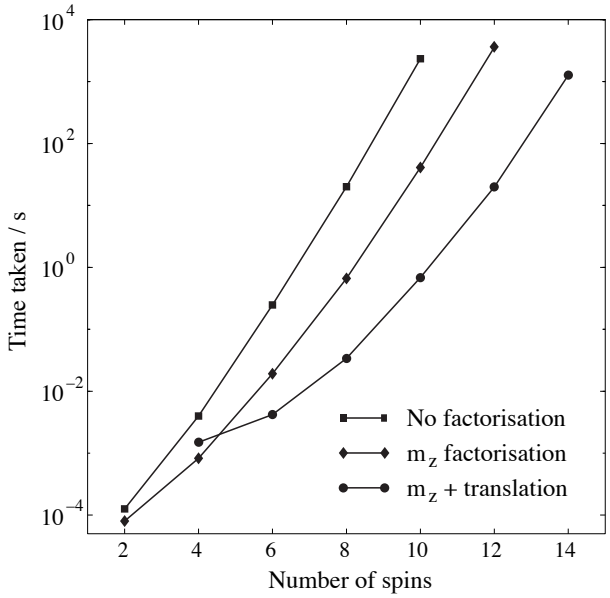

Figure 4.25: Time taken for calculation (on a Sun Ultra 5 workstation) of magnetisation exchange under spin diffusion in a two spin unit cell as a function of the total number of spins, N_{total}. From Ref. [204].

number (free-precession Hamiltonians), the size of the largest block is :

$$\frac{N_{\mathrm{total}}!}{[(N_{\mathrm{total}}/2)!]^2} \quad (N_{\mathrm{total}} \text{ even}) \qquad \frac{N_{\mathrm{total}}!}{\left(\frac{N_{\mathrm{total}}+1}{2}\right)!\left(\frac{N_{\mathrm{total}}-1}{2}\right)!} \quad (N_{\mathrm{total}} \text{ odd}) \tag{4.152}$$

This raises the limit to about 12 spins (largest matrix 924×924).

If we also make use of the translation symmetry, about 14 spins (i.e. 7 unit cells) can be handled comfortably (with two spins per unit cell). Note how the improvement increases with increasing N–the general method of direct calculation of the matrix blocks presented above is somewhat inefficient for very small systems such as $N = 2$. Note also that the reduction in block size is effectively only a function of the total number of unit cells. For instance, if we considered 9 units cells arranged in one dimension, the block sizes would be reduced by a factor of about 9. If these cells were arranged in a two-dimensional 3×3 grid, the blocks would be reduced first by a factor of three due to the translation symmetry along one dimension, and a further factor of three due to the second direction of translation symmetry. It is also worth noting that the savings would be even greater for problems where there is only one spin per unit cell. In this case, the largest matrix for a system of 16 spins is only 810×810.

Rather than look at the maximum number of spins that can be handled, it is

also useful to consider the time-saving for calculations with a fixed number of spins. For systems of 12 spins, for example, the translation symmetry factorization gains over two orders of magnitude in calculation time. This is sufficient to convert some otherwise intractable problems into feasible ones.

The remaining figures illustrate the questions that can be addressed using this approach to multi-spin systems. In these spin-diffusion problems, we follow the evolution of the z-magnetisation of spin number 1 (the spin with the initial polarization). In the eigenbasis of the Hamiltonian, the time domain signal is simply:

$$s(t) = \sum_{jk} |I'_{1z}|^2_{jk} e^{i(\omega_j - \omega_k)t} \tag{4.153}$$

where I'_{1z} is the I_{1z} operator transformed into the eigenbasis of the Hamiltonian, whose eigenvalues are given by ω_j, ω_k etc. The spectra of Figures 4.26 to 4.28 are computed as histograms from the zero-quantum frequencies $\omega_j - \omega_k$ and the transition amplitudes $A_{jk} = |I'_{1z}|^2$.

Fig. 4.26 shows the zero-quantum spectra as the number of three-spin unit cells, N, is increased, cf. Fig. 4.22. The spectrum for $N = 1$ is obviously the zero-quantum spectrum for the isolated spin system. For $N = 2$ and $N = 3$, the limited number of spins result in spectra of discrete frequencies. With 15 spins ($N = 5$), however, the spectrum is essentially continuous at this resolution. The corresponding spectra for two spin unit cells (not shown) also converge to a continuous spectrum at about 14 spins. Continuous does not imply featureless, however; the fact that the system consists of discrete three-spin systems still influences the spectrum, and the spin dynamics in these systems still reveals the fundamental quantum nature of the system [238]. That said, it should be remembered that such pronounced features might be particular to one-dimensional systems. In addition, the spectra are expected to vary with the crystallite orientation, and so these features will tend to be obscured in powder samples.

Fig. 4.27 examines which couplings are necessary to reproduce the zero-quantum spectrum of a large lattice fragment. Eliminating all the couplings between unit cells, Fig. 4.27 (a), necessarily results in the zero-quantum spectrum of an isolated two spin pair. Adding the couplings between spins in neighboring unit cells, Fig. 4.27 (b), results in a spectrum which reproduces in essence the spectrum where the couplings between all the spins have been included, Fig. 4.27 (d). While couplings between unit cells must be included if intramolecular couplings are to have any effect, it is clearly reasonable to neglect the couplings between remote unit cells. This would result in Hamiltonian blocks that were relatively sparse, although *not* amenable to further block-diagonalisation. Approximations would be necessary to translate this into a more efficient calculation.

Taking Figures 4.26 and 4.27 together, it is reasonable to conclude that the critical factor in the transition from spectra of discrete frequencies (characteristic of isolated systems) towards the smooth spectra of large systems is the number of possible coherences (i.e. the size of density matrix) rather than the number of couplings

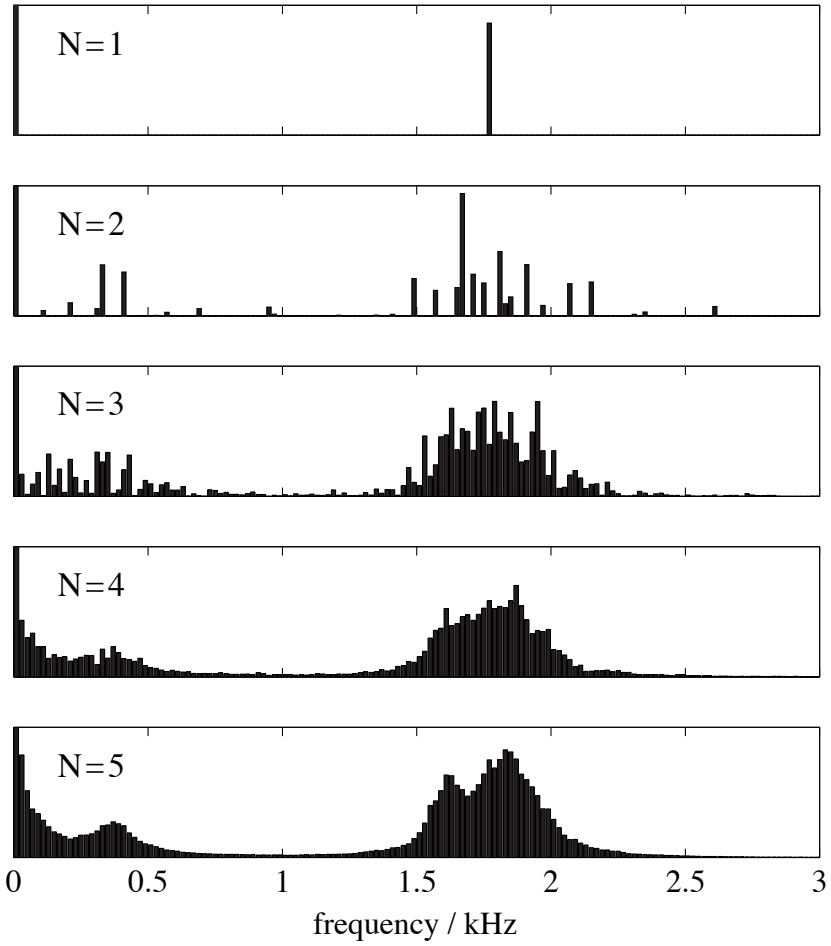

Figure 4.26: Zero quantum spectra (positive frequency only) for spin 1 of a three-spin unit cell as a function of the number of unit cells, N. The inter-cell spacing is twice the internuclear spacing within the cells ($R/r = 2$, see Fig. 4.22 for the geometry used) and the resolution of the histograms is 20 Hz (the vertical scale differs between plots). From Ref. [204].

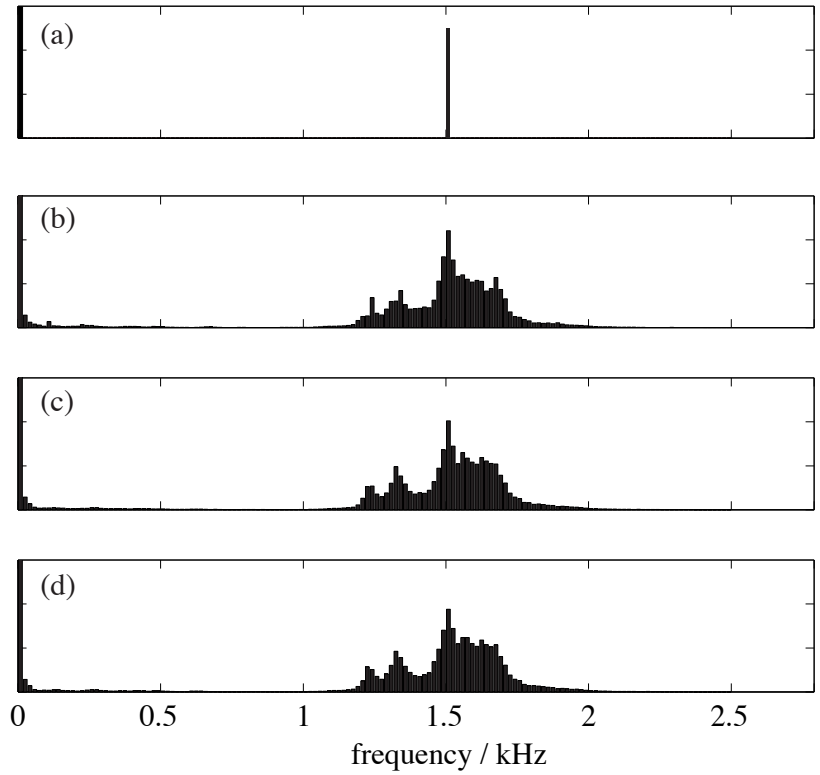

Figure 4.27: Zero quantum spectra (positive frequency only) for spin 1 of a two-spin unit cell lattice ($N = 7$) with different "orders" of dipolar couplings: (a) only couplings within the unit cell (~ 1100 Hz), (b) couplings between cells up to nearest neighbor (~ 200 Hz), (c) up to next nearest neighbor couplings (~ 20 Hz), (d) up to next next nearest neighbor (~ 6 Hz). The inter-cell spacing is twice the internuclear spacing within the cells ($R/r = 2$) and the resolution of the histograms is 17 Hz. The same vertical scale is used except for (a). From Ref. [204].

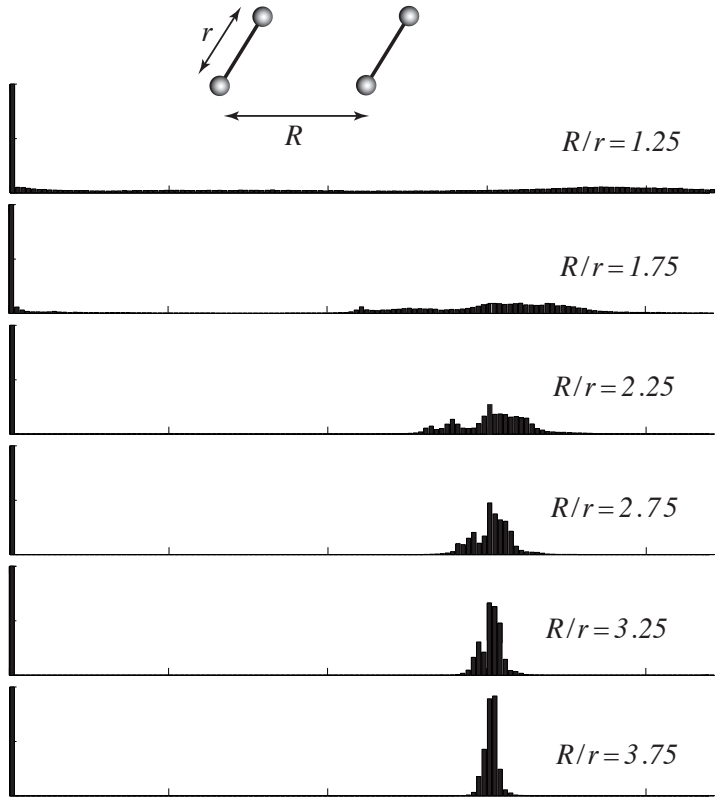

Figure 4.28: Zero quantum spectra (positive frequency only) for spin 1 of a two spin unit cell ($N = 7$) as a function of the ratio R/r. The histograms have a resolution of 17 Hz and are plotted to the same (arbitrary) vertical scale. From Ref. [204].

in the Hamiltonian. Clearly more theoretical work, in conjunction with simulations, is required to express these general deductions in a more rigorous fashion.

Finally, Fig. 4.28 considers how the zero-quantum spectra are affected by the separation between the unit cells (relative to the length scale within the cells). Although this is clearly of little practical relevance, it is important in understanding the effect of intermolecular interactions in extended systems. When the separation between unit cells is very large ($R \gg r$), the spectrum is indistinguishable from that of the isolated spin system. As R/r decreases, the spectrum broadens (zero-frequency spike apart) as might be expected cf. band theory for electrons in periodic systems. In the limit of $R \sim r$, the unit cell is no longer distinct and the spectrum is extremely broad. The intermediate case is interesting, however, since the spectra can be described neither simply in terms of a perturbed isolated spin system nor a wideline spectrum. R/r is typically around 3 for ^{13}C nuclei in organic systems.

4.7.5 Conclusions

Using the translational symmetry, we are able to study the transition from small to extended periodic systems and probe the relative importance of factors such as weak long-range couplings and the separation between molecules in neighboring unit cells.

The exploitation of the translational symmetry of crystalline systems permits a substantial reduction of the time required to compute exact spin dynamics in multi-spin systems, and increases the maximum size of systems that can be studied. This approach has been tested on spin diffusion problems in static samples. Application to spinning samples is relatively straightforward. The necessity to calculate the (homogeneous) Hamiltonian for many points in the rotor cycle does limit the size of the problem that can be considered in a reasonable calculation time, but this is offset to some extent by the empirical observation that fewer spins are required for convergence of MAS spectra for spinning speeds that are moderate or fast compared to the dominant anisotropic interactions. A comparison with perturbation theories applied in the case of MAS [260, 261] would be very interesting.

In principle, the extension to multiple dimensions is also straightforward. The total number of spins that can be considered is still limited, which rather restricts the size of the two-dimensional lattice that can be simulated. It should be possible, however, to observe visible convergence as a function of the number of unit cells for two-dimensional lattices of single-spin systems.

One initially attractive possibility is to exploit the full symmetry of the space group when factorising the Hamiltonian, rather than just the translation symmetry. It is important to remember, however, that the Hamiltonian *cannot* be simply factorised with respect to the symmetry operations of the *point* group of the unit cell (or, to be more accurate, those operations that permute nuclei). For symmorphic space groups (those without screw axes and glide planes), this factorization is only possible for special values of the k vector [262], in particular $k = 0$, since the translation-adapted states with general values of k do not have a well-defined symmetry with respect to the point group operations. Since the calculations are limited by the size of the largest matrix, the inability to factor the Hamiltonian blocks for general values of k makes further symmetry factorization uninteresting. The situation is somewhat more complicated for nonsymmorphic space groups. In these cases, extensive permutation symmetry could factor the Hamiltonian into smaller blocks, at the cost of a significant increase in complication and reduction in generality. It is worth pointing out, however, that molecular motion that is rapid on the NMR time can result in cases with very high symmetries. For example, the dipolar coupling Hamiltonian in the plastic crystal adamantane is symmetric with respect to any permutation of spins within the same molecule.

Another important direction for future research is to use these exact simulations as a benchmark for approximate treatments. Such treatments, e.g. based on perturbation theory [217, 260, 261], would be computationally less demanding and

more likely to accommodate much greater numbers of spins. Classical treatments of spin-diffusion [263, 264] in terms of simple exchange of z-magnetisation have been effective in fitting experimental results for even quite complex systems [265], as have "average product operator treatments" for multiple-quantum dynamics [266]. Although the spectra obtained here from large fragments are clearly smooth, they remain multi-body systems and the observed simplicity is probably deceptive. The theoretical challenge remains considerable.

Finally one of the fundamental questions in solid-state since its early development, is the shape of dipolar signals. A lot of discussions are based on moment analysis, and others introduce the tools of memory functions. The spin kinetics of the quantum-statistical problem seem complicated and because of the size of the problem, any exact computational effort is forced to fail. What we have developed here is a simple method to increase the size of the spin system we can treat numerically exactly. It would be very interesting to check whether such a small spin system (say 16 spins) reproduces roughly the lineshapes that we can predict from theoretical reasoning.

In this Chapter we have taken a trip through nuclear spin diffusion dynamics. Of course it would be very simplistic to believe that definite answers can be found in multi-body problems using numerical approaches. However, we have shown that the original "*ab-initio*" methods we have developed can provide a lot of physical insight in such complicated problems.

Chapter 5

Perspectives

Scalar couplings have a great potential in solid-state NMR of organic compounds. As we have shown in the previous chapters, liquid-like techniques can be easily applied in the solid-state, provided that powerful methods for very high resolution are available. The feasibility of multiple quantum filtering and heteronuclear two-dimensional correlation spectroscopy was demonstrated in Chapter 2. Development of multi-dimensional multiple correlation experiments using scalar couplings seems promising, especially in the light of recent technical (fast MAS, high power decoupling) and theoretical (new pulse sequences) advances.

As we have shown in Chapter 3, simple models can be used to develop new decoupling sequences. Using computer models, numerically optimized sequences can be found and in the particular case of homonuclear decoupling, their experimental efficiency is excellent. The DUMBO approach can, in principle, be adapted to many problems in NMR such as heteronuclear decoupling, dipolar recoupling, cross polarization giving rise to sequences that are robust with respect to experimental imperfections, or that are designed for a particular purpose (selective decoupling etc.). The modulation of the Hamiltonian by sample spinning needs to be included in order to find sequences that are adapted to fast MAS. We are currently working on this problem.

Of course, the success of numerical simulations depend on the spin model we use. Here only simple spin models were considered but these seem to be sufficient to reproduce the experimental conditions for homonuclear decoupling. In contrast, we have also seen that for spin diffusion numerical simple numerical models seems not sufficient to reproduce experiments. A lot of development was made in Chapter 4 in order to improve the spin model by including more spins. Exact and approximative work in this field seems promising for explaining complicated spin dynamics, and rendering the simulation tool more efficient. For example, work in the simulation of dipolar signals in solid state NMR (a fundamental problem for spin dynamics) is currently in progress.

Appendix A

Pulse Sequences

General notations

```
;set:
;p3 = 90 degree 1H pulse
;p11 : theta flip pulse
;p12 : pi/2-theta flip pulse
;p15 : CP contact time
;p31 : TPPM pulse
;valeur dans le fq1list = on resonance
;valeur dans le fq2list = +offset resonance
;valeur dans le fq3list = -offset resonance
;valeur dans le fq4list = optimum on resonance for DUMBO-1
```

A.1 Proton-Proton Correlation using FSLG

```
;pl1 = proton rf power

define loopcounter nfid
"nfid=td1/2"
"p11=p3*547/900"    ;first prepulse with magic flip angle
"p12=p3-p11"        ;second prepulse with complementary flip angle

#include <solids.incl>

1 ze
2 d1 protect        ;repetition time delay
  10u fq1:f1        ;on resonance = fq1 = fq1list
  10u pl1:f1        ;set proton power level
  trigg             ;additional trigger available on HP router
  p3:f1 ph1         ;90 degree proton pulse +y -y
```

```
  1u
  p11:f1 ph11       ;first proton prepulse +y

  1u fq2:f1         ;set the offset on fq2 = fq2list
3 (p6 ph4):f1       ;Lee-Goldburg pulse on +x
  p13:f1 fq3:f1     ;small pulse (0.6u) to set the offset fq3=fq3list
  (p6 ph5):f1       ;Lee-Goldburg pulse on -x
  p13:f1 fq2:f1     ;small pulse (0.6u) to set the offset fq2=fq2list
  lo to 3 times l0  ;FSLG loop during t1

  1u fq1:f1         ;on resonance for detection = fq1 = fq1list
  p12:f1 ph11       ;second prepulse +y
  1u
  p3:f1 ph2         ;last 90 proton pulse +x +x -x -x +y +y -y -y

  1u:f1 ph10        ;reset of the DDS phase
  2u adc ph31       ;start ADC with ph31 signal routing
  aq
  rcyc=2
  10m wr #0 if #0 zd
  1m ip1
  lo to 2 times 2
  1m ip1
  1m ip1             ;States
  1m iu0
  1m iu0
  1m iu0
  1m iu0
  lo to 2 times nfid
exit

ph1=+y -y
ph2=+x +x -x -x +y +y -y -y
ph4=+x
ph5=-x
ph11=+y
ph10=0
ph31=0 2 2 0 1 3 3 1
```

A.2 Proton-Proton Correlation using DUMBO-1

```
;pl1 = proton power
```

```
define loopcounter nfid
"nfid=td1/2"

#include <solids.incl>

1 ze
2 d1 protect           ;repetition time delay
  10u fq1:f1           ;on resonance = fq1 = fq1list
  10u pl1:f1           ;set proton power level
  trigg                ;additional trigger available on HP router
  p3:f1 ph1            ;90 degree proton pulse +y -y
  1u
  p11:f1 ph11          ;first prepulse on proton

  1u fq4:f1            ; chose the optimum offset for DUMBO-1 decoupling
  1.5u:f1 ph10         ; reset the DDS phase
  d0 cpds3:f1          ; first Dumbo during d11
  3u do:f1

  1u fq1:f1            ;on resonance for detection = fq1 = fq1list
  p12:f1 ph12          ;second prepulse on proton
  1u
  p3:f1 ph2            ;90 degree proton pulse

  1u:f1 ph10           ;reset of the DDS phase
  2u adc ph31          ;start ADC with ph31 signal routing
  aq
  rcyc=2
  10m wr #0 if #0 zd
  1m ip1
  lo to 2 times 2
  1m ip1
  1m ip1             ;States
  1m id0
  lo to 2 times nfid
exit

ph1=+y -y
ph2=+y +y -x -x -y -y +x +x
ph11=+y -y
ph12=+y
ph10=0
ph31=0 2 1 3 2 0 3 1
```

A.3 J-Multiple Quantum Filters

A.3.1 Single-Quantum Proton Filter

```
;p0 : evolution of J
;p2 : X 180 degree pulse
;p6 : FSLG-360 pulse
;p13 : phase/freq. setting comp.
;p21 : complementary of the magic flip pulse
;pl1 : X power during CP
;sp0 : max H power during ramped CP
;pl11 : X power during 180
;pl12 : H power during pulses
;important : p0 has to be synchronized with the rotation

define loopcounter count
"count=p0/(p13+p13+p6+p6)"
;"p11=(p3*547)/900"
;"p21=p3-p11"

1 ze
2 d1 do:f2                        ;repetition time delay
  1u:f2 ph10                      ;reset the DDS phase
  10u pl1:f1                      ;set X power level
  10u pl2:f2                      ;set proton power level
  1u fq1:f2                       ;on proton resonance = fq1 = fq1list
  p3:f2 ph1                       ;proton 90 pulse +/- y
  3u
  (p15 ph5):f1 (p15:sp0 ph0):f2   ;Ramped Field on proton +x
                                  ;Square Field on X +x
  1u pl12:f2 pl11:f1              ;set power levels on both channels

  1u fq2:f2                       ;set the offset on fq2 = fq2list
3 (p6 ph14):f2                    ;Lee-Goldburg pulse on +x
  p13:f2 fq3:f2                   ;small pulse (0.6u) to set fq3=fq3list
  (p6 ph15):f2                    ;Lee-Goldburg pulse on -x
  p13:f2 fq2:f2                   ;small pulse (0.6u) to set fq2=fq2list
  lo to 3 times count             ;loop for the first FSLG period during p0

  1u fq1:f2                       ;on resonance for filter pulses fq1=fq1list
  (p3 ph2):f2                     ;first pi/2 pulse on protons +y/-y
  (p2 ph4):f1                     ;pi pulse on X
  0.3u
  (p3 ph11):f2                    ;second pi/2 on proton -y
```

```
  1u fq2:f2                       ;set the offset on fq2 = fq2list
4 (p6 ph14):f2
  p13:f2 fq3:f2
  (p6 ph15):f2
  p13:f2 fq2:f2
  lo to 4 times count             ;loop for the second FSLG period during p0

  1u fq1:f2                       ;on resonance for decoupling during t2
  1u cpd2:f2                      ;TPPM decoupling
  1u:f1 ph10                      ;reset of the DDS phase
  2u adc ph31                     ;start ADC with ph31 signal routing
  aq
  1m do:f2
  rcyc=2
  10m wr #0

exit

ph0= +x
ph1= +y -y
ph2= +y +y -y -y
ph3= -x
ph4= +y +y +y +y -x -x -x -x
     -y -y -y -y +x +x +x +x
ph5= +x
ph14=+x
ph15=-x
ph11=-y
ph10=0
ph31=0 2 2 0 2 0 0 2
```

A.3.2 Double-Quantum Proton Filter

```
;p0 : evolution of J
;p2 : X 180 degree pulse
;p6 : FSLG-360 pulse
;p13 : phase/freq. setting comp.
;pl1 : X power during CP
;sp0 : max H power during CP
;pl11 : X power during 180
;pl12 : H power during pulses
;important : p0 has to be synchronized with the rotation

define loopcounter count
"count=p0/(p13+p13+p6+p6)"
```

```
"p11=(p3*547)/900"
"p12=p3+p11"

1 ze
2 d1 do:f2                          ;repetition time delay
  1u:f2 ph10                        ;reset the DDS phase
  10u pl1:f1                        ;set X power level
  10u pl2:f2                        ;set proton power level
  1u fq1:f2                         ;on proton resonance: fq1=fq1list
  p3:f2 ph1                         ;proton 90 pulse +/- y
  3u
  (p15 ph5):f1 (p15:sp0 ph0):f2     ;Ramped Field on proton +x
                                    ;Square Field on X +x
  1u pl12:f2 pl11:f1                ;set power levels on both channels

  1u fq2:f2                         ;set the offset on fq2 = fq2list
3 (p6 ph14):f2
  p13:f2 fq3:f2
  (p6 ph15):f2
  p13:f2 fq2:f2
  lo to 3 times count               ;loop for the first FSLG +/-x period during p0

  1u fq1:f2                         ;on resonance for filter pulses: fq1=fq1list
  (p11 ph11):f2                     ;first H magic prepulse -y
  0.5u
  (p3 ph2):f2                       ;first 90 H pulse with phase 0 1 2 3
  (p2 ph4):f1                       ;pi pulse on X
 ; 1u
  (p3 ph12):f2                      ;second 90 H pulse with phase +y
  0.5u
  (p11 ph13):f2                     ;second H magic prepulse with phase +y

  0.6u fq2:f2                       ;loop for the second FSLG +/-x period during p0
4 (p6 ph16):f2
  p13:f2 fq3:f2
  (p6 ph17):f2
  p13:f2 fq2:f2
  lo to 4 times count

  1u fq1:f2                         ;on resonance for TPPM decoupling during t2
  1u cpd2:f2                        ;TPPM decoupling
  1u:f1 ph10                        ;reset of the DDS phase
  2u adc ph31                       ;start ADC with ph31 signal routing
  aq
  1m do:f2
  rcyc=2
```

```
  10m wr #0

exit

ph0= +x
ph1= +y -y
ph2= +y +y -x -x -y -y +x +x
ph4= +y +y +y +y +y +y +y +y
     -x -x -x -x -x -x -x -x
     -y -y -y -y -y -y -y -y
     +x +x +x +x +x +x +x +x
ph5= +x
ph14=+x +x +y +y -x -x -y -y
ph15=-x -x -y -y +x +x +y +y
ph11=-y -y +x +x +y +y -x -x
ph12=+y +y +y +y +y +y +y +y
     +y +y +y +y +y +y +y +y
     +y +y +y +y +y +y +y +y
     +y +y +y +y +y +y +y +y
     -x -x -x -x -x -x -x -x
     -x -x -x -x -x -x -x -x
     -x -x -x -x -x -x -x -x
     -x -x -x -x -x -x -x -x
     -y -y -y -y -y -y -y -y
     -y -y -y -y -y -y -y -y
     -y -y -y -y -y -y -y -y
     -y -y -y -y -y -y -y -y
     +x +x +x +x +x +x +x +x
     +x +x +x +x +x +x +x +x
     +x +x +x +x +x +x +x +x
     +x +x +x +x +x +x +x +x
ph13=+y
ph16=+x
ph17=-x
ph10=0
ph31=0 2 2 0 0 2 2 0
     2 0 0 2 2 0 0 2
     0 2 2 0 0 2 2 0
     2 0 0 2 2 0 0 2
     2 0 0 2 2 0 0 2
     0 2 2 0 0 2 2 0
     2 0 0 2 2 0 0 2
     0 2 2 0 0 2 2 0
```

A.3.3 Triple-Quantum Proton Filter

```
;p0 : evolution of J
;p2 : X 180 degree pule
;p6 : FSLG-360 pulse
;p13 : phase/freq. setting comp.
;pl1 : X power during CP
;sp0 : max H power during CP
;pl11 : X power during 180
;pl12 : H power during pulses
;important : p0 has to be synchronized with the rotation

define loopcounter count
"count=p0/(p13+p13+p6+p6)"
"p11=(p3*547)/900"
"p12=p3-p11"                    ;(pi/2-theta) on -y or (pi/2+theta) on +y

1 ze
2 d1 do:f2                       ;repetition time delay
  1u:f2 ph10                     ;reset the DDS phase
  10u pl1:f1                     ;set X power level
  10u pl2:f2                     ;set proton power level
  1u fq1:f2                      ;on proton resonance = fq1 = fq1list
  p3:f2 ph1                      ;proton 90 pulse +/- y
  3u
  (p15 ph5):f1 (p15:sp0 ph0):f2  ;Ramped Field on proton +x
                                 ;Square Field on X +x
  1u pl12:f2 pl11:f1             ;set power levels on both channels

  1u fq2:f2                      ;loop for the first FSLG +/- x period during p0
3 (p6 ph14):f2
  p13:f2 fq3:f2
  (p6 ph15):f2
  p13:f2 fq2:f2
  lo to 3 times count

  1u fq1:f2                      ;on resonance for filter pulses = fq1 = fq1list
  (p11 ph11):f2                  ;first H magic prepulse -y
  (1u ph0):f2                    ;reset the phase to +x because we will use the DDS
   0.5u
  (p3 ph2):f2  (p2 ph4):f1       ;first 90 H pulse with phase 0 1 2 3 4 5
                                 ;and pi pulse on X
  (1u ph10):f2                   ;reset the DDS phase
  0.5u
  (p12 ph11):f2                  ;second H prepulse (pi/2-theta) on -y
```

```
                                ;or (pi/2+theta) on +y.

  1u fq2:f2                     ;loop for the first FSLG +/- x period during p0
4 (p6 ph14):f2
  p13:f2 fq3:f2
  (p6 ph15):f2
  p13:f2 fq2:f2
  lo to 4 times count

  1u fq1:f2                     ;on resonance for TPPM decoupling during detection
  1u cpd2:f2                    ;TPPM decoupling
  2u adc ph31                   ;start ADC with ph31 signal routing
  1u:f1 ph10
  aq
  1m do:f2
  rcyc=2
  10m wr #0

exit

ph0= +x
ph1= +y -y
;ph2= (6) 0 0 1 1 2 2 3 3 4 4 5 5
ph2= (12) 3 3 5 5 7 7 9 9 11 11 1 1
ph4= +y +y +y +y +y +y +y +y +y +y +y +y
     -x -x -x -x -x -x -x -x -x -x -x -x
     -y -y -y -y -y -y -y -y -y -y -y -y
     +x +x +x +x +x +x +x +x +x +x +x +x
ph5= +x
ph14=+x
ph15=-x
ph11=-y
ph12=+y
ph10=0
ph31=0 2 2 0 0 2 2 0 0 2 2 0
     2 0 0 2 2 0 0 2 2 0 0 2
```

A.4 MAS-J-HMQC using FLSG

```
;p0 : evolution of J
;p2 : X 180 degree pule
;p6 : FSLG-360 pulse
;p13 : phase/freq. setting comp.
```

```
;largeur spectrale : l'inverse de l'increment
;cad de (p6+p13)*4*2*l1
;a multiplier encore par 1.7
;choisir nd0 egal a 1
;important : p0 has to be synchronized with the rotation

define loopcounter nfid
"nfid=td1/2"
define loopcounter count
"count=p0/(p13+p13+p6+p6)"
"p11=p3*547/900"

1 ze
2 d1 do:f2                  ;recycle delay
  1u:f2 ph10
  10u pl1:f1                ;preselect pl1 drive power level for F1
  10u pl2:f2
  1u fq1:f2
  p3:f2 ph1                 ;proton 90 pulse +y, -y

  2u pl22:f2
  (p15 ph5):f1 (p15 ph0):f2 ;Cross Polarization

  1u pl12:f2 pl11:f1
  1u fq2:f2
3 (p6 ph14):f2              ;first tau LG period FSLG sur X
  p13:f2 fq3:f2
  (p6 ph15):f2
  p13:f2 fq2:f2
  lo to 3 times count

  1u fq1:f2
  (p11 ph11):f2             ;first magic pulse on protons with phase -y
   1u
  (1u ph30):f2              ;ph30 is incremented for quadrature detection in F1
  (p3 ph2):f2               ;first pi/2 pulse on protons with phase +y
   1u
  (1u ph10):f2              ;reset of the phase for quadrature detection in F1
  (p11 ph6):f2              ;second magic pulse with phase +y
   1u fq2:f2
5 (p6 ph14):f2              ;LG period during t1 FSLG sur X
  p13:f2 fq3:f2
  (p6 ph15):f2
  p13:f2 fq2:f2
  lo to 5 times l0
```

```
  (p6 ph14):f2
  p13:f2 fq3:f2
  (p6 ph15):f2 (p2 ph4):f1  ;pi pulse on carbon inserted in
  p13:f2 fq2:f2             ;one FSLG cycle

6 (p6 ph14):f2
  p13:f2 fq3:f2
  (p6 ph15):f2
  p13:f2 fq2:f2
  lo to 6 times l0

   1u fq1:f2
  (p3 ph11):f2              ;second pi/2 on proton with -y phase
  1u fq2:f2
4 (p6 ph14):f2              ;second tau LG period
  p13:f2 fq3:f2
  (p6 ph15):f2
  p13:f2 fq2:f2
  lo to 4 times count

  1u fq1:f2
  1u cpd2:f2               ;TPPM Decoupling
  1u:f1 ph10
  2u adc ph31              ;start ADC with ph31 signal routing
  aq
  1m do:f2
  rcyc=2
  10m wr #0 if #0 zd
  1m ip30
  lo to 2 times 2
  1m ip30
  1m ip30                   ;States
15 1m iu0
   1m iu0
  lo to 15 times l1
  lo to 2 times nfid
exit

ph0= +x
ph1= +y -y
ph2= +y +y -y -y
ph3= -x
ph4= +y +y +y +y -x -x -x -x
     -y -y -y -y +x +x +x +x
ph5= +x +x +x +x
```

```
ph6=+y
ph14=+x
ph15=-x
ph11=-y
ph12=+y
ph10=0
ph30=0
ph31=0 2 2 0 2 0 0 2
```

A.5 MAS-J-HMQC using DUMBO-1

```
;J-H2QC MAS experiment with States quadrature mode

;p1 : X 180 degree pulse
;p13 : phase/freq. setting comp.
;pl1 : X CP power
;pl2 : H 90 power before CP
;pl11 : X 180 power
;pl12 : H DUMBO and pulses power
;pl13 : H TPPM power
;pl22 : H CP power

define loopcounter nfid
"nfid=td1/2"

1 ze
2 d1 do:f2                      ;repetition time delay
  1u:f2 ph10                    ;reset the DDS phase
  10u pl1:f1                    ;set X power level
  10u pl2:f2                    ;set proton power level
  1u fq1:f2                     ;on proton resonance = fq1 = fq1list
  p3:f2 ph1                     ;proton 90 pulse +/- y

  2u pl22:f2                    ;set proton CP power level
  (p15 ph5):f1 (p15 ph0):f2     ;Cross Polarization

  1u pl12:f2 fq2:f2             ;setting RF powers
  1u pl11:f1                    ;and optimum on-resonance for DUMBO-1

  1.5u:f2 ph10                  ;first DUMBO-1 during p0
  d11 cpds3:f2
  3u do:f2

  (p11 ph11):f2                 ;first prepulse
```

```
  1.5u
  (p3 ph2):f2                    ;pi/2 on H
  1.5u
  (p12 ph12):f2                  ;second prepulse

  1.5u:f2 ph10                  ;DUMBO-1 during t1
  d0 cpds4:f2
 (p1 ph21):f1                    ;pi pulse on X
  d0
  1.5u do:f2

  (p3 ph11):f2                   ;pi/2 on H

  1.5u:f2 ph10                   ;second Dumbo during p0
  d11 cpds3:f2
  3u do:f2

  1.5u pl13:f2 fq1:f2            ;setting decoupling power and offset
  1u cpd2:f2                     ;TPPM decoupling
  1u:f1 ph10
  2u adc ph31                    ; start ADC with ph31 signal routing
  aq
  1m do:f2
  rcyc=2
  10m wr #0 if #0 zd
  1m ip2
  lo to 2 times 2
  1m ip2
  1m ip2                 ;States
  1m id0
  lo to 2 times nfid
exit

ph0= 1
ph1= 0 2
ph2= 1 1 3 3
ph3= 1
ph4= 1
ph5= 0
ph6= 2
ph14= 0
ph11= 3
ph12= 1
ph21= 0 0 0 0
ph10= 0
ph31= 0 2 2 0
```

Appendix B

180° Composite Pulses

No	Sequence – Ref.	Number of π rotations
1	180_0	1.0
2	$90_{90}180_090_{90}$ [120]	2
3	$90_0240_{90}90_0$ [123]	2.3
4	$90_0360_{120}90_0$ [124]	3.0
5	$270_{180}360_090_{90}270_{270}360_{90}90_0$ [267]	8.0
6	$180_{120}180_{240}180_{120}$ [141]	3.0
7	$90_0225_{180}315_0$ [134]	3.5
8	$158_{180}171.2_0342.8_{180}145.5_081.2_{180}85.3_0$ [267]	5.5
9	$180_0180_0180_{120}180_{60}180_{120}180_0180_0$— [130] $180_{120}180_{60}180_{120}180_{120}180_{120}180_{240}$— $180_{180}180_{240}180_{60}180_{60}180_{180}180_{120}$— $180_{180}180_{120}180_{120}180_{240}180_{180}180_{240}$—	25.0
10	$79_0276_{106}79_0$ [135]	2.4
11	$64_0146_{185}320_{310}77_{192}$ [135]	3.4
12	$63_0140_{148}340_{240}140_{148}63_0$ [135]	4.1
13	$52_094_{139}66_{196}323_{251}143_{159}63_{10}$ [135]	4.1
14	$54_0135_{163}177_{295}381_{11}177_{295}135_{163}54_0$ [135]	6.2
15	$\mathrm{F2}{=}170_{[-0.92]}170_{[0.92]}$ [149]	1.9
16	$\mathrm{F3}{=}180_{[-1.55]}180_{[0]}180_{[1.55]}$ [149]	3.0
17	$\mathrm{F4}{=}166_{[-2.2]}198_{[-0.66]}198_{[0.66]}166_{[2.20]}$ [149]	4.0
18	$\mathrm{F5}{=}175_{[-2.9]}190_{[-1.4]}195_{[0]}190_{[1.4]}175_{[2.9]}$ [149]	5.1
19	$\mathrm{F6}{=}166_{[-3.6]}195_{[-2.06]}182_{[-0.66]}182_{[0.66]}195_{[2.06]}166_{[3.6]}$ [149]	6.0
20	$\mathrm{P5F3}{=}\mathrm{F3}_0\mathrm{F3}_{150}\mathrm{F3}_{60}\mathrm{F3}_{150}\mathrm{F3}_0$ [149]	9.5
21	$\mathrm{P5F4}{=}\mathrm{F4}_0\mathrm{F4}_{150}\mathrm{F4}_{60}\mathrm{F4}_{150}\mathrm{F4}_0$ [149]	15.0
22	$\mathrm{P5F5}{=}\mathrm{F5}_0\mathrm{F5}_{150}\mathrm{F5}_{60}\mathrm{F5}_{150}\mathrm{F5}_0$ [149]	25.7
23	$\mathrm{P5F6}{=}\mathrm{F6}_0\mathrm{F6}_{150}\mathrm{F6}_{60}\mathrm{F6}_{150}\mathrm{F6}_0$ [149]	30.0
24	$\mathrm{S}{=}55_{230}49_{285}93_{33}49_{61}14_{138}103_{237}35_{213}$— [136] $32_{187}122_{162}46_{198}122_{233}24_{88}66_{49}66_{23}57_{269}42_{224}$	5.4
25	$\mathrm{L}{=}54_{333}191_{215}162_{259}231_{34}117_{14}146_{307}$— [136] $221_{78}108_{36}168_{182}177_{292}215_{208}109_{209}$— $131_{356}217_{339}60_{190}14_{229}$	12.9
26	$169_{57.2}168.4_{301.9}168.8_{56.6}$ [137]	2.8
27	$158.9_0157.7_{92.1}317.5_{308.7}157.4_{92.8}$ [137]	4.4
28	$179.7_{89.9}360_{289}360_{71.3}179.7_{270.4}180_0$ [137]	7
29	$350.8_0222.3_{179.8}52.8_0$ [137]	3.5
30	$210.2_{73.5}117.9_{132.7}189.3_{43.7}318.4_{166.7}$ [137]	4.6
31	$150.6_{247.1}342.1_{181.7}180.3_{319.9}342.1_{181.7}150.6_{247.1}$ [137]	6.5
32	$\mathrm{BB1}(180){=}180_{104.5}360_{313.4}180_{104.5}180_0$ [132]	5.0
33	$\mathrm{BB2}(180){=}180_{90}360_{315}180_{90}180_0$ [132]	5.0

Table B.1: Broadband 180° composite pulses. X_Y means a square pulse of flip angle X and phase Y, both in degrees. $X_{[Z]}$ means a square pulse of flip angle X in degrees, or a block of pulses X and frequency Z in ω_1 units. The range for $\omega_1/\omega_1^{\mathrm{nom}}$ and $\Omega/\omega_1^{\mathrm{nom}}$ is defined from inversions having $\langle I_z\rangle < 0.984$ corresponding to an angle θ between 170° and 190°.

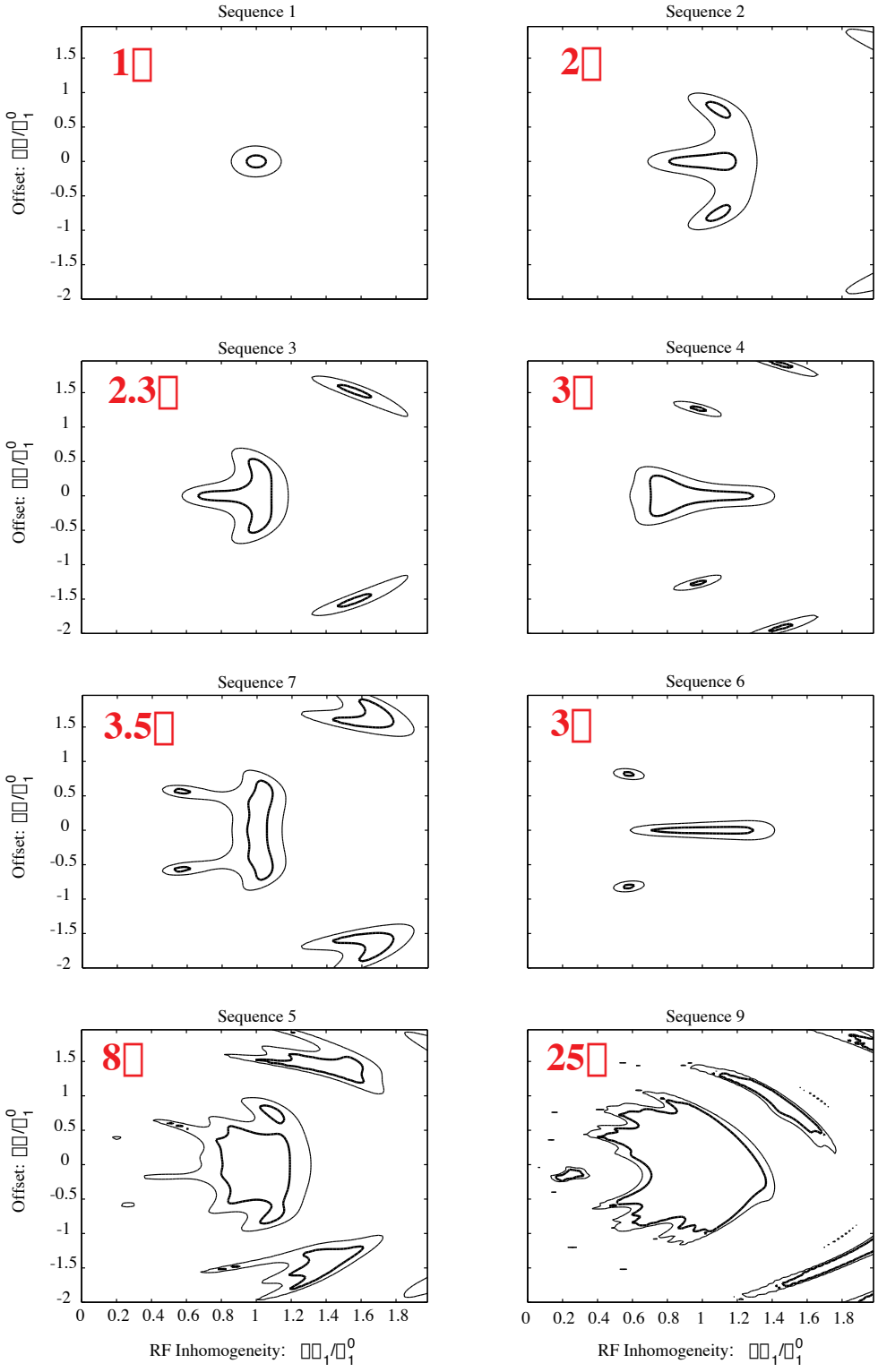

Figure B.1: Contour levels for the composite pulses of table B.1. The two contour levels presented here correspond to $I_z = -0.9$ and $I_z = -0.984$. All figures have the same scale for rf and offset mismatch. On the top left corner of each figure the total flip angle of the pulse is shown.

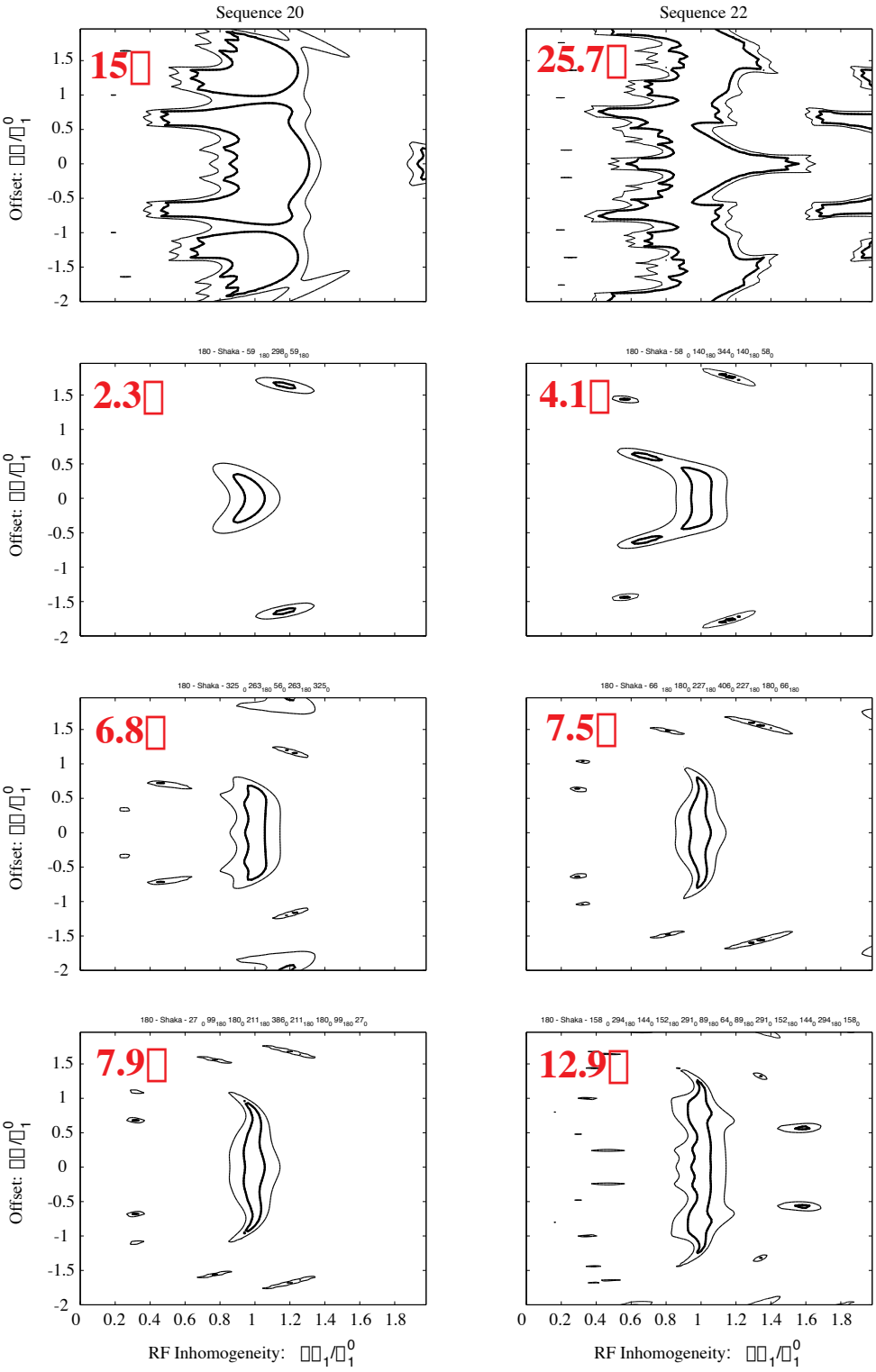

Figure B.2: Contour levels for the composite pulses of table B.1. The two contour levels presented here correspond to $I_z = -0.9$ and $I_z = -0.984$. All figures have the same scale for rf and offset mismatch. On the top left corner of each figure the total flip angle of the pulse is shown.

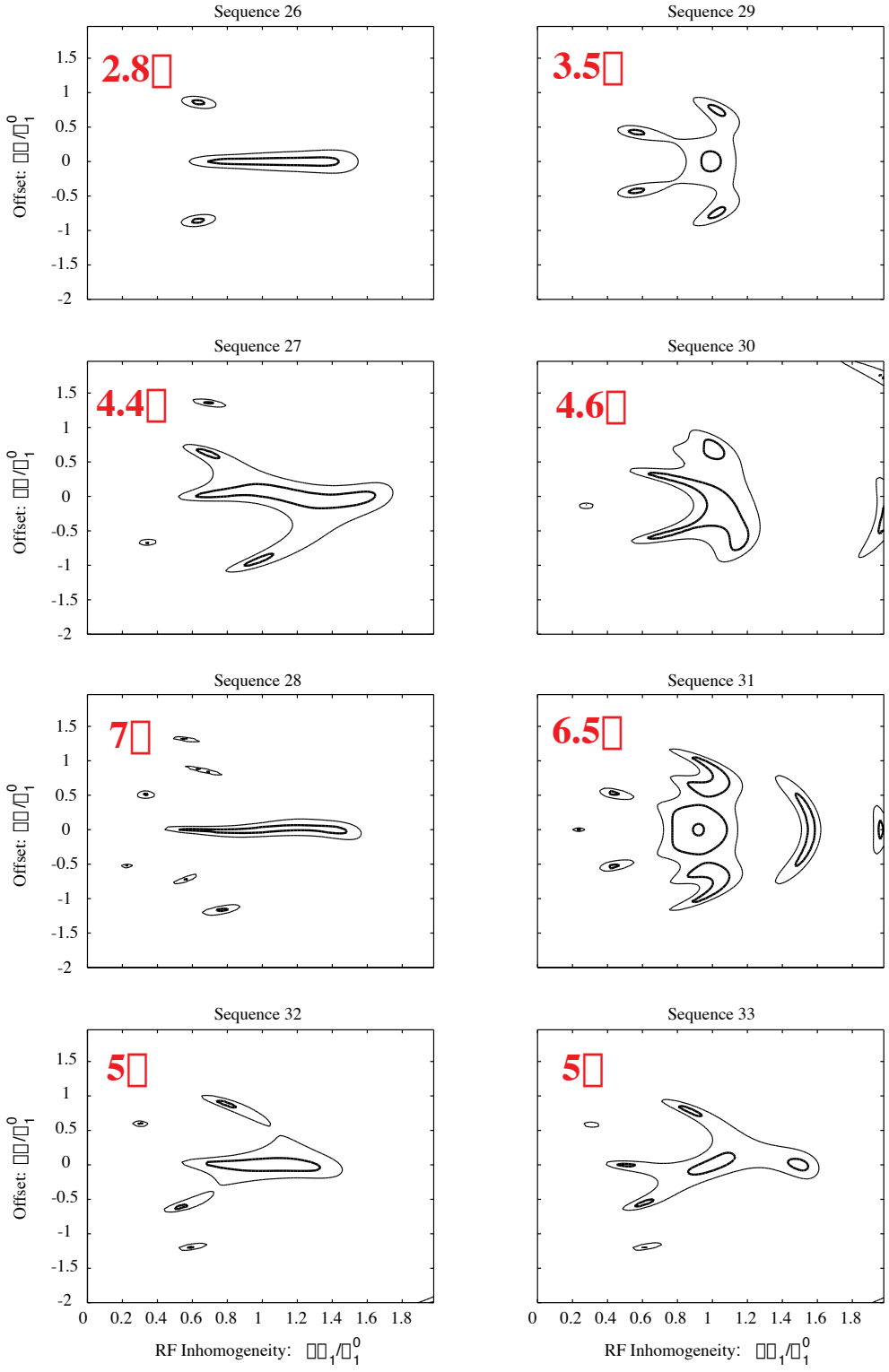

Figure B.3: Contour levels for the composite pulses of table B.1. The two contour levels presented here correspond to $I_z = -0.9$ and $I_z = -0.984$. All figures have the same scale for rf and offset mismatch. On the top left corner of each figure the total flip angle of the pulse is shown.

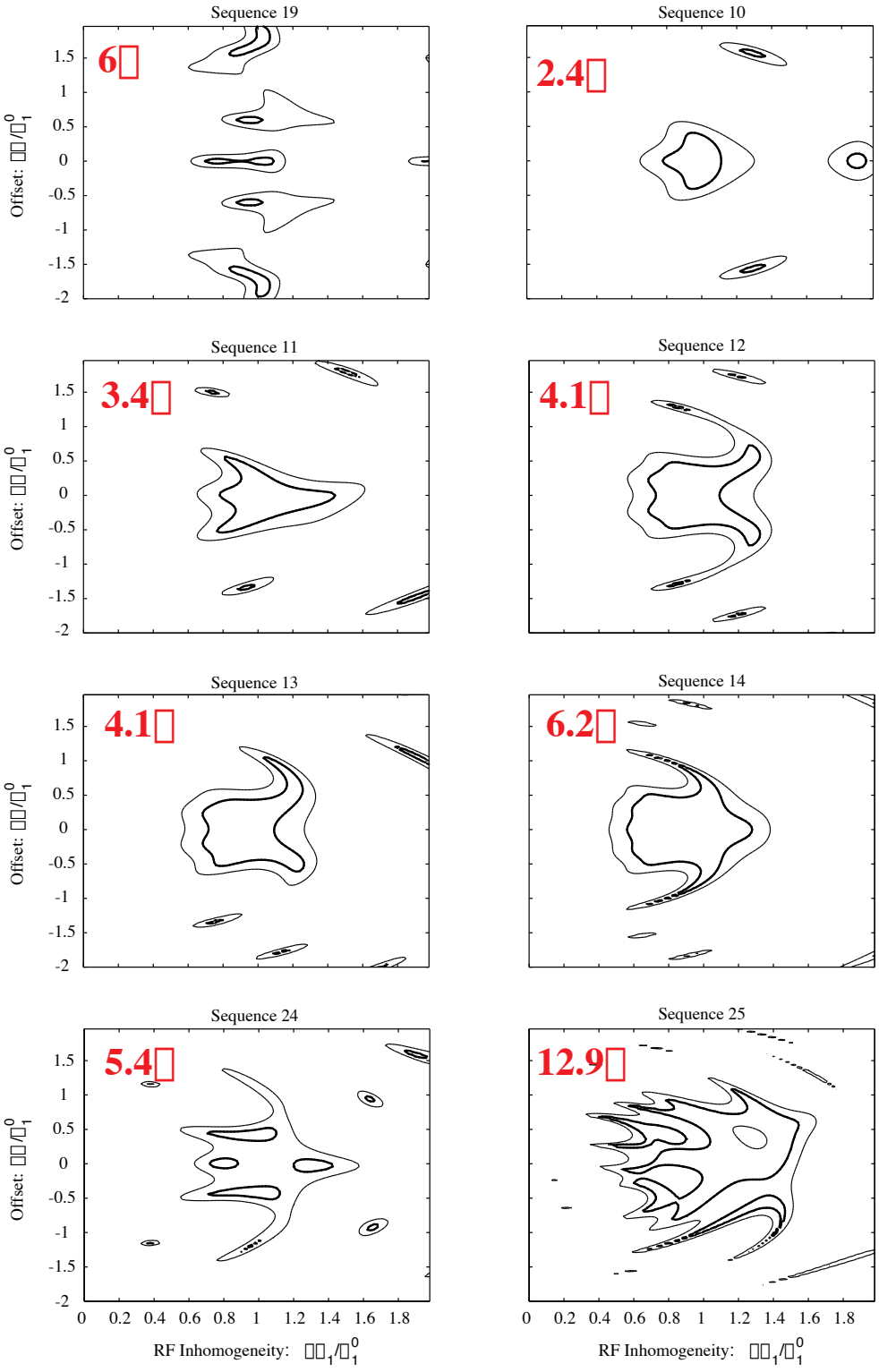

Figure B.4: Contour levels for the composite pulses of table B.1. The two contour levels presented here correspond to $I_z = -0.9$ and $I_z = -0.984$. All figures have the same scale for rf and offset mismatch. On the top left corner of each figure the total flip angle of the pulse is shown.

Bibliography

[1] K. Schmidt-Rohr and H. W. Spiess, Multidimensional solid-state NMR and polymers (Academic Press, London, 1994).

[2] M. Mehring, Principles of high resolution NMR in solids (Springer-Verlag, Berlin, 1983).

[3] U. Haeberlen, High resolution NMR in solids: Selective averaging (Academic Press, New York, 1976).

[4] L. Emsley, D. Laws and A. Pines, Lectures on pulsed NMR (3rd edition) (Proccedings of the International School of Physics "Enrico Fermi", Amsterdam, 1999).

[5] E. R. Andrew, A. Bradbury and R. G. Eades, Nature 182 (1958) 1659.

[6] A. Pines, M. G. Gibby and J. S. Waugh, J. Chem. Phys. 56 (1972) 1776.

[7] A. Pines, M. G. Gibby and J. S. Waugh, J. Chem. Phys. 59 (1973) 569.

[8] D. T. Pegg, D. M. Doddrell and M. R. Bendall, J. Chem. Phys. 77 (1982) 2745.

[9] G. A. Morris and R. Freeman, J. Am. Chem. Soc. 101 (1979) 760.

[10] M. H. Levitt and R. Freeman, J. Magn. Reson. 39 (1980) 533.

[11] C. LeCocq and J.-Y. Lallemand, J. Chem. Soc. Chem. Comm. 119 (1981) 150.

[12] S. L. Patt and J. N. Shoolery, J. Magn. Reson. 46 (1982) 535.

[13] F.-K. Pei and R. Freeman, J. Magn. Reson. 48 (1982) 318.

[14] H. J. Jakobsen, O. W. Sørensen, W. S. Brey and P. Kanya, J. Magn. Reson. 48 (1982) 328.

[15] M. Alla and E. Lippmaa, Chem. Phys. Lett. 37 (1976) 260.

[16] E. F. Rybaczewski, B. L. Neff, J. S. Waugh and J. S. Sherfinski, J. Chem. Phys. 67 (1977) 1231.

[17] G. G. Webb and K. W. Zilm, J. Am. Chem. Soc. 111 (1989) 2455.

[18] N. Sethi, J. Magn. Reson. 94 (1991) 352.

[19] D. P. Burum and A. Bielecki, J. Magn. Reson. 95 (1991) 184.

[20] X. Wu and K. W. Zilm, J. Magn. Reson. A 102 (1993) 205.

[21] C. H. Wu, A. Ramamoorthy and S. J. Opella, J. Magn. Reson. A 109 (1994) 270.

[22] J. Z. Hu, J. Harper, C. Taylor, R. J. Pugmire and D. M. Grant, J. Magn. Reson. 142 (2000) 326.

[23] K. W. Zilm and D. M. Grant, J. Magn. Reson. 48 (1982) 524.

[24] A. Lesage, S. Steuernagel and L. Emsley, J. Am. Chem. Soc. 120 (1998) 7095.

[25] T. Terao, H. Miura and A. Saika, J. Chem. Phys. 75 (1981) 1573.

[26] B. C. Gerstein, R. G. Pembleton, R. C. Wilson and L. M. Ryan, J. Chem. Phys. 66 (1977) 361.

[27] B. C. Gerstein, C. Chow, R. G. Pembleton and R. C. Wilson, J. Phys. Chem. 81 (1977) 565.

[28] R. E. Taylor, R. G. Pembleton, L. M. Ryan and B. C. Gerstein, J. Chem. Phys. 71 (1979) 4541.

[29] L. M. Ryan, R. E. Taylor, A. J. Paff and B. C. Gerstein, J. Chem. Phys. 72 (1980) 508.

[30] D. P. Burum, Concepts in Magnetic Resonance 2 (1990) 213.

[31] P. Caravatti, G. Bodenhausen and R. R. Ernst, Chem. Phys. Lett. 89 (1982) 363.

[32] P. Caravatti, L. Braunschweiler and R. R. Ernst, Chem. Phys. Lett. 100 (1983) 305.

[33] J. E. Roberts, S. Vega and R. G. Griffin, J. Am. Chem. Soc. 106 (1984) 2506.

[34] D. P. Burum and A. Bielecki, J. Magn. Reson. 94 (1991) 645.

[35] C. E. Bronnimann, C. F. Ridenour, D. R. Kinney and G. E. Maciel, J. Magn. Reson. 97 (1992) 522.

[36] C. W. B. Lee and R. D. Griffin, Biophys. J. 55 (1989) 355.

[37] R. A. Santos, R. A. Wind and C. E. Bronnimann, J. Magn. Reson. B 105 (1994) 183.

[38] Z. Gu, C. F. Ridenour, C. E. Bronnimann, T. Iwashita and A. McDermott, J. Am. Chem. Soc. 118 (1996) 822.

[39] B. J. Van Rossum, H. Forster and H. J. M. De Groot, J. Magn. Reson. 124 (1997) 516.

[40] A. Bielecki, A. C. Kolbert and M. H. Levitt, Chem. Phys. Lett. 155 (1989) 341.

[41] A. Bielecki, A. C. Kolbert, H. J. M. De Groot, R. G. Griffin and M. H. Levitt, Adv. Magn. Reson. 14 (1990) 111.

[42] M. H. Levitt, A. C. Kolbert, A. Bielecki and D. J. Ruben, Solid State NMR 2 (1993) 151.

[43] M. Lee and W. I. Goldburg, Phys. Rev. A 140 (1965) 1261.

[44] J. S. Waugh, L. M. Huber and U. Haeberlen, Phys. Rev. Lett. 20 (1968) 180.

[45] M. Hohwy and N. C. Nielsen, J. Chem. Phys. 109 (1998) 3780.

[46] P. Mansfield, M. J. Orchard, D. C. Stalker and K. H. B. Richards, Phys. Rev. B 7 (1973) 90.

[47] W.-K. Rhim, D. D. Elleman and R. W. Vaughan, J. Chem. Phys. 59 (1973) 3740.

[48] D. P. Burum and W. K. Rhim, J. Chem. Phys. 71 (1979) 944.

[49] D. P. Burum, M. Linder and R. R. Ernst, J. Magn. Reson. 44 (1981) 173.

[50] D. G. Cory, J. Magn. Reson. 94 (1991) 526.

[51] S. Hafner and H. W. Spiess, J. Magn. Reson. A 121 (1996) 160.

[52] S. Hafner and H. W. Spiess, Solid State NMR 8 (1997) 17.

[53] M. Hohwy, P. V. Bower, H. J. Jakobsen and N. C. Nielsen, Chem. Phys. Lett. 273 (1997) 297.

[54] C. S. Yannoni and H.-M. Vieth, Phys. Rev. Lett. 37 (1976) 1230.

[55] H. Liu, S. J. Glaser and G. P. Drobny, J. Chem. Phys. 93 (1990) 7543.

[56] H. Geen, J. Phys. B: At. Mol. Opt. Phys. 29 (1996) 1699.

[57] U. Haeberlen and J. S. Waugh, Phys. Rev. 175 (1968) 453.

[58] D. E. Demco, S. Hafner and H. W. Spiess, J. Magn. Reson. A 116 (1995) 36.

[59] M. Edén and M. H. Levitt, J. Chem. Phys. 111 (1999) 1511.

[60] M. Carravetta, M. Edénn, X. Zhao, A. Brinkmann and M. H. Levitt, Chem. Phys. Lett. 321 (2000) 205.

[61] O. W. Sørensen, G. W. Eich, M. H. Levitt, G. Bodenhausen and R. R. Ernst, Progr. NMR Spectroscopy 16 (1983) 163.

[62] N. Bloembergen, Physica 15 (1949) 386.

[63] N. Bloembergen, S. Shapiro, P. S. Pershan and J. O. Artman, Phys. Rev. 114 (1959) 445.

[64] M. Goldman, Spin temperature and nuclear magnetic resonance in solids. (Clarendon Press, Oxford, 1970).

[65] S. Zhang, B. H. Meier and R. R. Ernst, Phys. Rev. Lett. 69 (1992) 2149.

[66] R. Brüschweiler and R. R. Ernst, Chem. Phys. Lett. 264 (1997) 393.

[67] J. S. Waugh, Mol. Phys. 95 (1998) 731.

[68] I. J. Lowe, Phys. Rev. Lett. 2 (1959) 285.

[69] E. R. Andrew, A. Bradbury and R. G. Eades, Nature 183 (1959) 1802.

[70] S. R. Hartmann and E. L. Hahn, Phys. Rev. 128 (1962) 2042.

[71] X. Wu, S. T. Burns and K. W. Zilm, J. Magn. Reson. A 111 (1994) 29.

[72] J. Virlet, The encyclopedia of NMR (J. Wiley & Sons, London, 1997).

[73] M. Mehring and J. S. Waugh, Phys. Rev. B 5 (1972) 3459.

[74] A. Bax, R. H. Griffey and B. L. Hawkins, J. Magn. Reson. 55 (1983) 301.

[75] A. Lesage, D. Sakellariou, S. Steuernagel and L. Emsley, J. Am. Chem. Soc. 120 (1998) 13194.

[76] A. Lesage, P. Charmont, S. Steuernagel and L. Emsley, J. Am. Chem. Soc. 122 (2000) 9739.

[77] D. Sakellariou, A. Lesage and L. Emsley, J. Magn. Reson. (2001) in press.

[78] A. E. Bennett, C. M. Rienstra, M. Auger, K. V. Lakshmi and R. G. Griffin, J. Chem. Phys. 103 (1995) 6951.

[79] M. Baldus and B. H. Meier, J. Magn. Reson. A 121 (1996) 65.

[80] A. Lesage, C. Auger, S. Caldarelli and L. Emsley, J. Am. Chem. Soc. 119 (1997) 7867.

[81] C. Auger, Une nouvelle technique de correlation deuterium-carbone pour l'attribution et la mesure des couplages quadrupolaires dans les materiaux orientes. Ph.D. thesis ENS–Lyon (1998).

[82] R. K. Hester, J. L. Ackerman, B. L. Neff and J. S. Waugh, Phys. Rev. Lett. 36 (1976) 1081.

[83] M. M. Maricq and J. S. Waugh, J. Chem. Phys. 70 (1979) 3300.

[84] T. Terao and S. Matshui, Phys. Rev. B 21 (1980) 3781.

[85] K. Wüthrich, NMR of proteins and nucleic acids (Wiley-Interscience, New York, 1986).

[86] O. B. Peersen, X. Wu and S. O. Smith, J. Magn. Reson. A 106 (1994) 127.

[87] S. Hediger, B. H. Meier, N. D. Kurur, G. Bodenhausen and R. R. Ernst, Chem. Phys. Lett. 223 (1994) 283.

[88] H. O. Kalinowski, S. Berger and S. Braun, Carbon-13 NMR spectroscopy (J. Wiley & Sons, Chichester, 1988).

[89] L. Guy, J. Vidal, A. Collet, A. Amour and M. Reboud-Ravaux, J. Med. Chem. 41 (1998) 4833.

[90] R. R. Ernst, G. Bodenhausen and A. Wokaun, Principles of nuclear magnetic resonance in one and two dimensions (Clarendon Press, Oxford, 1989).

[91] G. Metz, X. Wu and S. O. Smith, J. Magn. Reson. A 110 (1994) 219.

[92] D. Marion, M. Ikura, R. Tschudin and A. Bax, J. Magn. Reson. 85 (1989) 393.

[93] M. Hohwy and N. C. Nielsen, J. Chem. Phys. 106 (1997) 7571.

[94] H. J. Reich, M. Jautelat, M. T. Messe, F. J. Weigert and J. D. Roberts, J. Am. Chem. Soc. 91 (1969) 7445.

[95] S. Hediger, Improvement of heteronuclear polarization transfer in solid-state NMR. Ph.D. thesis ETH–Zurich (1997).

[96] C. P. Slichter, Principles of magnetic resonance (Springer, Berlin, 1978).

[97] D. Sakellariou, A. Lesage, P. Hodgkinson and L. Emsley, Chem. Phys. Lett. 319 (2000) 253.

[98] D. Sakellariou and L. Emsley, Proton solid-state NMR spectroscopy using continuous phase modulation (2000) in preparation.

[99] M. E. Rose, Elementary theory of angular momentum (Dover, New York, 1957).

[100] L. Viola, E. Knill and S. Lloyd, Phys. Rev. Lett 82 (1999) 2417.

[101] L. Viola, S. Lloyd and E. Knill, Phys. Rev. Lett. 83 (1999) 4888.

[102] F. J. Dyson, Phys. Rev. 75 (1949) 486.

[103] F. J. Dyson, Phys. Rev. 75 (1949) 1736.

[104] W. Magnus, Comm. Pure & Appl. Math. 7 (1954) 649.

[105] R. M. Wilcox, J. Math. Phys. 8 (1967) 962.

[106] J. Zhou, C. Ye and B. C. Sanctuary, J. Chem. Phys. 101 (1994) 6424.

[107] J. Zhou and C. Ye, Solid State NMR 5 (1995) 213.

[108] Y. Ishii and T. Terao, J. Chem. Phys. 109 (1998) 1366.

[109] R. Courant and D. Hilbert, Methods of mathematical physics vol. 1 (Wiley-Interscience, New York, 1989).

[110] G. E. Maciel, C. E. Bronnimann and B. L. Hawkins, Adv. Magn. Reson. 14 (1990) 125.

[111] D. P. Burum, D. G. Cory, K. K. Gleason, D. Levy and A. Bielecki, J. Magn. Reson. A 104 (1993) 347.

[112] L. Zheng, K. W. Fishbein, R. G. Griffin and J. Herzfeld, J. Am. Chem. Soc. 115 (1993) 6254.

[113] S. Ding and C. A. McDowell, J. Magn. Reson. A 115 (1995) 141.

[114] E. Vinogradov, P. K. Madhu and S. Vega, Chem. Phys. Lett. 314 (1999) 443.

[115] D. J. States, R. A. Haberkorn and D. J. Ruben, J. Magn. Reson. 48 (1982) 286.

[116] W. H. Press, S. A. Teukolsky, W. T. Vetterling and B. P. Flannery, Numerical recipes in c: The art of scientific computing (Cambridge University Press, Cambridge, 1992).

[117] M. Edén, Y. K. Lee and M. H. Levitt, J. Magn. Reson. A 120 (1996) 56.

[118] M. M. Maricq, J. Chem. Phys. 85 (1986) 5167.

[119] J. R. Sachleben, S. Caldarelli and L. Emsley, J. Chem. Phys. 104 (1996) 2518.

[120] M. H. Levitt and R. Freeman, J. Magn. Reson. 33 (1979) 473.

[121] M. H. Levitt, Progres in NMR Spectroscopy 18 (1986) 61.

[122] M. H. Levitt, The encyclopedia of NMR (J. Wiley & Sons, London, 1997).

[123] R. Freeman, S. P. Kempsell and M. H. Levitt, J. Magn. Reson. 38 (1980) 453.

[124] M. H. Levitt, J. Magn. Reson. 48 (1982) 234.

[125] M. H. Levitt, J. Magn. Reson. 50 (1982) 95.

[126] C. Counsell, M. H. Levitt and R. R. Ernst, J. Magn. Reson. 63 (1985) 133.

[127] M. H. Levitt and R. Freeman, J. Magn. Reson. 43 (1981) 65.

[128] R. Tycko, Phys. Rev. Lett. 51 (1983) 775.

[129] R. Tycko, E. Schneider and A. Pines, J. Chem. Phys. 81 (1984) 680.

[130] R. Tycko, H. M. Cho, E. Schneider and A. Pines, J. Magn. Reson. 61 (1985) 90.

[131] A. J. Shaka and A. Pines, J. Magn. Reson. 71 (1987) 495.

[132] S. Wimperis, J. Magn. Reson. A 109 (1994) 221.

[133] A. J. Shaka, J. Keeler, M. B. Smith and R. Freeman, J. Magn. Reson. 61 (1985) 175.

[134] Z. Starčuk and V. Sklenář, J. Magn. Reson. 62 (1985) 113.

[135] D. J. Lurie, J. Magn. Reson. 70 (1986) 11.

[136] C. S. Poon and R. M. Henkelman, J. Magn. Reson. 99 (1992) 45.

[137] N. Sunitha Bai, M. Ramakrishna and R. Ramachandran, J. Magn. Reson. A 102 (1993) 235.

[138] K. Scheffler, J. Magn. Reson. B 109 (1995) 175.

[139] M. H. Levitt and R. R. Ernst, J. Magn. Reson. 55 (1983) 247.

[140] R. Tycko and A. Pines, J. Magn. Reson. 60 (1984) 156.

[141] R. Tycko and A. Pines, Chem. Phys. Lett. 111 (1984) 462.

[142] J. S. Waugh, J. Magn. Reson. 49 (1982) 517.

[143] J. S. Waugh, J. Magn. Reson. 50 (1982) 30.

[144] A. J. Shaka, C. J. Lee and A. Pines, J. Magn. Reson. 77 (1988) 274.

[145] D. Abramovich and S. Vega, J. Magn. Reson. A 105 (1993) 30.

[146] Ē. Kupče and R. Freeman, J. Magn. Reson. A 115 (1995) 273.

[147] Ē. Kupče and R. Freeman, J. Magn. Reson. A 117 (1995) 246.

[148] Ē. Kupče and R. Freeman, J. Magn. Reson. A 118 (1996) 299.

[149] T. Fujiwara and K. Nagayama, J. Magn. Reson. 77 (1988) 53.

[150] J. Baum, R. Tycko and A. Pines, J. Chem. Phys. 79 (1983) 4643.

[151] C. Moler and C. Van Loan, Society for Industrial and Applied Mathematics (SIAM Review) 20 (1978) 801.

[152] A. J. Shaka and R. Freeman, J. Magn. Reson. 63 (1985) 596.

[153] A. J. Shaka and R. Freeman, J. Magn. Reson. 64 (1985) 145.

[154] R. Kemp-Harper, P. Styles and S. Wimperis, J. Magn. Reson. A 123 (1996) 230.

[155] B. H. Meier, Adv. Magn. Reson. 18 (1994) 1.

[156] M. Linder, P. M. Henrichs, J. M. Hewitt and D. J. Massa, J. Chem. Phys. 82 (1985) 1585.

[157] D. L. VanderHart, J. Magn. Reson. 72 (1987) 13.

[158] A. Kubo and C. A. McDowell, J. Chem. Phys. 89 (1988) 63.

[159] R. R. Eckman, P. M. Henrichs and A. J. Peakock, Macromolecules 30 (1997) 2474.

[160] P. M. Henrichs and M. Linder, J. Magn. Reson. 58 (1984) 458.

[161] I. Schnell, S. P. Brown, H. Y. Low, H. Ishida and H. W. Spiess, J. Am. Chem. Soc. 120 (1998) 11784.

[162] A. Z. Genack and A. G. Redfield, Phys. Rev. B 12 (1975) 78.

[163] W. Zhang and D. G. Cory, Phys. Rev. Lett. 80 (1998) 1324.

[164] S. V. Pogrebnyak and E. A. Shadchin, Sov. Phys. Solid State 22 (1980) 1514.

[165] N. M. Szeverenyi, M. J. Sullivan and G. E. Maciel, J. Magn. Reson. 47 (1982) 462.

[166] D. Suter and R. R. Ernst, Phys. Rev. B 25 (1982) 6038.

[167] D. Suter and R. R. Ernst, Phys. Rev. B 32 (1985) 5608.

[168] A. Kubo and C. A. McDowell, J. Chem. Soc. Faraday Trans. 1 84 (1988) 3713.

[169] F. M. Mulder, W. Heiner, M. van Duin, J. Lugtenburg and H. J. M. de Groot, J. Am. Chem. Soc. 120 (1998) 12891.

[170] J. Jeener, B. H. Meier, P. Bachmann and R. R. Ernst, J. Chem. Phys. 71 (1979) 4546.

[171] G. Bodenhausen, R. Freeman and G. A. Morris, J. Magn. Reson. 23 (1976) 171.

[172] G. A. Morris and R. Freeman, J. Magn. Reson. 29 (1978) 433.

[173] P. Caravatti, G. Bodenhausen and R. R. Ernst, J. Magn. Reson. 55 (1983) 88.

[174] P. Caravatti, M. H. Levitt and R. R. Ernst, J. Magn. Reson. 68 (1986) 323.

[175] T. A. Cross and S. J. Opella, J. Am. Chem. Soc. 105 (1983) 306.

[176] H. T. Edzes and J. P. C. Bernards, J. Am. Chem. Soc. 106 (1984) 1515.

[177] P. Caravatti, Neuenschwander and R. R. Ernst, Macromolecules 19 (1986) 1889.

[178] P. Caravatti, J. A. Deli, G. Bodenhausen and R. R. Ernst, J. Am. Chem. Soc. 104 (1982) 5506.

[179] C. E. Bronnimann, N. M. Szeverenyi and G. E. Maciel, J. Chem. Phys. 79 (1983) 3694.

[180] K. Takegoshi and C. A. McDowell, J. Chem. Phys. 84 (1986) 2084.

[181] D. Reichert, G. Hempel, R. Poupko, Z. Luz, Z. Olejniczak and P. Tekely, Solid State NMR 13 (1998) 137.

[182] P. Tekely, M. J. Ptrzebowski, Y. Dusausoy and Z. Luz, Chem. Phys. Lett. 291 (1998) 471.

[183] P. M. Henrichs, M. Linder and J. M. Hewitt, J. Chem. Phys. 85 (1986) 7077.

[184] H. Kessemeier and R. E. Norberg, Phys. Rev. 155 (1967) 321.

[185] N. J. Clayden, J. Magn. Reson. 68 (1986) 360.

[186] B. H. Meier and R. R. Ernst, J. Am. Chem. Soc. 101 (1979) 6441.

[187] R. Willem, Progress in NMR Spectroscopy 20 (1987) 1.

[188] S. Caldarelli and L. Emsley, J. Magn. Reson. 130 (1998) 233.

[189] P. Hodgkinson and L. Emsley, J. Magn. Reson. 139 (1999) 46.

[190] F. Lado, J. D. Memory and G. W. Parker, Phys. Rev. B 4 (1971) 1406.

[191] S. Vega and A. Pines, J. Chem. Phys. 66 (1977) 5624.

[192] A. Wokaun and R. R. Ernst, J. Chem. Phys. 67 (1977) 1752.

[193] S. Vega, J. Chem. Phys. 68 (1978) 5518.

[194] A. Abragam, The principles of nuclear magnetism (Oxford University Press, Oxford, England, 1961).

[195] J. J. Sakurai, Modern quantum mechanics (Addison-Wesley, 1989).

[196] D. A. McArthur, E. L. Hahn and R. E. Walstedt, Phys. Rev. 188 (1969) 609.

[197] D. E. Demco, J. Tegenfeldt and J. S. Waugh, Phys. Rev. B 11 (1975) 4133.

[198] V. Deininghaus and M. Mehring, Phys. Rev. B 24 (1981) 4945.

[199] T. T. P. Cheung and R. Yaris, J. Chem. Phys. 72 (1980) 3604.

[200] A. Abragam and M. Goldman, Nuclear magnetism: order and disorder (International Series of Monographs in Physics, Oxford, 1981).

[201] S. Macura and R. R. Ernst, Mol. Phys. 41 (1980) 95.

[202] A. Kumar, R. R. Ernst and K. Wüthrich, Biochem. Biophys. Res. Commun. 95 (1980) 1.

[203] P. Hodgkinson and L. Emsley, Prog. Nucl. Magn. Reson. Spectrosc. 36 (2000) 201.

[204] P. Hodgkinson, D. Sakellariou and L. Emsley, Simulation of extended pediodic systems of nuclear spins (2000).

[205] R. S. Dumont, S. Jain and A. Bain, J. Chem. Phys. 106 (1997) 5928.

[206] N. R. Jagannathan, S. S. Rajan and E. Subramanian, J. Chem. Cryst. 24 (1994) 75.

[207] M. S. Lehmann, T. K. Koetzle and W. C. Hamilton, J. Am. Chem. Soc 94 (1972) 2657.

[208] M. G. Colombo, B. H. Meier and R. R. Ernst, Chem. Phys. Lett. 146 (1988) 189.

[209] D. P. Raleigh, M. H. Levitt and R. G. Griffin, Chem. Phys. Lett. 146 (1988) 71.

[210] F. M. Lurie and C. P. Slichter, Phys. Rev. A 133 (1964) 1108.

[211] M. H. Levitt, D. Suter and R. R. Ernst, J. Chem. Phys. 84 (1986) 4243.

[212] M. Hamermesh, Group theory and its application to physical problems (Dover, New York, 1989).

[213] M. Toda, R. Kubo and N. Saitô, Statistical physics I : Equilibrium statistical mechanics (Springer-Verlag, 1992).

[214] R. Brüschweiler, J. Magn. Reson. 124 (1997) 122.

[215] É. B. Fel'dman and S. Lacelle, J. Chem. Phys. 108 (1998) 4709.

[216] A. G. Redfield, Adv. Magn. Reson. 1 (1965) 1.

[217] D. Sakellariou, P. Hodgkinson and L. Emsley, Chem. Phys. Lett. 293 (1998) 110.

[218] R. Brüschweiler, Chem. Phys. Lett. 270 (1997) 217.

[219] N. R. Skrynnikov and R. Brüschweiler, Chem. Phys. Lett. 281 (1997) 239.

[220] B. H. Meier, Chem. Phys. Lett. 188 (1992) 201.

[221] L. Müller, A. Kumar, T. Baumann and R. R. Ernst, Phys. Rev. Lett. 32 (1974) 1402.

[222] J. H. Shirley, Phys. Rev. B 138 (1965) 979.

[223] A. Schmidt and S. Vega, J. Chem. Phys. 96 (1992) 2655.

[224] O. Weintraub and S. Vega, J. Magn. Reson. A 105 (1993) 245.

[225] A. E. Bennett, R. G. Griffin and S. Vega, NMR Basic Principles and Progress 33 (1994) 1.

[226] T. O. Levante, M. Baldus, B. H. Meier and R. R. Ernst, Mol. Phys. 86 (1995) 1195.

[227] M. H. Levitt, D. P. Raleigh, F. Creuzet and R. G. Griffin, J. Chem. Phys. 92 (1990) 6347.

[228] S. Ray, V. Ladizhansky and A. J. Vega, J. Magn. Reson. 135 (1998) 427.

[229] B. N. Provotorov, Soviet Physics JETP 14 (1962) 1126.

[230] M. M. Maricq, Phys. Rev. B 31 (1985) 127.

[231] D. Marks, N. Zumbulyadis and S. Vega, J. Magn. Reson. A 122 (1996) 16.

[232] M. Ernst, B. H. Meier, M. Tomaselli and A. Pines, J. Chem. Phys. 108 (1998) 9611.

[233] P. R. Levstein, G. Usaj and H. M. Pastawski, J. Chem. Phys. 108 (1998) 2718.

[234] E. O. Stejskal, J. Schaefer and J. S. Waugh, J. Magn. Reson. 28 (1977) 105.

[235] D. Marks and S. Vega, J. Magn. Reson. A 118 (1996) 157.

[236] M. H. Levitt and L. Di Bari, Phys. Rev. Lett. 69 (1992) 3124.

[237] A. G. Redfield, Phys. Rev. 98 (1955) 1787.

[238] D. Sakellariou, P. Hodgkinson, S. Hediger and L. Emsley, Chem. Phys. Lett. 308 (1999) 381.

[239] P. Robyr, B. H. Meier and R. R. Ernst, Chem. Phys. Lett. 162 (1989) 417.

[240] A. J. Shaka and J. Keeler, Progress in NMR Spectroscopy 19 (1987) 47.

[241] É. B. Fel'dman and K. T. Summanen, Phys. Stat. Sol. (b) 127 (1985) 509.

[242] B. E. Scruggs and K. K. Gleason, Chem. Phys. 166 (1992) 367.

[243] É. B. Fel'dman and S. Lacelle, Chem. Phys. Lett. 253 (1996) 27.

[244] É. B. Fel'dman and M. G. Rudavets, Chem. Phys. Lett. 311 (1999) 453.

[245] W. Jones and N. H. March, Theoretical solid state physics (Dover, New York, 1973).

[246] E. B. Wilson, J. Chem. Phys. 27 (1957) 60.

[247] P. L. Corio, Chem. Rev. 60 (1960) 363.

[248] P. L. Corio, Structure of high-resolution NMR spectra (Academic Press, New York, 1966).

[249] É. B. Fel'dman, R. Bruschweiler and R. R. Ernst, Chem. Phys. Lett. 294 (1998) 297.

[250] M. Engelsberg, I. J. Lowe and J. L. Carolan, Phys. Rev. B 7 (1973) 924.

[251] N. Boden and Y. K. Levine, Mol. Phys. 29 (1975) 1221.

[252] D. Kouzoudis, Journal of Magnetism and Magnetic Materials 173 (1997) 259.

[253] S. R. White, Physics Reports 301 (1998) 187.

[254] K. Fabricius and B. M. McCoy, Phys. Rev. B 57 (1998) 8340.

[255] É. B. Fel'dman and A. K. Khitrin, Sov. Phys. JETP 71 (1990) 538.

[256] G. Cho and J. P. Yesinowski, J. Phys. Chem. 100 (1996) 15716.

[257] J. Jeener, Adv. Magn. Reson. 10 (1982) 1.

[258] S. Lee, W. Richter, S. Vathyam and W. S. Warren, J. Chem. Phys. 105 (1996) 874.

[259] P. Diehl, H. Kellerhals and E. Lustig, NMR Basic Princ. Prog. 6 (1972) 1.

[260] C. Filip, X. Filip, D. E. Demco and S. Hafner, Mol. Phys. 92 (1997) 757.

[261] C. Filip, S. Hafner, I. Schnell, D. E. Demco and H. W. Spiess, J. Chem. Phys. 110 (1999) 423.

[262] M. Lax, Symmetry properties in solid state and molecular physics (Wiley, New York, 1974).

[263] C. Tang and J. S. Waugh, Phys. Rev. B 45 (1992) 748.

[264] D. K. Sodickson and J. S. Waugh, Phys. Rev. B 52 (1995) 6467.

[265] Z. Olender, D. Reichert, A. Müller, H. Zimmermann, R. Poupko and Z. Luz, J. Magn. Reson. A 120 (1996) 31.

[266] D. H. Levy and K. K. Gleason, J. Phys. Chem. 96 (1992) 8125.

[267] A. J. Shaka and R. Freeman, J. Magn. Reson. 55 (1983) 487.

Curriculum Vitæ

Born in Athens (Greece) 22/3/1974.

Studies

- 1991: High School certificate (Option Mathematics, Physics, Chemistry), mention excellent , congratulations of the jury, 3rd place on the national test of chemistry, participation in the olympiade of chemistry (Lodz 1991 - Poland).
- 1992: 1st year in the department of Chemistry of the university of Athens, 1st on the classement, scholarship for 1 year.
- 1993: 2nd year in the department of Chemistry of the university of Athens, 1st on the classement, scholarship for 1 year.
- 1994: 3rd year in the department of Chemistry of the university of Athens, transfer through exchange program to the École Normale Supérieure de Lyon.
- 1995: License of Chemistry - Physics at the École Normale Supérieure de Lyon, Mention A.B.
- 1996: Matrise of Chemistry - Physics at the École Normale Suprieure de Lyon, Mention A. B., Scholarship for 1 year.
- 1997: Masters in elementary constituents of matter in the Institute of Nuclear Physics of university Claude Bernard Lyon-1, 2nd on the classement, government bursary for PhD studies (3 years). Magistèr e des sciences de la matière (certificate equivalent to that of chemical engineers).
- 1998–2000: PhD thesis in the laboratory of Stereochemistry and Molecular Interactions of the ENS-Lyon under the direction of Pr. L. Emsley.

Languages

- English, French and Greek ...

Publication List

Articles

- **D. SAKELLARIOU**, P. HODGKINSON and L. EMSLEY, *"Quasi Equilibria in Solid-State NMR"*, Chem. Phys. Lett., **293**, 110, (1998).
- A. LESAGE, **D. SAKELLARIOU**, S. STEUERNAGEL and L. EMSLEY, *"Carbon-Proton Chemical Shift Correlation in Solid-State NMR by Through-Bond Multiple-Quantum Spectroscopy"*, J. Am. Chem. Soc., **120**, 13194 (1998).
- A. LESAGE, **D. SAKELLARIOU**, L. EMSLEY and S. STEUERNAGEL, *"A New Carbon-Proton Chemical Shift Correlation Experiment for Solid-State NMR"*, Bruker Report, **147**, 7 (1999).
- **D. SAKELLARIOU**, P. HODGKINSON, S. HEDIGER and L. EMSLEY, *"Experimental observation of Periodic Quasi Equilibria in Solid-State NMR"*, Chem. Phys. Lett., **308**, 381, (1999).
- **D. SAKELLARIOU**, A. LESAGE, P. HODGKINSON and L. EMSLEY, *"Homonuclear Dipolar Decoupling in Solid-State NMR using Continuous Phase Modulation"*, Chem. Phys. Lett, **319**, 253, (2000).
- P. HODGKINSON, **D. SAKELLARIOU** and L. EMSLEY, *"Simulation of Extended Pediodic Systems of Nuclear Spins"*, Chem. Phys. Lett. , **326**, 515, (2000).
- Z. YAO, H.-T. KWAK, **D. SAKELLARIOU**, L. EMSLEY and P. J. GRANDINETTI, *"Sensitivity Enhancement of the Central Transition NMR Signal of Quadrupolar Nuclei under Magic-Angle Spinning"*, Chem. Phys. Lett., **327**, 85, (2000).

Patents

- International Patent No 198341445.8: "Method to Improve Resolution of Two-Dimensional Heteronuclear Correlation Spectra in Solid-State NMR"

Oral Presentations

- Title: "Heteronuclear Chemical Shift Correlation in Solid-State NMR by Through-Bond Multiple-Quantum Spectroscopy", 14^{th} International Meeting on NMR Spectroscopy", Royal Society, Edinbourg, 1999.
- Title: "Heteronuclear Chemical Shift Correlation in Solid-State NMR by Through-Bond Multiple-Quantum Spectroscopy", Alpine Conference on Solid-State NMR, Chamonix, 1999.